ERDC/GSL TR-23-4

US Army Corps of Engineers®
Engineer Research and Development Center

ERDC
ENGINEER RESEARCH & DEVELOPMENT CENTER

Naval Expeditionary Runway Construction Criteria

P-8 Poseidon Pavement Requirements

W. Jeremy Robinson, Jeremiah M. Stache, Jeb. S. Tingle,
Carlos R. Gonzalez, Anastasios M. Ioannides,
and James T. Rushing

March 2023



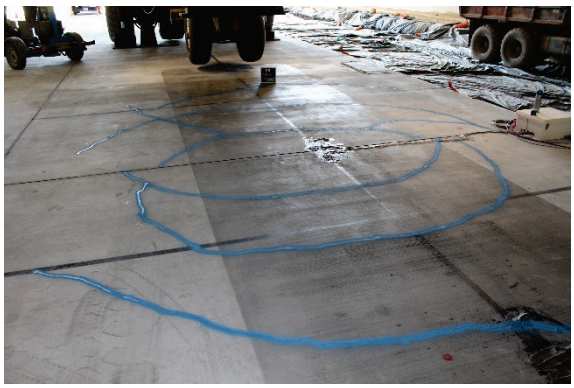


Geotechnical and Structures Laboratory

The US Army Engineer Research and Development Center (ERDC) solves the nation's toughest engineering and environmental challenges. ERDC develops innovative solutions in civil and military engineering, geospatial sciences, water resources, and environmental sciences for the Army, the Department of Defense, civilian agencies, and our nation's public good. Find out more at www.erdc.usace.army.mil.

To search for other technical reports published by ERDC, visit the ERDC online library at https://erdclibrary.on.worldcat.org/discovery.

ERDC/GSL TR-23-4
March 2023

Naval Expeditionary Runway Construction Criteria

P-8 Poseidon Pavement Requirements

W. Jeremy Robinson, Jeremiah M. Stache, Jeb S. Tingle, Carlos R. Gonzalez, Anastasios M. Ioannides, and James T. Rushing

Geotechnical and Structures Laboratory
US Army Engineer Research and Development Center
3909 Halls Ferry Road
Vicksburg, MS 39180-6199

Final report

Prepared for Naval Facilities Engineering and Expeditionary Warfare Center (NAVFAC EXWC)
1100 23rd Ave.
Port Hueneme, CA 93043

Under Project No. 488187; Funding Account Code B36399

Abstract

A full-scale airfield pavement test section was constructed and trafficked by the US Army Engineer Research and Development Center to determine minimum rigid and flexible pavement thickness requirements to support contingency operations of the P-8 Poseidon aircraft. Additionally, airfield damage repair solutions were tested to evaluate the compatibility of those solutions with the P-8 Poseidon. The test items consisted of various material thickness and strengths to yield a range of operations to failure allowing development of performance predictions at a relatively lower number of design operations than are considered in traditional sustainment pavement design scenarios. Test items were trafficked with a dual-wheel P-8 test gear on a heavy-vehicle simulator. Flexible pavement rutting, rigid pavement cracking and spalling, instrumentation response, and falling-weight deflectometer data were monitored at select traffic intervals. The results of the trafficking tests indicated that existing design predictions were generally overconservative. Thus, minimum pavement layer thickness recommendations were made to support a minimum level of contingency operations. The results of full-scale flexible pavement experiment were utilized to support an analytical modeling effort to extend flexible pavement thickness recommendations beyond those evaluated.

Contents

Figures and Tables

Figures

Tables

Preface

This study was conducted for the Naval Facilities Engineering and Expeditionary Warfare Center (NAVFAC EXWC) and the Naval Expeditionary Combat Command under Project No. 488187, Funding Account Code B36399. Mr. Michael L. Ringen, NAVFAC, provided technical guidance and review during the project. Mr. Scott Barradas, NAVFAC, provided program oversight. Mr. Jeb S. Tingle, senior scientific technical manager, Geotechnical and Structures Laboratory (GSL), US Army Engineer Research and Development Center (ERDC), was the ERDC program manager.

The work was performed by the Airfields and Pavements Branch (GMA) of the Engineering Systems Division (GM), ERDC-GSL. At the time of publication, Ms. Anna M. Jordan was chief, GMA; Mr. Justin S. Strickler was chief, GM; and Mr. Nicholas Boone was the technical director for Force Projection and Maneuver Support. The deputy director of ERDC-GSL was Mr. Charles W. Ertle II, and the director was Mr. Bartley P. Durst.

COL Christian Patterson was the commander of ERDC, and Dr. David W. Pittman was the director.

1 Introduction

1.1 Background

The P-8 Poseidon aircraft presents a unique structural challenge for military airfield pavements. Reported increases in load-related distresses from P-8 trafficking are likely due to greater gear loads compared to fighter aircraft coupled with greater tire pressures compared to cargo aircraft. The close spacing of the dual-tire gear configuration has also been damaging to pavement joints. In addition, airfield damage repair (ADR) technologies have not been validated for the P-8 loading; thus, their performance under P-8 loading conditions is unknown. Currently, UFC 3-260-02 (USACE 2001) outlines performance criteria for conventional flexible and rigid airfield pavements based on the California bearing ratio (CBR) vertical stress-based methodology and Westergaard's thin plate theory, respectively. There are also performance criteria established for these pavement systems using layered elastic analysis. These performance criteria were based upon diverse military aircraft systems with significantly different loading conditions, and their applicability to the P-8's military gear configuration is uncertain. In addition, conventional airfield pavement design criteria are based upon the design of enduring pavement systems sustaining many aircraft operations over a lengthy service life. Furthermore, there is currently no formal performance model established for anything related to airfield crater repairs except for the airfield matting distress model outlined in reports such as MP-4-29 (Foster and Burns 1952), TR No. 3-539 (Thompson and Burns 1960) and the semi-prepared runway criteria discussed in TR S-70-5 (Hammitt and Aspinall 1970). Current ADR performance criteria is based upon empirical testing to meet minimum mission requirements. Consequently, there is a need to gather performance data in terms of simulated P-8 aircraft traffic over nonstandard expeditionary pavement structures and ADR sections.

1.2 Objective

The objective of this research was to develop improved rigid and flexible pavement performance criteria for expeditionary operations of the fully loaded P-8 aircraft. These criteria were based on results from a full-scale instrumented test section trafficked by a simulated P-8 gear.

There were two distinct components to the effort: (1) evaluation of the minimum structural pavement design required to support expeditionary operations and (2) evaluation of the compatibility/performance of P-8 operations on emerging ADR technologies.

1.3 Scope

The performance of relatively thin pavement structures and emerging ADR technologies were evaluated under simulated P-8 traffic. Full-scale instrumented pavement test sections were constructed to fully characterize the pavement structural support requirements for the P-8 aircraft. The test program included two distinct evaluations: (1) the suitability of emerging ADR technologies for supporting P-8 aircraft operations and (2) the minimum structural requirements for designing, building, and operating expeditionary airfields to sustain a limited number of P-8 sorties. The full-scale instrumented pavement sections were designed with different layer thicknesses and surface types (flexible pavement and rigid pavement).

1.4 Approach

The test sections were trafficked with the US Army Engineer Research and Development Center's (ERDC's) Heavy Vehicle Simulator (HVS) using authentically configured actual P-8 aircraft wheels loaded to simulate the maximum operational weight of the aircraft. The performance of the various expeditionary pavement sections was recorded and used to establish pass-to-failure performance data to validate or adjust the existing pavement performance curve as required. The performance in terms of passes to failure of the emerging ADR technologies was also recorded to verify the compatibility of these new expedient ADR solutions for use with the P-8 aircraft. In addition, pavement response data were collected from the pavement instrumentation to inform mechanistic pavement models suitable to adapt current pavement design and evaluation criteria for the P-8. Finally, the construction of the different full-scale pavement sections provided information regarding the constructability of these pavement features in expeditionary environments. These performance data can be used to mitigate risk by increasing confidence in the performance criteria while providing the Navy with options for expeditionary airfield designs for the P-8 that reduce construction costs. The results of the full-scale experimentation were used to draft new criteria documents for the construction of Navy expeditionary airfields.

2 Test Plan and Layout

A large, full-scale pavement test section was constructed under cover in Hangar 2 at ERDC. Construction under cover minimized the influence of soil moisture changes caused by variable weather conditions throughout the duration of the test.

The full-scale test sections were designed to accomplish the objectives of the test program given the constraints imposed by the available funding and schedule. Thus, a full matrix of independent variables was cost prohibitive and would have taken years to accomplish. The test sections were designed to provide the required information to evaluate existing performance models for the P-8, to provide enough performance data to modify the models for improved low-pass criteria if necessary, and to validate the performance compatibility of the P-8 with new expeditionary ADR technologies.

Figure 1 shows a plan view of the P-8 Runway Construction Criteria full-scale test section for rigid and flexible pavements. This test section supported the evaluation of ADR technology compatibility with the P-8 and the evaluation of the minimum structural requirements for expeditionary runways supporting the P-8. Figure 2 shows a profile view outlining the structural layering of the individual test items.

Figure 1. Plan view of P-8 runway construction criteria test section.

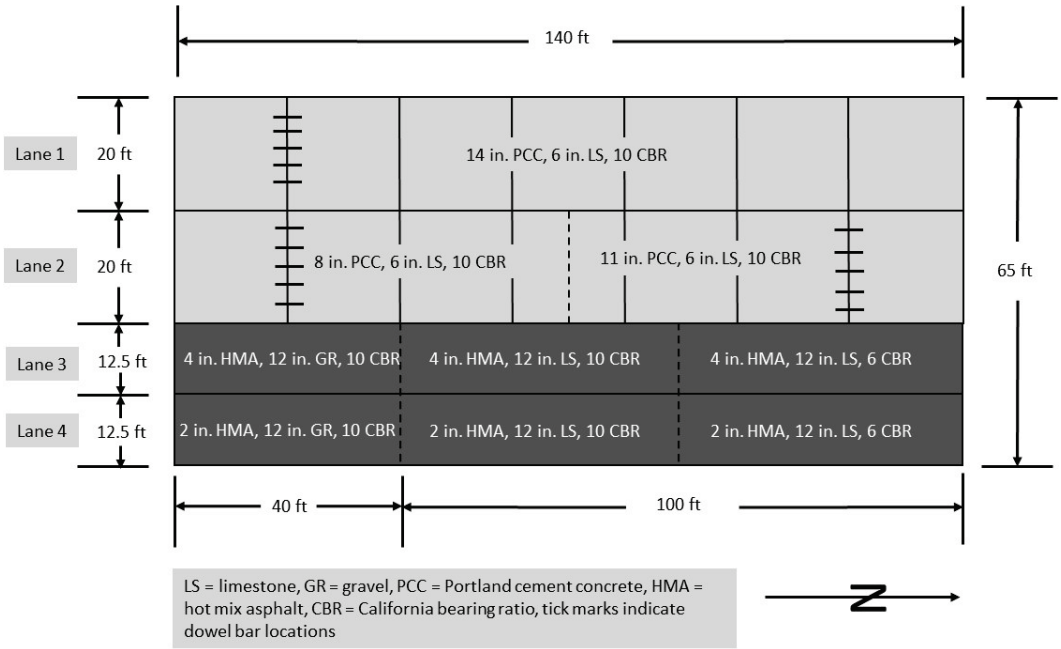

Figure 2. Profile view of P-8 construction criteria test lanes.

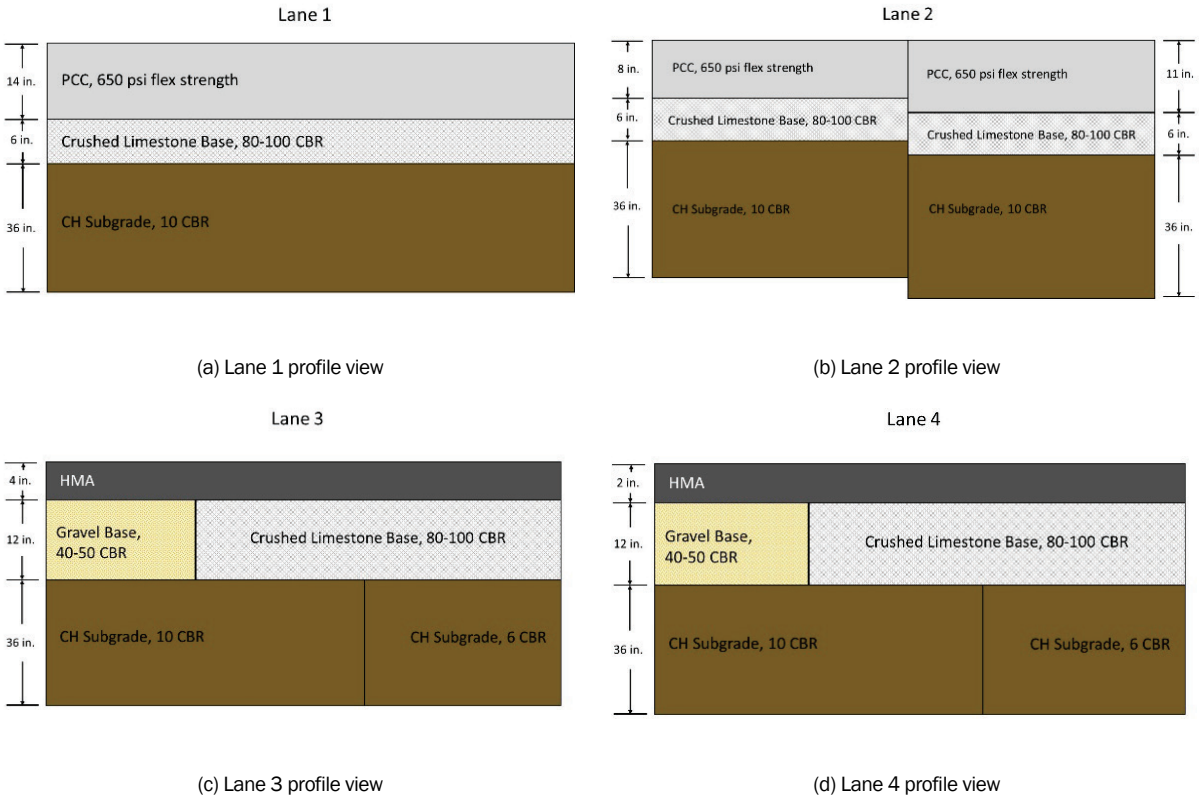

(a) Lane 1 profile view

(b) Lane 2 profile view

(c) Lane 3 profile view

(d) Lane 4 profile view

2.1 Pavement Structural Requirements

Figure 1 shows that test Lanes 1 and 2 each consisted of seven 20 ft by 20 ft[1] slabs of PCC. Lane 1 was comprised of 14 in. thick PCC over a 6 in. thick crushed limestone subbase/working platform over a 10 CBR high-plasticity (CH) subgrade. Lane 1 served two purposes: (1) to provide an upper end performance point for PCC pavements (approximately 5,000–10,000 passes) and (2) to provide a location for evaluation of the Expedient and Expeditionary Airfield Damage Repair (E-ADR) technologies. Lane 2 consisted of two thickness of PCC (8 in. and 11 in.) placed over a 6 in. thick crushed limestone subbase/working platform over a 10 CBR CH subgrade. The purpose of Lane 2 was to provide P-8 performance data for relatively thin PCC slabs (designed for approximately 100–500 passes) and medium thicknesses of PCC (designed for approximately 750–3,000 passes). Dowel-bar assemblies were installed along one joint in each PCC test item to

[1] For a full list of the spelled-out forms of the units of measure used in this document, please refer to *US Government Publishing Office Style Manual*, 31st ed. (Washington, DC: US Government Publishing Office, 2016), 248–252, https://www.govinfo.gov/content/pkg/GPO-STYLEMANUAL-2016/pdf/GPO-STYLEMANUAL-2016.pdf.

investigate load transfer. The assemblies consisted of 1.25 in. diam epoxy-coated dowel bars 18 in. long and spaced at 12 in. intervals. Lanes 3 and 4 were designed to collect P-8 performance data on relatively thin hot mix asphalt (HMA) flexible pavements. Lane 3 consisted of a 4 in. thick layer of HMA placed over 12 in. of a low-quality crushed gravel base over a 10 CBR CH subgrade. The same 4 in. thick HMA layer was placed over 12 in. of high-quality base material over two different CH subgrade strengths (6 and 10 CBR). Current Navy criteria allow 4 in. as the minimum HMA thickness for conventional airfield flexible pavements. Lane 4 consisted of the same pavement cross sections with only 2 in. of HMA as an absolute minimum design for limited traffic in an expeditionary environment. The inclusion of the lower-quality crushed gravel base provided pavement performance data for situations in which a quality base course meeting Navy standards was unavailable or where the airfield was previously built by other entities. Flexible pavement designs are sensitive to subgrade strength; thus, the two subgrade strengths provided performance data for dissimilar site conditions allowing meaningful evaluation of current performance criteria.

The test items contained a suite of instrumentation consisting of both rigid and flexible pavement strain gauges, earth pressure cells, single-depth deflectometers (SDD), moisture probes, pore-water pressure transducers, and temperature probes. Instrumentation is described in detail in Chapter 5.

Simulated aircraft traffic was applied using a dual-wheel P-8 tire configuration mounted on ERDC's HVS. The dual-wheel gear configuration was loaded to a nominal total force of 89,000 lbf that was verified prior to trafficking using a set of calibrated mobile aircraft scales. Tire pressures were maintained at 220 psi throughout testing and were monitored daily. Details regarding simulated aircraft traffic can be found in Chapter 7.

2.2 ADR Capabilities

For the evaluation of ADR technologies, simulated "craters" were cut through the PCC surface in Lane 1. Each repair technology was constructed within a simulated crater, and the HVS was used to evaluate the performance of the repairs under simulated P-8 traffic. Table 1 outlines the repair technologies that were evaluated.

Table 1. ADR technology combinations.

Repair Number	Surface	Backfill	Subgrade
1	Fiberglass reinforced panels	Geosynthetic reinforced sand	CH
2	Fiberglass reinforced panels	Crushed limestone	CH
3	Fiberglass reinforced panels	Cement stabilized sand	CH
4	Stone and grout	Compacted debris	CH
5	Rapid-setting concrete mix	Compacted debris	CH
6	Calcium sulfoaluminate concrete	Compacted debris	CH

2.3 Analysis Approach

A detailed analysis was conducted to evaluate the performance of the ADR technologies, rigid pavement test items, and flexible pavement items. The compatibility of emerging ADR methods with the P-8 aircraft was directly evaluated, and the number of P-8 passes that each method sustained prior to failure of the system was directly measured. The pavement performance data were analyzed to determine the minimum PCC or HMA thickness necessary to support P-8 operations. Instrumentation response data (stress, strain, and deflection) were used to validate mechanistic pavement response models that allow the extension of the models to other pavement structures of interest. The instrumentation data were used to validate or modify pavement performance models by relating critical pavement response parameters (stress, strain, or deflection at critical locations) to the damage resulting from cumulative traffic passes. These data provided improved and validated models for extending pavement design and evaluation methods to low-volume airfield pavement structures.

Specifically, the following comparisons were made from this study:

- Comparison of passes to failure of emerging ADR methods
- Effect of PCC thickness on passes to failure
- Effect of PCC thickness on measured instrumentation response
- Effect of HMA thickness on passes to failure
- Effect of HMA thickness on measured instrumentation response
- Effect of base course strength on passes to failure
- Effect of base course strength on measured instrumentation response
- Effect of subgrade CBR strength on passes to failure
- Effect of subgrade CBR on measured instrumentation response
- Effect of gross load on pavement response.

3 Materials

Laboratory tests were performed to characterize each component layer material as well as underlying subgrade soils. Material characterization test results are presented in the following paragraphs.

3.1 Subgrade

The design subgrade soil consisted of a locally sourced CH, commonly referred to as Vicksburg buckshot. This material has been used extensively in test section construction principally for its ability to maintain moisture content (and consequently design strength) over an extended time. A particle-size analysis indicated the material consisted of 96.8% fines passing the No. 200 sieve. The soil had a liquid limit (LL) of 85%, a plasticity limit (PL) of 29%, and a plasticity index (PI) of 56%, as determined by American Society for Testing and Materials (ASTM) D4318 (ASTM 2017c). According to the Unified Soil Classification System (USCS) (ASTM 2017a), the soil was classified as CH and an A-7-6 according to the American Association of State and Highway Transportation Officials (AASHTO) classification system (AASHTO 2012).

Modified Proctor compaction tests (ASTM D1557 [2012]) were performed to determine the relationship between moisture content and dry density. The maximum dry density was found to be 106.1 pcf at an optimum moisture content of 17.5% (ASTM 2012). Graphical results of the moisture-density relationship test are shown in Figure 3.

To determine an in-place moisture content at the targeted 10 CBR and 6 CBR, a suite of ASTM D1883 laboratory CBR tests was performed (ASTM 2016). These tests were conducted at moisture contents ranging from approximately 20% to approximately 40%. Based on the relationship between moisture content and CBR, a target moisture content of 28% was selected to achieve a 10 CBR, and a target moisture content of 32% was selected to achieve a 6 CBR. The relationship between CBR and moisture content is presented graphically in Figure 4.

Figure 3. Clay subgrade moisture/density relationship.

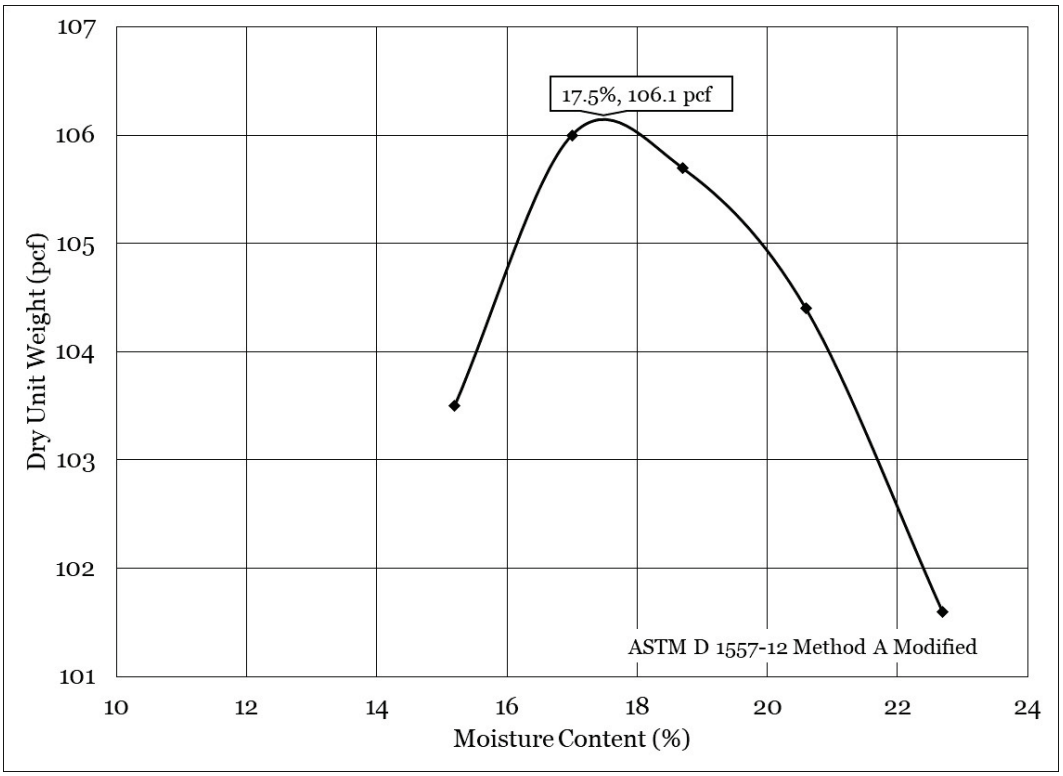

Figure 4. Clay subgrade California bearing ratio (CBR)/moisture content relationship.

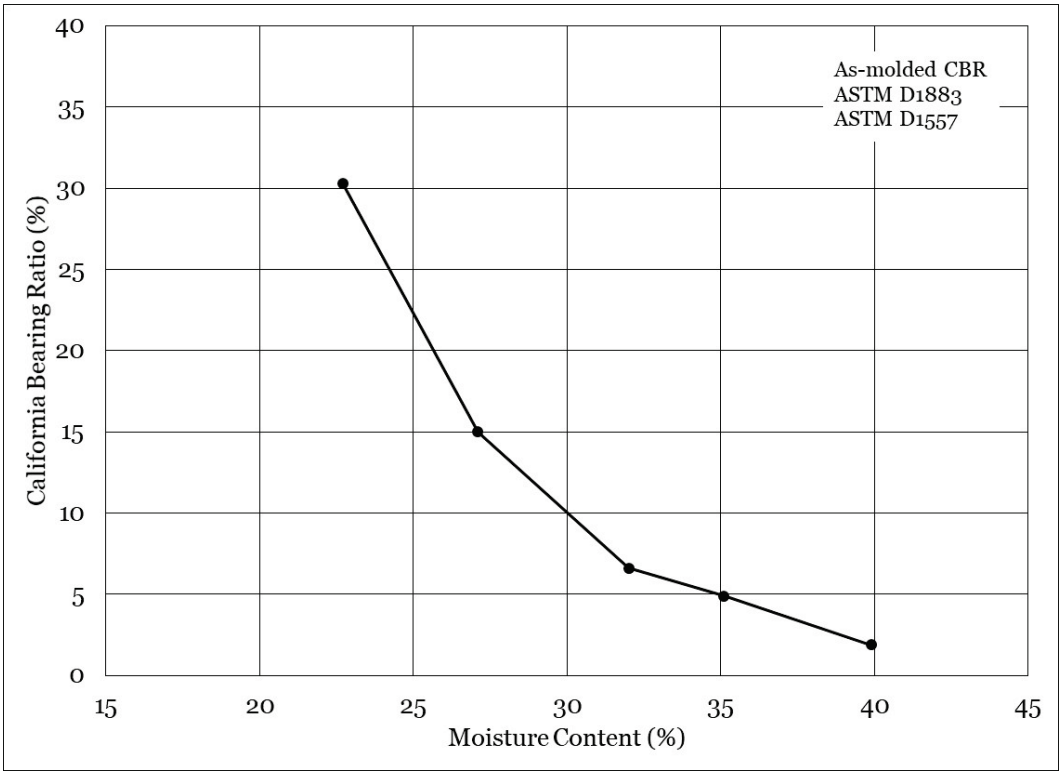

3.2 Base Course

Crushed limestone (LS) and crushed gravel (GR) (Figure 5) were used to construct the flexible aggregate base courses, and LS was used to construct a working platform for concrete placement. LS was selected to represent a strong base (historically this material yields an in situ CBR of 100+) and the GR to represent a base material that may be substantially weaker yet representative of materials that could be encountered in pavement sections in less developed theaters of operation. Material characterization results are summarized in the following sections.

Figure 5. Base course aggregates.

(a) Crushed limestone base (b) Crushed gravel base

3.2.1 LS Base

The gradation for the LS base is shown in Figure 6. ASTM procedure D2487 was used to determine that the base course was comprised of 66.2% gravel, 25.3% sand, and 8.5% nonplastic fines passing the No. 200 sieve (ASTM 2017a). The coefficient of curvature (C_c) was calculated as 7.63, and the coefficient of uniformity (C_u) was 68.21. The LS aggregate base was classified as a poorly graded gravel with silt and sand (GP-GM) according to the USCS (ASTM 2017a) and an A-1-a according to the AASHTO procedure (AASHTO 2012). Modified Proctor compaction tests (Figure 7) were performed in accordance with ASTM D1557 Method C Modified (ASTM 2012). The maximum dry density was 147.9 pcf at an optimum moisture content of 5.2%.

Figure 6. Limestone aggregate particle-size analysis.

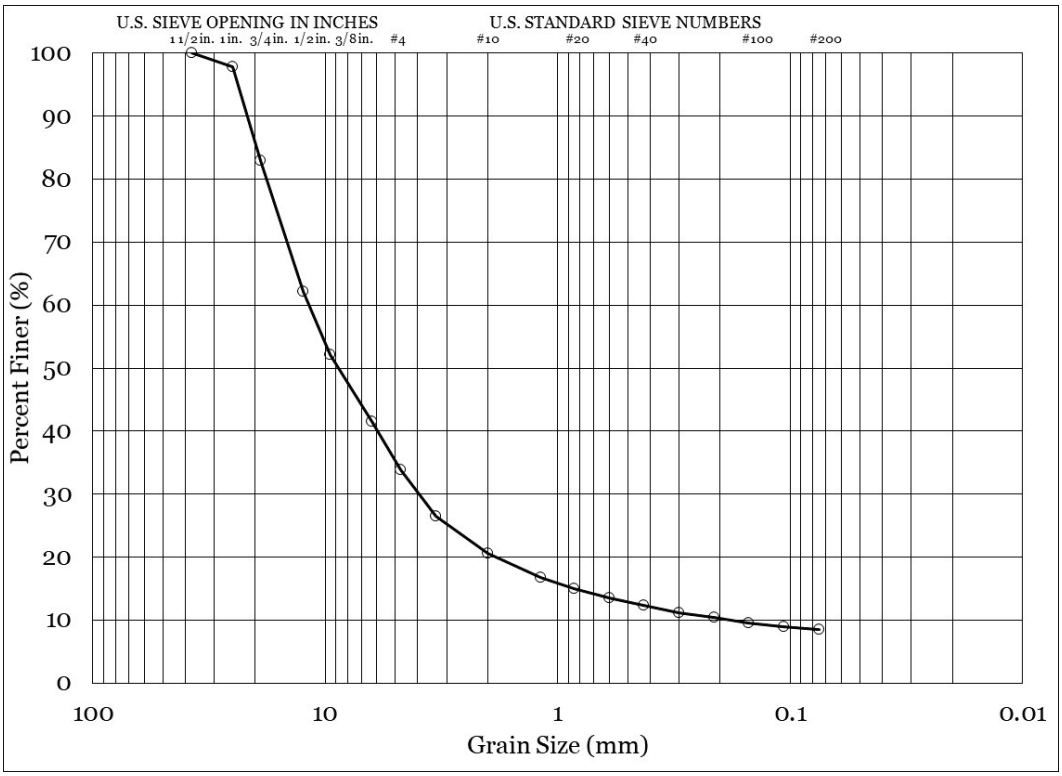

Figure 7. Limestone aggregate moisture/density relationship.

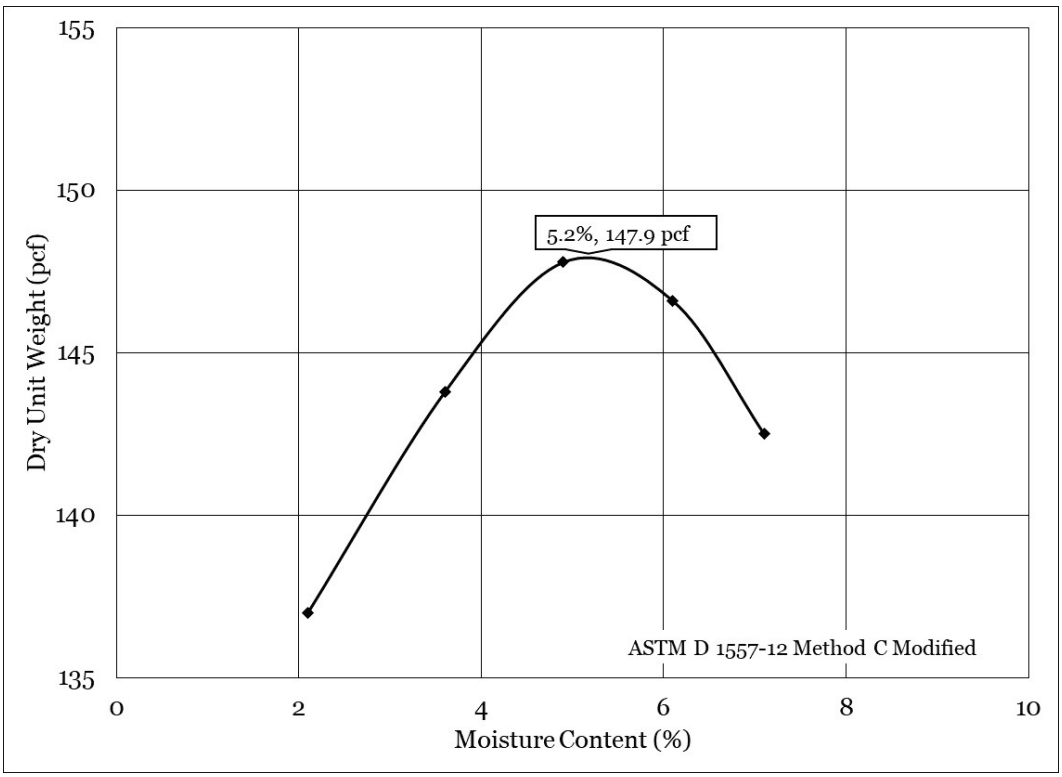

3.2.2 GR Base

The gradation for the crushed gravel is shown in Figure 8. The GR base course was comprised of 38% gravel, 58% sand, and 3.5% nonplastic fines passing the No. 200 sieve. The Cc was calculated as 1.51, and the Cu was 10.56. The GR aggregate base was classified as a well-graded sand (SW) according to the USCS (ASTM 2017a) and an A-1-a according to the AASHTO procedure (AASHTO 2012). Modified Proctor compaction tests (Figure 9) were performed in accordance with ASTM D1557 Method B Modified (ASTM 2012). The maximum dry density was 115.1 pcf at an optimum moisture content of 8.4%.

Figure 8. Crushed gravel base particle-size analysis.

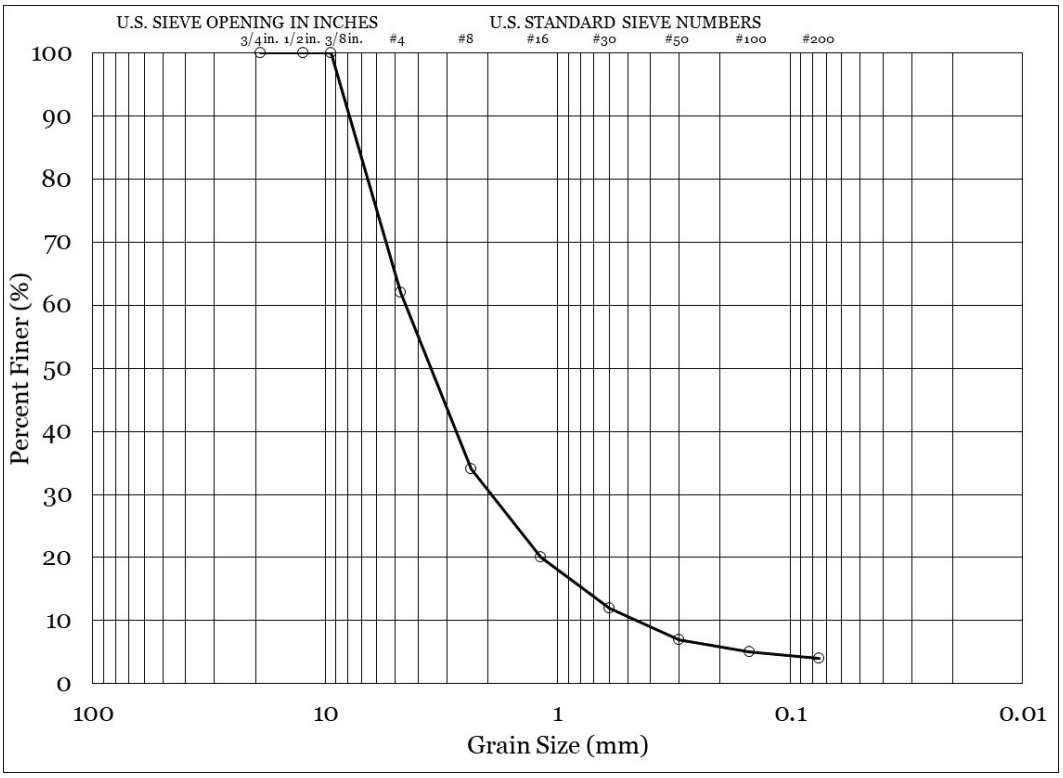

Figure 9. Crushed gravel base moisture/density relationship.

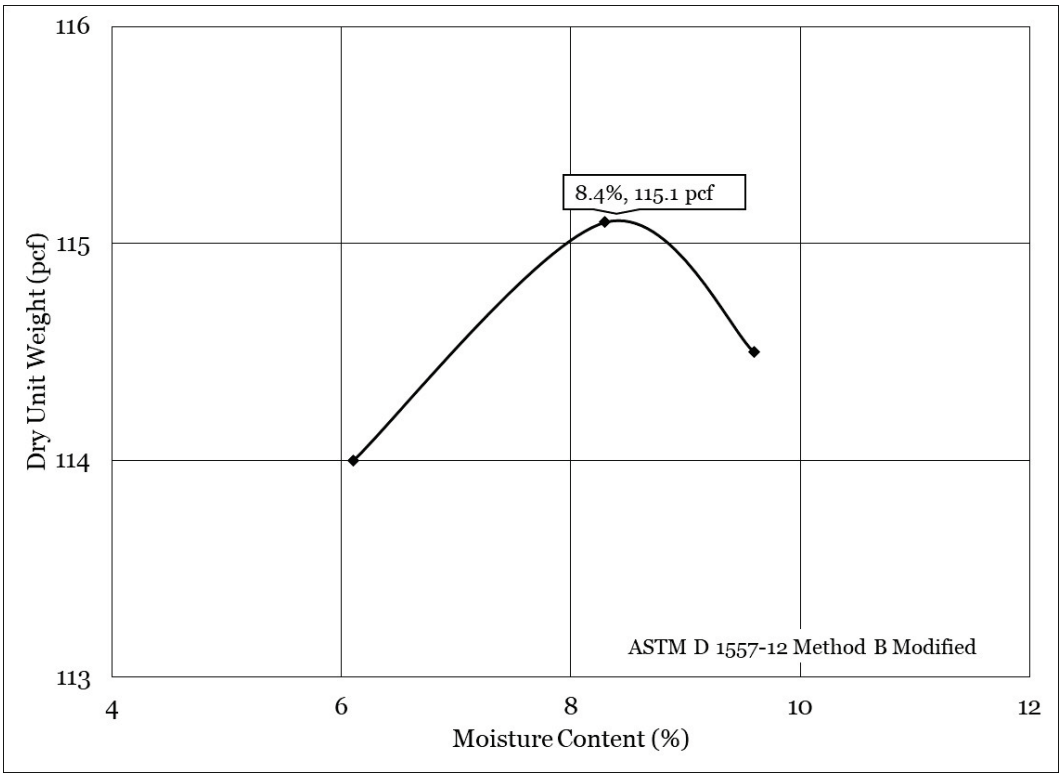

3.3 HMA

A 9.5 mm nominal maximum aggregate size (NMAS) HMA surface mixture was selected for placement of the wearing surface of the flexible test items. The HMA mixture was one that is representative of a typical airfield mix and consisted of 40% limestone aggregate, 59% gravel/sand, and 1% hydrated lime. Recycled asphalt pavement (RAP) was not allowed, and natural sand was limited to 15% of the total aggregate blend. Pertinent mixture properties are summarized in Table 2.

3.4 PCC

A 5,000 psi design compressive strength PCC mixture was selected for placement of the surface of the rigid pavement test items. Additionally, the PCC mixture had a design flexural strength of 650 psi. Cementitious materials consisted of a Type 1 portland cement and a Class C fly ash. Coarse aggregate consisted of an angular crushed limestone aggregate that was classified as a #57 stone (i.e., 1 in. maximum aggregate size.) Pertinent mixture properties are provided in Table 3.

Table 2. Hot-mix asphalt design properties.

Test Property		Design Value
N_{design}		75
Binder Grade		PG 67-22
Mixing Temp (°F)		310
Compaction Temp (°F)		300
Percent Passing (%)	1.0 in. (25.0 mm)	100
	3/4 in. (19.0 mm)	100
	1/2 in. (12.5 mm)	100
	3/8 in. (9.5 mm)	99
	#4 (4.75 mm)	74
	#8 (2.36 mm)	47
	#16 (1.18 mm)	33
	#30 (0.60 mm)	23
	#50 (0.30 mm)	12
	#100 (0.15 mm)	7
	#200 (0.075 mm)	5.3
Aggregate specific gravity (G_{sb})		2.592
Percent binder by total mass (P_b [%])		5.7
Theoretical maximum specific gravity (G_{mm})		2.410
Voids in Mineral Aggregate (%)		15.9
Voids Filled with Asphalt (%)		74.8
P_{200}/P_{be}		1.0

Table 3. Portland cement concrete mixture properties.

Material Type	Description	Design Quantity	Specific Gravity	Volume (ft^3)
Cement	Type 1	526 lb	3.15	2.68
Fly Ash	Class C	132 lb	2.63	0.80
Coarse Aggregate	#57 Limestone	1900 lb	2.69	11.32
Fine Aggregate	Concrete Sand	1083 lb	2.64	6.57
Water	Potable	32 gal.	1.00	4.28
Admixture	Water Reducer	26 oz	–	–
Admixture	Air Entraining	3 oz	–	–
		Air Content	5.00%	1.35
		Yield	3908 lb	27.00
		Unit Weight	144.7 lb/ft^3	
		Design Compressive Strength	5,000 psi	
		Design Slump	4 in.	
		Water/Cementitious Ratio	0.41	

4 Test Section Construction

4.1 Excavation

A 140 ft by 65 ft test section was constructed in ERDC's Hangar 2 Accelerated Pavement Test Facility. The test section consisted of four lanes, each with a different pavement and subgrade combination that are described in detail in Chapter 2. Excavation was completed to a depth of approximately 5 ft using a John Deere 130G tracked excavator (Figure 10). The excavated area was uniformly graded using a motor grader and was recompacted using a smooth drum vibrator roller. After excavation, the bottom and sides of the test section were lined with a 6 mil plastic sheeting to separate the natural subgrade from the constructed subgrade and to encapsulate the pavement test section to prevent moisture migration into/out of the design pavement layers.

Figure 10. Test section excavation and preparation.

(a) John Deere 130G tracked excavator (b) 6 mil plastic sheeting in bottom of excavation

4.2 Subgrade

The CH material described in section 3.1 was used as the subgrade for the entire test section. As previously noted, two moisture contents were targeted to achieve 6 and 10 CBR. Samples were taken from the stockpile to determine the natural moisture content by oven drying, ASTM D2216 (ASTM 2019), or microwave drying, ASTM D4643 (ASTM 2017d). After determining the natural moisture content, the material was spread using multiple loaders to facilitate processing the material to the desired moisture content. If the results of moisture content determinations indicated that the material was above the desired moisture content, natural drying of the material was allowed to occur. If the results of moisture content determinations indicated the material was below the desired moisture content, water was added using

a hydroseeder. Mixing and tilling of the material was performed using a John Deere 6430 tractor with a Frontier RT2308 tiller attachment (Figure 11) to ensure a uniform moisture content was obtained throughout the material. The material was tilled, restockpiled, respread, and tilled again to achieve moisture uniformity. This process was repeated multiple times until moisture uniformity was achieved. Moisture samples were taken frequently throughout the process to monitor changes in moisture content. After the material achieved the desired moisture content, it was stockpiled and covered with a heavy-duty tarp to mitigate moisture content changes prior to placement in the test section.

Figure 11. Mixing and processing equipment.

(a) John Deere 6430 tractor (b) Frontier RT2308 tiller attachment

To prepare the test section for subgrade placement, wooden grade stakes ensured each lift of clay was placed and compacted near a uniform height. Front-end loaders were used to place material within the test section. A CAT 277 Compact Track Loader (CTL) (Figure 12) was used to spread the clay in the test section. After each loose lift was placed, the material was compacted using an Ingram 10000 pneumatic roller and a Dynapac CA25 smooth wheel roller. The Ingram 10000 pneumatic roller had a gross weight of approximately 70,000 lb applied to sets of pneumatic tires inflated to 120 psi. During the compaction process, a Troxler 3440 nuclear density gauge (ASTM D6938) was used to measure density (ASTM 2017b). After completion of the compaction process for each lift, the clay layer was covered with 6 mil plastic sheeting to mitigate a loss of moisture from the placed clay layer. Quality control testing was performed on each lift to ensure strength requirements were achieved and to measure uniformity throughout the test section. The ASTM D4429 field CBR test (ASTM 2009a) was performed on each lift as a quality control test. After all lifts of the subgrade were completed, a motor grader was used to finalize the desired elevation of the test section. Gauges were installed after the grading process was complete.

Figure 12. Material placement equipment.

(a) CAT 277 CTL

(b) Ingram 10000 pneumatic roller

(c) Smooth-drum vibrator roller

(d) Motor grader

4.3 Base Course

After the subgrade was completed, an aggregate base layer was placed. The aggregate base layer was not processed to a desired moisture content outside of the test section. Instead, the aggregate base layer was placed in the test section with a front-end loader and spread using a CTL. The aggregate base layer was compacted at its natural moisture content using a smooth drum vibratory roller. A nuclear density gauge and CBR tests were performed to ensure strength requirements were achieved. A motor grader was used to achieve the final desired elevation.

4.4 Surface Layers

Placement of the PCC and HMA surface layers were completed by contracting local suppliers. ERDC personnel performed construction oversight and material acceptance.

5 Instrumentation

Instrumentation was installed to monitor pavement response during test section trafficking. Sensors installed in the rigid pavement test items included earth pressure cells (EPCs), surface strain gauges (SSG), and embedded strain gauges (ESG). Sensors installed in the flexible pavement test items included EPCs, SDDs, and asphalt strain gauges (ASGs). Pore-water pressure transducers, temperature sensors, and moisture sensors were installed to monitor environmental parameters. Figures 13 and 14 show the plan and profile view of the typical instrumentation layout for a rigid pavement test item, respectively. Figures 15 and 16 show the plan and profile view of the typical instrumentation layout for a flexible pavement test item, respectively.

Figure 13. Plan view of typical PCC instrumentation layout.

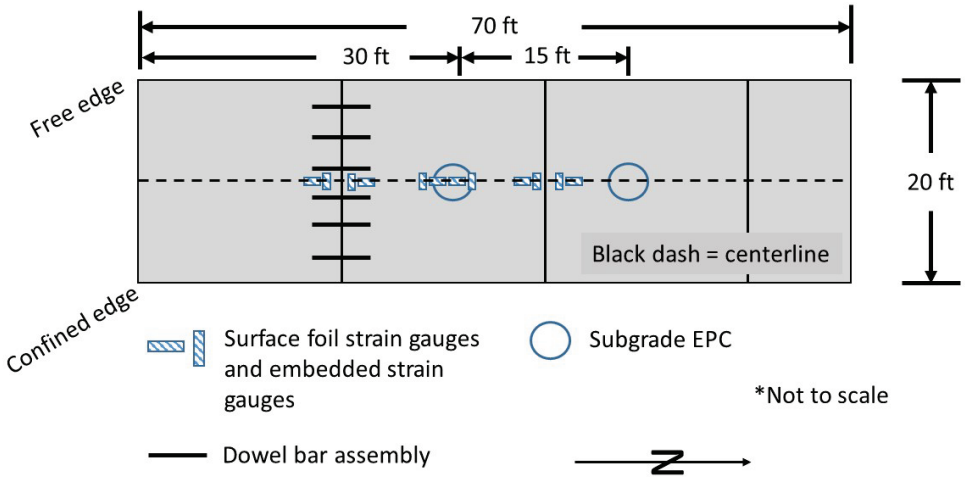

Figure 14. Profile view of typical PCC instrumentation layout.

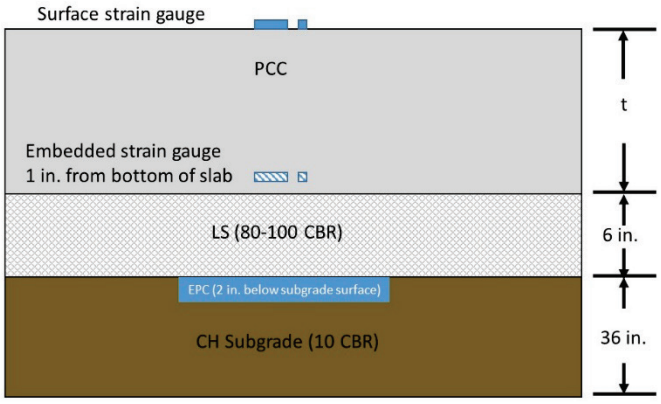

PCC = Portland cement concrete; LS = crushed limestone base; CH = high-plasticity clay; CBR = California bearing ratio; t = thickness (in.)

Figure 15. Plan view of typical HMA instrumentation layout.

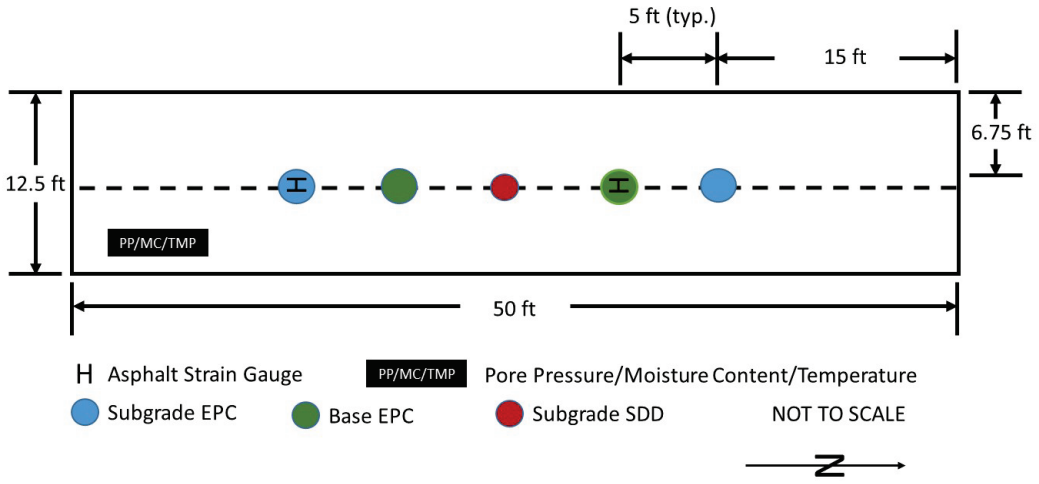

Figure 16. Profile view of typical HMA instrumentation layout.

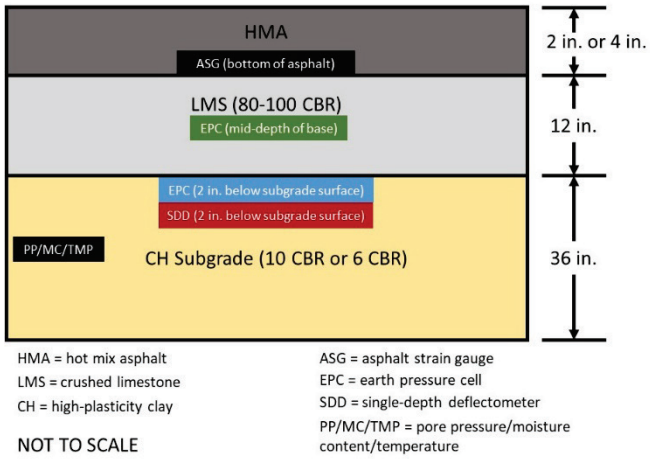

5.1 Subgrade and Base Vertical Pressure Cells

Vertical stresses in the base course and subgrade were measured using 9 in. diam Geokon EPCs. EPCs provided a quantitative measurement of the vertical distribution of the stresses within each traffic lane during testing. Cells with a maximum pressure range up to 145 psi were installed in the subgrade of the PCC and HMA test items, and EPCs with a maximum pressure range of 325 psi were installed in the base course of the HMA test items. The EPCs in the base course were located 2 in. below the top of the base and at middepth of the base course of the HMA test items. The EPCs placed in the subgrade of the PCC and HMA test items were located 2 in. below the top of the subgrade. Figure 12 shows an EPC being installed 2 in. below the surface of the subgrade at the interface with the base course.

Installation (Figure 17) commenced by locating each EPC at the preplanned station within each test item and carefully outlining the excavation area to minimize disturbance to adjacent soils. Measurements were made using a rod and level to determine pre-excavation elevation and to benchmark proper placement depth. The EPC area was excavated to the target depth, the bottom of the excavation was carefully leveled, and a thin layer of clean sand was evenly spread to ensure the gauge maintained full contact with the underlying subgrade soils. Shallow trenches (approximately 1 in. deep) were excavated to the edge of each test item for wire placement and protection from subsequent construction activities. After excavation was complete, an EPC was placed in the excavation, and its alignment was verified. Design subgrade soils were placed around each EPC and were compacted with a pneumatic hammer to minimize density variations in the disturbed area.

Figure 17. EPC installation technique.

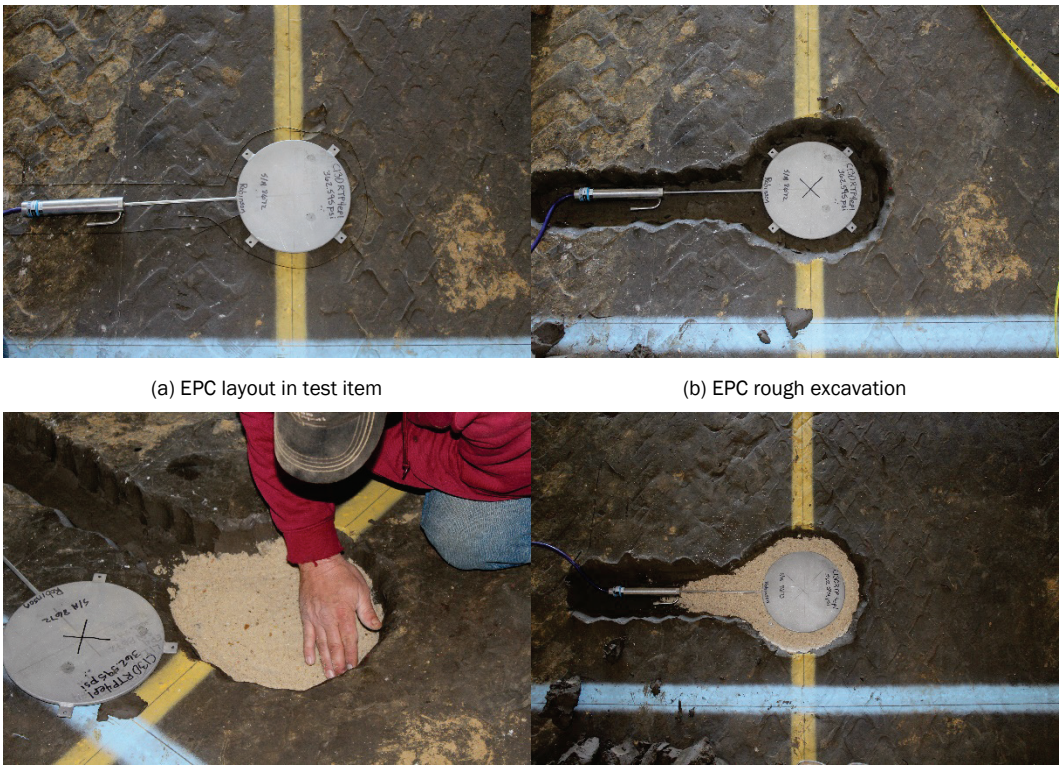

(a) EPC layout in test item

(b) EPC rough excavation

(c) Spreading thin sand layer

(d) Placement completed

5.2 Rigid Pavement Strain Gauges

Embedded concrete strain gauges, manufactured by Bridge Diagnostics Inc., were used to measure tensile strain near the bottom of the rigid pavement. Capable of measuring ± 2,000 microstrains, the gauges were 9 in. long and

were comprised of a full Wheatstone bridge circuit with four active 350 ohm strain gauges. Each gauge was installed 1 in. above the bottom of the concrete layer. Four-inch-long spikes with an oversized nut welded to the head of the spike were used to secure the gauges prior to concrete placement. Spikes were driven into the prepared base course such that the center of the welded nut was 1 in. above the prepared base course. The threaded ends of each concrete gauge were fed through the welded nut and a second nut was used to secure the threaded end of a concrete gauge. Lead wires from a gauge array were secured together and routed outside the test area. Photographs of an embedded concrete strain gauge array are shown in Figure 18.

Figure 18. Embedded concrete strain gauge installation.

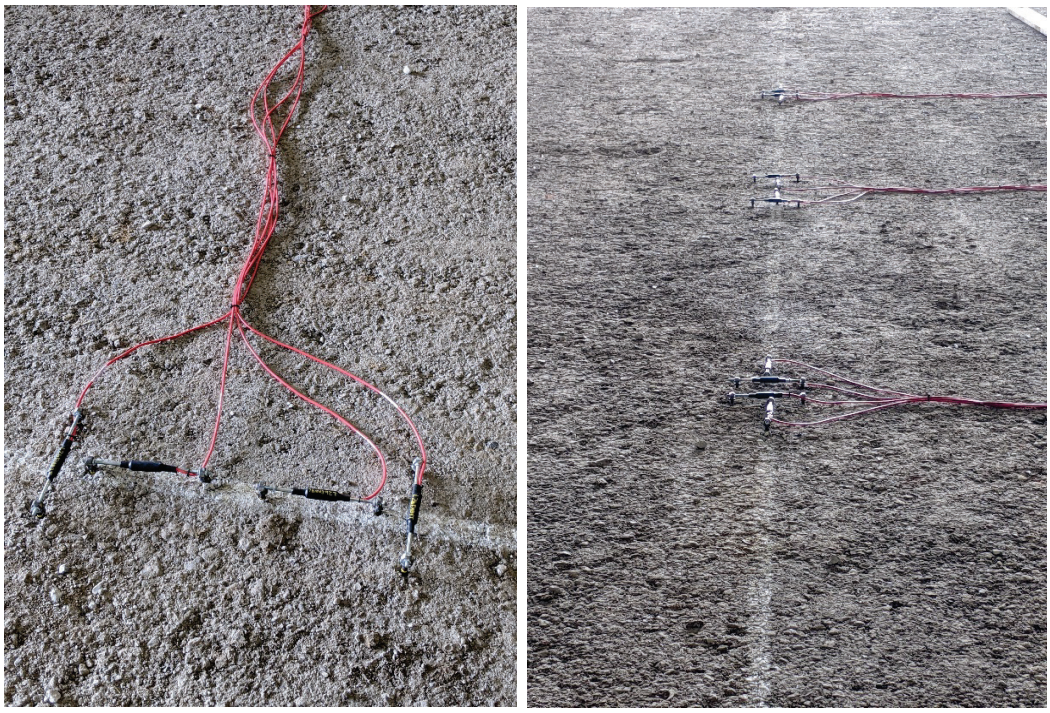

(a) Close-up of ESG (b) Strain array along traffic centerline

SSGs were installed after completion of a 28-day PCC curing period. SSGs consisted of a linear measurement gauge mounted on a polymide backing and were manufactured by HBM (model no. 1-LY43-6/350). The gauge locations were prepared by first filling surface voids in the PCC surface with a 5 min rapid-cure general purpose epoxy. After the epoxy sufficiently hardened, 120-grit sandpaper was used to smooth the area and eliminate surface irregularities during epoxy placement. After the surface was determined to be sufficiently smooth, a rapid evaporating cleaner similar to acetone was used to remove debris and dust from the sanding operation.

After the surface was adequately cleaned, Devcon 5-min gel epoxy (No. 21045) was applied to the back of the gauge. A gauge was placed on the prepared location and Mylar tape was used to secure the gauge during adhesive curing. A thin protective layer of adhesive was applied over the gauge and allowed to cure. At the conclusion of the adhesive cure period, the Mylar tape was removed. A protective coating that consisted of Micro-Measurements Gagekote #8 was applied over the entire gauge area while leaving the wire solder tabs exposed.

Wires were soldered to the gauge tabs and a final coating of Gagekote #8 was applied over the gauge, solder tabs, and wire leads to provide a secondary protective coating. A layer of 1/8 in. thick foam tape followed by a layer of aluminum foil tape was placed over the installed gauge to act as a mechanical barrier. Gagekote #8 was applied around the edges and seams of the tapes to mitigate moisture intrusion.

5.3 SDD

Vertical deflections in the subgrade were measured using SDDs assembled by ERDC. One SDD was placed in the middle of each test item along the centerline of traffic. The SDD was placed such that the shaft was anchored at a depth of 8 ft from the top of the subgrade. A linear variable displacement transducer (LVDT) with a range of ±1 in. was placed in the housing such that it was in contact with both the anchor rod and the surface plate, as shown in Figure 19. Thus, the LVDT measured movement of the plate 2 in. below the base-subgrade interface relative to the control point located at a depth of 8 ft.

Figure 19. SDD schematic.

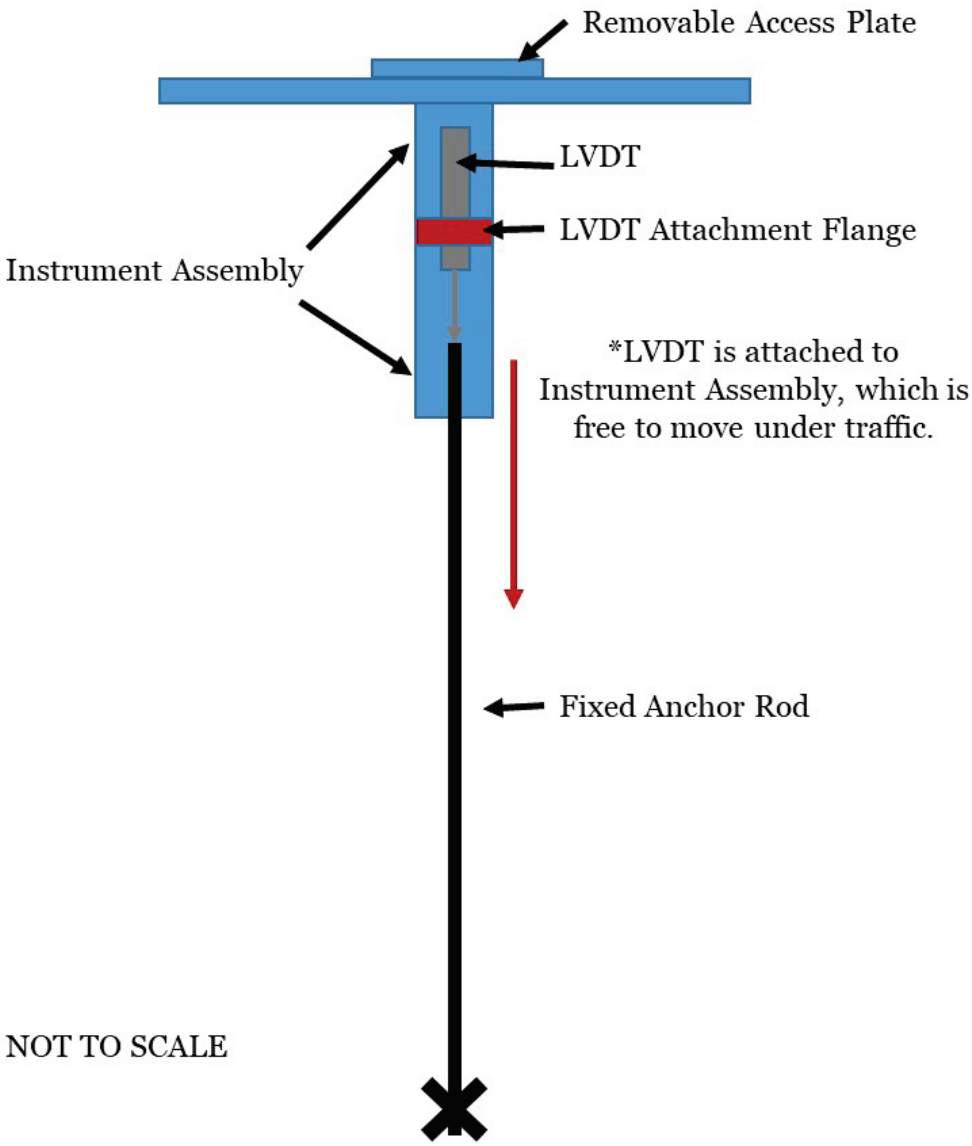

Like EPC installation, each SDD was located at a preplanned location and excavated such that the top of the removable access plate was 2 in. below the existing subgrade elevation. A borehole was advanced at the center of the plate location to a depth of approximately 8 ft by using earth-auger drilling techniques. Rapid-setting concrete was placed in the borehole, and the instrument assembly was lowered to the target depth. After the concrete had sufficiently cured, the LVDT was installed through a removable access plate such that the tip of the LVDT was in contact with the fixed anchor rod. Subgrade soils were then compacted over the surface of the SDD assembly. Photographs summarizing SDD installation are shown in Figure 20.

Figure 20. Single-depth deflectometer installation.

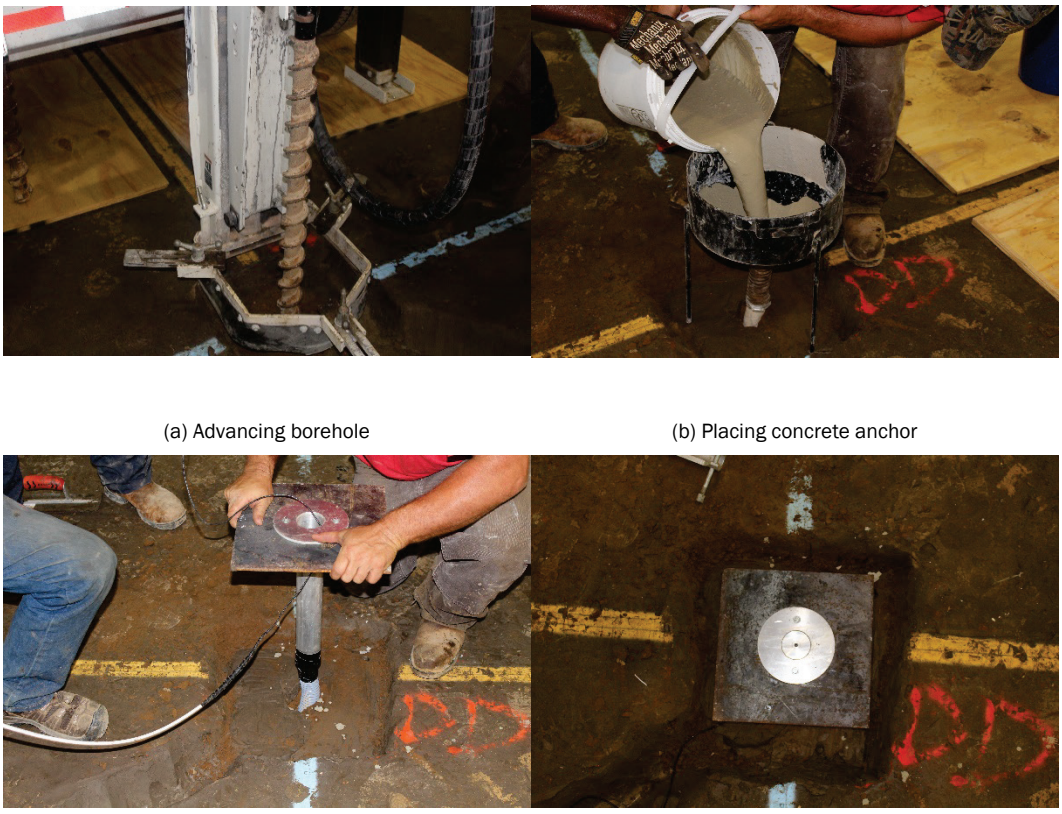

(a) Advancing borehole (b) Placing concrete anchor

(c) Setting gauge assembly (d) Completed installation

5.4 ASG

Tensile strain at the bottom of an HMA layer provides a quantitative measure of the pavement response during trafficking. The tensile strain at the bottom of the HMA is a key response parameter linked to fatigue damage in the HMA layer. For this study, strain at the bottom of the HMA surface was measured using dynamic ASGs in the longitudinal (i.e., with traffic) direction. The ASGs were manufactured by Tokyo Sokki and could measure a range of ±5,000 microstrains. The gauges were adhered to the surface of the base course with a heated asphalt binder, and HMA from the asphalt paver was placed as cover over each of the gauges immediately prior to paving the entire test section. This process is shown in Figure 21.

Figure 21. ASG installation.

(a) Trenching for wire

(b) Adhered to surface

(c) Covering with HMA

(d) Compacted prior to paving

6 Pavement Characterization

6.1 As-Built Properties

Quality control tests were performed during construction of each material lift to ensure target values were achieved and to monitor material consistency. Dry density and moisture content were measured using a nuclear moisture density device in accordance with ASTM D6938 (ASTM 2017b) to verify the uniformity of each material lift. Field in-place CBR tests were performed in general accordance with ASTM D4429 (ASTM 2009a) on each compacted lift to ensure target values were achieved. To further characterize the strength of the completed base and subgrade layers, Dynamic Cone Penetrometer (DCP) tests were performed in accordance with ASTM D6951 (ASTM 2018). HMA cores were obtained from each flexible pavement test item, and core densities were determined in accordance with AASHTO T166 (AASHTO 2016). Unconfined PCC compressive strength was determined in accordance with ASTM C39 (ASTM 2021a), and PCC flexural strength was determined in accordance with ASTM C78 (ASTM 2021b). As-built properties are summarized in Table 4 for the rigid traffic lanes and Table 5 for the flexible traffic lanes.

6.2 DCP

A series of DCP tests was performed to characterize the strength of the unbound gravel pavement layers. DCP tests were performed after completion of HMA placement, following the procedures described by ASTM D 6951 (ASTM 2018). Measured values of the DCP index (millimeters of penetration per hammer blow) were converted to CBR strength by using the relationship developed by Webster et al. (1992) and Webster et al. (1994).

6.3 Falling-Weight Deflectometer

Falling-weight deflectometer (FWD) tests were performed on the surface of the test items after construction and prior to trafficking. The measured impulse stiffness modulus (ISM) was used to evaluate the stiffness of the constructed pavement section and to provide a baseline for subsequent comparison under traffic. The ISM is the ratio of the applied load to the measured plate deflection with greater values representing a stiffer pavement structure. ISM results are discussed in Chapter 7.

6.4 Fresh PCC Test Results

Field tests were conducted during PCC placement to document the as-delivered properties and to verify consistency during the placement. Field tests included slump (ASTM 2020), temperature (ASTM 2017e), and air content (ASTM 2009b). Five compressive strength test cylinders and three flexural strength beams were cast for subsequent laboratory testing at each field test collection point. Three independent samples were obtained at approximately evenly spaced intervals (i.e., approximately every 60 cubic yd) during the concrete placement. The entire placement utilized a pump truck, and fresh PCC samples were obtained from the pump truck discharge pipe. A summary of field measurement test results is provided in Table 6.

Table 4. Rigid pavement as-built properties.

Property	L1 Item 1	L1 Item 2	L2 Item 1	L2 Item 2
CH Subgrade (TDD = 92.0 pcf @ TMC = 29.0%)				
Wet Density (pcf)	119.0 ± 1.5	118.5 ± 2.0	119.9 ± 1.6	120.3 ± 1.2
Dry Density (pcf)	93.3 ± 2.2	92.9 ± 2.1	94.5 ± 1.8	95.3 ± 1.6
Nuclear Moisture (%)	27.0 ± 2.1	26.9 ± 1.3	26.5 ± 1.3	26.1 ± 1.7
Compaction (%)	101.4	100.9	102.7	103.6
OD Moisture (%)	29.1 ± 1.9	29.5 ± 1.6	29.3 ± 1.0	29.2 ± 1.8
In-Place CBR (%)	9.9 ± 0.8	9.9 ± 0.8	10.1 ± 0.8	10.0 ± 0.8
Aggregate Base (MDD = 147.9 pcf @ OMC = 5.2%)				
Wet Density (pcf)	145.1 ± 2.0	144.1 ± 1.9	146.8 ± 1.9	148.6 ± 3.3
Dry Density (pcf)	139.9 ± 1.9	138.9 ± 1.6	140.9 ± 2.2	142.1 ± 3.3
Nuclear Moisture (%)	3.7 ± 0.3	3.8 ± 0.6	4.2 ± 0.6	4.6 ± 0.4
Compaction (%)	94.6	93.9	95.3	96.1
OD Moisture (%)	3.1 ± 0.6	3.6 ± 0.3	3.7 ± 0.3	4.1 ± 0.4
In-Place CBR (%)				
Thickness (in.)	6.0 ± 0.4	6.4 ± 0.2	6.1 ± 0.3	6.0 ± 0.3
PCC Surface				
CS (psi) @ 28 days	6540 ± 350			
TS (psi) @ 28 days	765 ± 55			
Thickness (in.)	NM	NM	7.4 ± 0.2	11.1 ± 0.3

TDD = target dry density, TMC = target moisture content, MDD = maximum dry density, OMC = optimum moisture content, OD = oven dry, NM = not measured, CBR = California bearing ratio, CS = compressive strength, TS = tensile strength

Table 5. Flexible pavement as-built properties.

Property	4 in. HMA, GR, 10 CBR	4 in. HMA, LS, 10 CBR	4 in. HMA, LS, 6 CBR	2 in. HMA, GR, 10 CBR	2 in. HMA, LS, 10 CBR	2 in. HMA, LS, 6 CBR
CH Subgrade (TDD = 92.0 pcf @ TMC = 29%, TDD = 88.4 @ TMC = 32%)						
Wet Density (pcf)	118.2 ± 1.8	116.2 ± 2.6	116.6 ± 1.8	117.6 ± 1.9	117.3 ± 1.9	116.5 ± 1.3
Dry Density (pcf)	93.1 ± 2.1	92.0 ± 2.4	90.7 ± 1.7	92.3 ± 2.3	91.9 ± 2.3	90.4 ± 1.4
Nuclear Moisture (%)	26.8 ± 2.1	26.1 ± 1.4	28.1 ± 1.8	27.9 ± 1.8	27.7± 2.6	28.5 ± 1.4
Compaction (%)	101.2	100.0	102.6	100.3	99.9	102.3
Oven-Dried Moisture (%)	29.1 ± 1.2	29.1 ± 1.0	31.8 ± 1.9	29.6 ± 1.1	29.4 ± 1.2	31.6 ± 2.1
In-Place CBR (%)	10.0 ± 0.7	10.0 ± 0.7	5.9 ± 0.5	9.8 ± 0.6	10.0 ± 0.8	5.9 ± 0.4
Aggregate Base (MDD = 147.9 pcf @ OMC = 5.2%; 115.1 pcf @ OMC = 8.4)						
Material Type	GR	LS	LS	GR	LS	LS
Wet Density (pcf)	111.7 ± 2.6	144.7 ± 1.1	143.8 ± 4.2	115.8 ± 2.8	147.4 ± 3.9	143.9 ± 3.7
Dry Density (pcf)	107.8 ± 3.2	138.9 ± 1.0	138.8 ± 3.9	109.2 ± 5.5	141.6 ± 4.1	139.3 ± 3.7
Nuclear Moisture (%)	3.7 ± 0.9	3.9 ± 0.5	3.6 ± 0.5	5.6 ± 3.1	3.8 ± 0.1	3.4 ± 0.2
Compaction (%)	93.6	93.9	93.8	94.9	95.7	94.2
Oven-Dried Moisture (%)		3.2 ± 0.4	2.8 ± 0.5		2.9 ± 0.9	2.8 ± 0.3
In-Place CBR (%)	30.5*	94 ± 14	100+	30.5*	83.± 13	71 ± 13
Thickness (in.)	12.4 ± 0.9	11.5 ± 0.5	12.2 ± 0.5	12.3 ± 0.8	12.0 ± 0.4	11.7 ± 0.4
HMA						
Compaction (%)	92.8	91.8	93.4	89.9	90.9	92.0
Thickness (in.)	3.2 ± 0.5	3.8 ± 0.2	3.8 ± 0.2	2.1 ± 0.2	2.0 ± 0.1	1.9 ± 0.3

TDD = target dry density, TMC = target moisture content, MDD = maximum dry density, OMC = optimum moisture content, *Estimated from DCP measurements

Table 6. Results of fresh PCC field tests.

Test No.	Slump (in.)	Temperature (°F)	Air Content (%)
Set 1	9.0	76.3	3.8
Set 2	9.0	75.4	4.0
Set 3	9.5	76.2	4.5

7 Traffic Testing

Accelerated test traffic was applied using a dual-wheel P-8 gear mounted on ERDC's HVS-A. The HVS is a fully automated pavement trafficking device capable of applying wheel loads ranging from 10,000 lbf to 100,000 lbf. Total traffic length is approximately 45 ft at speeds ranging from 4 to 9 mph. Additionally, the HVS has an integrated climate control system that controls the temperature of the test area. While not critical for PCC pavement testing, HMA pavements are sensitive to fluctuations in pavement temperature. Thus, the climate control system was used to maintain the HMA pavement temperature at 77 ± 5°F during test section trafficking. An alarm system was activated to notify the operator if temperatures inside the test chamber exceeded the preset threshold. A photograph of the ERDC HVS-A is shown in Figure 22.

Figure 22. ERDC Heavy Vehicle Simulator (HVS-A).

7.1 P-8 Gear Configuration

The P-8 gear configuration used for trafficking all test items is shown in Figure 23. The P-8 gear consisted of two actual P-8 tires and wheels with a custom machined axle for securing the tires to the HVS carriage. The

total load on the dual-wheel configuration was 89,000 lbf; this load was verified prior to traffic testing using a set of portable aircraft scales. The tire inflation pressures were monitored daily and maintained at 220 psi.

Figure 23. P-8 gear on HVS.

(a) Front view (b) Side view

Center-to-center spacing of the test tires was 39.5 in. This spacing was slightly greater than the actual tire spacing (33.5 in.) on the P-8 aircraft–a difference required to accommodate test gear mounting limitations on the HVS carriage.

Prior to test section trafficking, tire imprints (Figure 24*a*) were obtained on an HMA-surfaced test area to measure actual tire contact area. The imprints were obtained by placing a thick piece of construction paper on the pavement surface, lowering the test gear, verifying the target load, and painting the tire outline with construction marking paint. The tire imprint was photographed with a scale and loaded into a computer-aided drawing program to facilitate accurate contact area determination (Figure 24*b*). A common assumption is that the tire contact area can be estimated by dividing the total wheel load by the tire inflation pressure; however, this assumption has been found to be inaccurate in some cases (Robinson 2021). Thus, the tire imprints can be used to investigate P-8 contact area assumptions.

A summary of tire contact measurements obtained from the tire imprints is shown in Table 7. The measured total contact areas were found to be relatively close to the assumed contact areas (within 2.5%). When the tire tread pattern was removed from the area determination,

researchers observed that the contact area was approximately 10% less than the assumed contact area.

Figure 24. Tire imprint of the P-8 test gear.

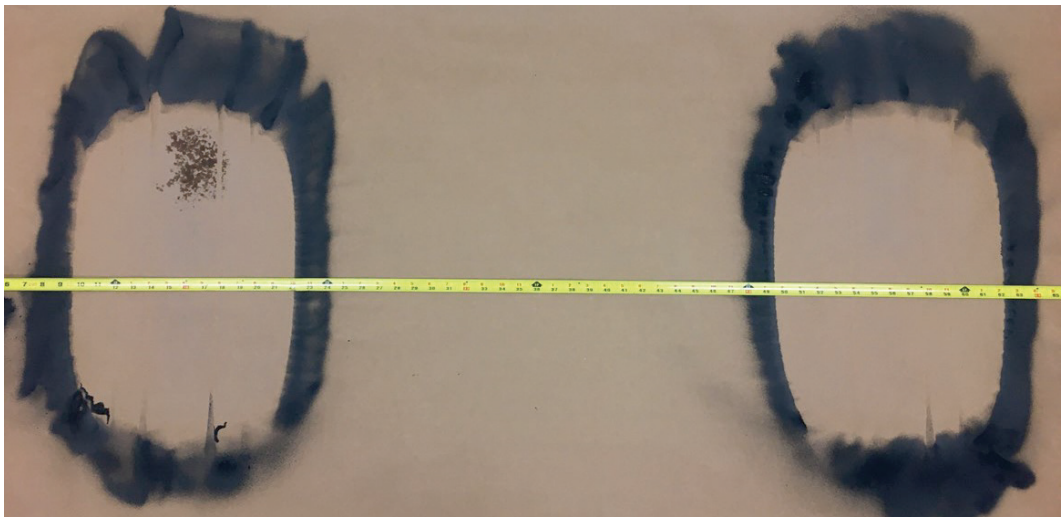

(a) Tire imprints obtained from P-8 test gear

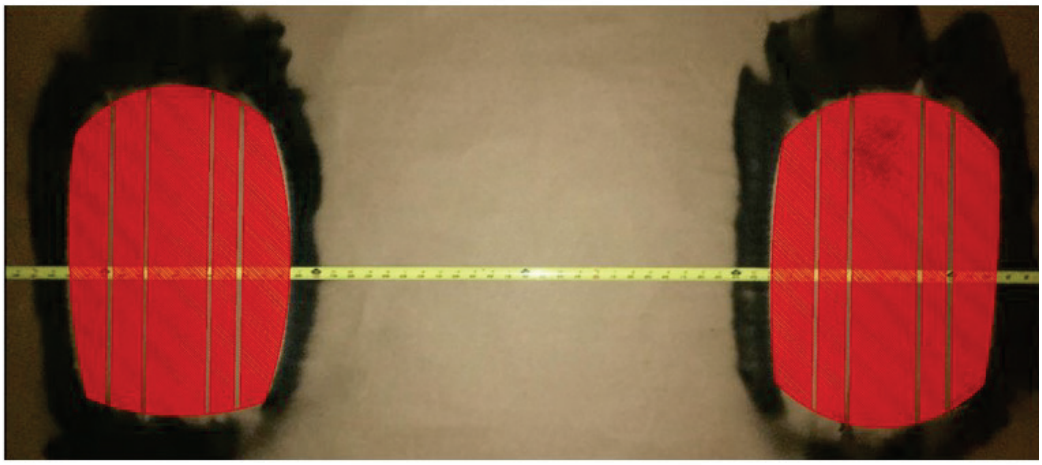

(b) Digital images made in a computer-aided drawing program

Table 7. Measurements from digitized tire imprints.

Test Tire	Length (in.)	Width (in.)	Total Area (in.²)	Area Minus Tread (in.²)	Assumed Area (in.²)
Left Tire	18.6	12.6	206.8	182.0	202.3
Right Tire	18.4	12.4	199.1	179.5	202.3

7.2 Wander Pattern

A bidirectional, normally distributed wander pattern was used to apply test traffic. Incorporating a wander pattern simulated the inherent variability

expected in a real-world trafficking scenario. The wander pattern used for this study is shown in Figure 25. The pattern consisted of a long sweep and a short sweep, where 158 total passes of the HVS comprised a full wander pattern resulting in a minimum pass-to-coverage ratio of 3.04.

Traffic was started for each test item with the center of the dual-wheel P-8 gear aligned on the centerline of the test section. The HVS applied test traffic parallel to the test item centerline on the forward pass and shifted one end of the carriage beam 2 in. on the return pass. Prior to initiating the next pass, the opposite end of the carriage beam shifted 2 in.; thus, the beam returned parallel to the traffic centerline (Figure 26). This process was repeated throughout the entire wander pattern; therefore, odd pass numbers were parallel to the traffic centerline, and even pass numbers were at a slight skew to the traffic centerline. It is important to understand the traffic operation and gear positioning of the HVS, particularly in early traffic and in relation to installed instrumentation, such that pertinent observations can be made.

Figure 25. Bidirectional normally distributed wander pattern.

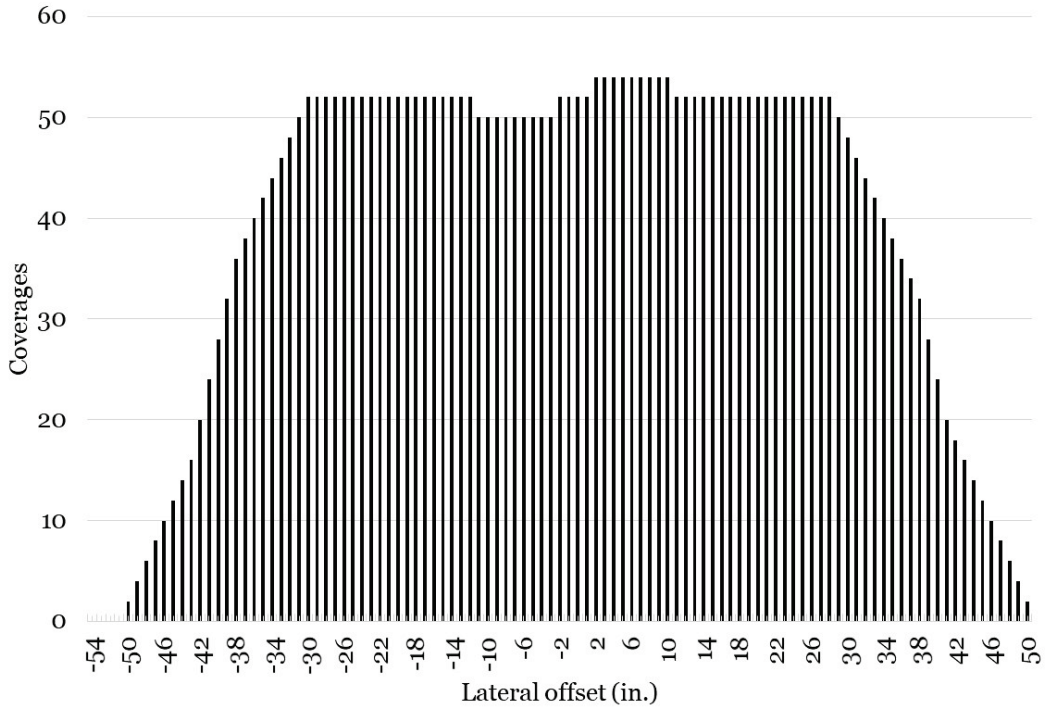

Figure 26. Example of HVS traffic wander methodology.

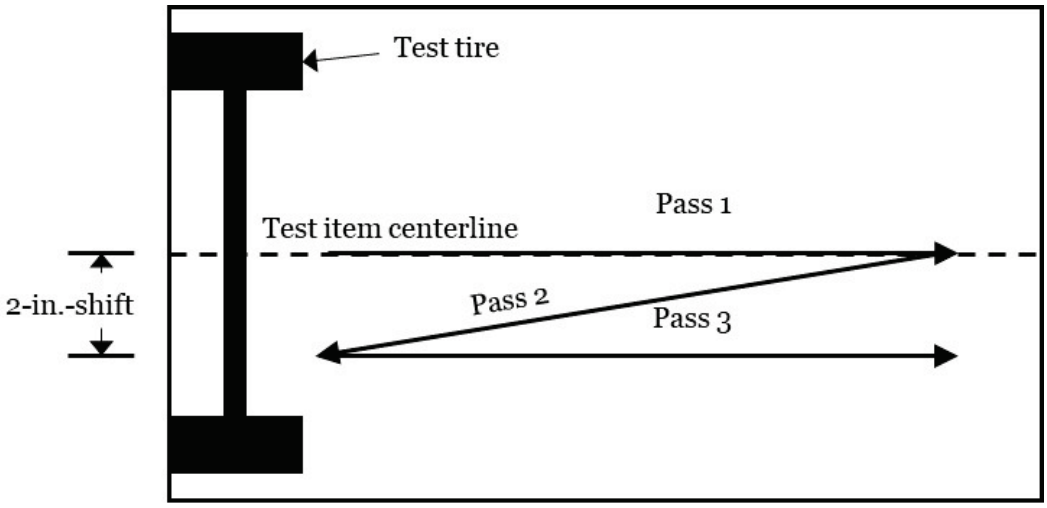

Not to scale; dimensions are exaggerated for clarity

8 Results: Pavement Structural Requirements

Results of trafficking tests to determine minimum pavement structural requirements are presented in this chapter. Data were interpreted to understand differences in pavement performance and instrumentation response under simulated aircraft trafficking. Inferences were made based on visual and measured responses. Data collected for this experiment are presented in tabular form in Appendix A through Appendix C.

8.1 Rigid Pavement

Three levels of deterioration were considered in selecting passes to failure for a PCC test item. Deterioration levels were selected based on a review of historical full-scale testing (Rollings 1988) such that failure criteria were consistent with existing design criterion datasets. The first failure deterioration level considered was "first crack," which was defined as when the absolute first crack was observed in 50% of the loaded test slabs. Note that in the case of this experiment, two loaded slabs comprised the traffic area; thus, 50% of the test slabs would be considered one slab. The second failure deterioration level considered was "shattered slab" and was defined as when sufficient inter-connected cracking had occurred to divide a slab into four distinct pieces. The third failure deterioration level considered was "complete failure" and was defined as when sufficient inter-connected cracking had occurred to divide a slab into six or more distinct pieces.

8.1.1 Lane 2 Item 1 (8 in. Thick PCC)

8.1.1.1 Heavy-Weight Deflectometer Results

Prior to applying simulated P-8 test traffic, a series of heavy-weight deflectometer (HWD) tests were conducted at strategic locations throughout the 8 in. thick PCC test item. The primary objectives were to evaluate pretraffic strength characteristics, to investigate the influence of the different joint construction techniques (dowelled and undowelled joints), and to investigate the influence of edge condition (free edge and confined edge). Tests were conducted near the edges of the test area, midslab, and near each joint. ISM, which is simply the total load applied to the HWD test plate divided by the deflection measured at the center of the base plate, was used as the basis of comparison. A graphical representation

of the pretrafficking HWD test locations is shown in Figure 27. The test locations are represented by circles and are appropriately scaled to reflect position within the test item. The *x*- and *y*-axis dimensions are in feet, and numerical values adjacent to each circle are the calculated ISM values (with units of kips/in.) at each test location. A dashed line at an *x*-coordinate of 20 represents the dowelled joint.

ISM values should be interpreted as greater values indicate a stiffer (i.e., stronger) pavement. In general, greater ISM values were observed adjacent to a confined edge, which was expected. For example, if one considers the test series conducted along an *x*-distance of approximately 1 ft, one observes that the lowest ISM (i.e., 910 kips/in.) was detected at *x, y* coordinates of 1, 4 that corresponded to a free-edge condition. As one moves up the *y*-axis toward a confined edge, a general increase in ISM is observed. Similar observations can be made throughout the test item.

Midslab ISM values were generally greater values, as expected due to increased stiffness away from joints. The average midslab ISM value was 1,953 kips/in. compared to 1,763 kips/in. along the dowelled joint and 1,104 kips/in. along the nondowelled joint.

Dowel bar inclusion improved average measured ISM values by a factor of approximately 1.6 when compared to the nondowelled joint. This was expected as the primary purpose of dowel bars is to improve load transfer and stiffness along a joint.

Similarly, HWD tests were conducted after the completion of traffic at the same locations allowing for meaningful comparisons. A graphical representation of posttraffic ISM values is shown in Figure 28. In general, meaningful decreases in ISM were noticed throughout the test item, an observation expected as the pavement deteriorated.

The dowelled joint ISM values decreased by approximately 38% and represented the greatest observed percentage decrease. This can be attributed to interconnected cracking creating a host of small slab pieces as well as loss of load transfer with deterioration. Midslab ISM values decreased by approximately 26% and continued to have the greatest ISM values posttraffic. A 17% decrease in ISM was observed along the nondowelled joint and, although the nondowelled joint experienced the lowest percentage decrease, the magnitude of measured ISM was lowest overall.

Similarly, joint load transfer efficiency (JE) in both a pretraffic and posttraffic condition were evaluated using HWD data (Table 8). In this case, joint transfer efficiency referred to the ratio of measured deflection measured equidistant on each side of a joint. Thus, deflection data were taken from the sensor located on the HWD load plate (i.e., D_0) and deflections measured one foot away (i.e., D_1) from the plate. The HWD was positioned such that the load plate was on one side of a joint and sensor D_1 was positioned on the opposite side of a joint.

Initial JE was found to be greater in the dowelled joint (average = 0.94) than the nondowelled joint (average = 0.77), as expected. Similarly, posttest data indicated that JE remained greater in the dowelled joint (average = 1.09) than the nondowelled joint (average = 0.89) at the conclusion of traffic. An improvement in JE was observed in the nondowelled joint with an increase in traffic and cracking in the vicinity of the joint, which was not expected. Team members hypothesize that cracking around the joint resulted in movement of individual pieces of the concrete slab in the joint vicinity under HWD loading. This movement resulted in greater contact forces at the joint, thereby increasing frictional load transfer.

Figure 27. Pretraffic HWD results (8 in. thick PCC).

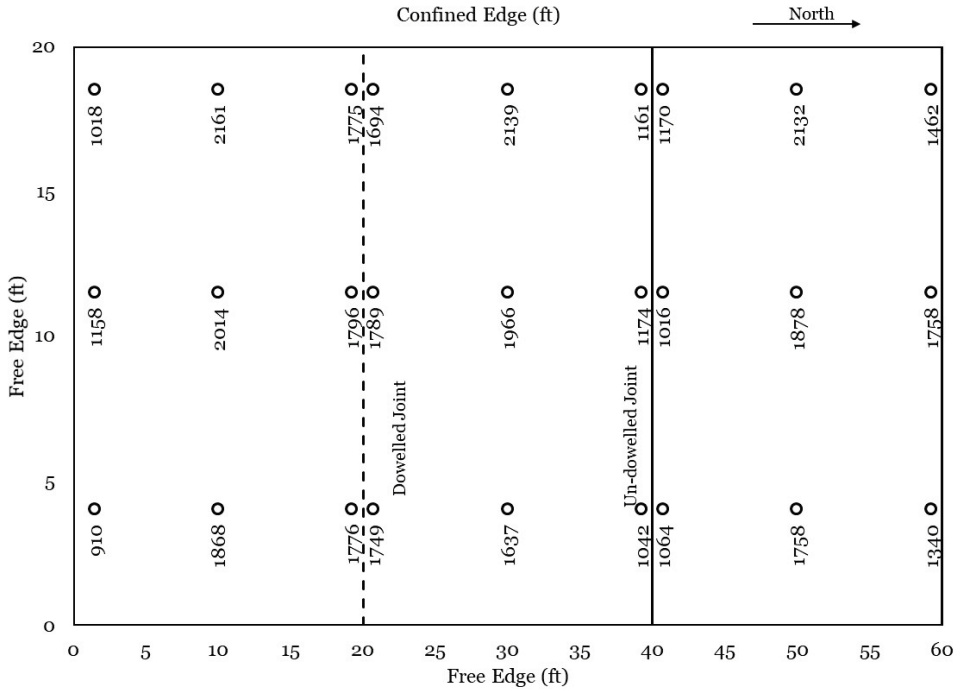

Figure 28. Posttraffic HWD results (8 in. thick PCC).

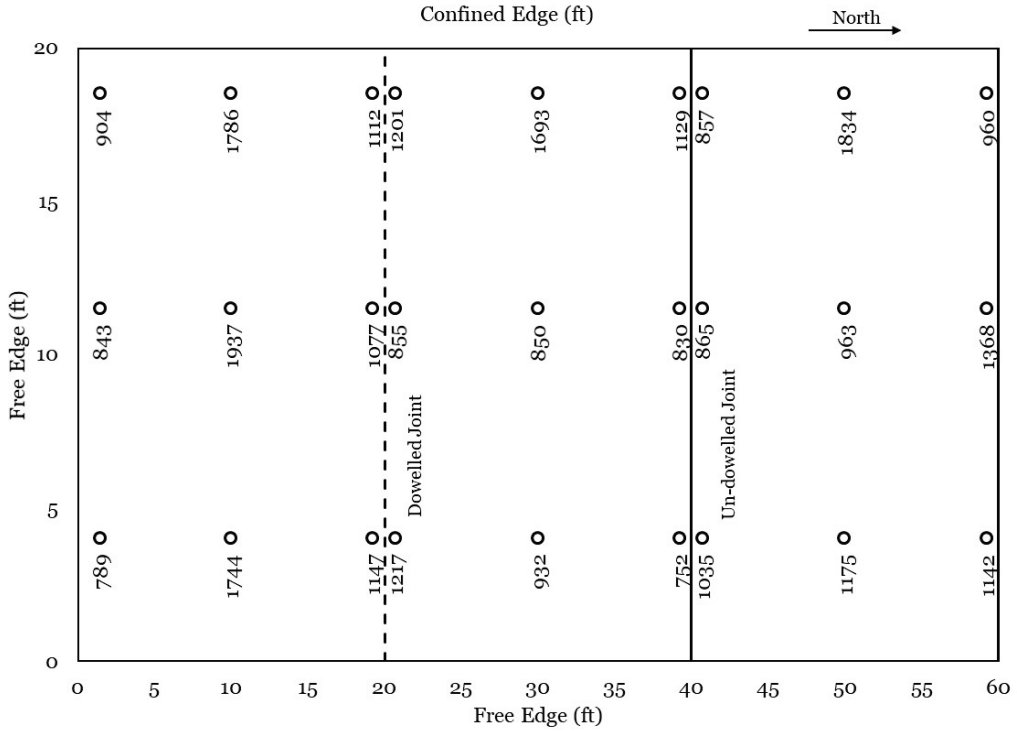

Table 8. HWD joint load transfer efficiency results (8 in. thick PCC).

Joint Condition	Location		JE (D_1/D_0)	
	X (ft)	Y (ft)	Pretraffic	Posttraffic
Dowelled	20	4	0.92	1.35
Dowelled	20	11.5	0.95	1.01
Dowelled	20	18.5	0.96	0.92
		Average	0.94	1.09
Nondowelled	40	4	0.85	0.77
Nondowelled	40	11.5	0.87	0.97
Nondowelled	40	18.5	0.60	0.92
		Average	0.77	0.89

8.1.1.2 Cracking Observations

Visual inspections were conducted routinely to monitor crack development. Each visual inspection consisted of a full examination of the test area, and, if a crack was identified, it was marked with striping paint, mapped, and measured. These observations were then used to

create electronic crack maps. Thus, accurate crack progression could be cataloged via a computer-aided drawing program.

The first crack was observed during the 500-pass inspection radiating from the undowelled joint in a "half-moon" pattern and extending across the traffic area. Researchers noted that the crack was not present at the 300-pass inspection; thus, the crack manifested somewhere between 300 and 500 passes.

A second crack was observed at 546 passes on the opposite side of the undowelled joint in the same half-moon pattern. As traffic continued, secondary cracks began to form both parallel to the initial cracks and migrating from the initial cracks. At the 3,000-pass level inspection, one slab had enough interconnected cracks to be divided into four individual pieces, achieving the shattered slab failure definition. At the 7,500-pass level inspection, the cracks had become interconnected to a point that the test area achieved the complete failure condition in which the slab was divided into six or more distinct pieces. All cracks were low severity cracks (crack width less than 1/8 in.), and no foreign object debris (FOD) development was observed. Maps showing the location and progression of crack development are shown in Figures 29 through 36.

Figure 29. Crack map at 500 passes.

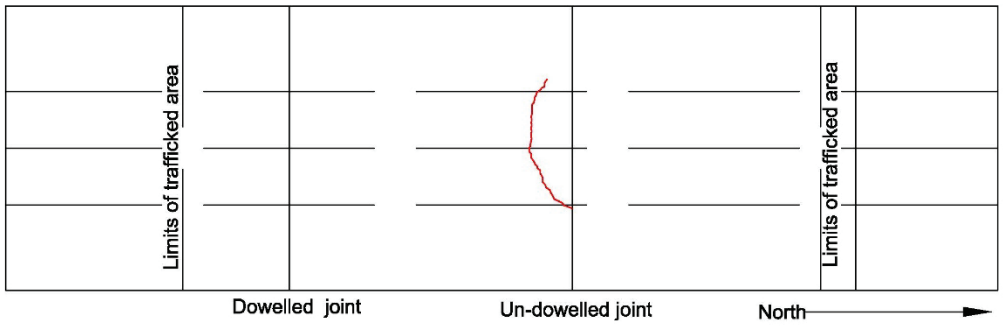

Figure 30. Crack map at 546 passes.

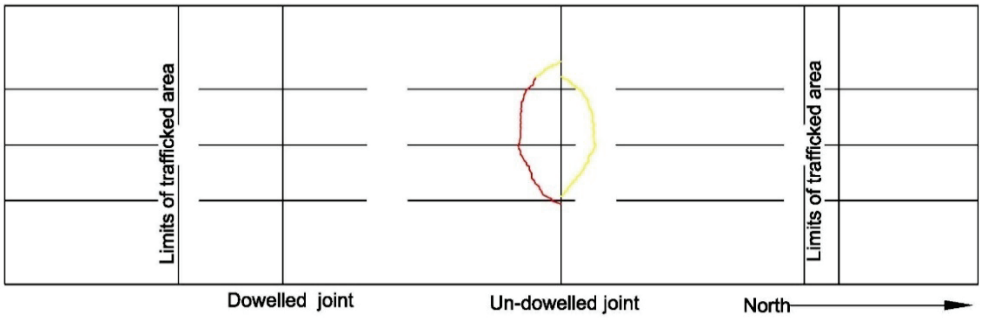

Figure 31. Crack map at 750 passes.

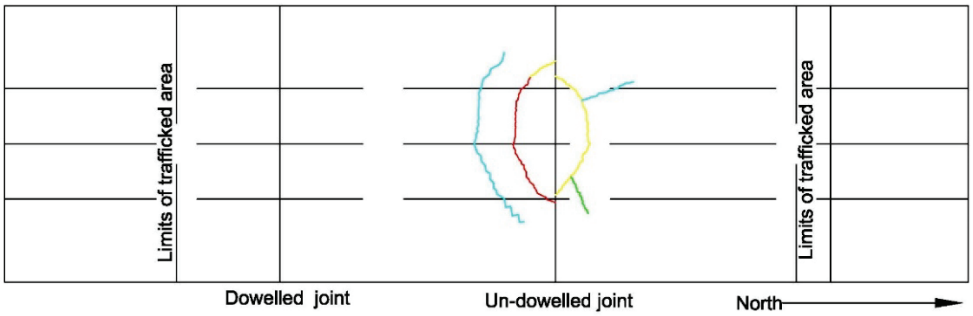

Figure 32. Crack map at 2,000 passes.

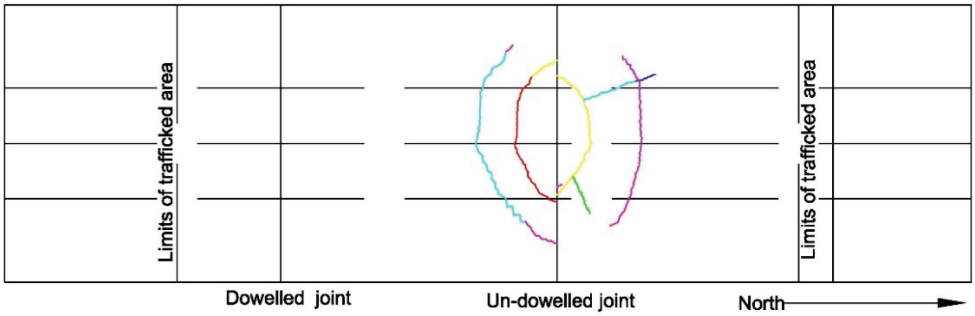

Figure 33. Crack map at 3,000 passes.

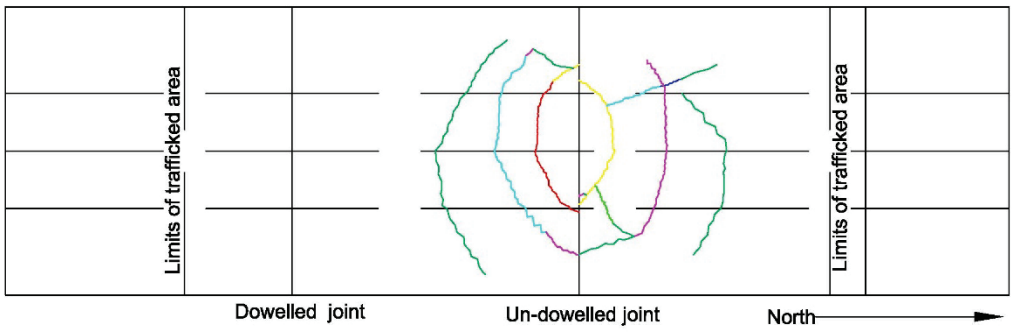

Figure 34. Crack map at 7,500 passes.

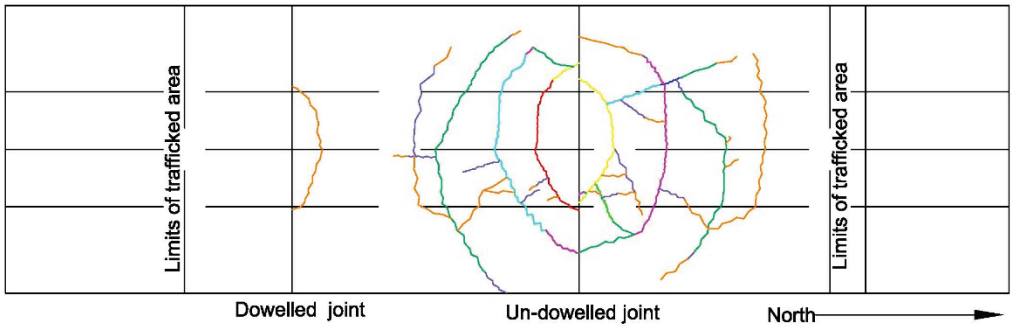

Figure 35. Crack map at 10,000 passes.

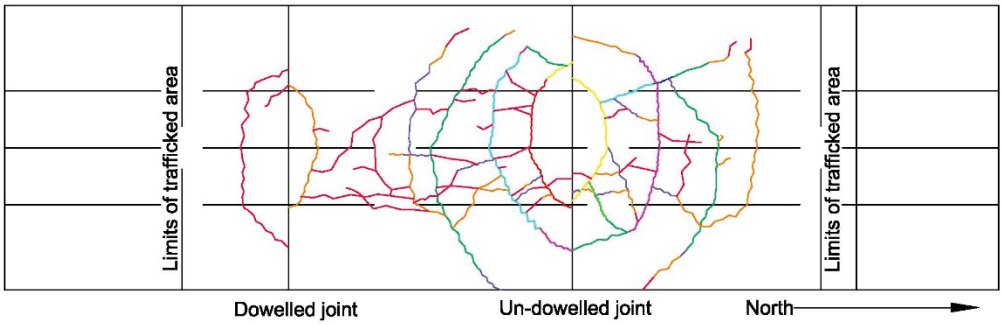

Figure 36. Crack map at 15,000 passes.

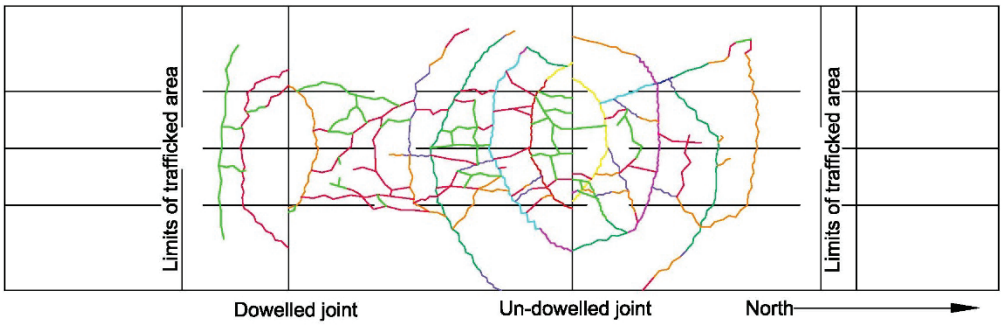

Additionally, cumulative crack length over the test item area was measured at select traffic intervals and plotted as shown in Figure 37. Total crack length generally increased from 500 to 750 passes. Thereafter, a modest increase was observed up to approximately 2,000 passes. Crack length development tended to increase thereafter up to the suspension of traffic.

A review of the crack maps and crack progression data assisted in determining a proper pass level to assign the various failure conditions.

A summary of the selected pass levels for each failure condition is provided in Table 9.

Table 9. Selected failure pass level for 8 in. thick PCC.

Criteria	South Slab	North Slab	Selected Failure Pass Level
First Crack	Between 300 & 500 passes	546 passes	400 passes
Shattered Slab	Between 6,000 & 7,500 passes	Between 2,000 & 3,000 passes	2500 passes
Complete Failure	7,500 passes	7,500 passes	7500 passes

Figure 37. Total crack length with traffic (8 in. thick PCC).

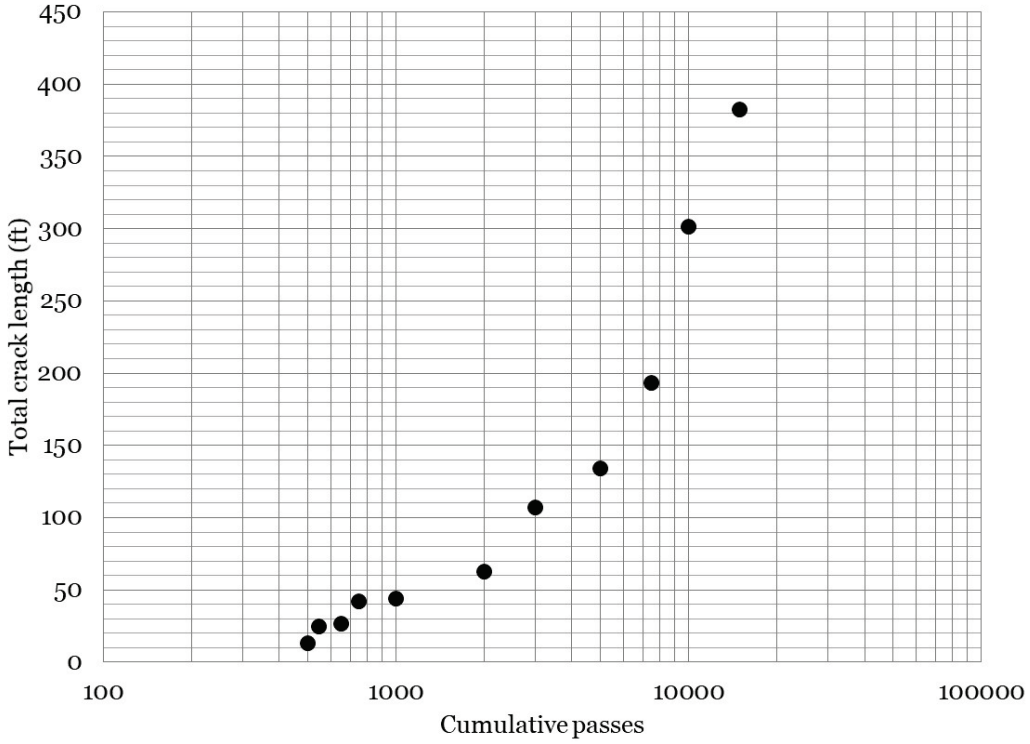

8.1.1.3 FWD Results

Falling-weight deflectometer data were collected at select traffic intervals during traffic application to monitor structural deterioration. An FWD was used during traffic application in lieu of a HWD due to clearance requirements under the HVS. FWD measurements were made at the dowelled joint, midslab, quarter-slab, and the nondowelled joint. A summary of ISM values for each condition with cumulative traffic passes is shown in Figure 38.

Initial measured ISM values in the midslab and quarter-slab locations were the highest measured values in most cases, and midslab values were greater than quarter-slab values. This was expected and attributed to increased stiffness as the test locations moved further from a joint (i.e., deflections decreased further from a joint.) The nondowelled joint had the lowest measured ISM, which is logical considering the nondowelled joint relied on interface friction to generate stiffness. Measured ISM values near the dowelled joint were slightly less than those measured at the midslab and quarter-slab locations; however, the data showed a meaningful stiffness improvement when compared to the nondowelled joint.

ISM values tended to decrease with an increase in traffic and an increase in pavement deterioration (i.e., cracking.) Meaningful decreases in ISM were observed in the dowelled joint, midslab, and quarter slab locations with an increase in cumulative traffic, initiating between the 1,000- and 2,500-pass level and continuing through traffic completion. Interestingly, decreases in measured ISM at the nondowelled joint did not display similar trends which was unexpected. However, a review of the measured JE with increased traffic (Figure 39) revealed that joint transfer generally improved in the nondowelled joint. It is hypothesized that cracking in the vicinity of the nondowelled joint resulted in slight movement of the individual slab pieces, thereby improving interlock in the measurement area. Note that a decrease in ISM at the nondowelled joint was observed near the 500-pass level, which was when the first crack was identified. Thereafter, as increased cracking occurred a rebound in stiffness was observed, which could support the previous hypothesis. Near the end of traffic as extensive cracking occurred, the team observed that all ISM values tended to converge.

Figure 38. ISM with traffic at various locations (8 in. thick PCC).

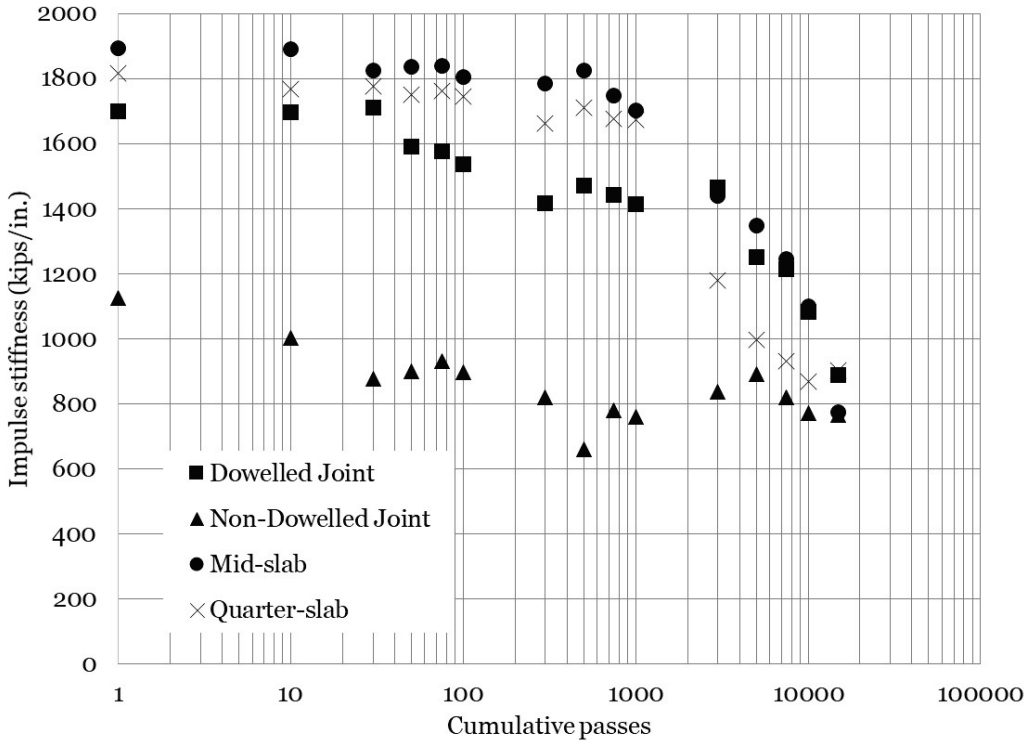

Figure 39. JE with traffic for dowelled and nondowelled joints (8 in. thick PCC).

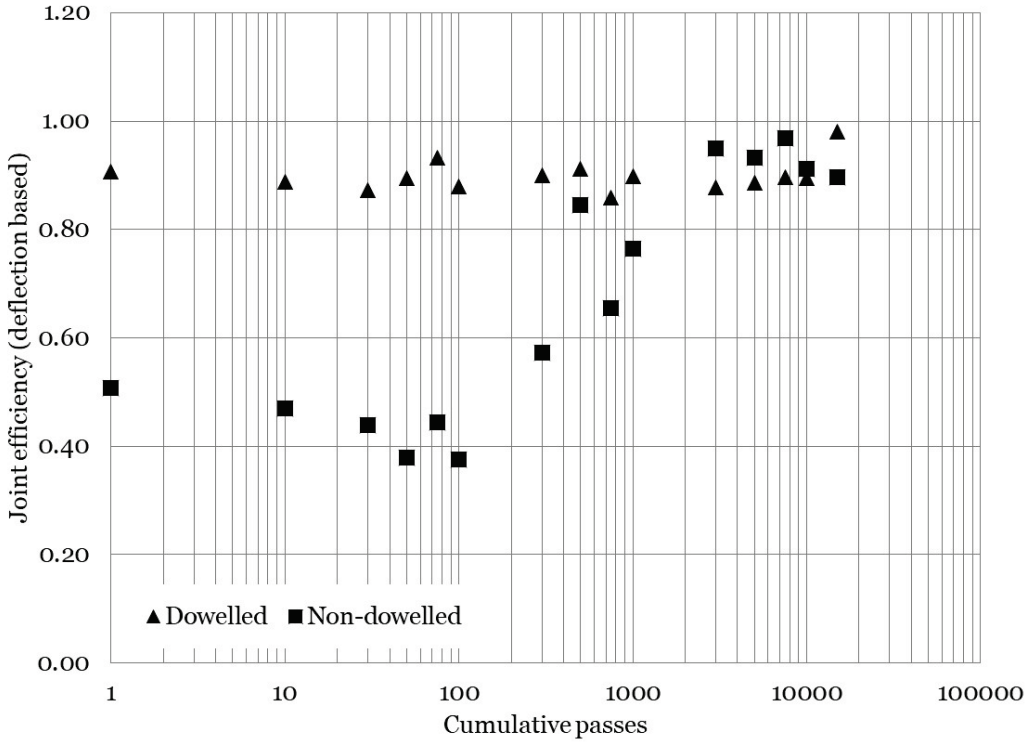

8.1.1.4 Subgrade Pressure Response

A summary of measured subgrade pressure is shown in Figure 40. Representative subgrade response values were determined by selecting the greatest measured response near the end of each selected traffic interval. Thus, the values represent a "best hit" when the test gear was directly over a subgrade EPC. Response values were calculated by subtracting the peak value and the minimum value for the event; thus, values represent dynamic measurements.

Maximum measured subgrade pressure was relatively consistent early in traffic (up to approximately 250 passes). Thereafter, an increase in measured pressure was observed to the completion of traffic. A meaningful increase in measured pressure was observed at the quarter-slab location near 2,500 passes, which corresponded with a shattered slab condition (see north slab observations in Table 9). A similar response can be observed between 6,000 and 7,500 passes for the midslab pressure cell (south slab). Thus, the earth pressure cell data agree with visual cracking observations.

Comparison of the pressure cell locations indicated that maximum measured pressure tended to diverge near 2,500 passes. Greater measured pressures were observed at the quarter slab location after 2,500 passes, which corresponded with differences in observed cracking. These data suggest that as cracking increased beyond the shattered slab condition, the load-carrying capability of the slabs decreased, and more of the applied load was transmitted to the underlying subgrade layer.

Figure 40. Subgrade pressure response with traffic (8 in. thick PCC).

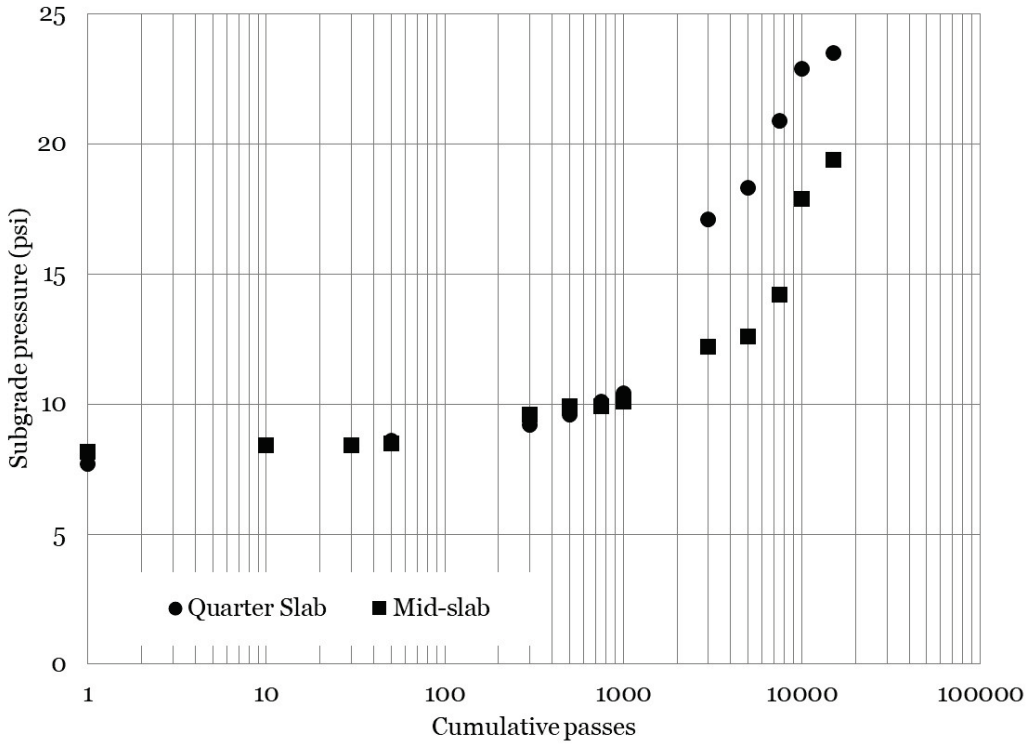

8.1.1.5 SSG Response

SSG response data for the nondowelled joint, dowelled joint, and midslab measurement locations are shown in Figures 41 to 43, respectively. As expected, the SSGs failed relatively early in the trafficking sequence. In general, measured response at the three measurement locations were similar in magnitude. Generally increasing trends were observed to the point of gauge failure. The gauges mounted adjacent to the dowelled joint provided data up to approximately 1,000 passes; values ranged from 200 to 300 microstrains at gauge failure.

Figure 41. SSG response of nondowelled joint (8 in. thick PCC).

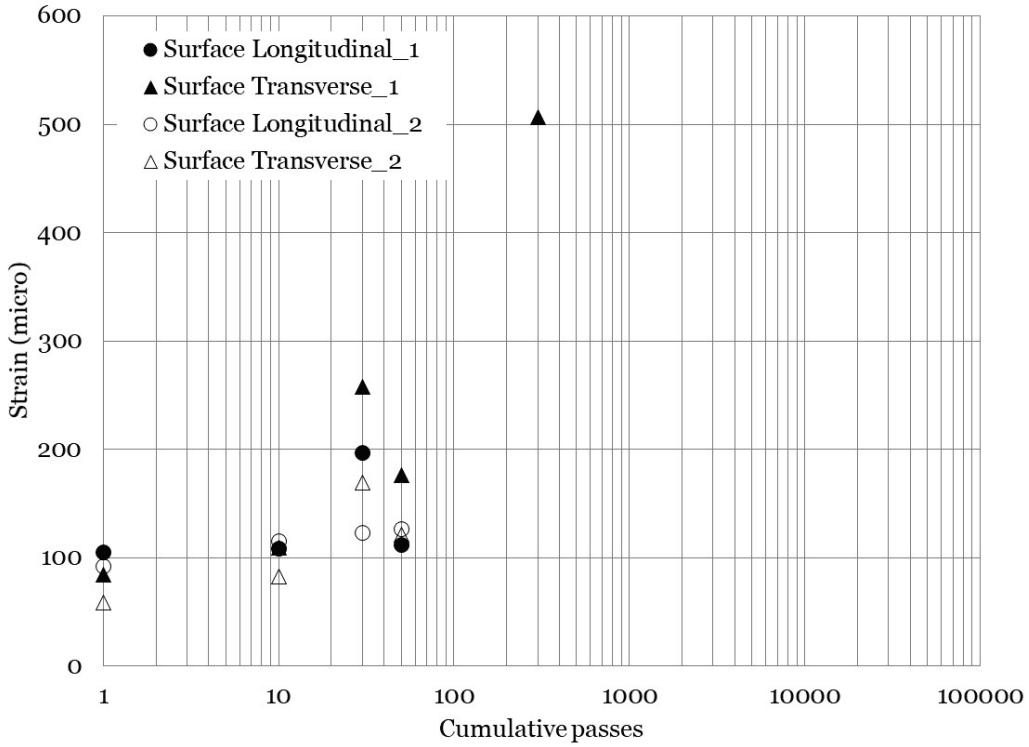

Figure 42. SSG response of dowelled joint (8 in. thick PCC).

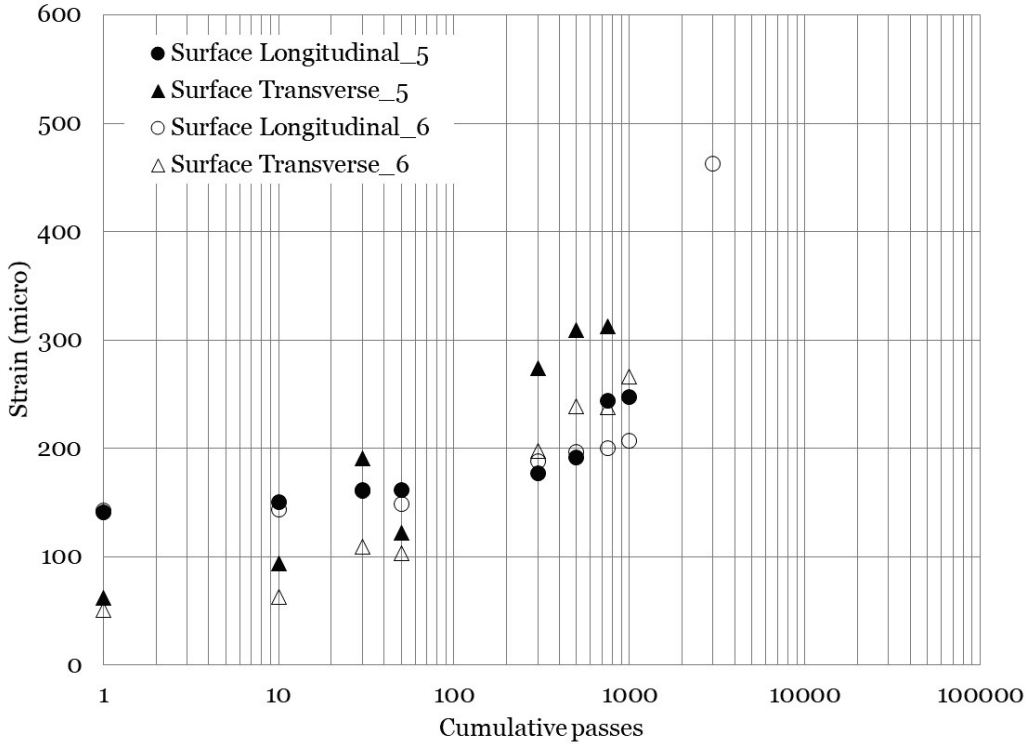

Figure 43. SSG response of midslab (8 in. thick PCC).

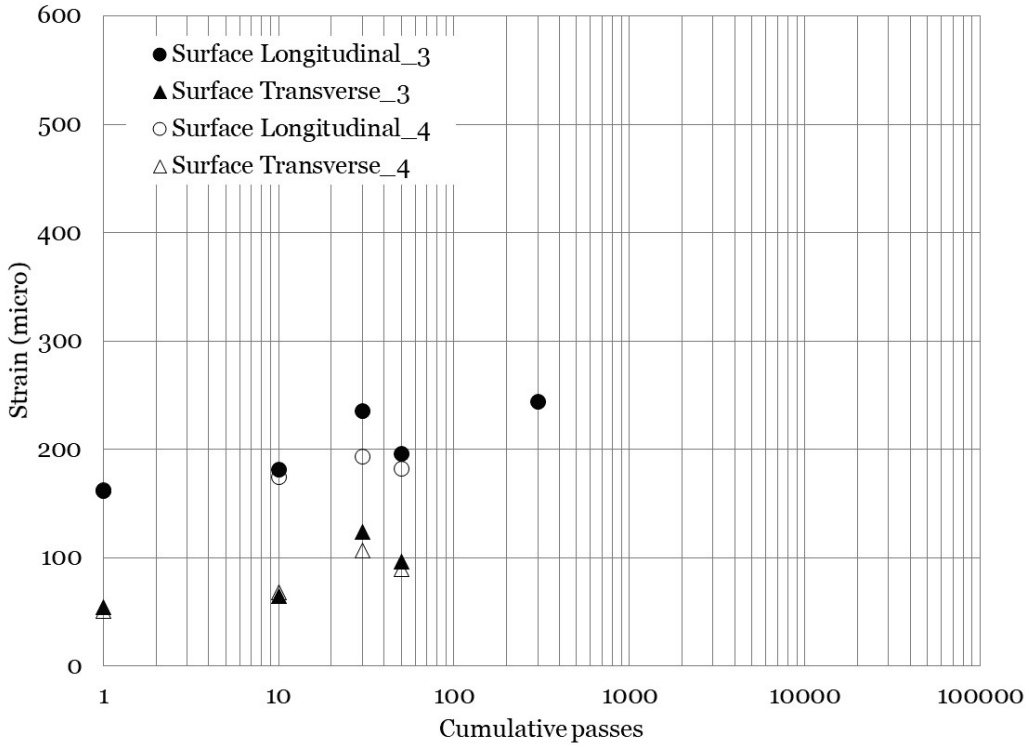

8.1.1.6 ESG Response

ESG response for the nondowelled, dowelled, and midslab measurement locations are shown in Figures 44 to 46, respectively. A review of the nondowelled joint response (Figure 44) revealed a considerable amount of data scatter, and response values ranged from less than 100 microstrains to approximately 550 microstrains. Of note, the data were generally consistent up to approximately 300 passes becoming much more variable thereafter. This could be an indication of damage (i.e., occurrence of cracking near the nondowelled joint prior to migrating to the surface.)

A review of the dowelled joint and midslab data indicate that similar strain magnitudes and trends were observed at these measurement locations. This suggests that dowel bar inclusion was effective at stiffening the pavement joint and that the joint behaved as a monolithic structure (i.e., the joint behavior was like a nonjointed area.) Like the nondowelled response, the dowelled response and midslab response tended to trend upward around 300 passes potentially indicating the start of pavement deterioration.

Figure 44. ESG response of nondowelled joint (8 in. thick PCC).

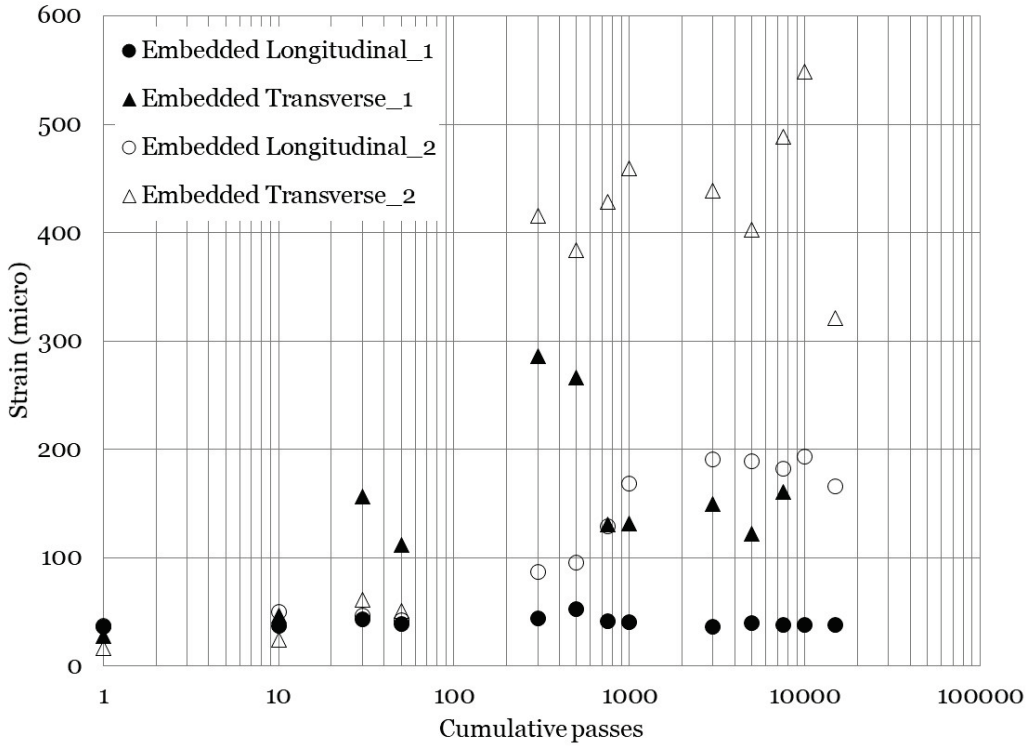

Figure 45. ESG response of dowelled joint (8 in. thick PCC).

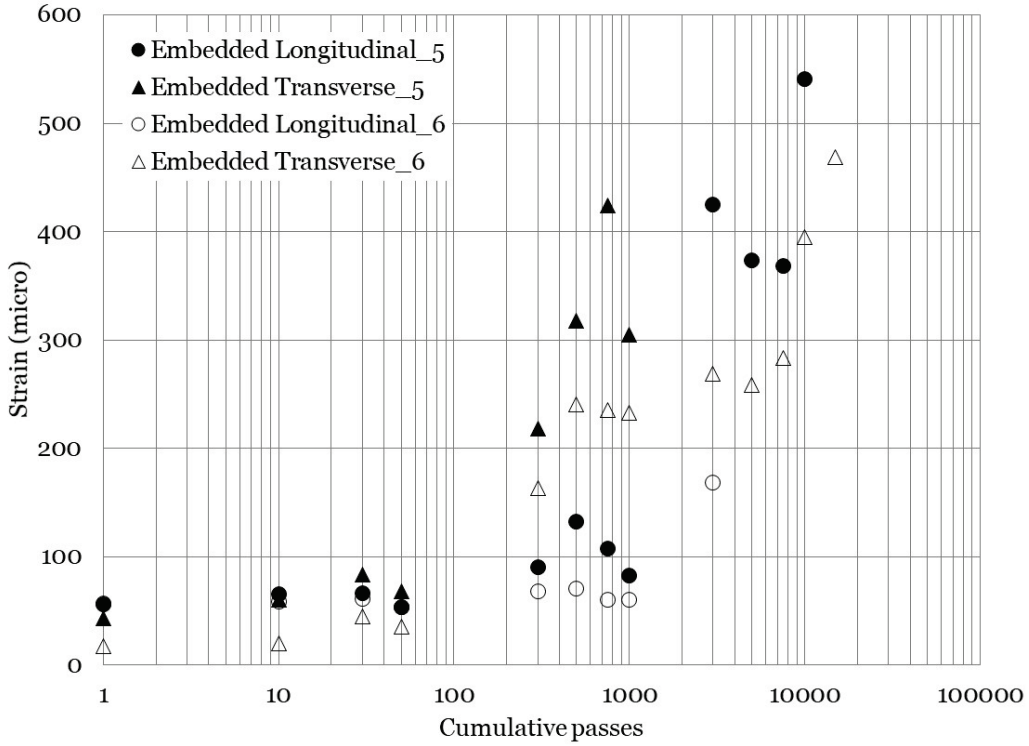

Figure 46. ESG response of midslab (8 in. thick PCC).

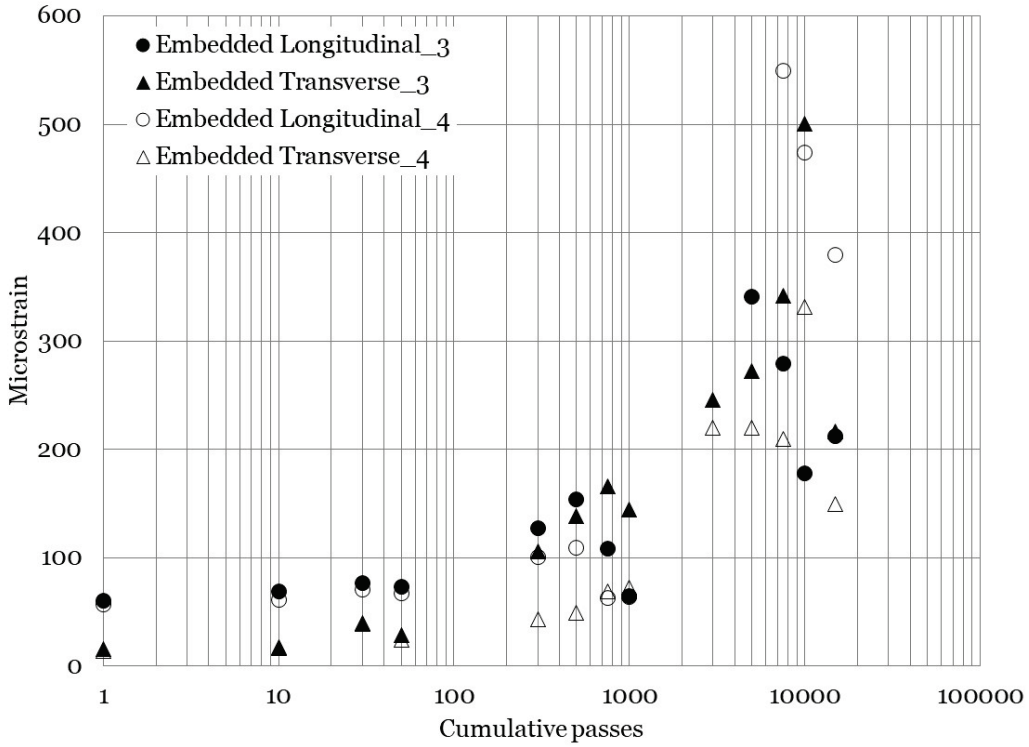

8.1.2 Lane 2 Item 2 (11 in. Thick PCC)

8.1.2.1 HWD Results

Prior to applying P-8 test traffic, a series of HWD tests were conducted at strategic locations throughout the 11 in. thick PCC test item. These tests quantified pretraffic strength characteristics, interrogated the influence of the difference joint construction techniques (dowelled and undowelled joints), and examined the influence of edge condition (free edge and confined edge). Tests were conducted near the edges of the test area, midslab, and near each joint. A graphical representation of the pretraffic HWD test locations is shown in Figure 47. The test locations are represented by circles and are appropriately scaled to reflect position within the test item. The *x*- and *y*-axis dimensions are in feet, and numerical values adjacent to each circle are the calculated ISM values (in kips/in.) at each test location. Greater ISM values indicate a stiffer (stronger) pavement.

As expected, midslab ISM values were generally the greatest observed values; this is attributed to increased overall stiffness away from a joint. The average midslab ISM value was 3,412 kips/in., compared to 2,041 kips/in. along the dowelled joint and 2,263 kips/in. along the nondowelled joint.

Dowel bar inclusion did not result in an improvement in average measured ISM values, an unexpected result. However, this suggests that the undowelled joint was not fully cracked prior to traffic application.

Similarly, HWD tests were conducted after the completion of traffic at the same locations making meaningful comparisons possible. A graphical representation of posttraffic ISM values is shown in Figure 48. In some cases, meaningful decreases in ISM were observed while in others, increases in ISM were observed.

Average dowel joint ISM values decreased by approximately 31% and average undowelled joint ISM values decreased by approximately 53%. Average midslab ISM values had a modest 1% increase after completion of traffic application, essentially no change. These data suggest that the joints were deteriorating with the application of traffic when compared to the midslab data.

Figure 47. Pretraffic HWD results (11 in. thick PCC).

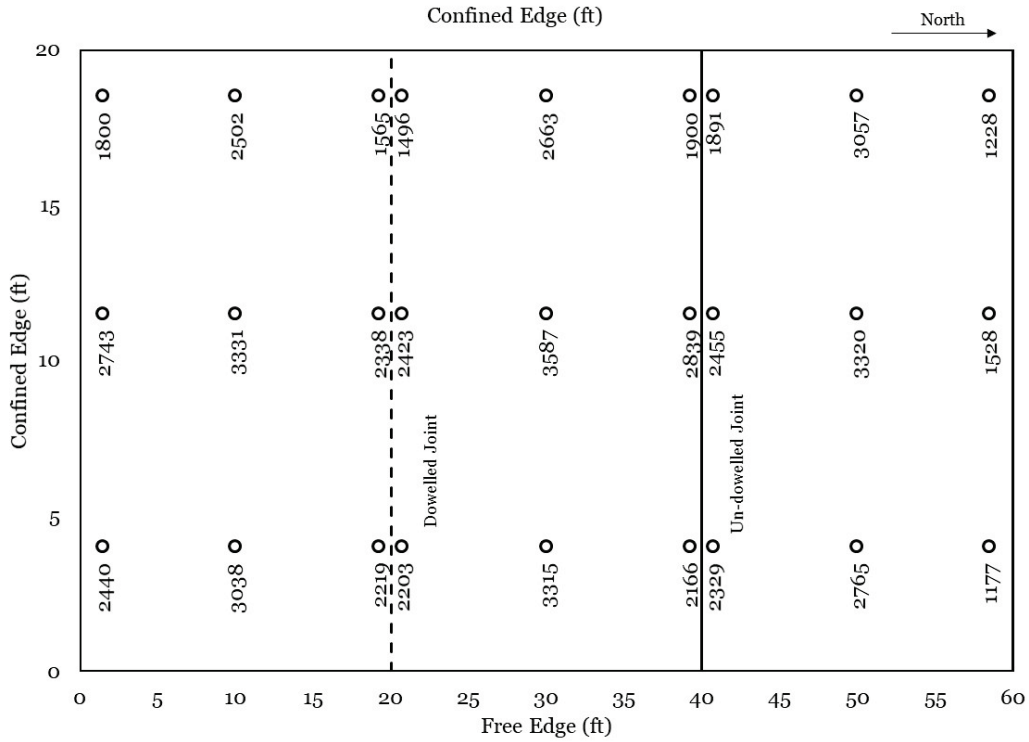

Figure 48. Posttraffic HWD results (11 in. thick PCC).

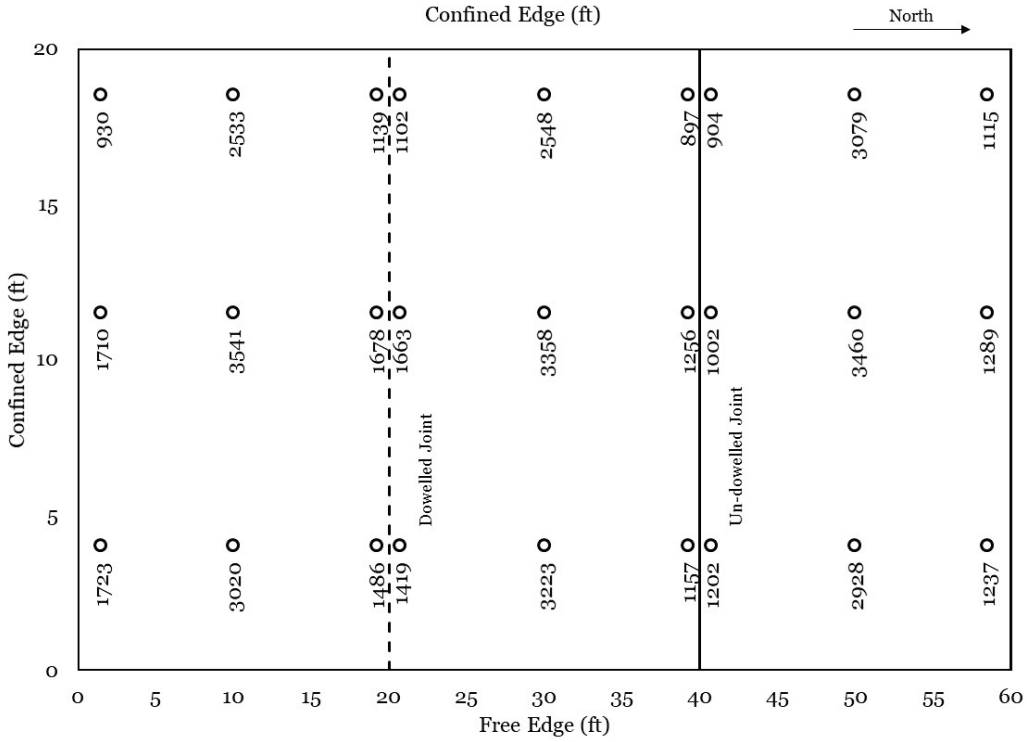

Results of HWD JE measurements are presented in Table 10. Pretraffic results indicated that the average JE was nearly equivalent in the dowelled and nondowelled joint. These data suggest that the nondowelled joint had not cracked full depth prior to traffic application. Posttraffic JE data indicated that the dowelled joint tended to maintain relatively good JE at the conclusion of traffic, while a meaningful reduction in JE was observed in the nondowelled joint.

Table 10. HWD joint load transfer efficiency results (11 in. thick PCC).

Joint Condition	Location		JE (D_1/D_0)	
	X (ft)	Y (ft)	Pretraffic	Posttraffic
Dowelled	20	4	1.08	0.91
Dowelled	20	11.5	1.09	0.86
Dowelled	20	18.5	0..86	0.92
		Average	1.01	0.89
Nondowelled	40	4	0.98	0.31
Nondowelled	40	11.5	1.03	0.16
Nondowelled	40	18.5	0.94	0.64
		Average	0.98	0.37

8.1.2.2 Cracking Observations

Visual inspection, conducted throughout all traffic intervals, did not discover any cracking on the surface of the 11 in. thick PCC test item.

8.1.2.3 FWD Results

FWD data were collected at select traffic intervals during traffic application to monitor structural deterioration; an FWD was used during traffic application in lieu of a HWD due to clearance requirement under the HVS. Measurements were made at the dowelled joint, midslab, quarter-slab, and the nondowelled joint. A summary of ISM values for each condition with cumulative traffic passes is shown in Figure 49.

The greatest measured ISM values were observed at the midslab and quarter-slab locations throughout traffic application. ISM values were observed to be generally consistent throughout traffic application, and a slight decrease in measured ISM at the midslab and quarter-slab locations was observed near the 20,000-pass data collection point. However, the visual inspection did not discover any indications of deterioration.

Interestingly, the nondowelled joint location had a greater pretraffic ISM than the dowelled joint location, suggesting that the nondowelled joint may not have been fully cracked at traffic initiation. As increased traffic was applied, ISM values at the two joint conditions tended to converge. ISM values at each joint location were less than both the midslab and quarter slab locations throughout traffic application.

JE with traffic is shown in Figure 50. The data tend to indicate that JE on the dowelled joint remained relatively consistent throughout traffic application, suggesting that little to no damage was imparted on the dowelled joint. The nondowelled joint experienced a decline in JE throughout traffic application. Relatively high JE values early in traffic suggest that the saw-cut joint had not cracked full-depth prior to traffic. The decline in JE was indicative of the saw-cut crack propagating full depth during traffic application.

Figure 49. ISM with traffic at various locations (11 in. thick PCC).

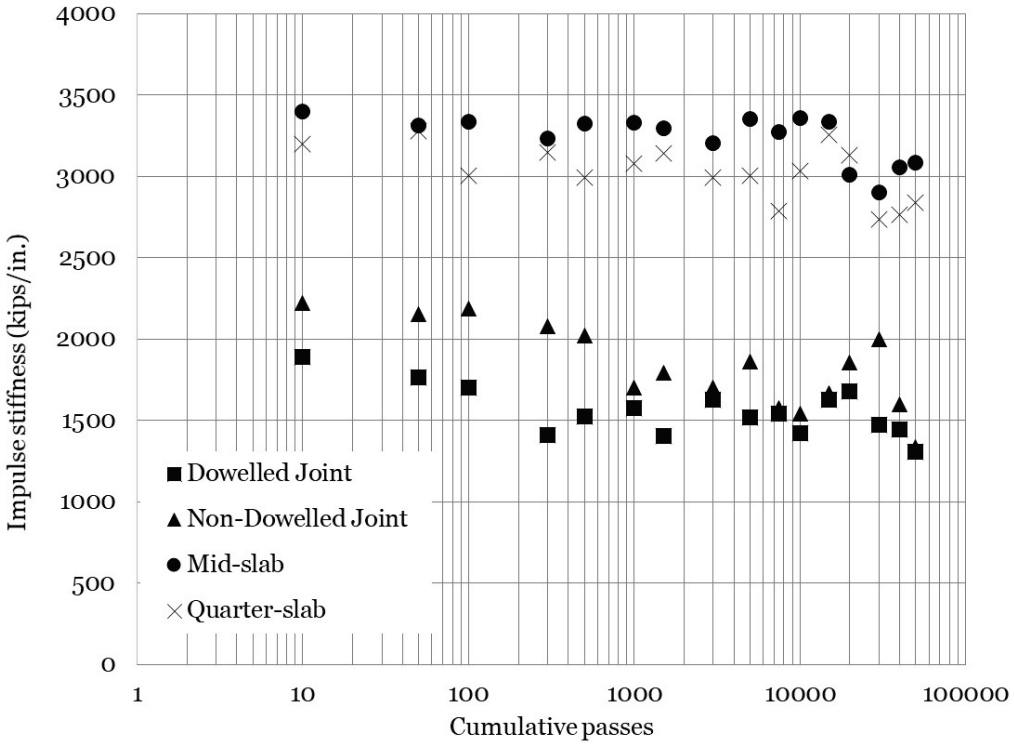

Figure 50. JE with traffic for dowelled and nondowelled joints (11 in. thick PCC).

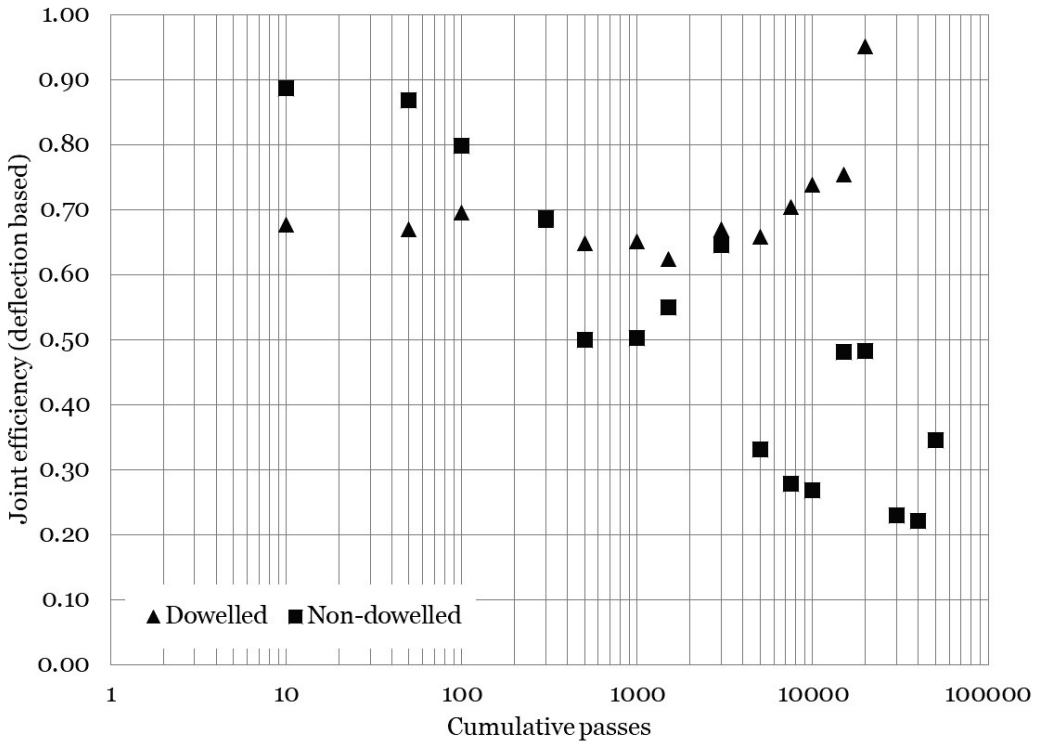

8.1.2.4 Subgrade Pressure Response

A summary of measured subgrade pressure is shown in Figure 51. Representative subgrade response values were determined by selecting the highest measured response near the end of each selected traffic interval. Thus, the values represent a "best hit" when the test gear was directly over a subgrade EPC. Response values were calculated by subtracting the peak value from the minimum value for the event; thus, values represent dynamic measurements.

The maximum measured subgrade pressures were relatively consistent throughout traffic application. Measured midslab values were relatively low (approximately 2 psi) for a majority of traffic applications, and a modest increase (approximately 1 psi) was observed later in traffic application. An EPC located at the dowelled joint was slightly greater (on the order of 4 psi) near the start of traffic and increased to approximately 7 psi near the end of traffic. The measured values in both cases are relatively low, suggesting that the 11 in. thick PCC was sufficiently thick to reduce pressure applied to the subgrade thus limiting potential deterioration in the subgrade layer.

Figure 51. Subgrade pressure response with traffic (11 in. thick PCC).

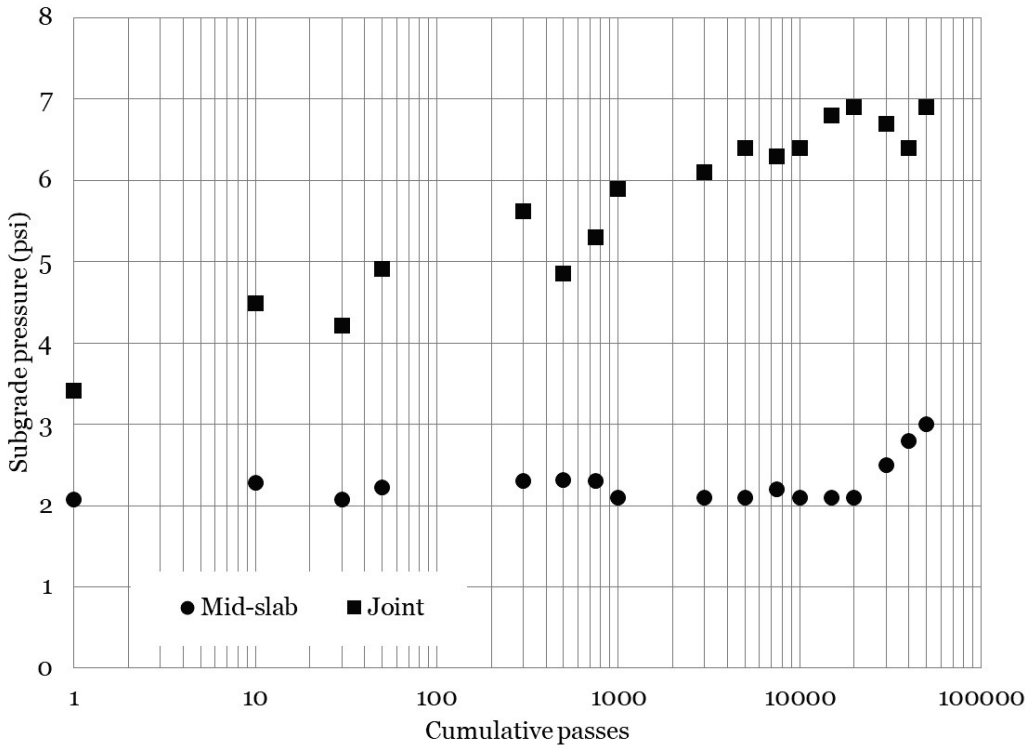

8.1.2.5 SSG Response

SSG response data for the nondowelled joint, dowelled joint, and midslab measurement locations are shown in Figure 52 to Figure 54, respectively. As expected, the SSGs failed relatively early in the traffic sequence.

A review of the SSG data generally showed that measured strains were consistent at all measurement locations. A comparison of the nondowelled and dowelled joint response data indicates a similar response was recorded, which agreed with measured FWD data.

Figure 52. SSG response of nondowelled joint (11 in. thick PCC).

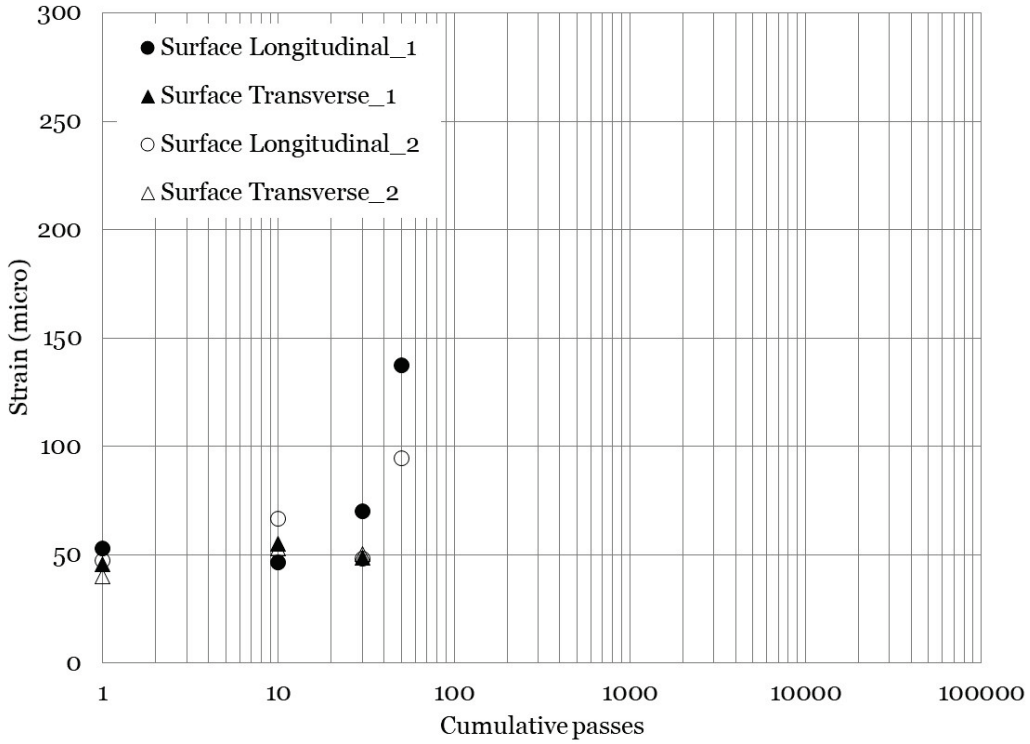

Figure 53. SSG response of dowelled joint (11 in. thick PCC).

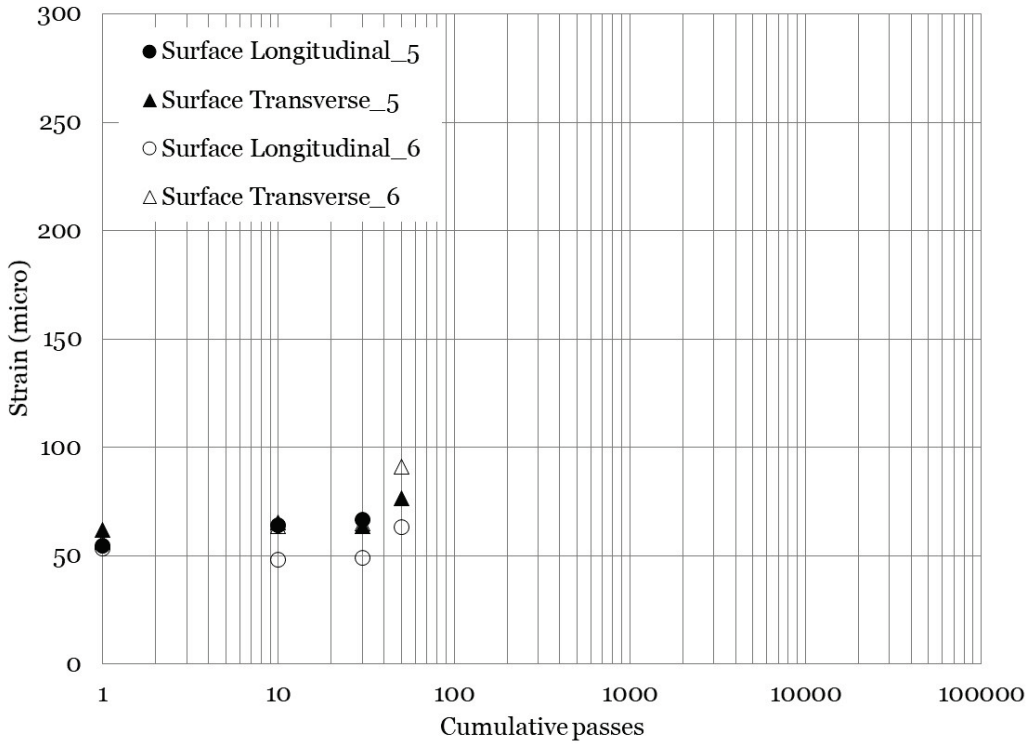

Figure 54. SSG response of midslab (11 in. thick PCC).

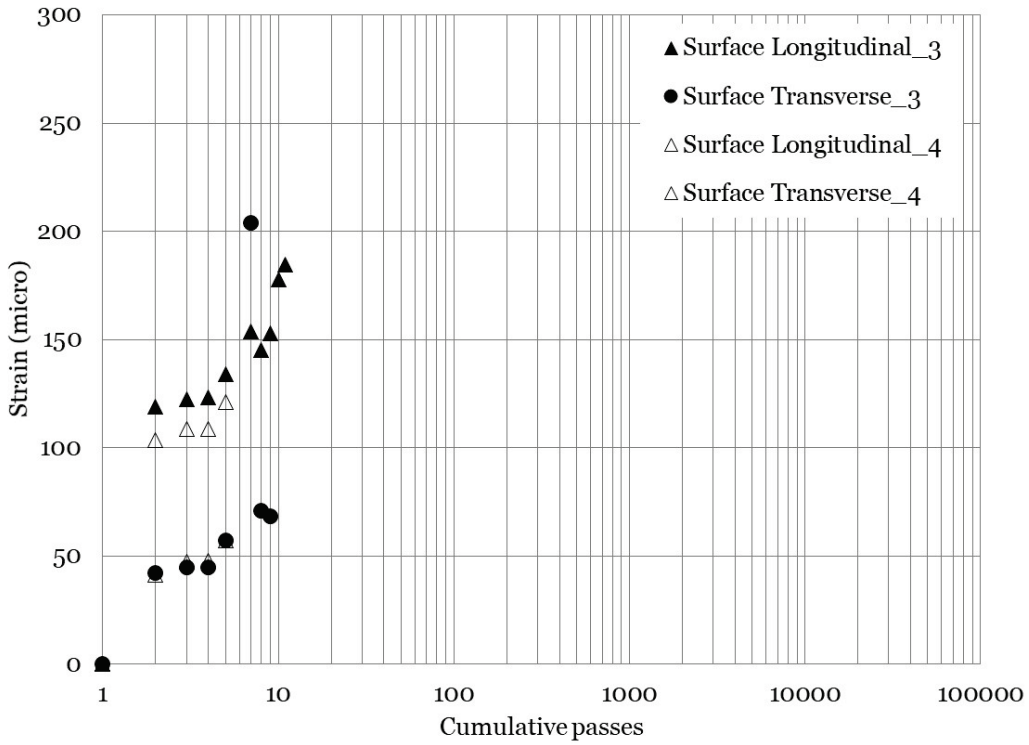

8.1.2.6 ESG Responses

ESG responses for the dowelled and midslab measurement locations are shown in Figures 55 and 56, respectively. An error in the instrument layout during construction resulted in failure to collect ESG data for the nondowelled joint.

Measured response early in traffic was similar for both measurement locations. With increasing traffic levels, little to no meaningful changes were observed in strain gauge response at the midslab locations, suggesting that no internal deterioration occurred at midslab. An increase in measured strain response was observed near 1,000 passes at the dowelled joint; however, a visual inspection did not identify deterioration (cracking in the vicinity of the joint).

Figure 55. ESG response of dowelled joint (11 in. thick PCC).

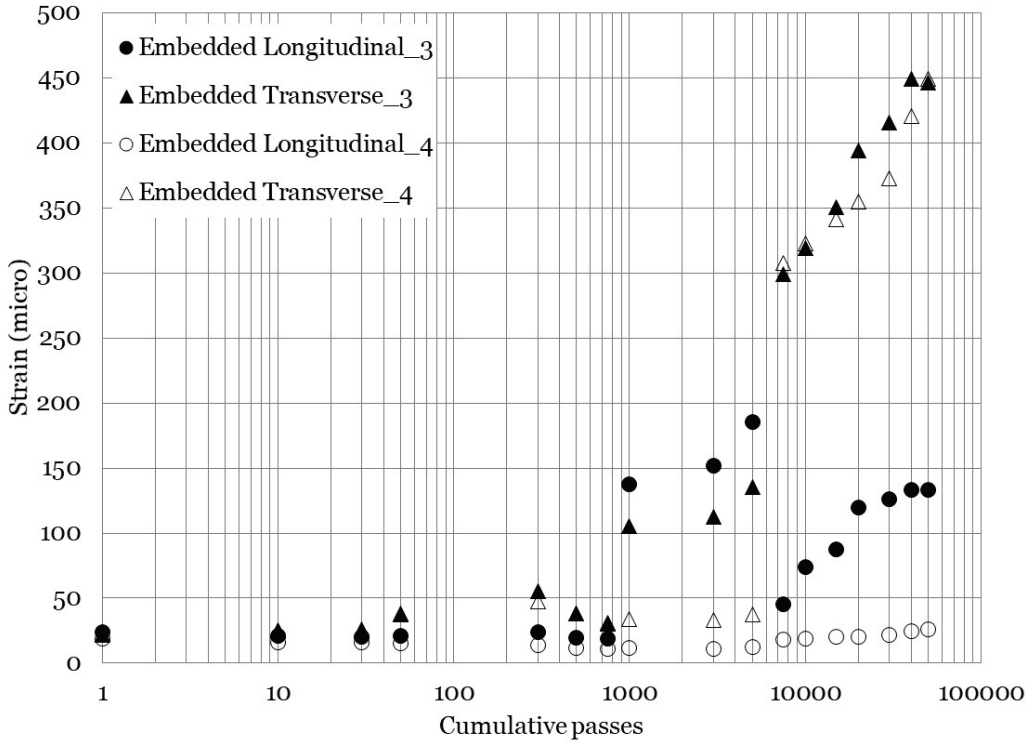

Figure 56. ESG response of midslab (11 in. thick PCC).

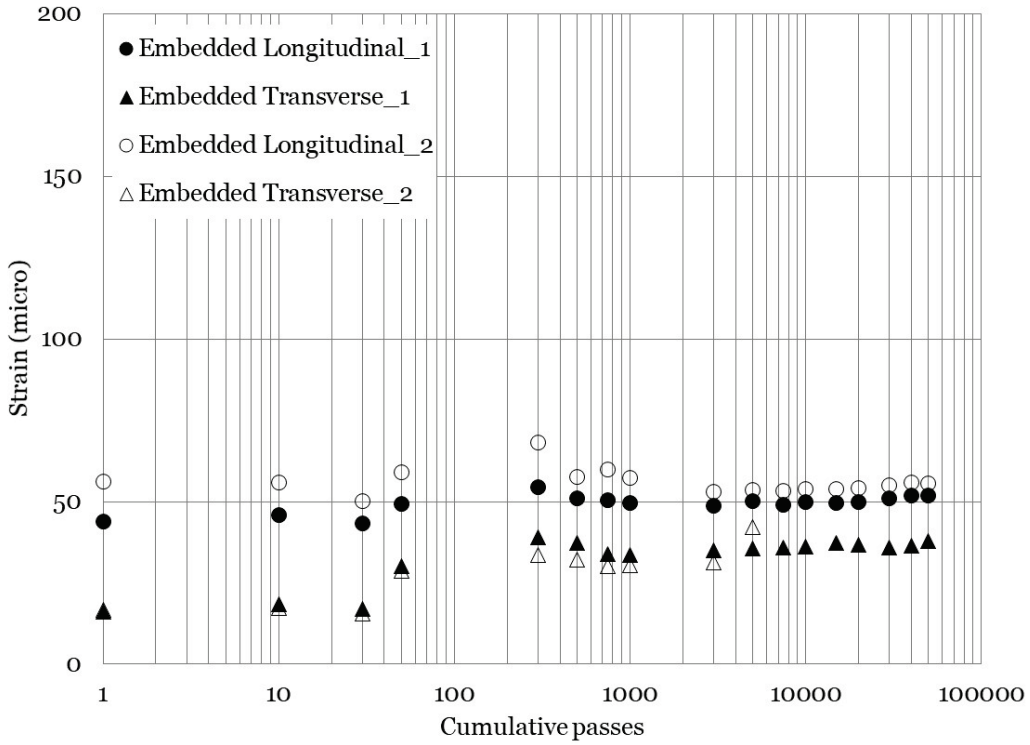

8.1.3 Lane 1 Item 1 (14 in. Thick PCC)

Because of the extensive number of traffic passes applied to the 11 in. thick PCC test item and the lack of observed deterioration, it was determined to not traffic the 14 in. thick PCC test item.

8.2 Flexible Pavement

Failure of the flexible pavement test items was defined as 1 in. of rutting for a permanent operation scenario and 2 in. of rutting for a contingency operation scenario. Rutting included both permanent deformation in the wheel path and upheaval outside the wheel path (Figure 57). Rutting magnitude was measured at multiple locations in each test item using a 12 ft long aluminum straightedge and a machined depth wedge.

Figure 57. Example of rut-depth and permanent-deformation measurement.

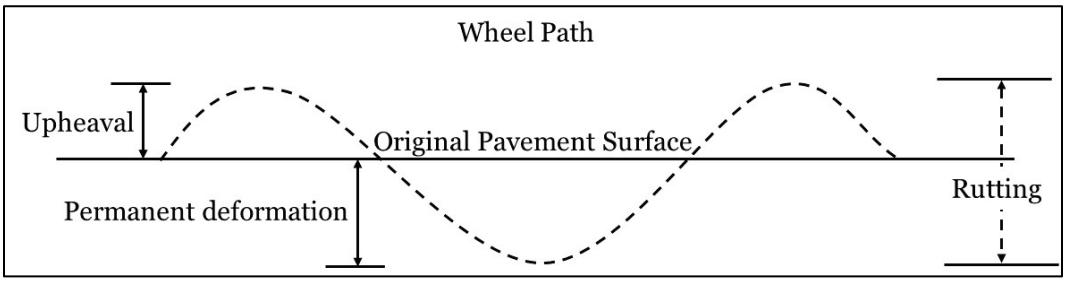

8.2.1 Rutting

Rut-depth progression for the flexible pavement test items is presented in Figure 58. Similarly, a summary of P-8 passes required to produce various rut depths is presented in Table 11. Rut depths were selected to match those currently defined as threshold values for varying levels of pavement condition determination: low (0.25 in. to 0.5), medium (0.5 in. to 1.0 in.), and high (>1.0 in.).

Rapid rut development was observed in the test items constructed with the GR base. The 2 in. thick HMA test item with the gravel base sustained approximately 0.5 in. of rutting for each pass of the P-8 test gear. An increase in HMA thickness was found to improve rutting performance, although the passes to failure remained relatively low. When traditional failure criteria are considered, (1.0 in. rutting) the 2 in. thick HMA test item with the gravel base was capable of sustaining only two passes of the P-8 test gear, and the 4 in. thick HMA test item sustained eight passes of the P-8 test gear. If contingency operations are considered (on the order of 2.0 in. of rutting), the 2 in. thick HMA test item with the gravel base sustained four passes of the P-8 test gear, and the 4 in. thick HMA test item sustained 20 passes of the P-8 test gear. Thus, pavements containing weak base layers (CBR values of approximately 30) should not be expected to sustain a meaningful number of P-8 operations without encountering heavy rutting damage. Visual inspection during traffic application revealed meaningful instability in the pavement evidenced by pumping of the surface. Additionally, the pavement instability resulted in the HVS having extreme difficulty traversing the pavement test section.

A meaningful improvement in rutting performance was observed when the base-course layer strength was increased. The 2 in. thick HMA and 4 in. thick HMA test items constructed with a highquality crushed limestone base over 10 CBR subgrade sustained over 200 passes for the

1.0 in. rutting criteria. This result highlights the importance of a competent aggregate base layer for heavy aircraft loads. Comparatively, the 2 in. thick HMA test item and 4 in. thick test item with the crushed limestone base sustained a similar number of passes to 1 in. rut depth, and, unexpectedly, the 2 in. thick HMA test item sustained 260 passes compared to 222 passes in the 4 in. thick HMA test item. This suggests that at greater subgrade CBR values, pavement rutting performance becomes less sensitive to HMA layer thickness, particularly at lower levels of rutting. After 1 in. of rutting occurred, the performance was similar for the 2 in. thick and 4 in. thick HMA test items further implying that pavement performance becomes less sensitive to HMA thickness at greater subgrade CBR values.

Reduction in subgrade strength from 10 to 6 CBR resulted in an approximate 60% to 70% reduction in passes to 1 in. rut depth. For 2 in. of HMA and a limestone base, the item with 6 CBR subgrade sustained 79 passes to 1 in. rut depth, and the item with 10 CBR subgrade sustained 260 passes. For 4 in. of HMA with the limestone base, the item with 6 CBR subgrade sustained 99 passes to 1 in. rut depth, and the item with 10 CBR subgrade sustained 222 passes. Similar trends were observed beyond 1 in. rut depth. In the case of contingency operations (allowing up to 2.0 in. of rut depth), then reduction in subgrade CBR results in approximately 50% reduction in passes to failure.

These rutting performance data indicate that a competent base layer is required to sustain a reasonable number of P-8 operations. The drastic difference in pavement rutting performance suggests that for the case of new construction, aggregate base layer materials should be required to meet existing materials specifications (i.e., CBR values ranging from 80 to 100.) Further, the data indicate that the HMA layer should be at least 4 in. thick to support a minimum of 500 operations of a P-8 aircraft in a contingency scenario.

Figure 58. Rut-depth progression with traffic.

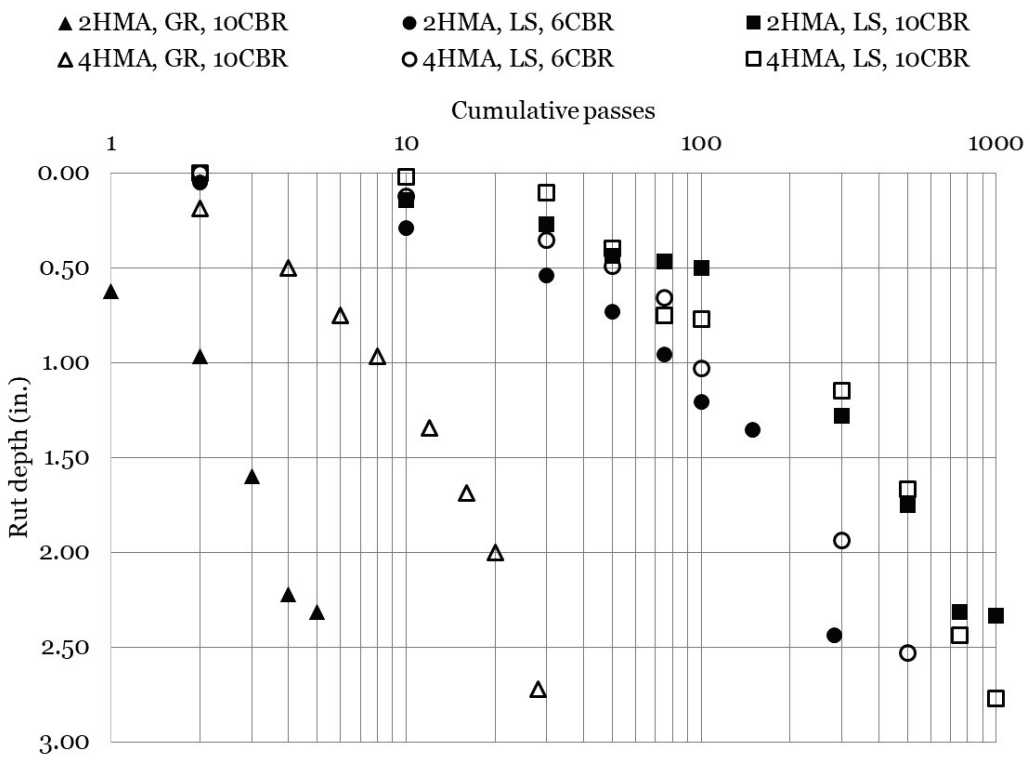

Table 11. Passes required to produce various rut depths.

	Rut Depth (in.)							
Passes to rut	0.25	0.50	0.75	1.00	1.25	1.50	2.00	2.50
2HMA, GR, 10CBR	1	1	1	2	3	3	4	7
4HMA, GR, 10CBR	2	4	6	8	11	14	20	26
2HMA, LS, 6CBR	9	27	52	79	114	168	230	290
4HMA, LS, 6CBR	21	52	81	99	148	203	321	489
2HMA, LS, 10CBR	27	100	180	260	292	356	611	833
4HMA, LS, 10CBR	40	57	75	222	340	436	608	797

Note: Values interpolated from measured rut-depth data.

8.2.2 ISM

FWD data were collected to monitor overall structural deterioration with increasing traffic levels. FWD data were collected at the locations of installed instrumentation in each test item so that pavement stiffness and instrumentation response were collected at the same locations. Average ISM values for each test item were calculated and used for analysis as presented in Figure 59. An attempt was made to collect FWD data at each

traffic collection point; however, significant pavement deterioration prevented successful FWD operation on occasion.

Initial pretraffic ISM values for the gravel base test items were low, as expected. The FWD identified changes in HMA thickness; a greater initial ISM value was noted in the 4 in. thick HMA test item compared to the 2 in. thick HMA test item over the gravel base. Loss of strength was observed with increasing passes, and the ISM of the 4 in. thick HMA test item approached the ISM of the 2 in. thick HMA test item at the completion of test traffic.

An increase in base course strength resulted in a meaningful increase in pavement stiffness. Initial ISM values in the 4 in. thick HMA test item with the limestone base over a 10 CBR subgrade were approximately 200 kips/in. greater than those observed in the comparative pavement section with gravel base. A similar trend was observed in the 2 in. thick HMA test items. Overall, the 4 in. thick HMA over limestone base over 10 CBR subgrade test item had the highest ISM value as expected. The 4 in. thick HMA item remained the best performer throughout traffic application, although a decline in stiffness was observed. A similar rate of stiffness decline was observed in the 2 in. thick HMA test item.

The FWD detected a reduction in subgrade CBR; a decrease in subgrade CBR from 10 to 6 resulted in a decrease in initial ISM. Notably, initial ISM values in the 4 in. thick HMA over 6 CBR subgrade test item were nearly equivalent to those measured in the 2 in. thick HMA over 10 CBR subgrade test item suggesting that increasing the subgrade CBR provided a stiffness enhancement equivalent to an additional 2 in. of HMA.

However, the team observed that as passes increased and pavement deterioration accumulated, ISM values tended to converge regardless of pavement cross section except for the 4 in. thick HMA over LS over 10 CBR test item. These data support the recommendation that to support a meaningful number of P-8 operations, a minimum 4 in. thick HMA layer over a competent base layer and a relatively stiff subgrade is required.

Figure 59. ISM with traffic.

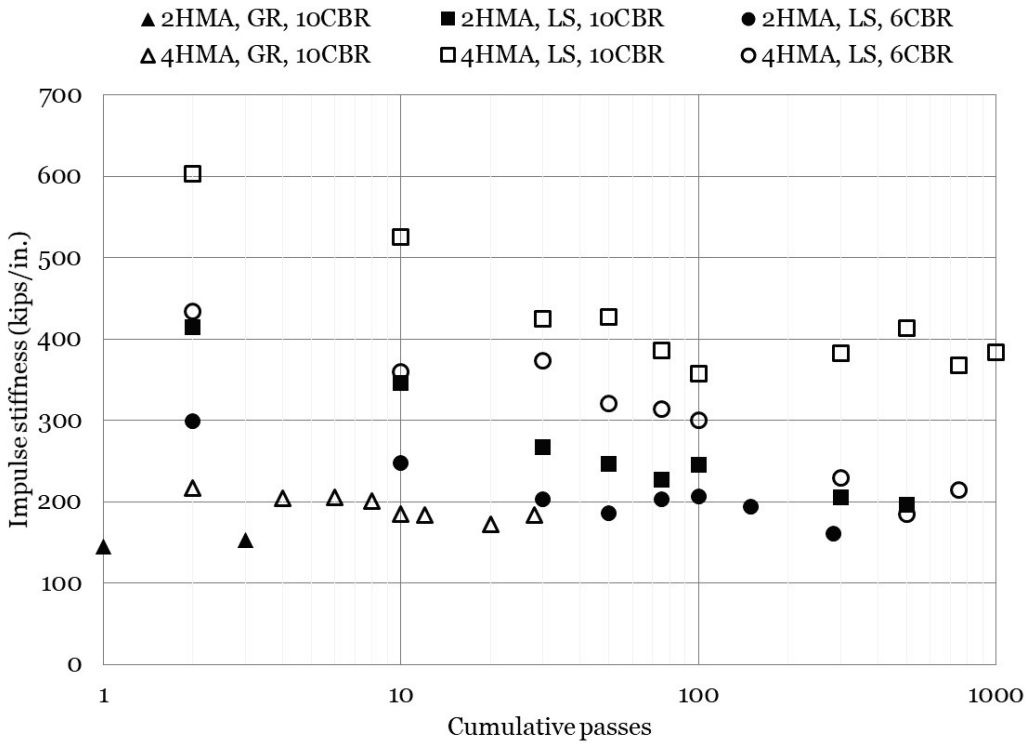

8.2.3 Subgrade pressure response

Subgrade vertical pressure response data are presented in Figure 60. When interpreting the maximum subgrade response, it is important to understand the P-8 gear position in relation to instrumentation location early in traffic application. The initial traffic pass was applied with the center of the test gear located at the centerline of the test item; thus, a test tire was not positioned directly over the installed instrumentation. As each additional traffic pass was applied, the HVS shifted the P-8 gear approximately 2 in. laterally in the wander pattern. Thus, the increase in measured pressure observed early in traffic could be attributed to a test tire moving closer to the installed instrumentation. Peak initial measured pressure (near 20 passes) occurred when a P-8 tire was directly over the installed instrumentation. Data presented after 100+ passes represent the maximum observed response or "best hit" during application of a full traffic pattern.

In all cases, an increase in measured subgrade vertical pressure response was observed as the test gear shifted closer to the subgrade EPC, and subgrade pressure tended to reach a steady state thereafter. Minor variation in measured subgrade pressure was observed with an increase in traffic

application; however, definitive trends could not be identified. In general, measured subgrade pressure ranged from approximately 50 to 80 psi.

Figure 60. Measured subgrade pressure response with traffic.

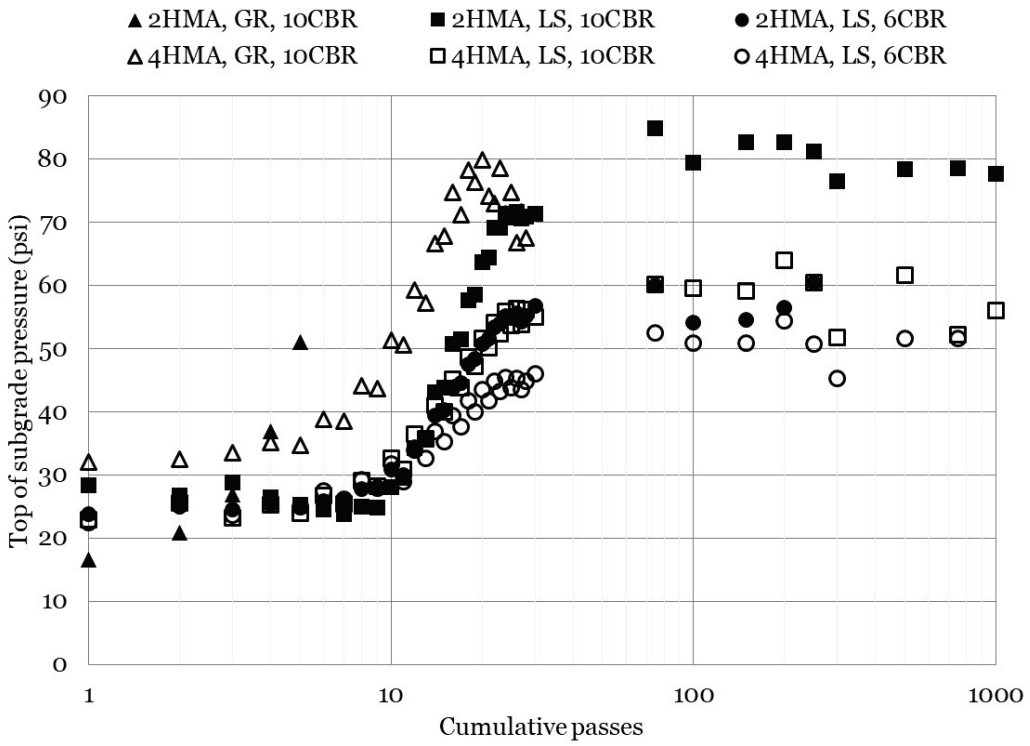

A series of equality plots were generated to aid understanding the effect of differing pavement cross-section properties on measured subgrade pressure. Equality plots are useful in interpreting the effect of HMA thickness and subgrade strength on measured subgrade pressure. Note that limited data were available for the gravel base test items due to rapid pavement failure; thus, equality plots for those data were not generated.

Figures 61 and 62 present equality plots to investigate the effect of HMA thickness for the limestone base test items with a 6 CBR subgrade and 10 CBR subgrade, respectively. In both cases measured subgrade pressure early in traffic (lower measured pressure response) were generally clustered around the line of equality (LOE). Later in traffic application (greater measured pressure response), it was observed that the data tended to trend below the LOE, indicating measured subgrade pressure was consistently less in the 4 in. thick HMA test items. In the 10 CBR subgrade comparison, the data tended to be further from the LOE, suggesting the influence of HMA thickness was more pronounced with an increase in subgrade CBR.

Figures 63 and 64 present equality plots to investigate the effect of subgrade CBR for the limestone base test items with a 4 in. thick HMA and 2 in. thick HMA layer, respectively. Measured subgrade pressure early in traffic application tended to be near the LOE, and measured subgrade pressure diverged from the LOE later in traffic application. In both cases, the data plotted below the LOE indicating that an increase in subgrade CBR resulted in an increase in measured subgrade pressure. The difference tended to be more pronounced in the 2 in. thick HMA comparison suggesting that measured subgrade pressure in thinner HMA pavement sections is more sensitive to subgrade CBR.

Figure 61. Subgrade pressure-effect of HMA thickness for LS base, 6 CBR subgrade.

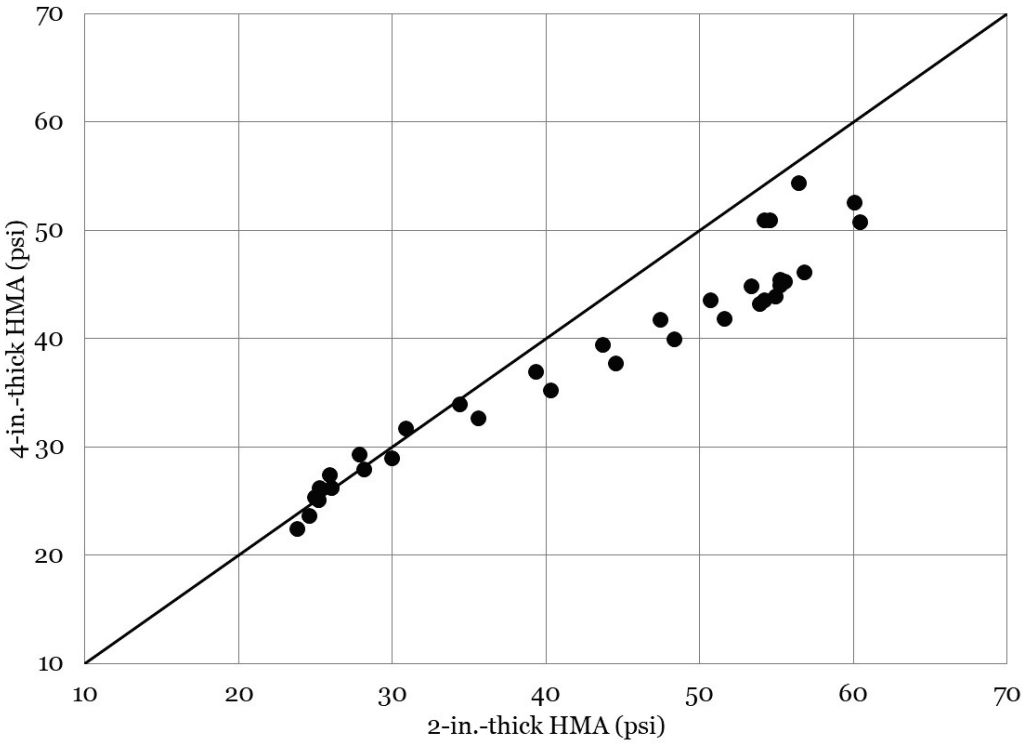

Figure 62. Subgrade pressure-effect of HMA thickness for LS base, 10 CBR subgrade.

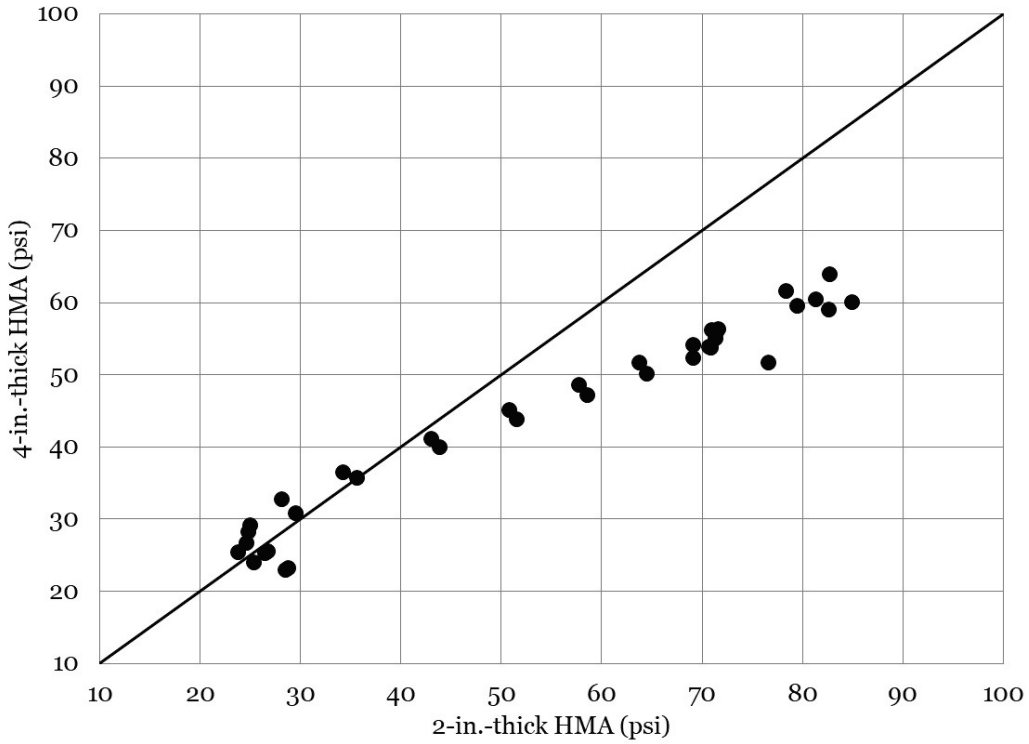

Figure 63. Subgrade pressure-effect of subgrade CBR for 4 in. HMA, LS base.

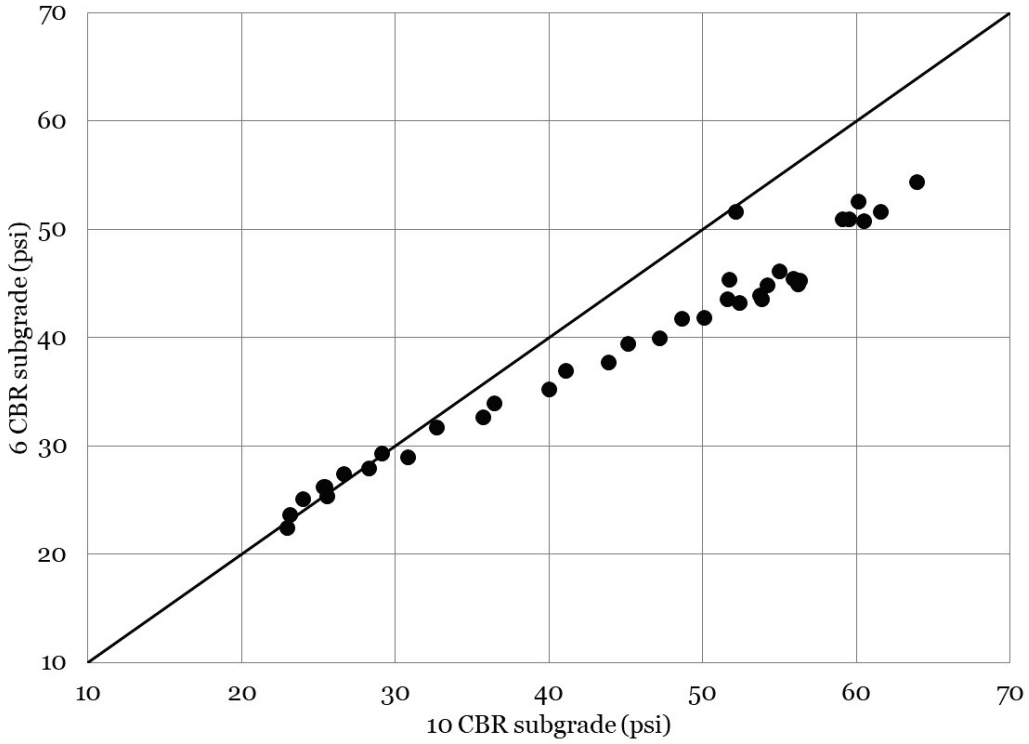

Figure 64. Subgrade pressure-effect of subgrade CBR for 2 in. HMA, LS base.

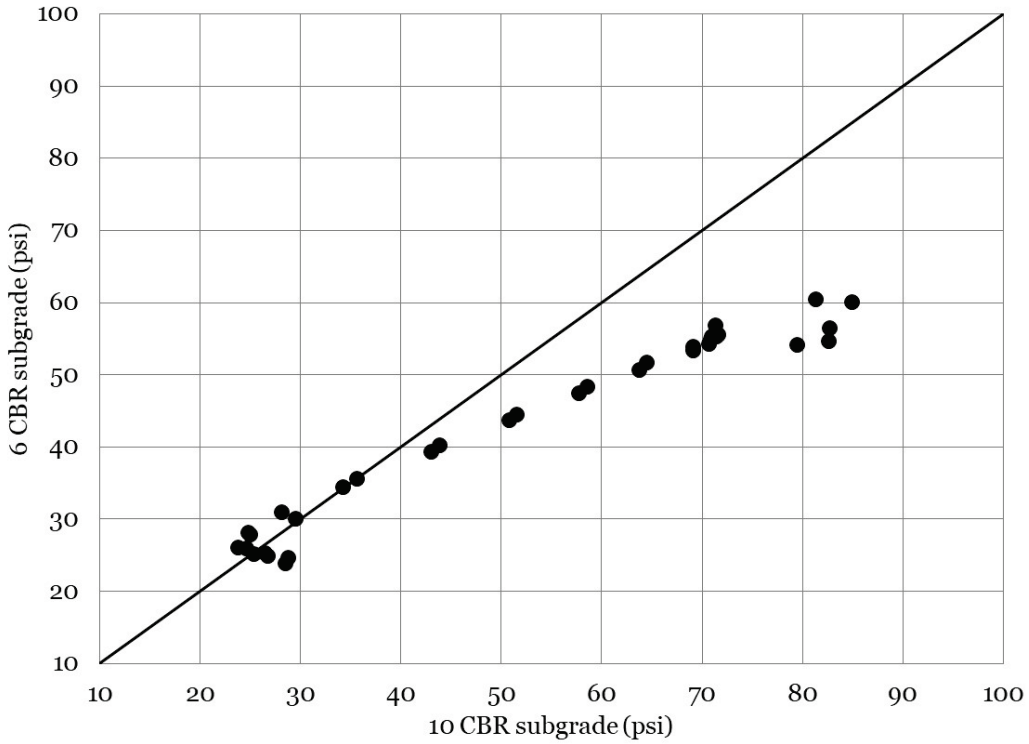

A statistical analysis of measured subgrade pressure response (Table 12) was conducted to determine if observed differences were statistically significant. A paired T-test was used because response measurements were collected at the same traffic interval, and similar construction techniques were used for all test items. A two-tailed rejection region was considered (i.e., the average difference between the observed values was zero.) All statistical measures were evaluated at $\alpha = 0.05$. It should be noted that comparisons that included the 2HMA over GR over 10 CBR test item had a small sample size due to rapid failure; thus, the robustness of the statistical comparison should be interpreted with caution.

In the case of comparisons made to the 4HMA over GR over 10 CBR test item (Table 12), researchers found that all the limestone base test items had statistically lower subgrade pressures.

Direct comparison of subgrade strength found that both the 4 in. thick HMA and 2 in. thick HMA resulted in statistically different average subgrade pressure. In both cases, researchers found that the 6 CBR subgrade yielded lower average subgrade pressure response.

Comparison of HMA thickness found that an increase in HMA thickness resulted in statistically different average subgrade pressure on both a 6 and 10 CBR subgrade. In both cases, the 4 in. thick HMA test item was found to be the better performer as expected.

Table 12. Statistical analysis of subgrade pressure response.

Comparison	*n*	*p*-Value	Significant	Better Performer	Difference (psi)[1]
4HMA, GR, 10 CBR vs. 2HMA, GR, 10 CBR	5	0.611	No	Same	0.0
4HMA, GR, 10 CBR vs. 4HMA, LS, 6 CBR	28	<0.001	Yes	4HMA, LS, 6 CBR	-23.4
4HMA, GR, 10 CBR vs. 2HMA, LS, 6 CBR	28	<0.001	Yes	2HMA, LS, 6 CBR	-19.0
4HMA, GR, 10 CBR vs. 4HMA, LS, 10 CBR	28	<0.001	Yes	4HMA, LS, 10 CBR	-18.8
4HMA, GR, 10 CBR vs. 2HMA, LS, 10 CBR	28	<0.001	Yes	2HMA, LS, 10 CBR	-12.7
2HMA, GR, 10 CBR vs. 4HMA, LS, 6 CBR	5	0.365	No	Same	0.0
2HMA, GR, 10 CBR vs. 2HMA, LS, 6 CBR	5	0.393	No	Same	0.0
2HMA, GR, 10 CBR vs. 4HMA, LS, 10 CBR	5	0.362	No	Same	0.0
2HMA, GR, 10 CBR vs. 2HMA, LS, 10 CBR	5	0.642	No	Same	0.0
4HMA, LS, 6 CBR vs. 2HMA, LS, 6 CBR	34	<0.001	Yes	4HMA, LS, 6 CBR	-4.7
4HMA, LS, 6 CBR vs. 4HMA, LS, 10 CBR	37	<0.001	Yes	4HMA, LS, 6 CBR	-5.3
4HMA, LS, 6 CBR vs. 2HMA, LS, 10 CBR	37	<0.001	Yes	4HMA, LS, 6 CBR	-13.2
2HMA, LS, 6 CBR vs. 4HMA, LS, 10 CBR	34	0.078	No	Same	0.0
2HMA, LS, 6 CBR vs. 2HMA, LS, 10 CBR	34	<0.001	Yes	2HMA, LS, 6 CBR	-9.3
4HMA, LS, 10 CBR vs. 2HMA, LS, 10 CBR	38	<0.001	Yes	4HMA, LS, 10 CBR	-10.2

[1]Average difference between datasets; *n* = number of observations.

8.2.4 Base Pressure Response

Base vertical pressure response data measured at the top of the base layer are presented in Figure 65. As noted with subgrade pressure response, early pressure measurements were a function of wheel position. Like subgrade pressure response, an increase in measured

pressure was observed as the test wheel moved closer to the earth pressure cell. Thereafter, a steady-state condition was achieved, and reported pressures represent the maximum observed pressure during a respective traffic interval.

Some variability was observed in the top of base measured response and could be attributed to material movement in the base course layer. Visual observation suggested that during traffic application there was meaningful movement in the pavement that was a function of the dual-wheel configuration. Researchers hypothesize there was a "kneading" action from the dual-wheel (material was in a state of upheaval at times and in a state of deformation at times) that was a function of the wander pattern and wheel position. Thus, sensors placed higher in the pavement would be expected to be more sensitive to wheel wander. In general, it was observed that top-of-base pressures ranged from approximately 150 psi to nearly 230 psi.

Figure 65. Measured top-of-base pressure response with traffic.

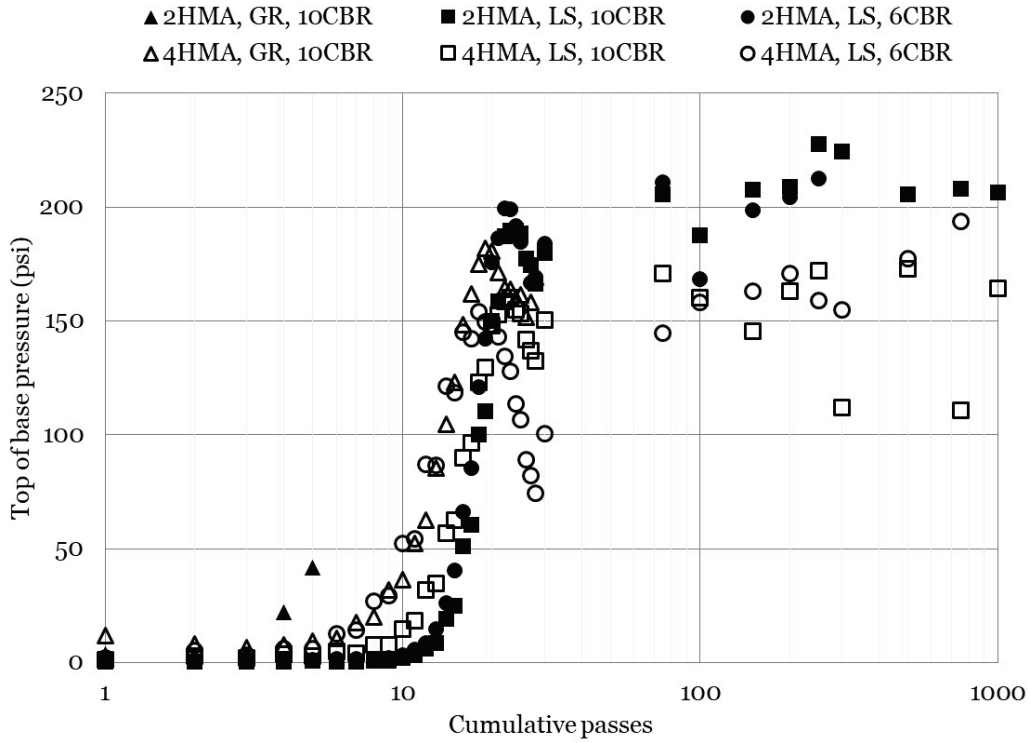

Equality plots for top-of-base pressure measurements are presented in Figure 66 through Figure 69. A review of Figures 66 and 67 provides insight into the effect of HMA thickness on 6 CBR subgrade and 10 CBR subgrade, respectively. In both cases, early data fall above the LOE,

indicating that measured pressures were greater in the 4 in. thick HMA test items when compared to the 2 in. thick HMA test items. While this was not expected, recall that in initial traffic the test wheels were not directly over the EPC. Thus, this could be attributed to differences in subsurface stress distribution that were a function of the dual-wheel gear configuration. Later in traffic at greater pressure levels, the data tend to cluster below the LOE indicating that greater pressure were measured in the 2 in. thick HMA test items, as expected. In both cases, the data tended to be similar distances from the LOE suggesting that subgrade CBR did not have a meaningful effect on top of base measured pressure. A review of Figures 68 and 69 confirms this suspicion because the steady-state data tended to be clustered both above and below the LOE.

Figure 66. Top-of-base pressure-effect of HMA thickness for LS base, 6 CBR subgrade.

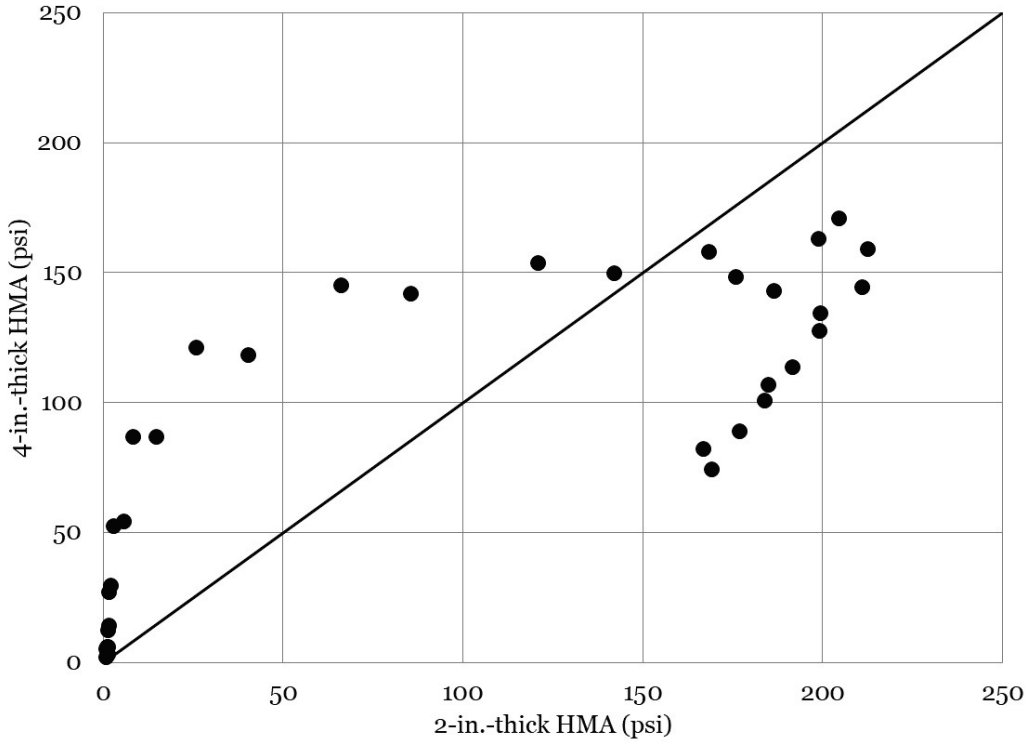

Figure 67. Top-of-base pressure-effect of HMA thickness for LS base, 10 CBR subgrade.

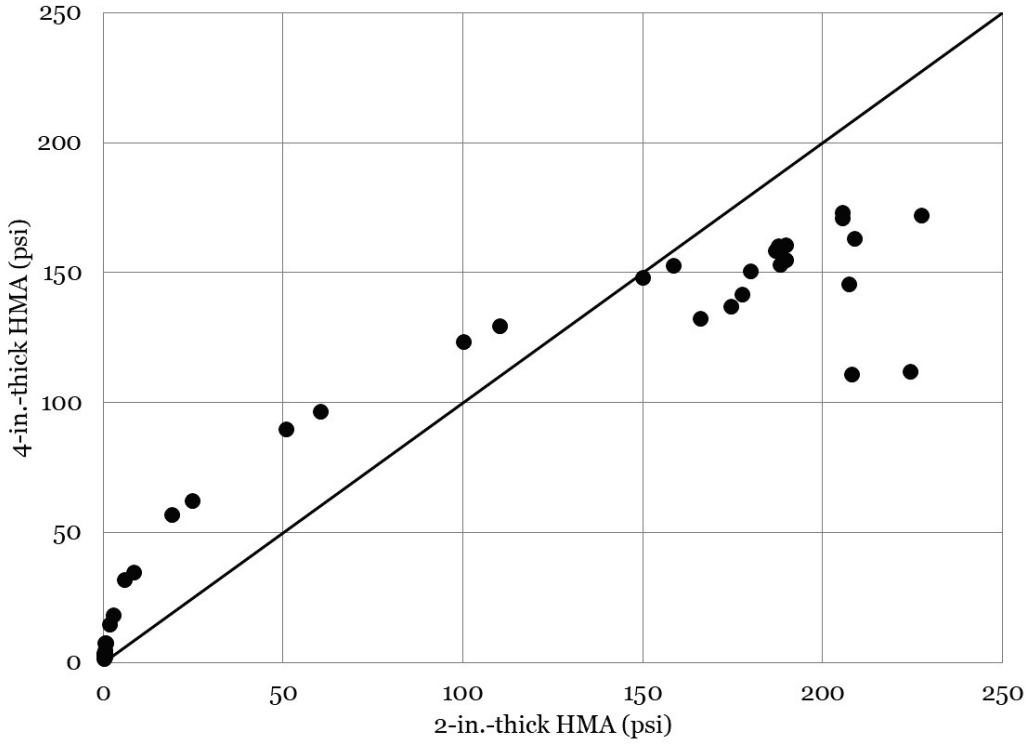

Figure 68. Top-of-base pressure-effect of subgrade CBR for 4 in. HMA, LS base.

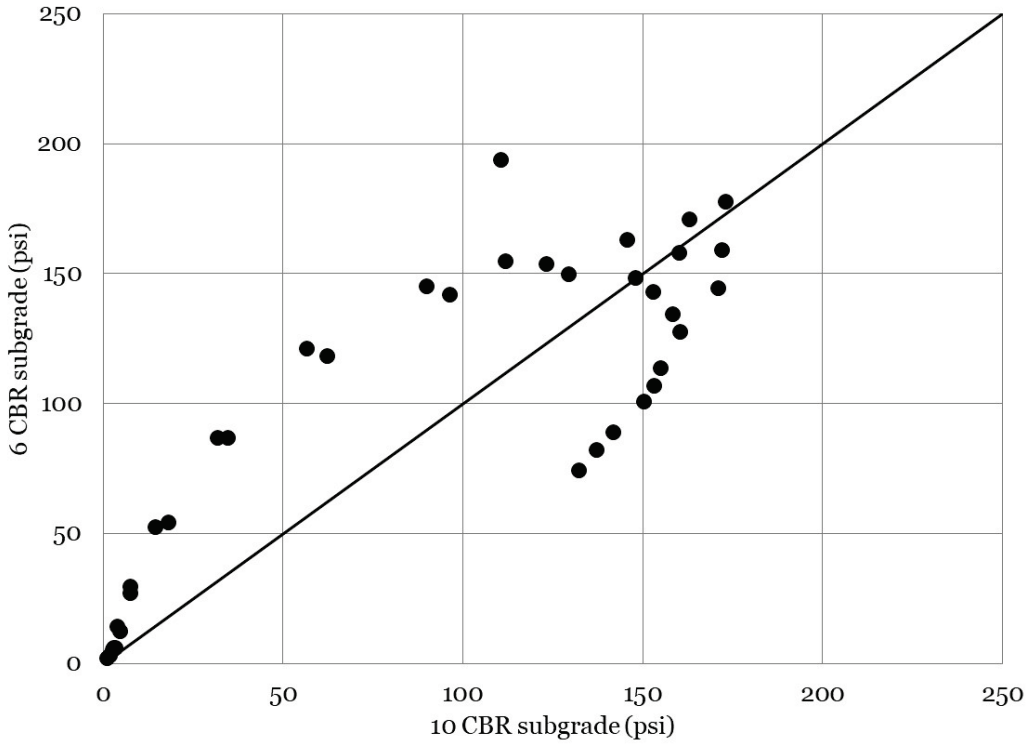

Figure 69. Top-of-base pressure-effect of subgrade CBR for 2 in. HMA, LS base.

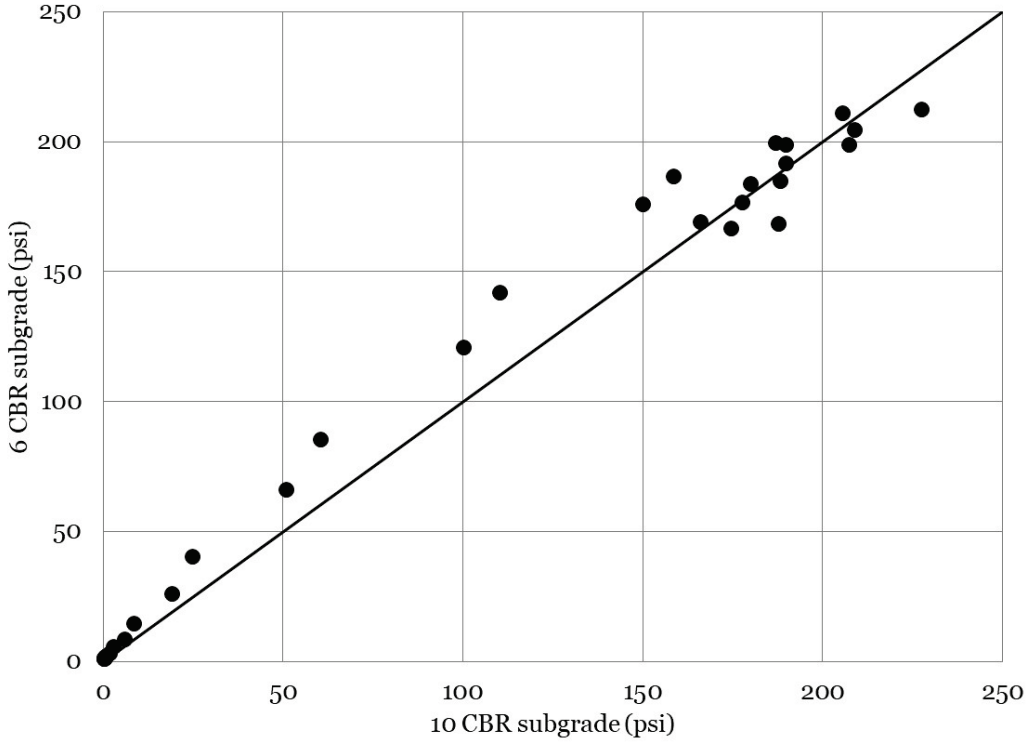

A statistical analysis of top-of-base pressure response is presented in Table 13. A comparison of subgrade strength found that differences in base pressure response were significant in the 2 in. thick HMA sections (p = 0.020) and that the 10 CBR subgrade resulted in a lower average top of base pressure. Comparison of the 4 in. thick HMA test item was unremarkable (p = 0.236) suggesting that subgrade CBR did not influence top-of-base pressure with a thicker HMA layer.

Similarly, if direct comparisons are made for HMA thickness on the same subgrade CBR value, it is observed that for the 6-CBR subgrade increasing HMA thickness did not result in a statistically significant difference in average top-of-base pressure (p = 0.508). Comparison of the 10 CBR subgrade was found to be statistically significant (p = 0.035), and the 4 in. thick HMA test item was found to be the better performer.

Table 13. Statistical analysis of top of base pressure response.

Comparison	*n*	*p*-Value	Significant	Better Performer	Difference (psi)[1]
4HMA, GR, 10 CBR vs. 2HMA, GR, 10 CBR	5	0.559	No	Same	0.0
4HMA, GR, 10 CBR vs. 4HMA, LS, 6 CBR	28	0.003	Yes	4HMA, LS, 6 CBR	-17.8
4HMA, GR, 10 CBR vs. 2HMA, LS, 6 CBR	28	0.008	Yes	2HMA, LS, 6 CBR	-20.0
4HMA, GR, 10 CBR vs. 4HMA, LS, 10 CBR	28	<0.001	Yes	4HMA, LS, 10 CBR	-25.1
4HMA, GR, 10 CBR vs. 2HMA, LS, 10 CBR	28	0.002	Yes	2HMA, LS, 10 CBR	-27.2
2HMA, GR, 10 CBR vs. 4HMA, LS, 6 CBR	5	0.287	No	Same	0.0
2HMA, GR, 10 CBR vs. 2HMA, LS, 6 CBR	5	0.192	No	Same	0.0
2HMA, GR, 10 CBR vs. 4HMA, LS, 10 CBR	5	0.224	No	Same	0.0
2HMA, GR, 10 CBR vs. 2HMA, LS, 10 CBR	5	0.176	No	Same	0.0
4HMA, LS, 6 CBR vs. 2HMA, LS, 6 CBR	34	0.508	No	Same	0.0
4HMA, LS, 6 CBR vs. 4HMA, LS, 10 CBR	37	0.236	No	Same	0.0
4HMA, LS, 6 CBR vs. 2HMA, LS, 10 CBR	37	0.643	No	Same	0.0
2HMA, LS, 6 CBR vs. 4HMA, LS, 10 CBR	34	0.016	Yes	4HMA, LS, 10 CBR	-10.6
2HMA, LS, 6 CBR vs. 2HMA, LS, 10 CBR	34	0.020	Yes	2HMA, LS, 10 CBR	-4.9
4HMA, LS, 10 CBR vs. 2HMA, LS, 10 CBR	38	0.035	Yes	4HMA, LS, 10 CBR	-12.7

[1]Average difference between datasets; *n* = number of observations.

Measured base pressure response at middepth of the base layer is presented in Figure 70. The lowest middepth pressure response was observed in the 4 in. thick HMA over LS base over 10 CBR subgrade test item, and the highest measured middepth pressure response was observed in the companion 2 in. thick HMA test item. In general, measured middepth base layer pressures ranged from 60 psi to 120 psi. A slight increasing trend was observed in most cases suggesting that damage was occurring in the base course layer with an increase in traffic passes.

Figure 70. Measured middepth base pressure response with traffic.

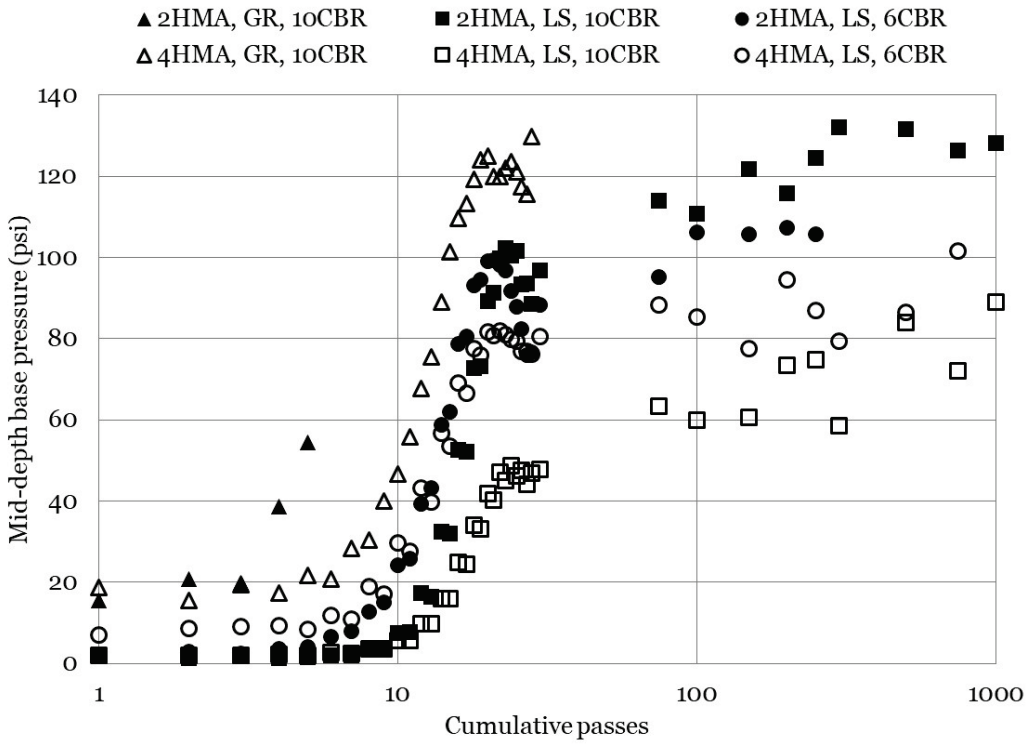

Equality plots for middepth base pressure measurements are presented in Figure 71 through Figure 74. A review of Figures 71 and 72 revealed that measured response data fell below the LOE, indicating that measured pressures were greater in the 2 in. thick HMA test items. The measured data tended to be further from the LOE in the case of a 10 CBR subgrade. A review of the 4 in. thick HMA equality plot (Figure 73) found that all measured data fell above the LOE, indicating that a reduction in subgrade CBR resulted in an increase in middepth base pressure. Measured pressures in the 2 in. thick HMA test items (Figure 74) fell both above and below the LOE suggesting that subgrade CBR had did not have a meaningful impact on middepth base pressure response in the thinner HMA test items.

Figure 71. Middepth base pressure-effect of HMA thickness for LS base, 6 CBR subgrade.

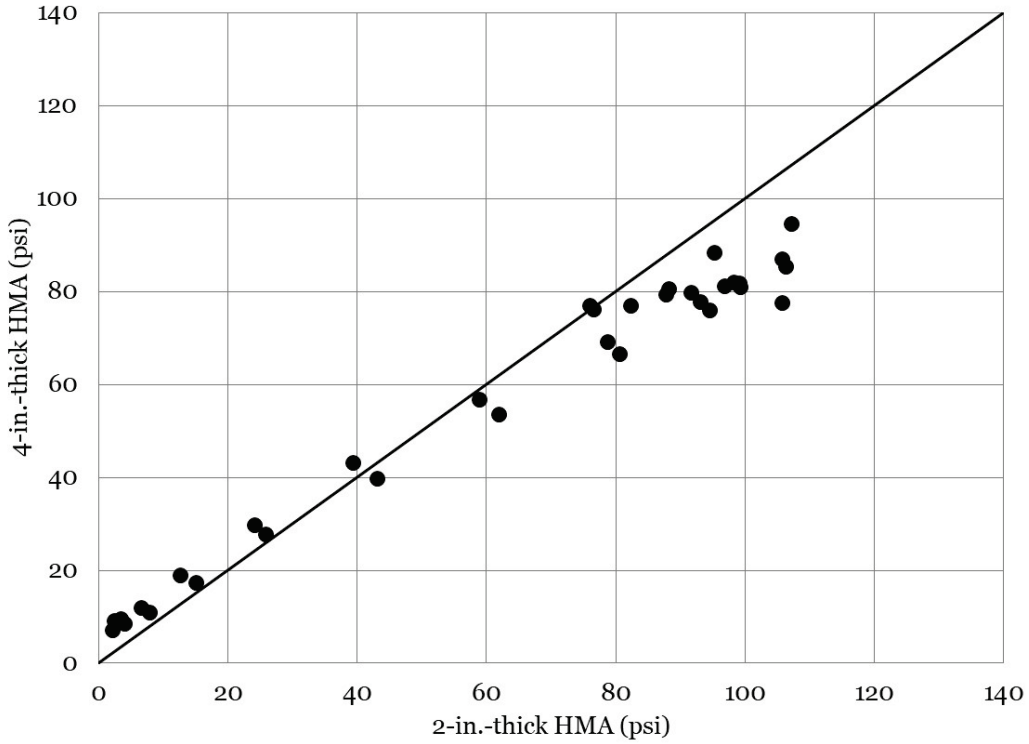

Figure 72. Middepth base pressure-effect of HMA thickness for LS base, 10 CBR subgrade.

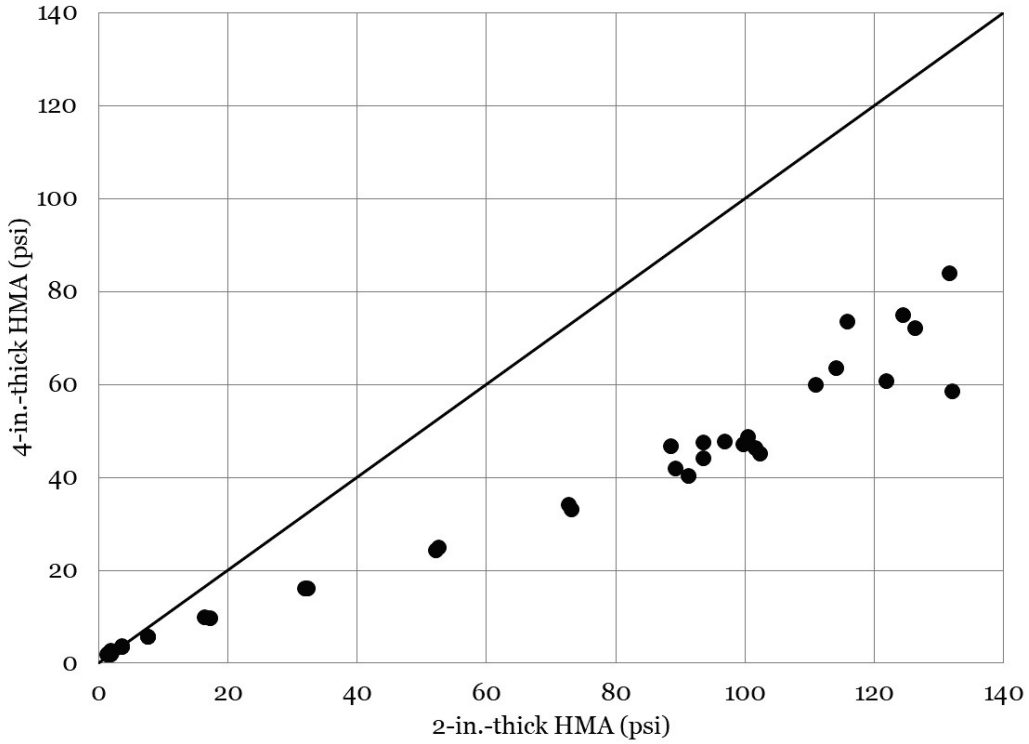

Figure 73. Middepth base pressure-effect of subgrade CBR for 4 in. HMA, LS base.

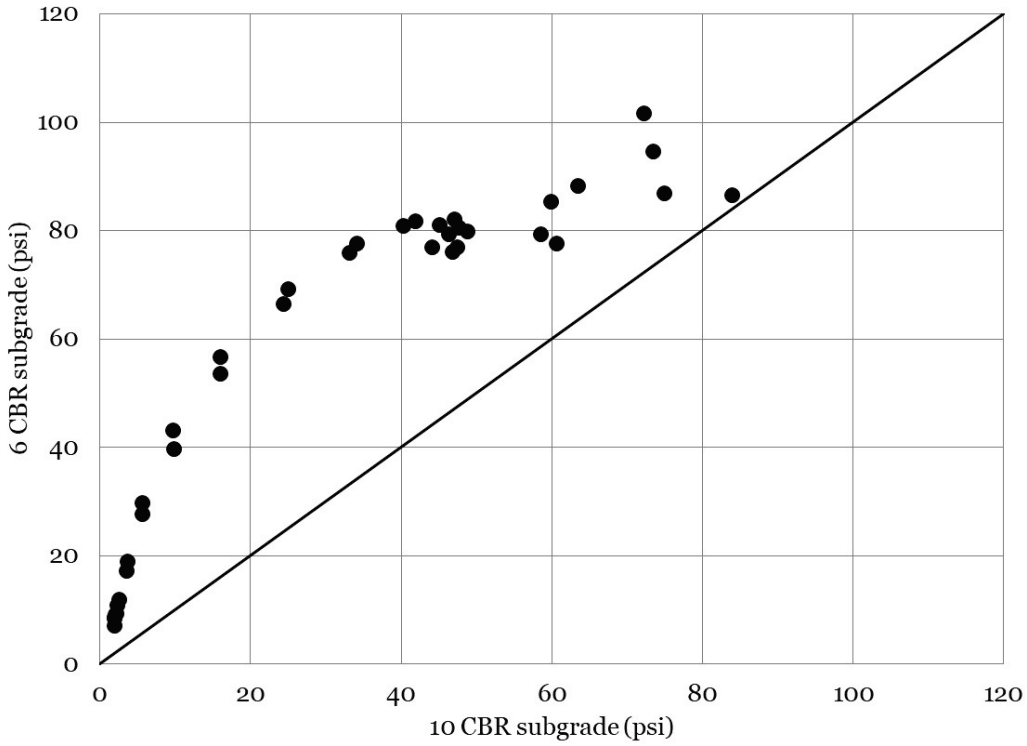

Figure 74. Middepth base pressure-effect of subgrade CBR for 2 in. HMA, LS base.

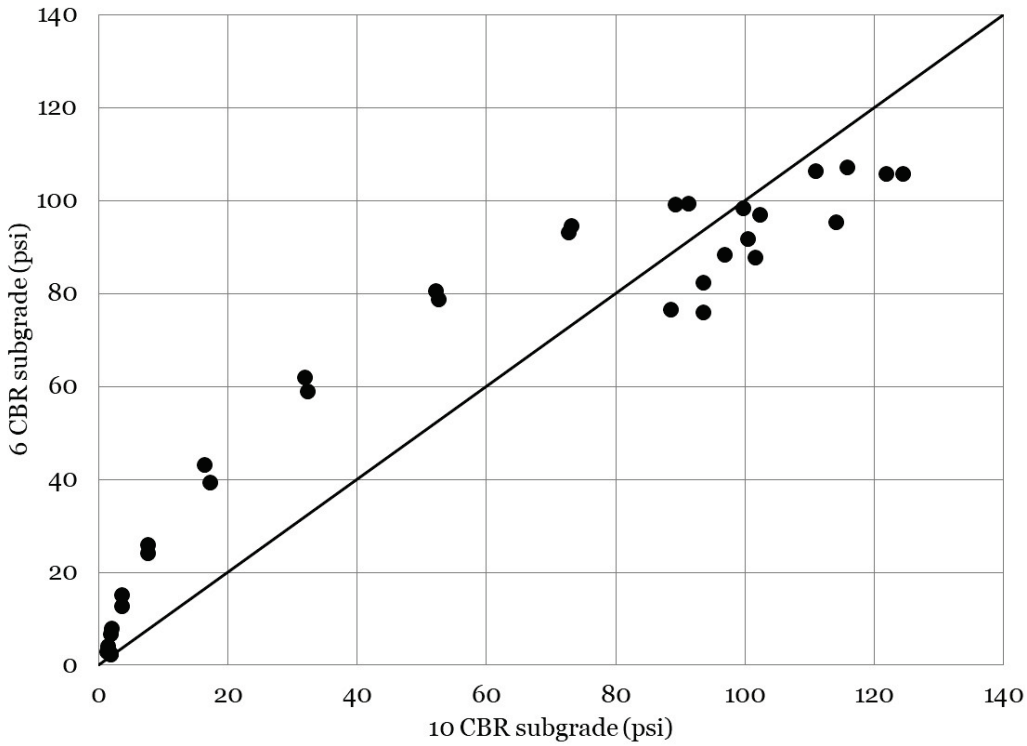

A summary of a statistical analysis of middepth base pressure response is presented in Table 14. A comparison of subgrade strength found that differences in average middepth base pressure response were not statistically significant in the 2 in. thick HMA, LS test items (p = 0.106) but were significant in the 4 in. thick HMA, LS test items (p < 0.001). In the 4 in. hick HMA, LS test items, the comparison indicated that the item constructed on a 10 CBR subgrade had a lower average middepth pressure response than the item constructed on a 6 CBR subgrade.

Direct comparison of HMA thickness on a 6 CBR subgrade, LS base was found to be statistically significant (p = 0.001), and the 4 in. thick test item was the better performer. Similarly, comparison of HMA thickness on a 10 CBR subgrade, LS base was statistically significant (p < 0.001), and the 4 in. thick test item was the better performer. These comparisons suggest that an increase in HMA thickness resulted in an improvement in middepth base pressure response. It was noted that the average difference in measured response with an increase in HMA thickness was much greater in the 10 CBR subgrade than the 6 CBR subgrade (i.e., 30.4 psi vs. 6.0 psi), suggesting that middepth pressure was sensitive to changes in subgrade strength.

Table 14. Statistical comparison of middepth pressure response.

Comparison	*n*	*p*-Value	Significant	Better Performer	Difference (psi)[1]
4HMA, GR, 10 CBR vs. 2HMA, GR, 10 CBR	5	0.171	No	Same	0.0
4HMA, GR, 10 CBR vs. 4HMA, LS, 6 CBR	28	<0.001	Yes	4HMA, LS, 6 CBR	-30.5
4HMA, GR, 10 CBR vs. 2HMA, LS, 6 CBR	28	<0.001	Yes	2HMA, LS, 6 CBR	-26.5
4HMA, GR, 10 CBR vs. 4HMA, LS, 10 CBR	28	<0.001	Yes	4HMA, LS, 10 CBR	-57.1
4HMA, GR, 10 CBR vs. 2HMA, LS, 10 CBR	28	<0.001	Yes	2HMA, LS, 10 CBR	-34.5
2HMA, GR, 10 CBR vs. 4HMA, LS, 6 CBR	5	0.041	Yes	4HMA, LS, 6 CBR	-21.3
2HMA, GR, 10 CBR vs. 2HMA, LS, 6 CBR	5	0.019	Yes	2HMA, LS, 6 CBR	-26.8
2HMA, GR, 10 CBR vs. 4HMA, LS, 10 CBR	5	0.019	Yes	4HMA, LS, 10 CBR	-27.8
2HMA, GR, 10 CBR vs. 2HMA, LS, 10 CBR	5	0.019	Yes	2HMA, LS, 10 CBR	-28.2
4HMA, LS, 6 CBR vs. 2HMA, LS, 6 CBR	34	0.001	Yes	4HMA, LS, 6 CBR	-6.0

Comparison	*n*	*p*-Value	Significant	Better Performer	Difference (psi)[1]
4HMA, LS, 6 CBR vs. 4HMA, LS, 10 CBR	37	<0.001	Yes	4HMA, LS, 10 CBR	-25.2
4HMA, LS, 6 CBR vs. 2HMA, LS, 10 CBR	37	0.181	No	Same	0.0
2HMA, LS, 6 CBR vs. 4HMA, LS, 10 CBR	34	<0.001	Yes	4HMA, LS, 10 CBR	-31.9
2HMA, LS, 6 CBR vs. 2HMA, LS, 10 CBR	34	0.106	No	Same	0.0
4HMA, LS, 10 CBR vs. 2HMA, LS, 10 CBR	38	<0.001	Yes	4HMA, LS, 10 CBR	-30.4

[1]Average difference between datasets; *n* = number of observations.

8.2.5 SDD Response

SDD response data are presented in Figure 75. These data represent the peak dynamic vertical deflection response under traffic and were determined by subtracting the local minimum and maximum value for each event. Steady-state subgrade dynamic deflections in the limestone base test items ranged generally from 0.15 in. to 0.30 in. In the case of the gravel base test items, dynamic subgrade deflection peaked at approximately 0.40 in.

Equality plots for dynamic SDD response measurements are presented in Figure 76 through Figure 78. Figure 76 indicates that dynamic deflections tended to be greater in the 2 in. thick HMA test item than the 4 in. thick HMA test item on 6 CBR subgrade. A review of Figure 77 indicated that the measured data tended to fall along the LOE early in traffic but departed from the LOE later in traffic suggesting that HMA thickness did not have meaningful effect on dynamic subgrade deflection on a firmer subgrade until later in traffic application.

Figures 78 and 79 can be used to investigate the effect of subgrade CBR on measured dynamic subgrade deflection. In both cases the data fell mostly above the LOE indicating that greater dynamic deflections were measured in the softer subgrade CBR test items regardless of HMA thickness.

Figure 75. Dynamic subgrade deflection with traffic.

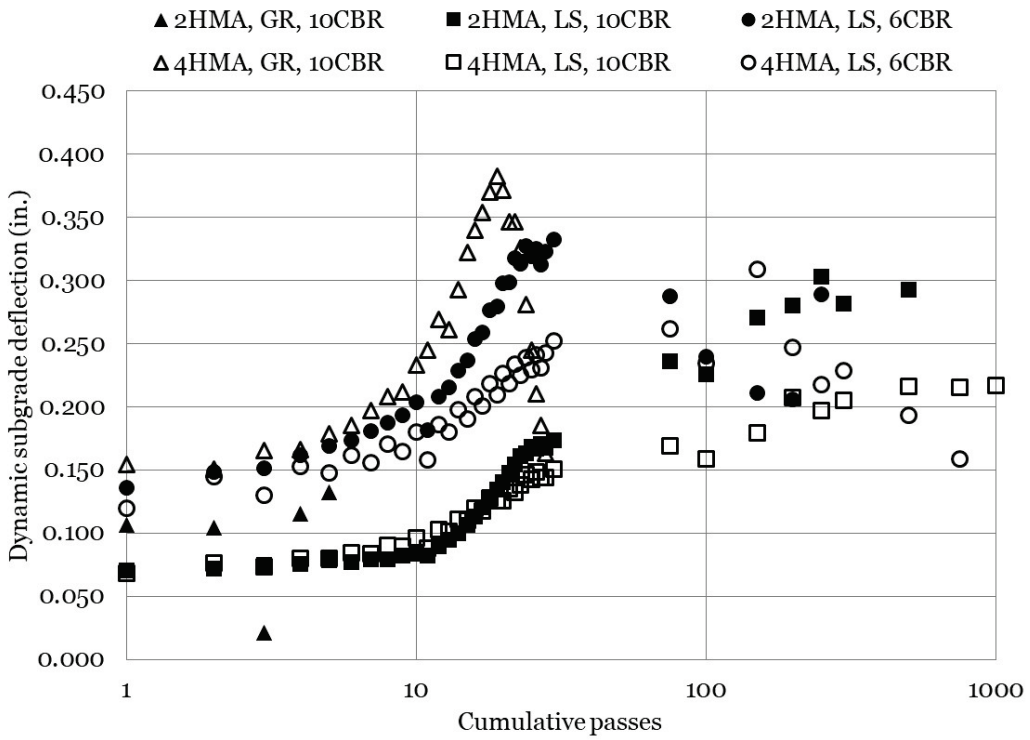

Figure 76. Dynamic deflection-effect of HMA thickness for LS base, 6 CBR subgrade.

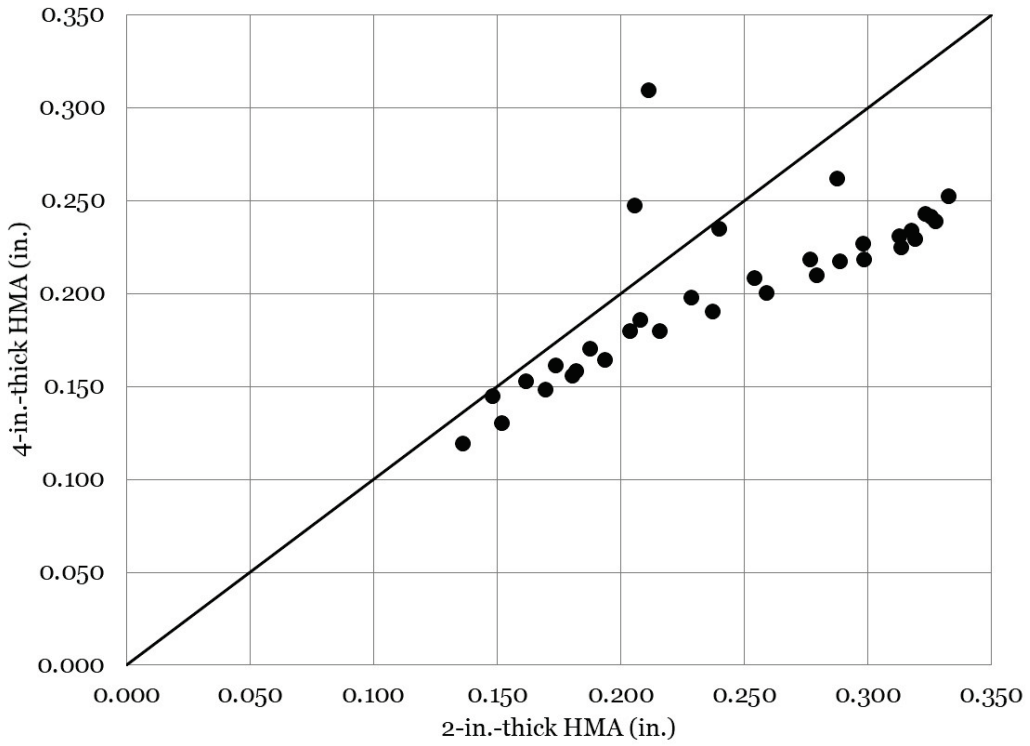

Figure 77. Dynamic deflection-effect of HMA thickness for LS base, 10 CBR subgrade.

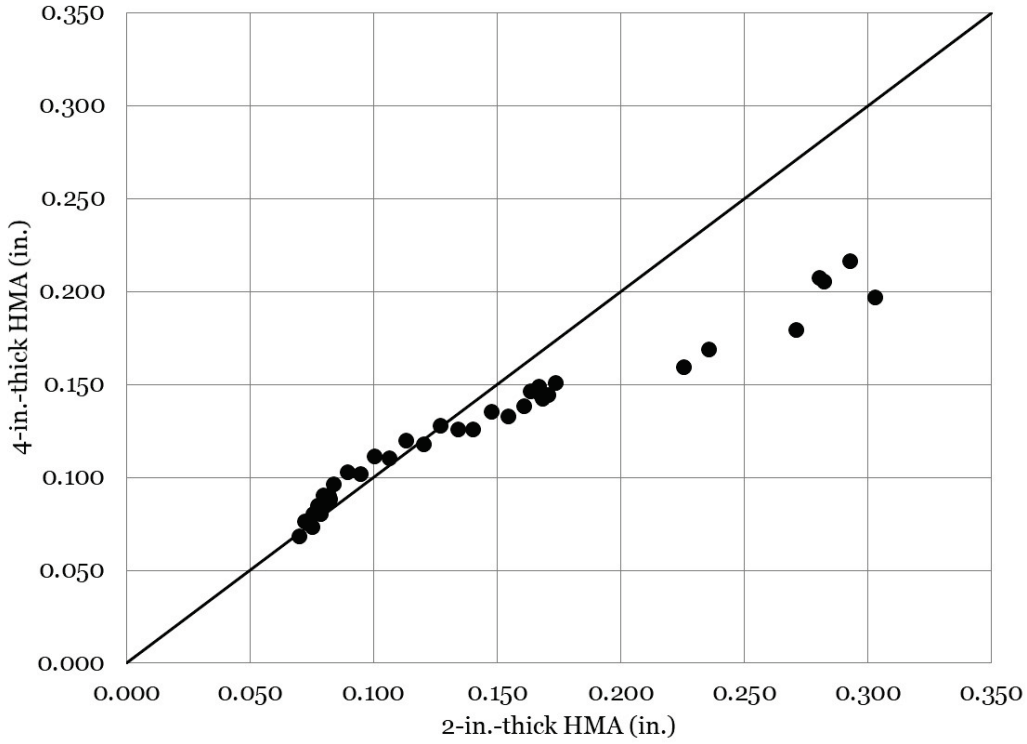

Figure 78. Dynamic deflection-effect of subgrade CBR for 4 in. HMA, LS base.

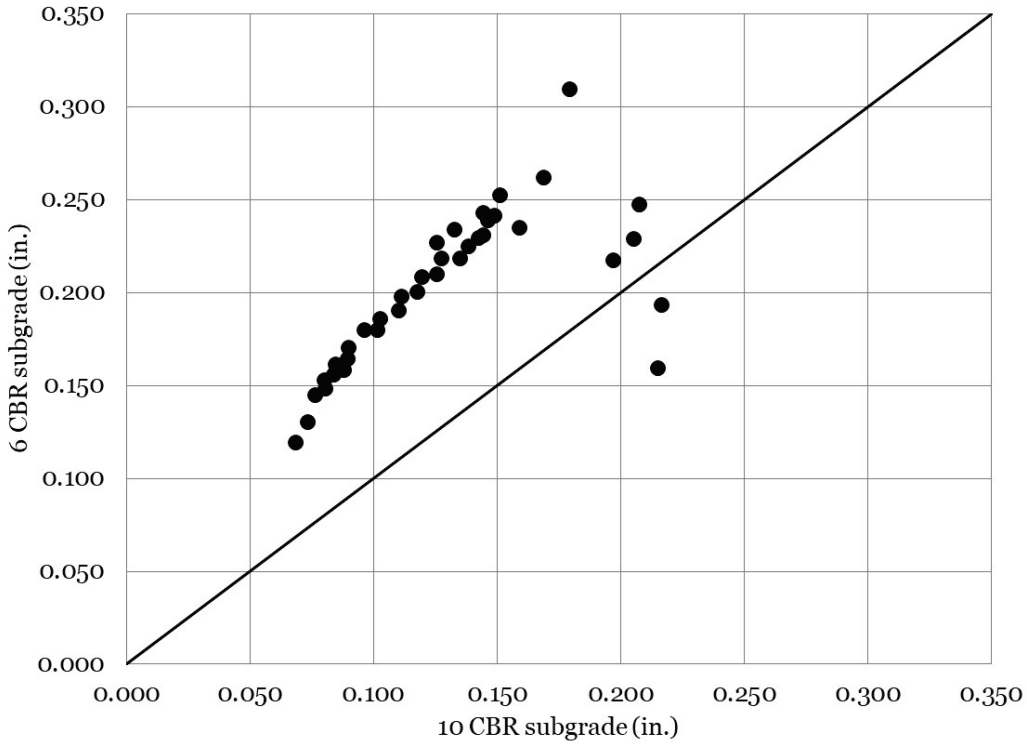

Figure 79. Dynamic deflection-effect of subgrade CBR for 2 in. HMA, LS base.

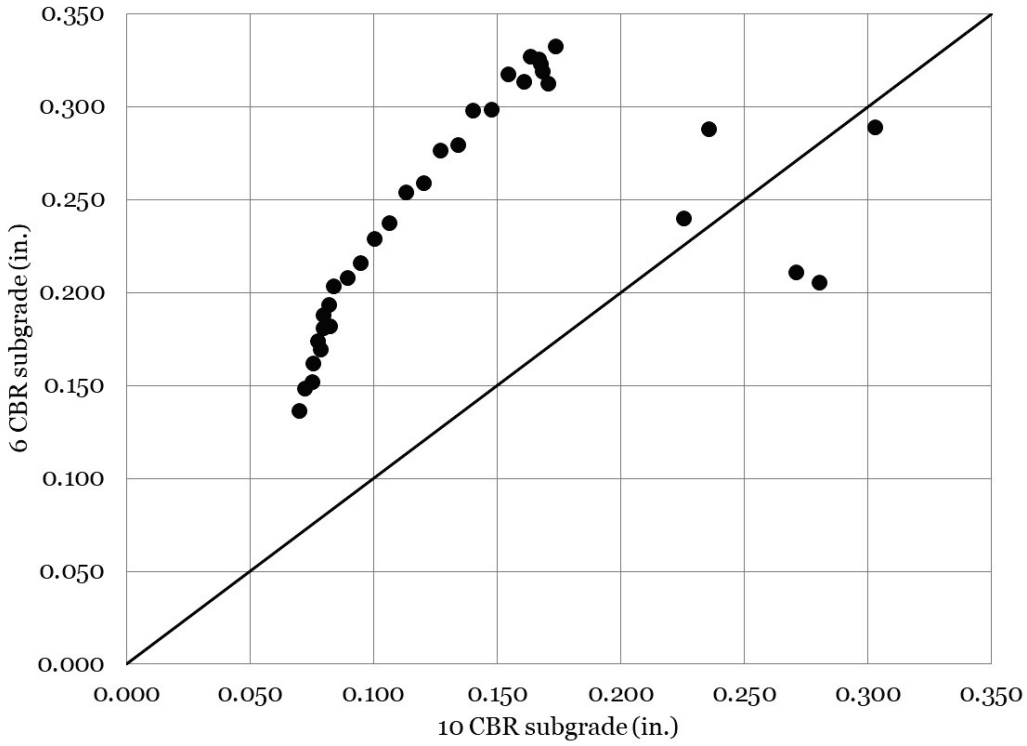

A statistical comparison of dynamic subgrade deflection response is presented in Table 15. Statistically significant differences in dynamic response were observed in terms of subgrade strength for both HMA thicknesses. In the case of both the 2 in. thick HMA over LS base test items and the 4 in. thick HMA over LS base test items, researchers observed that average dynamic subgrade deflection was less in the 10 CBR subgrade test item.

A comparison of HMA thickness on the 6 CBR subgrade found that an increase in thickness resulted in a statistically significant improvement ($p < 0.001$) in average dynamic subgrade deflection. Similar observations were made on the 10 CBR subgrade. Thus, it can be concluded that an increase in HMA thickness resulted in an improvement in dynamic subgrade deflection.

Table 15. Statistical comparison of dynamic subgrade deflection response.

Comparison	*n*	*p*-Value	Significant	Better Performer	Difference (in.)[1]
4HMA, GR, 10 CBR vs. 2HMA, GR, 10 CBR	5	0.025	Yes	2HMA, GR, 10 CBR	-0.067
4HMA, GR, 10 CBR vs. 4HMA, LS, 6 CBR	28	<0.001	Yes	4HMA, LS, 6 CBR	-0.064
4HMA, GR, 10 CBR vs. 2HMA, LS, 6 CBR	28	0.188	No	Same	0.000
4HMA, GR, 10 CBR vs. 4HMA, LS, 10 CBR	28	<0.001	Yes	4HMA, LS, 10 CBR	-0.146
4HMA, GR, 10 CBR vs. 2HMA, LS, 10 CBR	28	<0.001	Yes	2HMA, LS, 10 CBR	-0.142
2HMA, GR, 10 CBR vs. 4HMA, LS, 6 CBR	5	0.068	No	Same	0.000
2HMA, GR, 10 CBR vs. 2HMA, LS, 6 CBR	5	0.036	Yes	2HMA, GR, 6 CBR	-0.058
2HMA, GR, 10 CBR vs. 4HMA, LS, 10 CBR	5	0.336	No	Same	0.000
2HMA, GR, 10 CBR vs. 2HMA, LS, 10 CBR	5	0.325	No	Same	0.000
4HMA, LS, 6 CBR vs. 2HMA, LS, 6 CBR	34	<0.001	Yes	4HMA, LS, 6 CBR	-0.040
4HMA, LS, 6 CBR vs. 4HMA, LS, 10 CBR	37	<0.001	Yes	4HMA, LS, 10 CBR	-0.073
4HMA, LS, 6 CBR vs. 2HMA, LS, 10 CBR	36	<0.001	Yes	2HMA, LS, 10 CBR	-0.105
2HMA, LS, 6 CBR vs. 4HMA, LS, 10 CBR	34	<0.001	Yes	4HMA, LS, 10 CBR	-0.121
2HMA, LS, 6 CBR vs. 2HMA, LS, 10 CBR	34	<0.001	Yes	2HMA, LS, 10 CBR	-0.105
4HMA, LS, 10 CBR vs. 2HMA, LS, 10 CBR	36	0.002	Yes	4HMA, LS, 10 CBR	-0.019

[1]Average difference between datasets; *n* = number of observations.

Accumulated (permanent) SDD measurements are presented in Figure 80. These data were determined by recording the baseline SDD response prior to each pass of the HVS and then recording the baseline after each pass of the HVS. Thus, the data represent cumulative deflection near the top of the subgrade. In general, the data followed expected trends; permanent deformation tended to increase as the test gear moved closer to the SDD. Measurement early in traffic indicated that the highest permanent subgrade deflection was measured in the 2HMA over GR over 10 CBR test item as expected. Permanent deflection measured near the top of the subgrade at the end of traffic ranged from approximately 0.6 in. to 1.0 in.

Equality plots to investigate the effect of HMA thickness of permanent subgrade deflection are presented in Figures 81 and 82. In both cases early measurements tended to fall above the LOE indicating that greater permanent subgrade deflection was measured in the 4 in. thick HMA test items. Later in traffic application the data trend below the LOE indicating that greater permanent deflections were measured in the 2 in. thick HMA test items.

Figures 83 and 84 can be used to investigate the effect of subgrade CBR for each HMA thickness. In both cases the data plotted well above the LOE, indicating that greater deflections were measured in the 6 CBR subgrade test items when compared to the 10 CBR subgrade test items.

Figure 80. Permanent subgrade deflection with traffic.

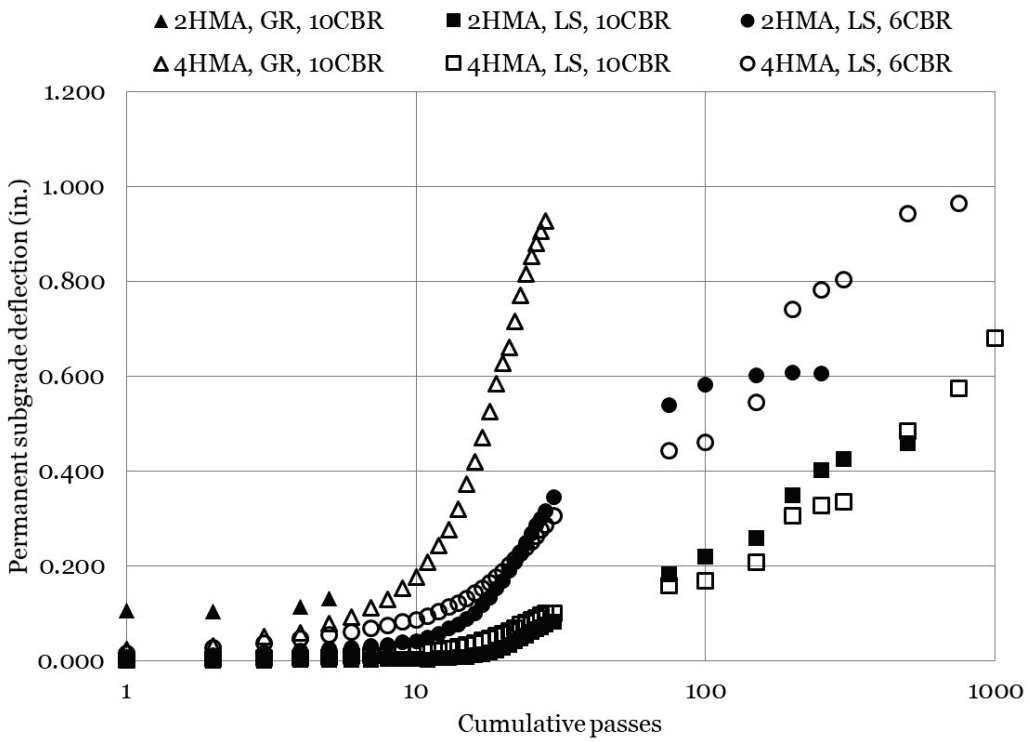

Figure 81. Permanent deflection-effect of HMA thickness for LS base, 6 CBR subgrade.

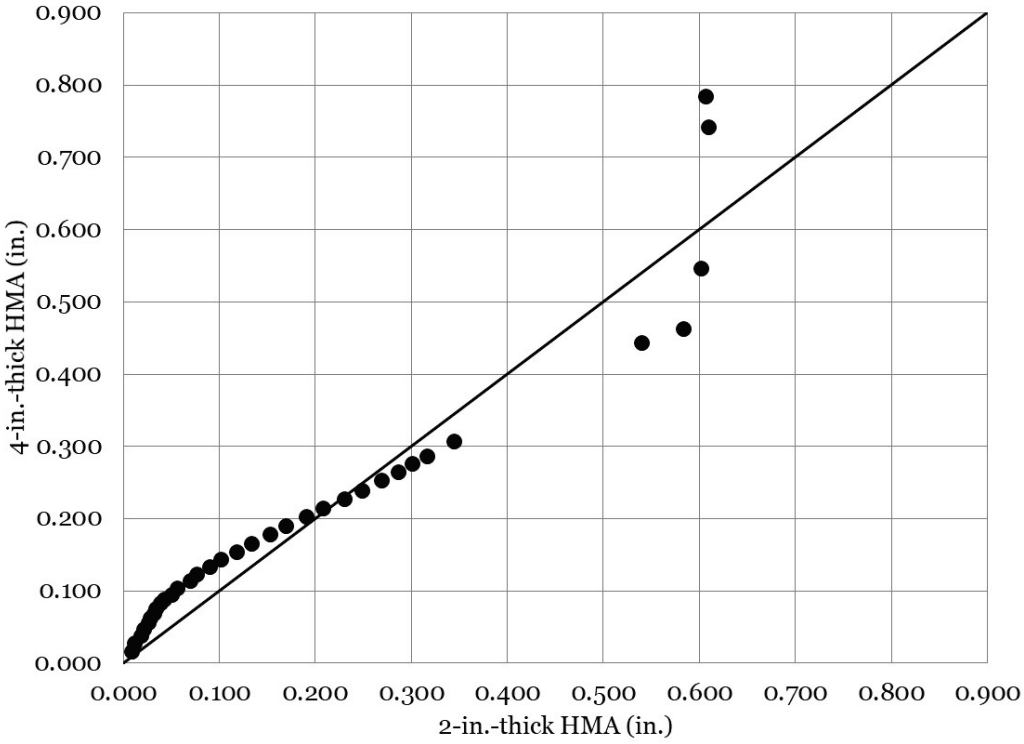

Figure 82. Permanent deflection-effect of HMA thickness for LS base, 10 CBR subgrade.

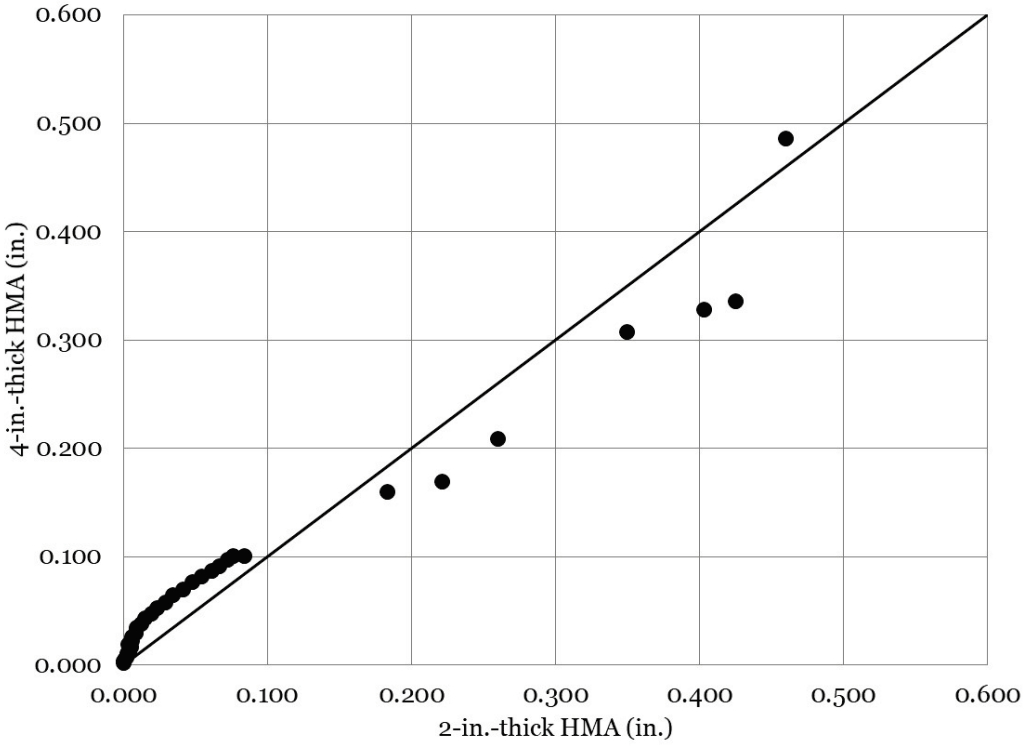

Figure 83. Permanent deflection-effect of subgrade CBR for 4 in. HMA, LS base.

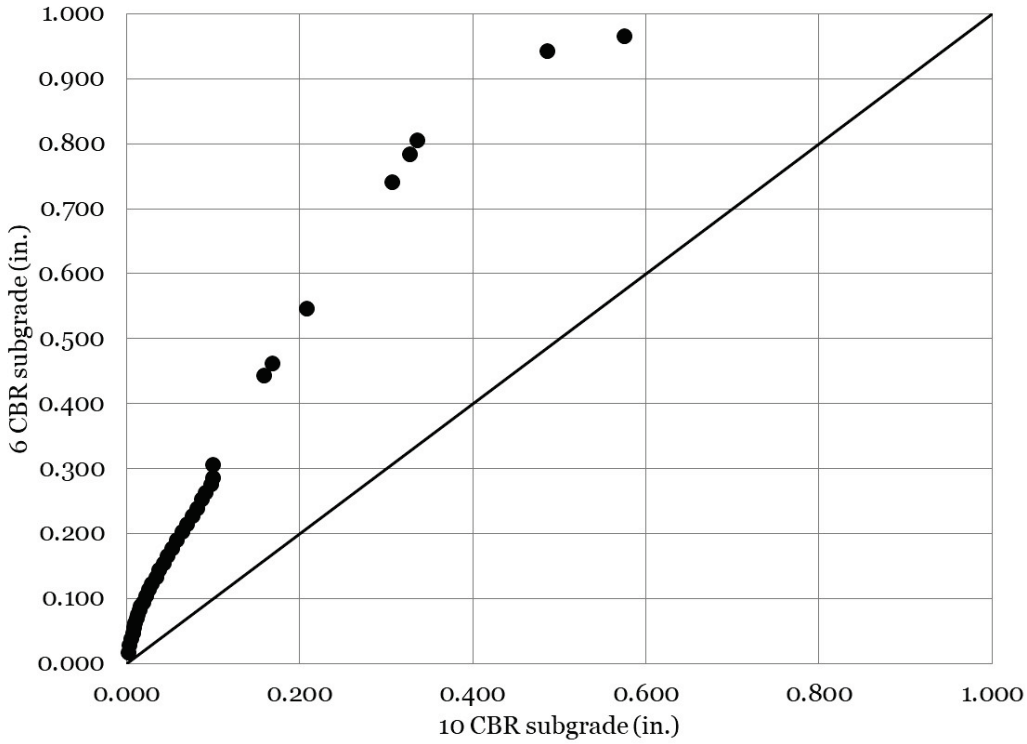

Figure 84. Permanent deflection-effect of subgrade CBR for 2 in. HMA, LS base.

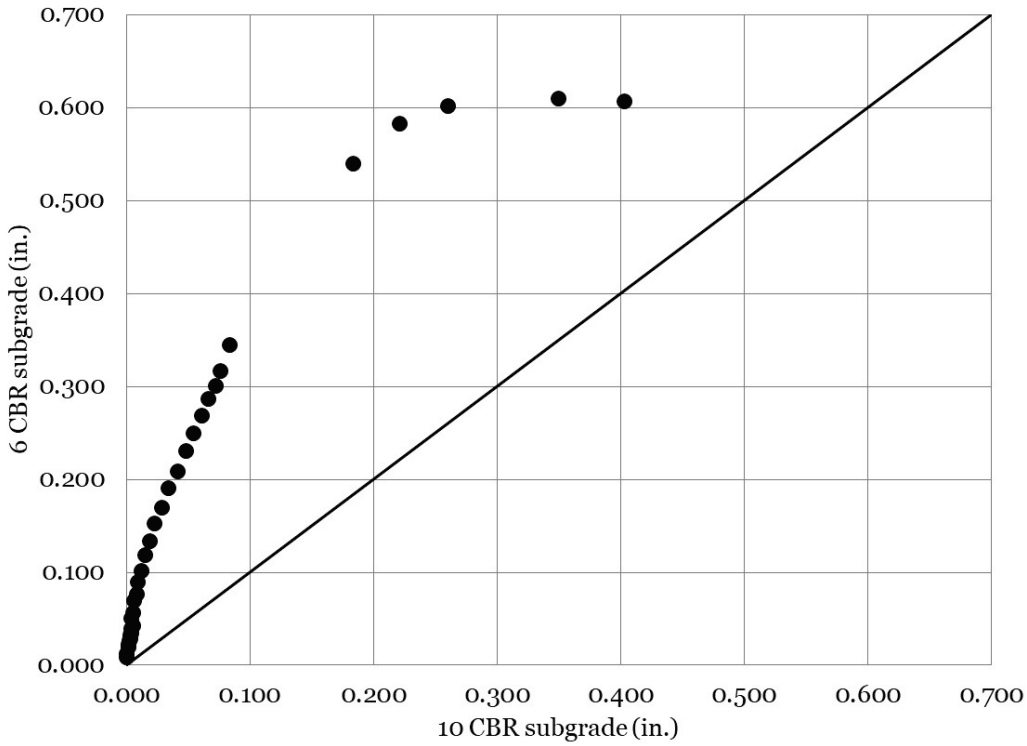

A statistical analysis of permanent subgrade deflection response is presented in Table 16. A comparison of subgrade strength on the 2 in. thick HMA over LS base test items was found to be statistically significant ($p < 0.001$), and the 10 CBR subgrade test item was found to be the better performer. Additionally, a comparison of subgrade strength on the 4 in. thick HMA over LS base test items was found to be statistically significant ($p < 0.001$), and the 10 CBR subgrade test item was found to be the better performer. Thus, an increase in subgrade strength resulted in an improvement in average permanent subgrade deflection response.

The comparisons of HMA thickness over LS base, on both a 6 and 10 CBR subgrade were unremarkable ($p = 0.072$ and $p = 0.216$, respectively) indicating that an increase in HMA thickness did not have a statistically significant effect on average permanent subgrade deflection.

Table 16. Statistical comparison of permanent subgrade deflection.

Comparison	*n*	*p*-Value	Significant	Better Performer	Difference (in.)[1]
4HMA, GR, 10 CBR vs. 2HMA, GR, 10 CBR	5	0.090	No	Same	0.0000
4HMA, GR, 10 CBR vs. 4HMA, LS, 6 CBR	28	<0.001	Yes	4HMA, LS, 6 CBR	-0.2708
4HMA, GR, 10 CBR vs. 2HMA, LS, 6 CBR	28	<0.001	Yes	2HMA, LS, 6 CBR	-0.2917
4HMA, GR, 10 CBR vs. 4HMA, LS, 10 CBR	28	<0.001	Yes	4HMA, LS, 10 CBR	-0.3702
4HMA, GR, 10 CBR vs. 2HMA, LS, 10 CBR	28	<0.001	Yes	2HMA, LS, 10 CBR	-0.3889
2HMA, GR, 10 CBR vs. 4HMA, LS, 6 CBR	5	0.158	No	Same	0.0000
2HMA, GR, 10 CBR vs. 2HMA, LS, 6 CBR	5	0.870	No	Same	0.0000
2HMA, GR, 10 CBR vs. 4HMA, LS, 10 CBR	5	0.123	No	Same	0.0000
2HMA, GR, 10 CBR vs. 2HMA, LS, 10 CBR	5	0.050	No	Same	0.0000
4HMA, LS, 6 CBR vs. 2HMA, LS, 6 CBR	34	0.072	No	Same	0.0000
4HMA, LS, 6 CBR vs. 4HMA, LS, 10 CBR	37	<0.001	Yes	4HMA, LS, 10 CBR	-0.1651
4HMA, LS, 6 CBR vs. 2HMA, LS, 10 CBR	36	<0.001	Yes	2HMA, LS, 10 CBR	-0.1654
2HMA, LS, 6 CBR vs. 4HMA, LS, 10 CBR	34	<0.001	Yes	4HMA, LS, 10 CBR	-0.1238
2HMA, LS, 6 CBR vs. 2HMA, LS, 10 CBR	34	<0.001	Yes	2HMA, LS, 10 CBR	-0.1326
4HMA, LS, 10 CBR vs. 2HMA, LS, 10 CBR	36	0.216	No	Same	0.0000

[1]Average difference between datasets; *n* = number of observations.

8.2.6 ASG Response

Longitudinal ASG response data are presented in Figure 85. Like other instrumentation response data, an increase in response was observed as the test gear transitioned from being centered on the traffic lane to receiving a direct hit from a test wheel. For longer-term trafficking, an increase in HMA strain was observed with an increase in traffic application. This was expected because the HMA layer continued to deform under increased traffic. In the limestone base layer items, the highest longitudinal HMA strain was measured in the 2HMA over 6 CBR subgrade test item as expected. The least longitudinal strain was observed in the 4HMA over 10

CBR subgrade test item, which was the stiffest overall item. The longitudinal strain gauge installed in the 4HMA over LS over 6 CBR test item failed after HMA paving; thus, data were not collected for this gauge.

Figure 86 shows that the data fell mostly along the LOE suggesting that HMA thickness had little influence on measured longitudinal HMA strain on a stronger subgrade. The effect of subgrade CBR on longitudinal HMA strain for the 2 in. thick HMA test items can be observed in Figure 87. The data generally plotted above the LOE indicating that greater longitudinal HMA strain was measured in the 6 CBR subgrade test item.

Figure 85. Longitudinal ASG response with traffic.

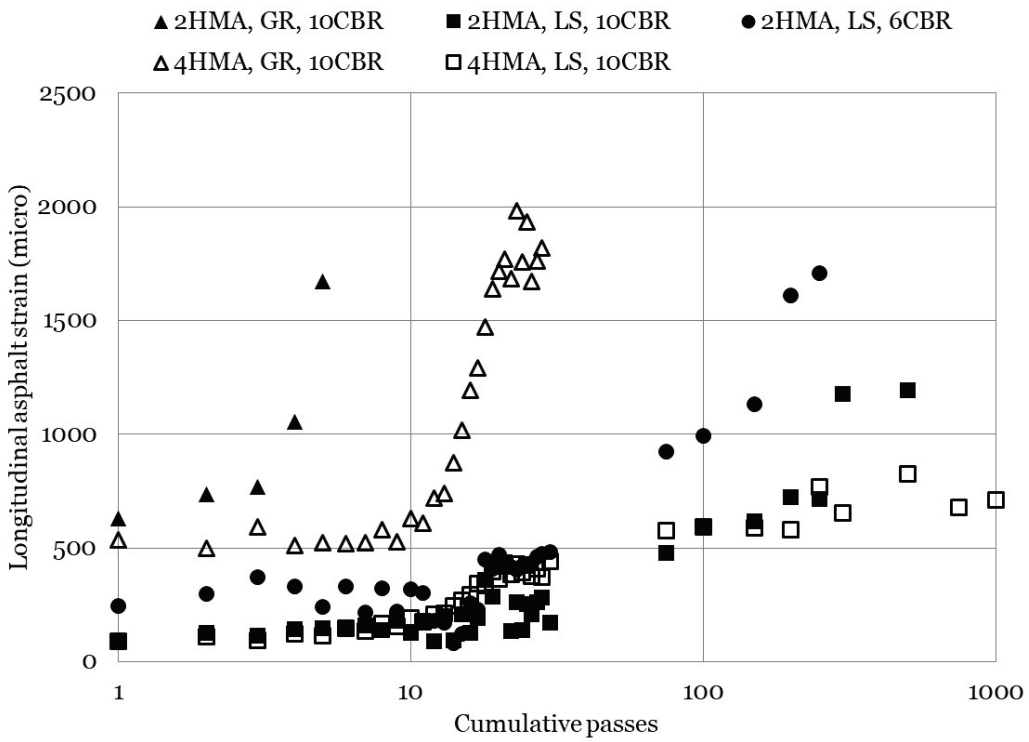

Figure 86. Longitudinal strain-effect of HMA thickness for LS base, 10 CBR subgrade.

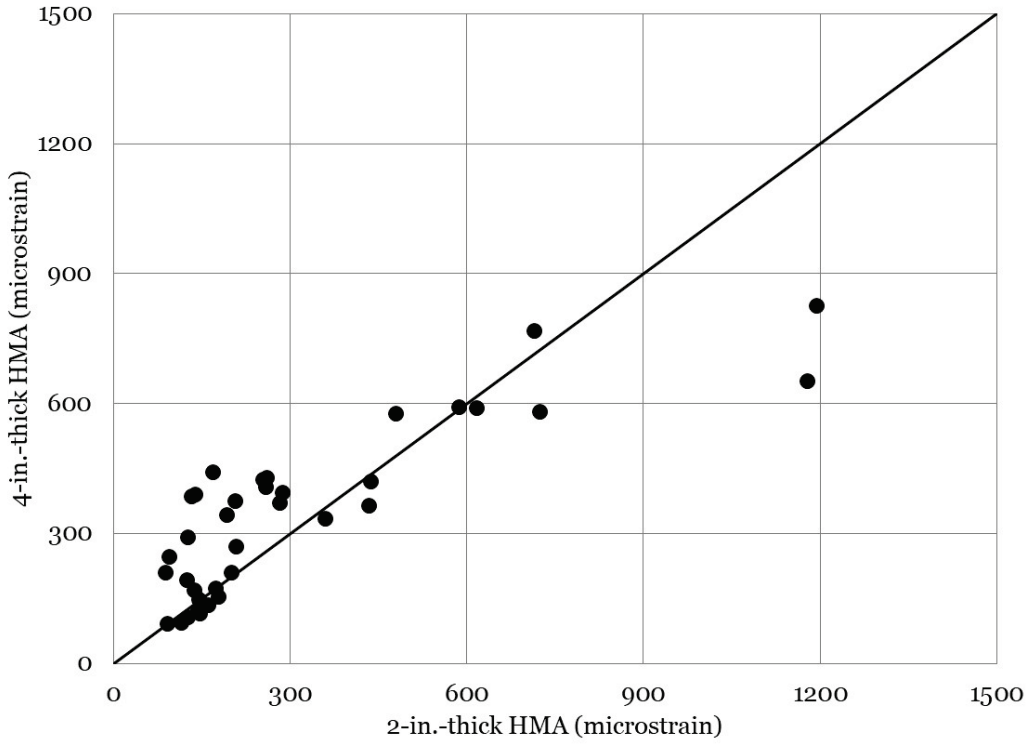

Figure 87. Longitudinal strain-effect of subgrade CBR for 2 in. HMA, LS base.

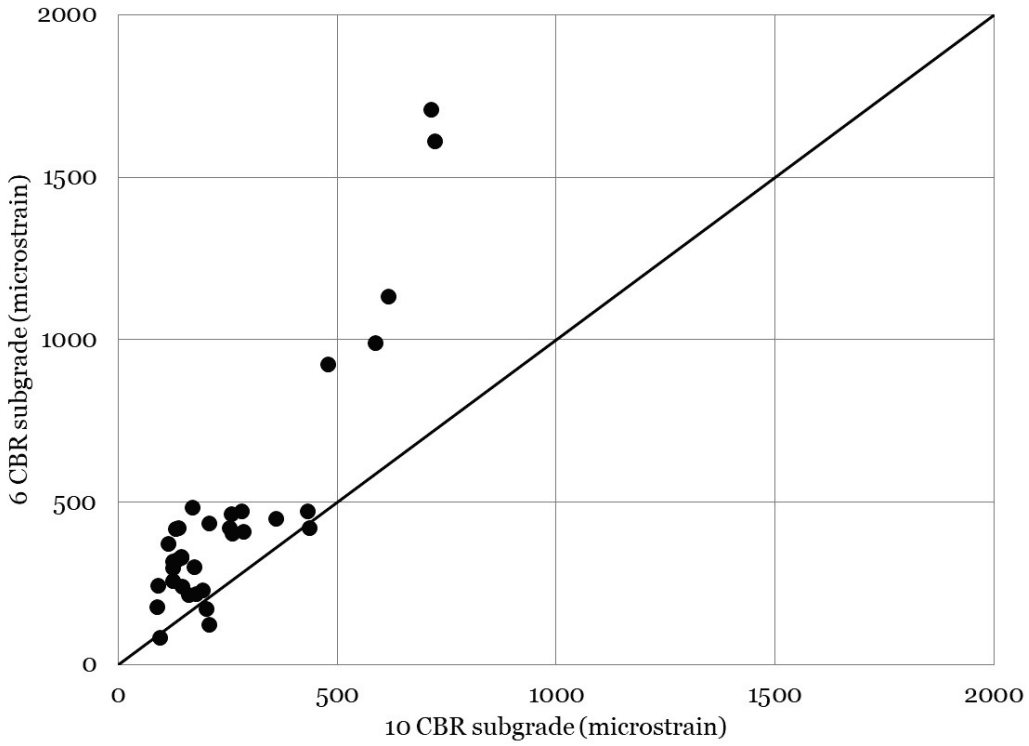

A statistical comparison of longitudinal ASG response is summarized in Table 17. For the 2 in. thick HMA over LS base test items, the team found that the 10 CBR subgrade resulted in a statistically significant ($p < 0.001$) improvement in average longitudinal HMA strain. No data were available for the 4 in. thick HMA, LS base test item due to a gauge malfunction.

Similarly, data were not available to make statistical inferences on the effect of HMA thickness on a 6 CBR subgrade. On a 10 CBR subgrade, it was found that differences between 2 in. and 4 in. of HMA were not statistically significant ($p = 0.195$).

A summary of transverse ASG measurements is presented in Figure 88. These data showed similar trends to those observed in the longitudinal strain gauge measurements. The highest strain was observed in the 2 in. thick HMA, LS, 6 CBR test item and the lowest strain was observed in the 4 in. thick HMA, LS, 10 CBR test item. An increasing trend was observed in all test data with an increase in traffic passes, corresponding to an increase in deformation in the HMA layer.

Figures 89 and 90 present equality plots to investigate the effect of HMA thickness for the 6 CBR subgrade and 10 CBR subgrade, respectively. For the 6 CBR subgrade, the data plotted below the LOE, indicating that greater transverse strains were measured in the 2 in. thick HMA test item. For the 10 CBR subgrade, the data tended to plot along the LOE early in traffic but diverged from the LOE later in traffic (greater strain values). These data suggest that HMA thickness is more influential on measured strain at lower subgrade CBR values where the overall pavement movement under load is higher. These observations are confirmed in Figures 91 and 92 where the 4 in. thick HMA equality plot (Figure 91) shows the data falling both above and below the LOE and the 2 in. thick HMA equality plot (Figure 92) shows the data falling entirely above the LOE.

Table 17. Statistical comparison of longitudinal ASG response.

Comparison	*n*	*p*-Value	Significant	Better Performer	Difference (micro.)[1]
4HMA, GR, 10 CBR vs. 2HMA, GR, 10 CBR	5	0.084	No	Same	0
4HMA, GR, 10 CBR vs. 4HMA, LS, 6 CBR	ND	ND	ND	ND	ND
4HMA, GR, 10 CBR vs. 2HMA, LS, 6 CBR	28	0.000	Yes	2HMA, LS, 6 CBR	-789
4HMA, GR, 10 CBR vs. 4HMA, LS, 10 CBR	28	0.000	Yes	4HMA, LS, 10 CBR	-847
4HMA, GR, 10 CBR vs. 2HMA, LS, 10 CBR	28	0.000	Yes	2HMA, LS, 6 CBR	-913
2HMA, GR, 10 CBR vs. 4HMA, LS, 6 CBR	ND	ND	ND	ND	ND
2HMA, GR, 10 CBR vs. 2HMA, LS, 6 CBR	5	0.027	Yes	2HMA, LS, 6 CBR	-675
2HMA, GR, 10 CBR vs. 4HMA, LS, 10 CBR	5	0.009	Yes	4HMA, LS, 10 CBR	-865
2HMA, GR, 10 CBR vs. 2HMA, LS, 10 CBR	5	0.009	Yes	2HMA, LS, 10 CBR	-847
4HMA, LS, 6 CBR vs. 2HMA, LS, 6 CBR	ND	ND	ND	ND	ND
4HMA, LS, 6 CBR vs. 4HMA, LS, 10 CBR	ND	ND	ND	ND	ND
4HMA, LS, 6 CBR vs. 2HMA, LS, 10 CBR	ND	ND	ND	ND	ND
2HMA, LS, 6 CBR vs. 4HMA, LS, 10 CBR	34	0.003	Yes	4HMA, LS, 10 CBR	-145
2HMA, LS, 6 CBR vs. 2HMA, LS, 10 CBR	34	0.000	Yes	2HMA, LS, 10 CBR	-207
4HMA, LS, 10 CBR vs. 2HMA, LS, 10 CBR	36	0.195	No	Same	0

[1]Average difference between datasets; *n* = number of observations.

Figure 88. Transverse ASG response with traffic.

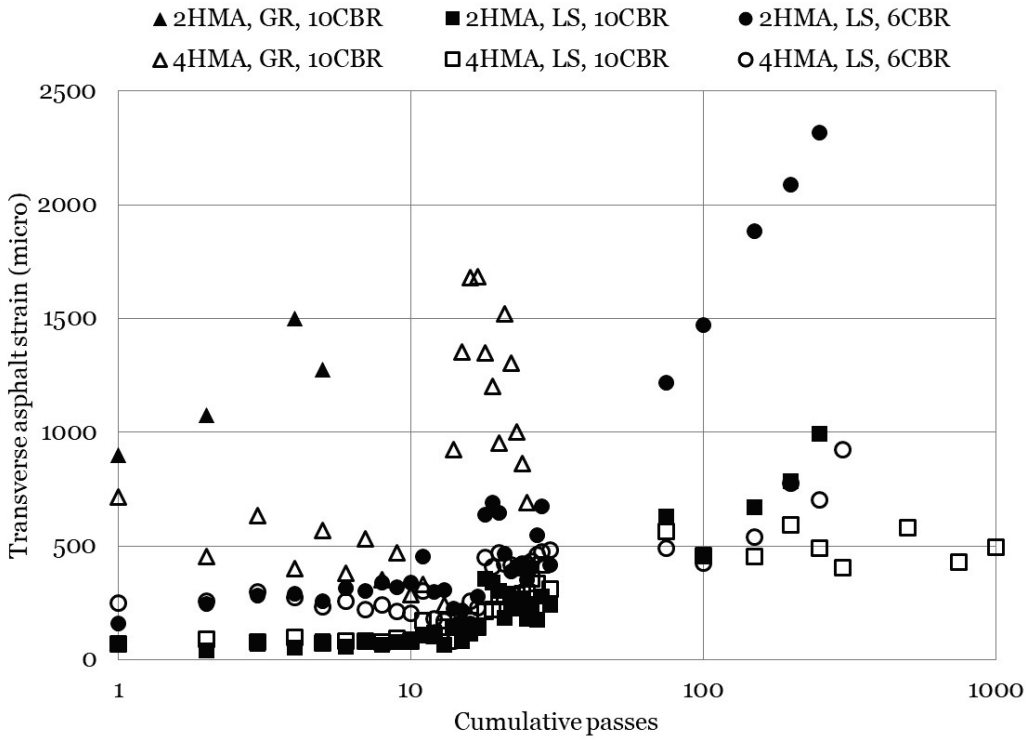

Figure 89. Transverse strain-effect of HMA thickness for LS base, 6 CBR subgrade.

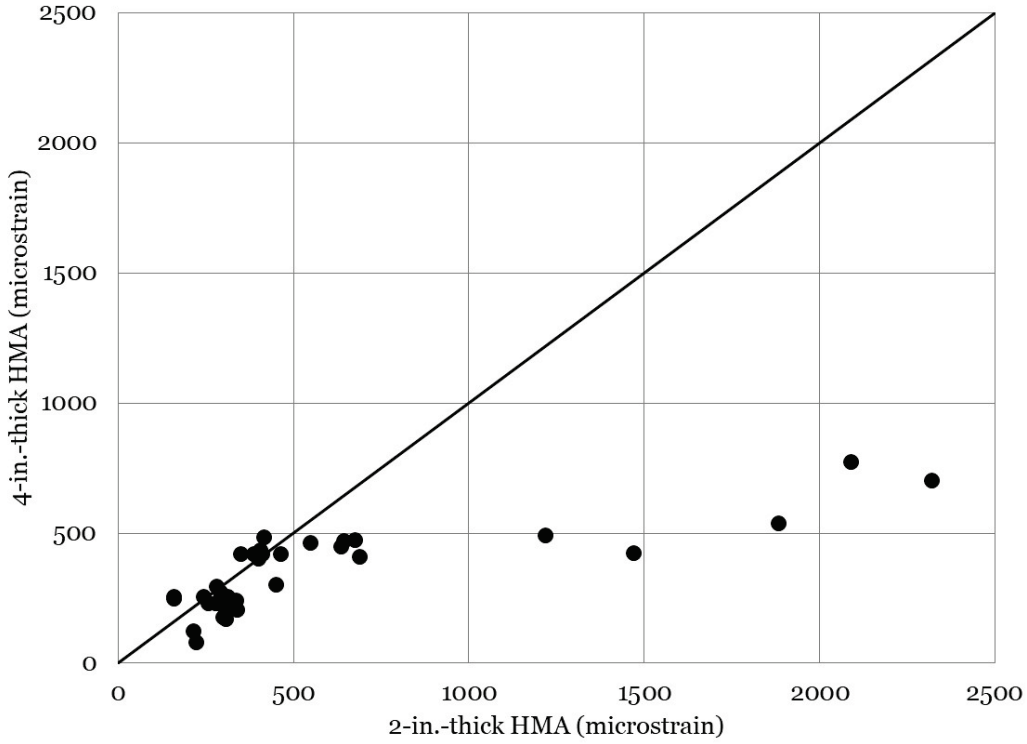

Figure 90. Transverse strain-effect of HMA thickness for LS base, 10 CBR subgrade.

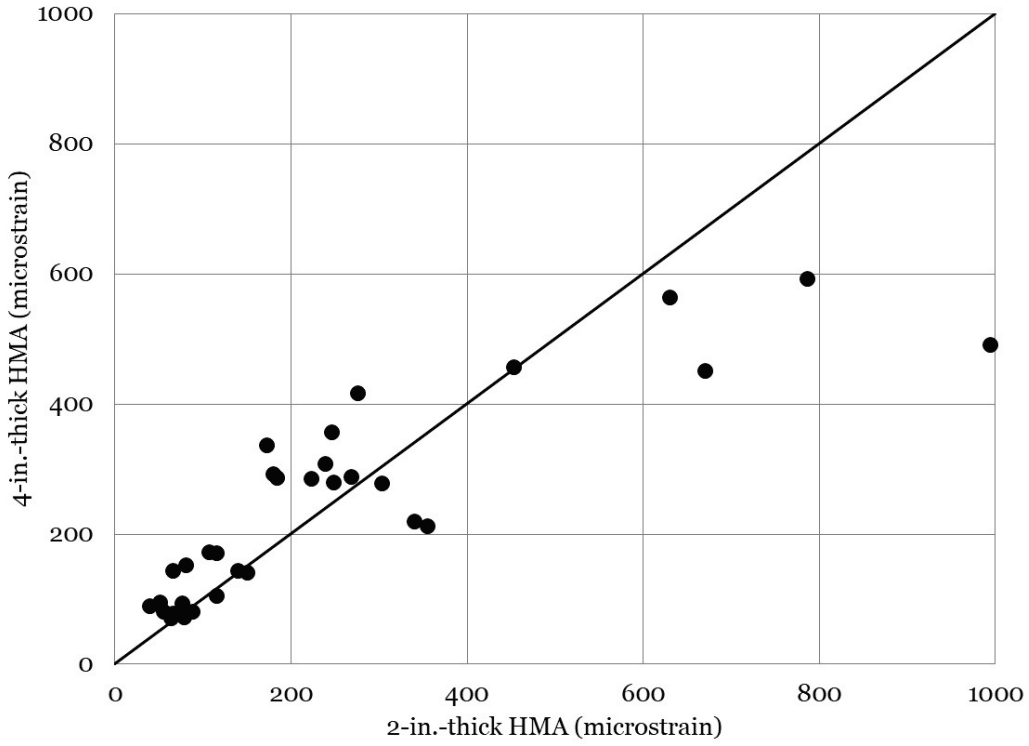

Figure 91. Transverse strain-effect of subgrade CBR for 4 in. HMA, LS base.

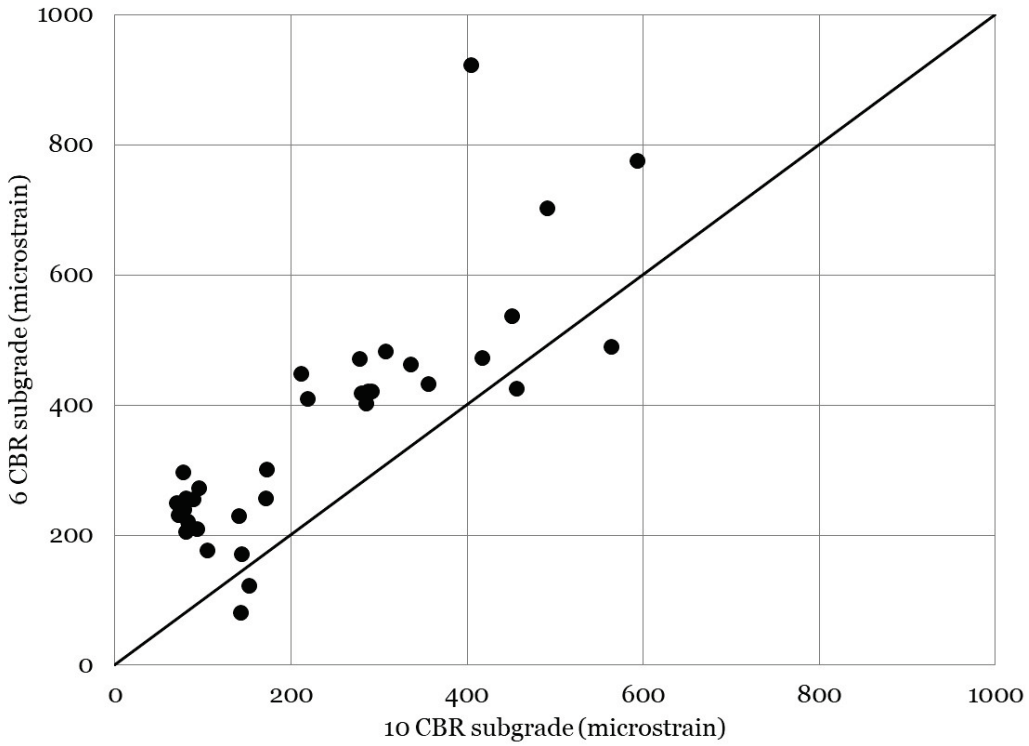

Figure 92. Transverse strain-effect of subgrade CBR for 2 in. HMA, LS base.

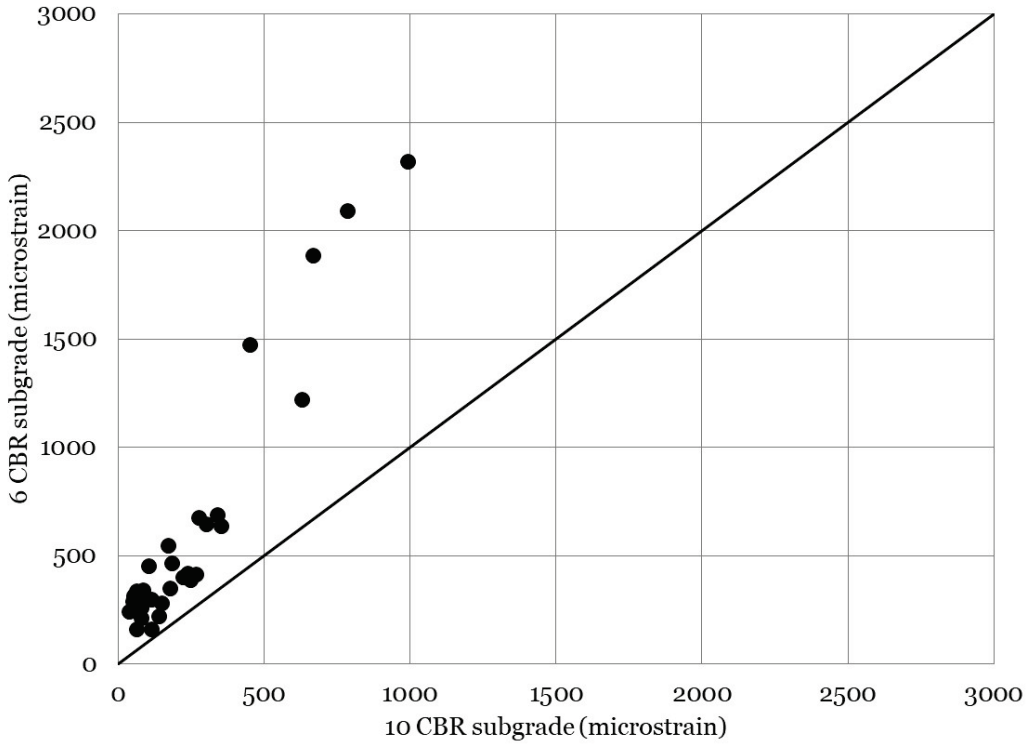

A statistical analysis of transverse ASG response is presented in Table 18. A comparison of subgrade strength on the 2 in. thick HMA, LS base test items was found to be statistically significant ($p < 0.001$), and research found that less average transverse HMA strain was measured in the 10 CBR subgrade test item. Similar results were observed in the 4 in. thick HMA, LS base test items.

A comparison of HMA thickness found that a statistically significant difference ($p = 0.004$) was observed on a 6 CBR subgrade, and the 4 in. thick HMA test item was found to be the better performer. A comparison of HMA thickness on a 10 CBR subgrade was found to be unremarkable ($p = 0.942$), suggesting that an increase in HMA thickness did not have a significant effect on average transverse strain in the case of a stiffer subgrade for the modest increase in HMA thickness evaluated in this study.

Table 18. Statistical comparison of transverse ASG response.

Comparison	*n*	*p*-Value	Significant	Better Performer	Difference (micro.)[1]
4HMA, GR, 10 CBR vs. 2HMA, GR, 10 CBR	4	0.040	Yes	4HMA, GR, 10 CBR	-654
4HMA, GR, 10 CBR vs. 4HMA, LS, 6 CBR	25	<0.001	Yes	4HMA, LS, 6 CBR	-513
4HMA, GR, 10 CBR vs. 2HMA, LS, 6 CBR	25	<0.001	Yes	2HMA, LS, 6 CBR	-450
4HMA, GR, 10 CBR vs. 4HMA, LS, 10 CBR	25	<0.001	Yes	4HMA, LS, 10 CBR	-640
4HMA, GR, 10 CBR vs. 2HMA, LS, 10 CBR	25	<0.001	Yes	2HMA, LS, 10 CBR	658
2HMA, GR, 10 CBR vs. 4HMA, LS, 6 CBR	4	0.005	Yes	4HMA, LS, 6 CBR	-936
2HMA, GR, 10 CBR vs. 2HMA, LS, 6 CBR	4	0.003	Yes	2HMA, LS, 6 CBR	-950
2HMA, GR, 10 CBR vs. 4HMA, LS, 10 CBR	4	0.003	Yes	4HMA, LS, 10 CBR	-1106
2HMA, GR, 10 CBR vs. 2HMA, LS, 10 CBR	4	0.003	Yes	2HMA, LS, 10 CBR	-1130
4HMA, LS, 6 CBR vs. 2HMA, LS, 6 CBR	34	0.004	Yes	4HMA, LS, 6 CBR	-230
4HMA, LS, 6 CBR vs. 4HMA, LS, 10 CBR	35	<0.001	Yes	4HMA, LS, 10 CBR	-129
4HMA, LS, 6 CBR vs. 2HMA, LS, 10 CBR	34	<0.001	Yes	2HMA, LS, 10 CBR	-132
2HMA, LS, 6 CBR vs. 4HMA, LS, 10 CBR	34	<0.001	Yes	4HMA, LS, 10 CBR	-348
2HMA, LS, 6 CBR vs. 2HMA, LS, 10 CBR	34	<0.001	Yes	2HMA, LS, 10 CBR	-346
4HMA, LS, 10 CBR vs. 2HMA, LS, 10 CBR	34	0.942	No	Same	0

[1]Average difference between datasets; *n* = number of observations.

9 Results: ADR Capabilities

ADR techniques were evaluated to determine compatibility with the P-8 aircraft. The ERDC has a long history of evaluating various airfield damage repair techniques and procedures, and several technical reports are available that provide generous details of each repair technique (Carruth 2020; Bell et al. 2019; Bell et al. in draft[1]). For the purposes of this report, a brief construction description is provided for each repair technique. All simulated craters were constructed and trafficked in Lane 1 (consisting of 14 in. thick PCC) for the evaluation. Two simulated craters were repaired and trafficked simultaneously. The crater repair techniques were paired to achieve similar passes to failure to increase testing efficiency. Results of construction quality control tests (when applicable) and traffic testing are presented in the following subsections. Due to the time sensitive nature of several of the repair techniques, detailed quality control data were not collected.

9.1 Repair 1: Geosynthetic Reinforced Sand with FRP

Repair 1 consisted of a geosynthetic reinforced sand backfill surfaced with a fiberglass reinforced polymer (FRP) foreign object debris cover. A simulated crater was excavated to a depth of 18 in., and the bottom of the excavation was leveled and recompacted. A 6-oz/yd^2, nonwoven geotextile was placed in the bottom of the excavation. An approximate 4 in. thick compacted sand layer was placed over the geotextile. Another geotextile was placed on the compacted sand layer, and a biaxial geogrid was placed directly on the geotextile. Thereafter, an approximate 4 in. thick compacted sand layer was placed over the geotextile/geogrid combination. This process was repeated until the simulated crater was filled. The FRP FOD cover was placed over the completed reinforced sand backfill layer and secured to the surrounding concrete slabs. Geosynthetic properties are summarized in Table 19.

[1] Bell, H. P., W. D. Carruth, J. W. Fisher, J. L. Daugherty, L. Garcia, A. B. Ward, W. C. Floyd, L. Edwards, J. S. Tingle, J. R. Davis, J. F. Rowland, C. R. Lloyd, and T. T. Henderson. (In draft). *Expedient and Expeditionary Airfield Damage Repair (E-ADR) Joint Capability Technology Demonstration (JCTD)*. Vicksburg, MS: US Army Engineer Research and Development Center.

Table 19. Geosynthetic properties.

Geotextile Properties		Geogrid Properties	
Weight	6 oz/yd^2	Aperture Dimensions	1.0 in. x 1.0 in.
Grab Tensile Strength	160 lbf	Rib Thickness	0.05 in.
Elongation at Break	50%	Tensile Strength at 2% Strain	410 lbf/ft
Apparent Opening Size	0.008 in.	Tensile Strength at 5% Strain	810 lbf/ft
Permittivity	1.5 sec^{-1}	Ultimate Tensile Strength	1,310 lbf/ft
UV Resistance at 500 hr	70%	UV Resistance at 500 hr	100%

Nuclear density gauge measurements were made on each compacted lift of sand to measure construction uniformity. Measurements were made in the center of the crater, near the side of the crater, and near a corner of the crater. The average wet density and standard deviation was 102.5 ± 1.8 pcf, average dry density was 98.2 ± 2.0 pcf, and average moisture content was 4.4 ± 0.8%. In general, the construction density measurements indicated that the sand backfill was uniformly constructed, and that material variability was within expected ranges for small-scale construction efforts.

Traffic was applied using the P-8 aircraft gear load configuration and wander pattern described in Chapter 7. Failure of the repair technique was considered to be 1.5 in. of permanent deformation (sag) in the FRP panel measured in a loaded condition. FRP tends to possess a meaningful amount of rebound; therefore, the mat was lightly loaded during elevation measurements to ensure that it was in contact with the underlying soils. A hydraulic pump and load piston were used to apply a seating load to the mat. The system consisted of a T-shaped I-beam that mounted on the hydraulic piston. The T-shaped beam was situated to contact the HVS carriage beam that provided a reaction force. A hydraulic pump was used to extend the piston and place approximately 2,000 lbf total seating load on the FRP panel consistent with historical experiments.

Results of loaded deformation for geosynthetic reinforced sand with FRP are provided in Figure 93. Permanent deformation was measured using rod and level, and rut depth was measured using a straightedge and machined depth wedge. A relatively linear increase in deformation was observed with an increase in traffic. The geosynthetic reinforced backfill surfaced with FRP sustained approximately 50 passes of the

P-8 gear before reaching the 1.5 in. failure criteria. No mat breakage and/or cracking was observed prior to failure. Photographs of the loaded FRP at the conclusion of traffic are shown in Figure 94.

Figure 93. Permanent deformation of geosynthetic reinforced sand with FRP.

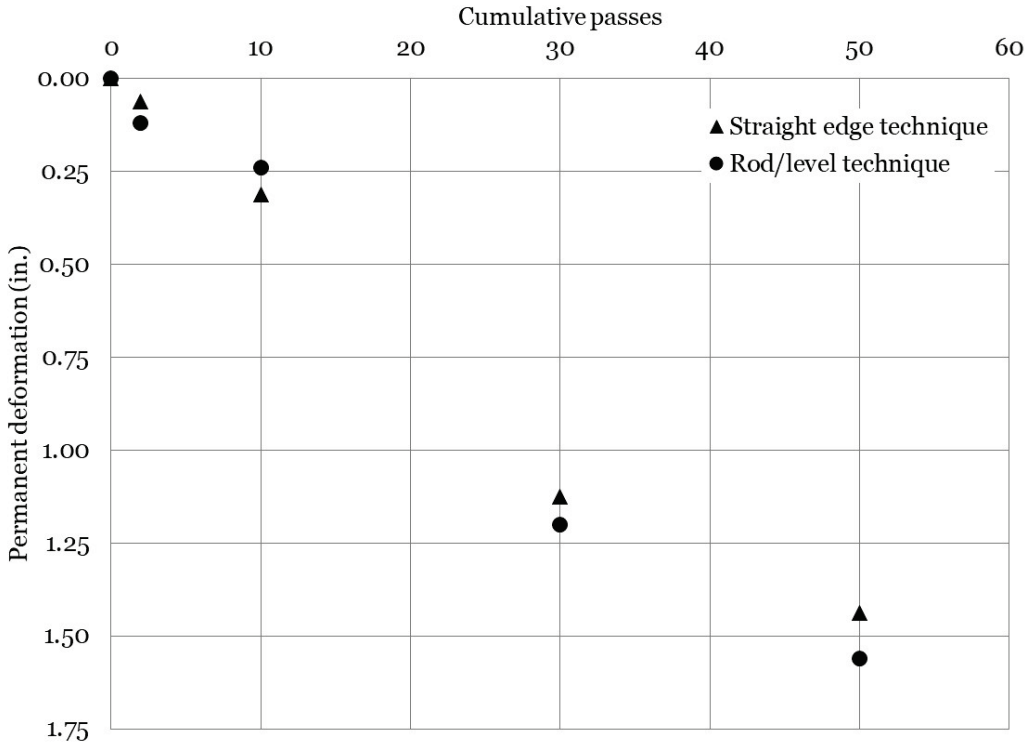

Figure 94. Photographs of geogrid stabilized backfill—posttraffic.

(a) Loaded FRP (b) Sand surface posttest

9.2 Repair 2: Crushed Limestone with FRP

Repair 2 consisted of a crushed limestone aggregate backfill surfaced with an FRP FOD cover. A simulated crater was excavated to a depth of 18 in., and the bottom of the excavation was leveled and recompacted. The crushed limestone backfill was placed in approximately 4 in. thick compacted lifts

until reaching the existing surface elevation of the surrounding concrete slabs. An FRP FOD cover was placed over the completed crushed limestone backfill layer and secured to the surrounding concrete slabs.

Nuclear density gauge measurements were made on each completed limestone aggregate backfill layer. Measurements were made in the center of the crater, near the side of the crater, and near a corner of the crater. The average wet density and standard deviation was 138.8 ± 4.4 pcf, average dry density was 133.8 ± 4.2 pcf, and average moisture content was 3.7 ± 0.5%. The dry density was less than would be anticipated in full-scale construction efforts; however, compaction was achieved with a small walk-behind vibratory plate compactor, and less compaction energy was available.

Results of loaded deformation for crushed limestone backfill with FRP are provided in Figure 95. Permanent deformation was measured using rod and level, and rut depth was measured using a straightedge and machined depth wedge. The crushed limestone repair technique sustained approximately 600 passes of the P-8 test gear before reaching the 1.5 in. failure criteria. No mat breakage and/or cracking was observed prior to failure. Photographs of the loaded FRP at the conclusion of traffic are shown in Figure 96.

Figure 95. Permanent deformation of crushed limestone backfill with FRP.

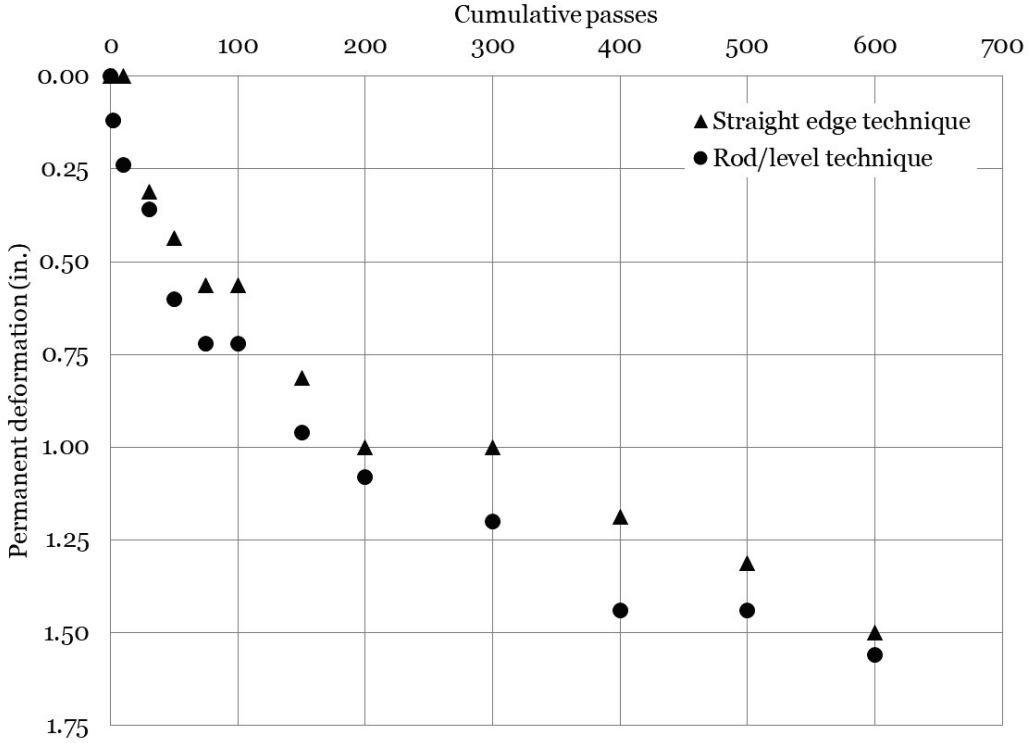

Figure 96. Photographs of posttest limestone backfill.

(a) Loaded FRP (b) Limestone surface posttest

9.3 Repair 3: Cement Stabilized Sand with FRP

Repair 3 consisted of a cement stabilized sand surfaced with a FRP FOD cover. A simulated crater was excavated to a depth of 16 in., and the bottom of the excavation was leveled and recompacted. Adjacent to the excavation, a sand stockpile, moisture conditioned to approximately 6–7%, was spread over an area approximately 10 ft wide by 20 ft long at a thickness of approximately 8 in. Ten 92.6 lb bags of cement were uniformly spread over the sand layer to target a 10% cement content. The cement was mixed into the sand using a mixer attachment on a CTL. Then, the mixture was agitated using a loader bucket on the CTL, respread, and mixed again. This process was repeated twice to ensure a uniform distribution of cement throughout the sand layer. After mixing the material was stockpiled and covered to prevent moisture loss during placement activities.

The cement-treated sand mixture was placed in the simulated crater in approximate 4 in. thick compacted lifts. Compaction consisted of four complete coverages of a jumping jack compactor over the entire repair area. This process was repeated until reaching the surface of the excavation. A metal screed was used to strike off excess material. Final surface smoothness was achieved with two passes of a vibratory plate compactor. An FRP FOD cover was placed over the completed cement stabilized backfill layer and anchored to the surrounding concrete slabs.

Nuclear density gauge measurements were made on the compacted cement-stabilized sand layers. Measurements were made in the center of the crater, near the side of the crater, and near a corner of the crater. Average wet density and standard deviation was 114.8 ± 2.9 pcf, average dry density was

110.1 ± 3.9 pcf, and average moisture content was 4.3 ± 0.5%. Dry density was generally in the range that would be expected for this material type.

Initial traffic was applied after approximately 24 hr of cure time and was continued up to 50 total passes. At this point, a hydraulic malfunction occurred on the HVS that resulted in a suspension of test traffic. Traffic was restarted after diagnosing and repairing the HVS hydraulic malfunction. The total down time was approximately 33 days. Thus, the cementitious repair materials had an unloading cure time that is outside normal airfield damage repair construction operations. This detail should be considered when interpreting the test results.

Results of loaded deformation for cement stabilized sand backfill with FRP are provided in Figure 97. Permanent deformation was measured using rod and level, and rut depth was measured using a straightedge and machined depth wedge. Little permanent deformation was observed. Traffic was halted at 3,500 total passes, which is considered a sustainment level of traffic. At the conclusion of traffic, approximately 0.25 in. of permanent deformation was measured. Thus, a cement-stabilized repair technique could sustain P-8 traffic passes well beyond a contingency (500-pass) scenario. Posttraffic photographs of the cement-stabilized repair are shown in Figure 98.

Figure 97. Permanent deformation of cement stabilized sand with FRP.

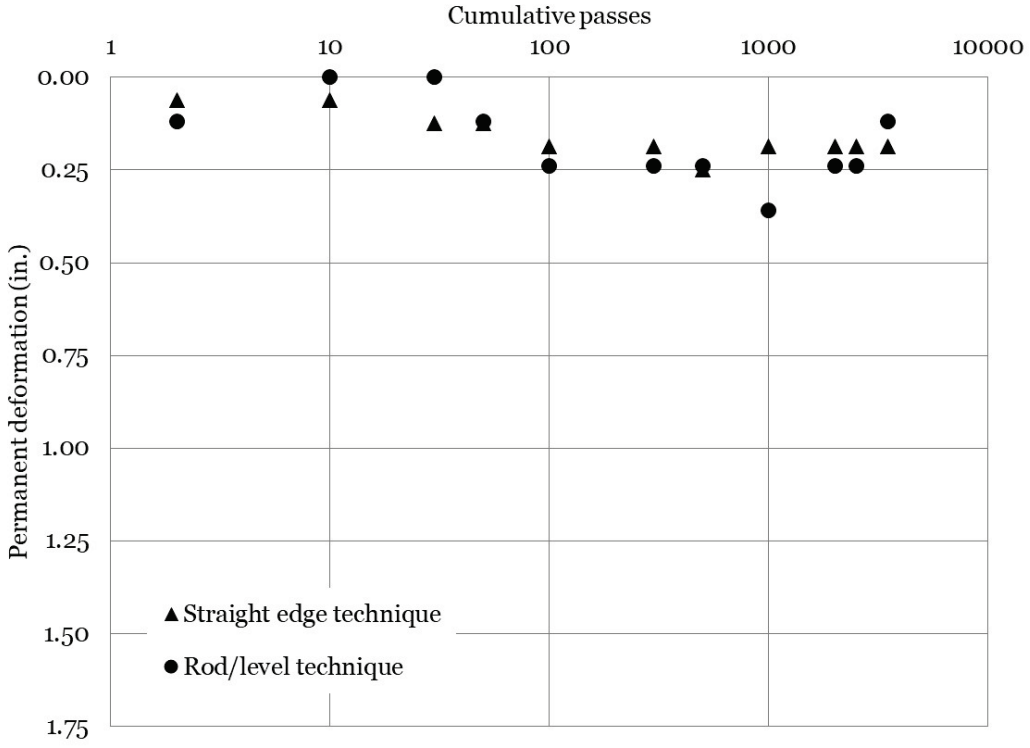

Figure 98. Photographs of posttest cement stabilized backfill.

(a) Overall view (b) Close-up view

9.4 Repair 4: Compacted Debris with Stone and Grout

Repair 4 consisted of a stone and grout repair technique. Reclaimed PCC debris was used as the backfill material. Relatively large pieces of PCC debris were broken using a backhoe equipped with a breaker attachment. The targeted maximum size of the debris was approximately 9 in. After oversized material had been removed and/or further reduced in size, a skeleton bucket on a CTL was used to screen the debris. The openings between teeth on the skeleton bucket were approximately 2.5 in., thus allowing material smaller than 2.5 in. to fall through the bucket and be discarded. Therefore, final processed reclaimed debris had particle sizes ranging from 9 in. to 2.5 in.

A simulated crater was excavated to a depth of 16 in., and the bottom of the excavation was leveled and recompacted. The processed PCC debris was placed in the excavation in one lift such that the debris was near the surface of the surrounding PCC slabs. A metal straightedge was slowly moved across the surface of the PCC debris to inspect for unusually large voids and/or pieces of debris that extended above existing grade. Large voids were filled by hand with additional small debris, and pieces extending above existing grade were either reoriented or removed and replaced. Small debris (i.e., particles ranging from ¾ to ½ in.) were placed in a 6 in. wide band around the perimeter of the crater. These materials allowed for proper grout penetration while reducing the potential for early joint spalling under traffic.

A mortar mixer was moved adjacent to the simulated crater and filled with 32 gal. of water. A 6.5 lb container of calcium chloride accelerator was added to the mix water. Five 92.5 lb, Type I portland cement bags were added to the water/accelerator mixture, and the mixer was allowed to agitate for 30 sec. The grout mixture was then poured over the PCC

debris, and the mixing and placing process was repeated until sufficient batches of material had been placed to fill all voids and reach the surface of the crater. A magnesium screed was used to strike off excess grout. After initial set (approximately 30 min) the repair was covered with plastic sheeting to prevent desiccation.

Initial traffic was applied after approximately 20 hr of cure time and was continued up to 50 total passes. At this point, a hydraulic malfunction occurred on the HVS resulting in suspension of test traffic. Traffic was restarted after diagnosing/repairing the HVS hydraulic malfunction. The total down time was approximately 33 days. Thus, the cementitious repair materials had an unloaded cure time that was outside normal construction operations; this fact should be considered when interpreting the test results.

Failure of the stone and grout repair technique was defined as one of more of the following: (1) high-severity shattered slab, (2) deflection in the interior of the repair greater than 1.5 in., (3) presence of a severe tire hazard, or (4) a high-severity joint spall with a length of at least 2 ft, a width of at least 6 in., and a depth of at least 2 in. over at least 50% of the spall length as determined by visual inspection.

Results of the trafficking test indicated that the stone and grout repair technique reached the limiting spall criteria at 2,000 passes. No damage was observed at the 500-pass inspection. Damage was first noted at the 1,000-pass inspection. While the spall met the limiting failure criteria at 2,000 passes, it did not present an operational concern for the HVS, and test traffic was continued until 3,500 passes. Photographs of spall progression are shown in Figure 99.

Pretraffic and posttraffic rod and level elevation measurements were made to assess deflection in the interior of the repair area. These measurements indicated that a global settlement on the order 0.30 in. occurred after the application of 3,500 P-8 passes. Simply, the repair tended to “punch” into the existing sublayers approximately 0.30 in.

To characterize the strength change of the stone and grout repair technique, FWD tests were conducted after the initial cure and at the conclusion of traffic. The FWD was positioned near the center of the repair, thus a portion of the deflection sensors were located on the in situ PCC pavement. Plate load and plate deflection were used for comparison purposes of pretraffic and posttraffic strength. The initial ISM for the stone and grout repair technique

was 2,385 kips/in. The final ISM for the stone and grout repair technique was 335 kips/in., representing a meaningful reduction in estimated load carrying capacity due to damage to the repair from traffic application.

Figure 99. Spalling in stone and grout repair.

(a) Joint spalling at 1,000 passes

(b) Joint spalling at 1,500 passes

(c) Joint spalling at 2,000 passes

9.5 Repair 5: Compacted Debris with Calcium-Sulfoaluminate (CSA) Concrete Mixture

Repair 5 consisted of the placement of debris backfill that was surfaced with a calcium-sulfoaluminate (CSA) concrete cap. A simulated crater was excavated to a depth of 26 in. Oversized debris was broken using a breaking attachment on a backhoe to a maximum aggregate size of approximately 12 in. (Figure 100). The 12 in. size debris was placed in a single layer in the bottom of a simulated crater (Figure 101*a*). A layer of sand was placed over the large-size debris and uniformly spread to fill in void space between the debris (Figure 101*b*). Thereafter, a layer of 9 in. size debris was placed in a single layer, and subsequently backfilled with sand to further fill remaining void space (Figure 101*c* and Figure 101*d*, respectively). The sand layer was placed in sufficient thickness such that the final CSA concrete capping layer would be 7 in. thick. The sand layer was compacted with a pneumatic jumping jack; a total of two uniform coverages were applied. Finally, a plate compactor was used to complete final compaction and to provide a uniform final surface. The depth was checked in multiple locations using a straightedge and folding carpenter's ruler, and any areas not meeting the thickness requirements were adjusted.

Figure 100. Processing debris backfill.

The CSA concrete surfacing material consisted of a rapid-setting cementitious mixture composed of ¾ in. maximum size recycled concrete aggregate (RCA), concrete sand, CSA cement, Type I portland cement, set retarding admixture, and water. The ¾ in. maximum size aggregate was created by crushing PCC debris in a CTL crusher bucket attachment.

Figure 101. Backfill placement process.

(a) Placement of 12 in. debris

(b) Placement of sand layer over 12 in. debris

(c) Placement of 9 in. debris

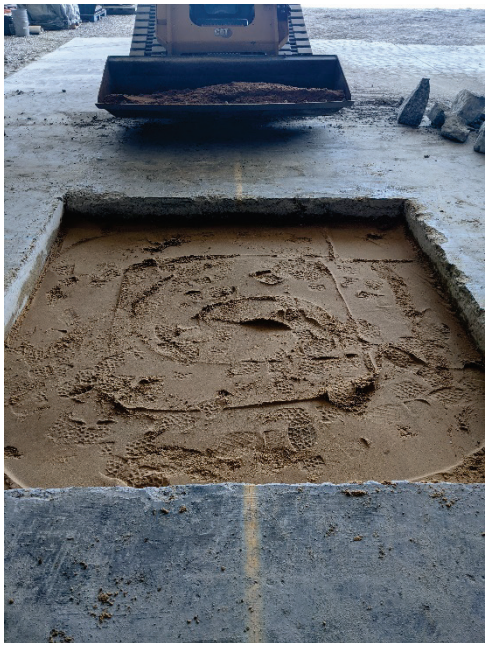

(d) Final sand layer prior to CSA placement

The CSA concrete surface material was prepared using a CTL mixing attachment. A second CTL with a split RCA/sand bucket was used to collect and transport component materials (Figure 102*a*). The RCA/sand bucket was divided with a steel plate such that the proper amount of each material type could be loaded on each side. The process consisted of initially loading the mixer attachment with the RCA and then adding the concrete sand. This aggregate combination was mixed for approximately 30 sec. Three 50 lb bags of CSA cement (Figure 102*b*) and one 47 lb bag of Type I portland cement were added to the mixture and dry mixed for approximately 30 sec (Figure 102*c*). Thereafter, approximately 17 gal. of water and a set-retarding admixture were added. The completed mixture was agitated for approximately 90 sec, and the completed mixture was discharged into the simulated crater (Figure 102*d*). This process was repeated until sufficient material was produced to achieve the target finish elevation.

Figure 102. CSA placement process.

(a) Loading sand into CTL mixer attachment

(b) Loading CSA cement into CTL mixer attachment

(c) Close-up of CTL mixing attachment chamber

(d) Placement of CSA mixture into crater

Initial traffic (100 passes) was applied after approximately 6 hr of cure time. Rod and level elevation measurements and visual inspection were conducted at select traffic intervals. Elevation measurements indicated a global settlement on the order of 1.4 in. occurred by the completion of 3,500 P-8 passes (Figure 103). Most settlement (approximately 1.2 in.) occurred in the first 2,000 P-8 passes.

Figure 103. Permanent deformation of CSA crater repair.

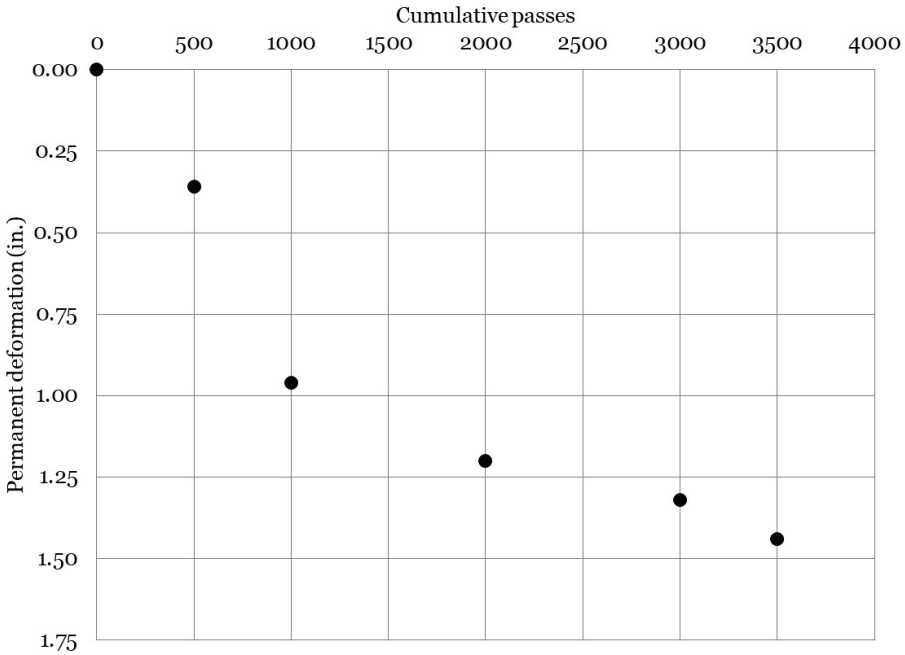

Joint spalling initiated at approximately 200 P-8 passes (Figure 104*a*). Although joint spalling increased with increased traffic passes (Figure 104), the spall did not progress to the point considered failure until 3,500 passes. Further, the spall did not present a meaningful tire hazard.

Figure 104. Joint spalling of CSA repair.

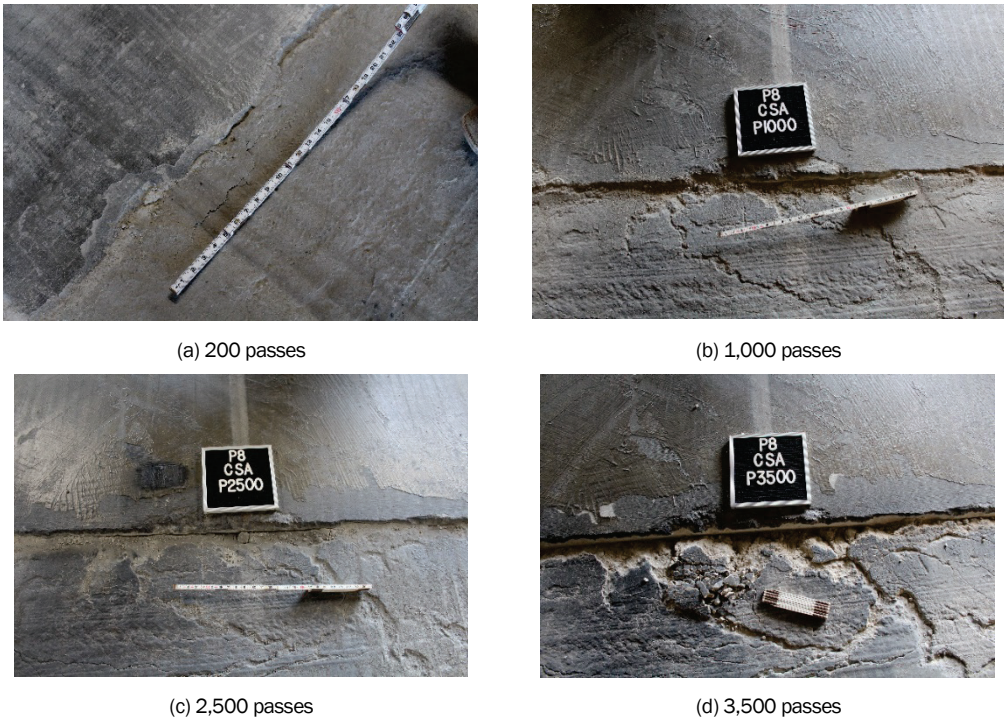

(a) 200 passes

(b) 1,000 passes

(c) 2,500 passes

(d) 3,500 passes

Strength change of the CSA repair technique was monitored using an FWD, and ISM values were determined at various traffic levels (Figure 105). The pretraffic ISM (after the 6 hr cure time) was approximately 1,150 kips/in. A rapid decline in ISM was observed up to 500 passes (see Figure 105), and ISM values tended to stabilize thereafter. A slight upward trend was noted after 2,000 passes that may be attributed to densification and/or particle reorientation. The final ISM at the conclusion of 3,500 passes was approximately 350 kips/in., similar to the final ISM reported for the stone-and-grout repair.

Figure 105. ISM for CSA crater repair.

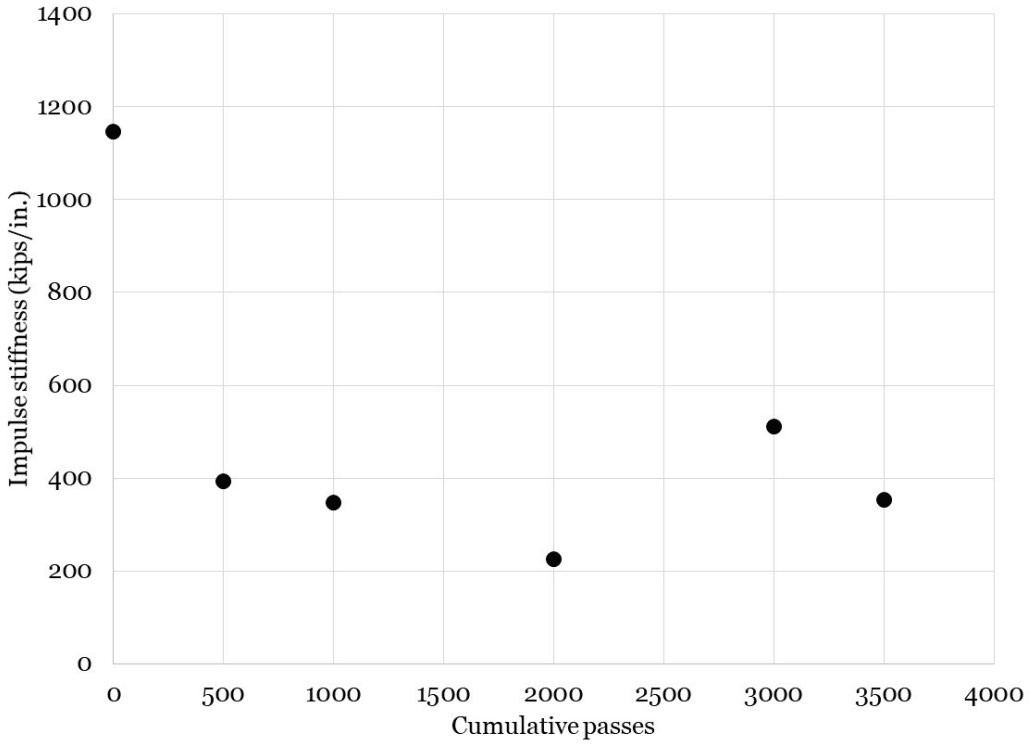

9.6 Repair 6: Rapid-Setting Flowable Fill Backfill with Rapid-Setting Concrete Mixture

Repair 6 consisted of a rapid-setting flowable fill backfill capped with a high-quality rapid-setting concrete. A simulated crater was excavated to a depth of 24 in., and the bottom of the excavation was carefully leveled. Rapid-setting flowable fill was used to construct a 14 in. thick backfill layer. An extendable boom forklift (Figure 106*a*) was used to position a super sack over the simulated crater, and the dry rapid-setting flowable fill blend was released into the crater and uniformly spread (Figure 106*b*) to achieve a 4 in. thick lift. Approximately 40 gal. of water was dispensed over the

surface of each lift via a 2 in. diam hose equipped with a shutoff nozzle and a flow meter (Figure 106*c*). Water was allowed to penetrate the dry-placed flowable fill for approximately 10 min, and the process was repeated until the target elevation was reached. For the final lift, approximately 30 gal. of water was dispensed over the surface to reduce the amount of standing water on the surface of the flowable fill (Figure 106*d*).

A 10 in. thick rapid-setting concrete cap was placed over the rapid-setting flowable fill backfill layer using a simplified volumetric mixer (Figure 106*e*). The repair was allowed to cure for approximately 2 hr (Figure 106*f*), after which the HVS was positioned over the crater. Test traffic was initiated after 2.75 hr from the time of rapid-setting cap placement.

Rod and level measurements and visual inspections were conducted at select traffic intervals. Elevation measurements indicated global settlement of 0.12 in. occurred at the conclusion of 3,500 P-8 passes.

Minor joint spalling (Figure 107) was observed in the rapid-setting concrete surface. The observed spalling did not meet the failure threshold, and there was minimal FOD development.

Stiffness changes in the rapid-setting repair were monitored using an FWD, and ISM values were determined at various traffic levels (Figure 108). The pretraffic ISM (after the 2.75 hr cure time) was approximately 2,960 kips/in. ISM values declined up to approximately 1,000 passes and generally stabilized thereafter. The final ISM at the conclusion of 3,500 passes was approximately 830 kips/in.

Figure 106. Placement of rapid-setting flowable fill/concrete cap.

(a) Positioning flowable fill over crater

(b) Spreading flowable fill to a uniform thickness

(c) Applying water to flowable fill layer

(d) Completed flowable fill lift

(e) RS mixture placement with volumetric mixer

(f) Completed rapid set crater surface

Figure 107. Joint spalling at 3,500 passes on rapid-setting (RS) crater repair.

(a) Joint spall at north edge (b) Joint spall at south edge

Figure 108. ISM for rapid-setting concrete crater repair.

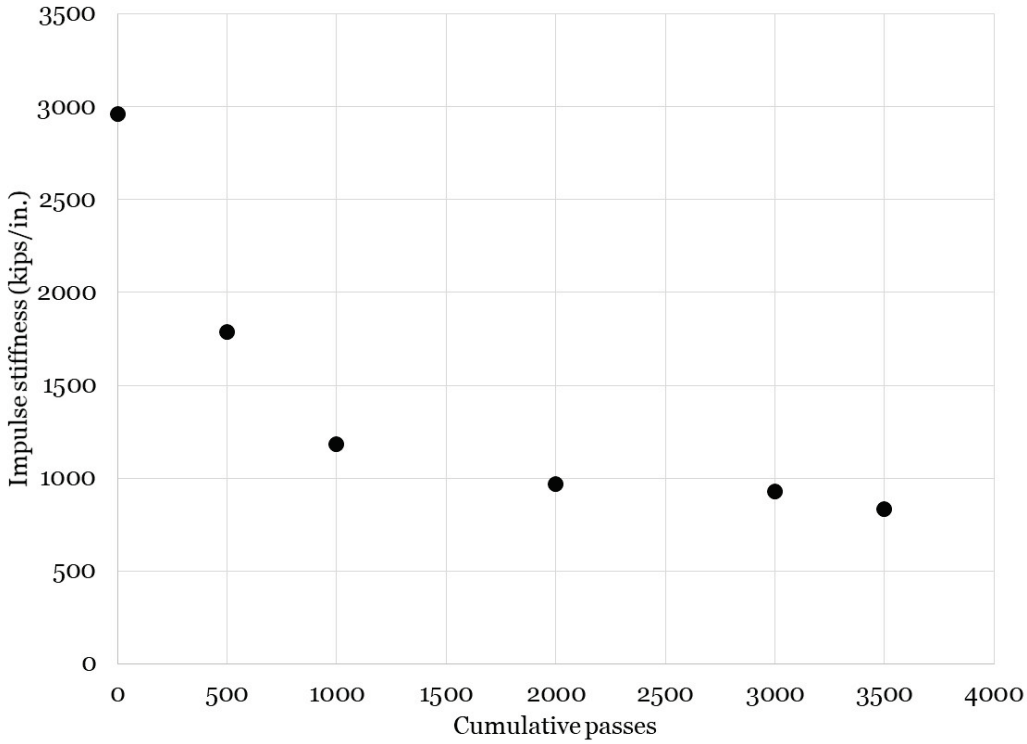

10 Forensic Investigation

A forensic investigation was performed to measure posttraffic material properties and to study the flexible pavement mode of failure. Trenches approximately 5 ft wide were excavated near the center cross section of each flexible pavement test item. Excavation began by saw-cutting the HMA surface and carefully removing it to minimize disturbance to the underlying base course. After forensic data were collected on the base layer, it was removed to expose the underlying subgrade layer. Layer deformation measurements, field CBR tests, nuclear density tests, and moisture content tests were made at each trench location.

10.1 Posttraffic Layer Permanent Deformation

A robotic total station was used to determine permanent layer deformation at 6 in. intervals on the surface of each excavated pavement layer. These results are shown in Figures 109 to 114. Photographs of the excavated cross sections are shown in Figure 115. Layer interfaces are highlighted by a red dashed line. Rutting in each layer was calculated by averaging the maximum elevation (upheaval) on each side of the wheel path and subtracting the minimum elevation (bottom of rut) within the wheel path. Additionally, a similar analysis technique was made on construction cross-section elevation measurements to remove any abnormalities during construction. This approach "zeroed" the data and allowed for capturing only deformation that could be attributed to traffic application. Thus, calculated rut-depth values via total station measurement techniques (Table 20) may be different from those measured with a straightedge. However, the measurements are useful in examining the magnitude of rutting in each layer relative to each other and understanding how each layer contributed to overall observed failure.

For the weak gravel base test items, surface deformation measurements indicated that the greatest deformation was generally measured in the base layer. This observation was expected, because the strength (CBR) of the gravel layer was well below current minimum specifications. The thickness of the relatively thin asphalt layers was inadequate to distribute the applied loads to the relatively weak base. Additionally, the deformation measurements reinforced the need for a competent aggregate layer to sustain the heavy wheel loads and high tire pressures from the P-8 test gear.

For test items containing a high-quality limestone base, general observations were that the greatest measured deformation occurred in the subgrade except for the 2 in. thick HMA on the 6 CBR subgrade. These data suggest that on the weaker subgrade, a 2 in. thick HMA layer was insufficient to adequately protect the aggregate base course. This observation reinforces the recommendation for a minimum 4 in. thick HMA layer.

Table 20. Individual layer deformation.

Test Item	Asphalt (in.)	Base (in.)	Subgrade (in.)
4 in. HMA, GR, 10 CBR	3.4	3.3	2.6
2 in. HMA, GR, 10 CBR	1.2	1.8	1.8
4 in. HMA, LS, 10 CBR	2.5	3.1	2.8
2 in. HMA, LS, 10 CBR	1.9	1.7	1.3
4 in. HMA, LS, 6 CBR	4.2	4.5	3.3
2 in. HMA, LS, 6 CBR	2.1	2.2	0.9

Figure 109. Posttraffic layer deformation for 4 in. HMA, GR, 10 CBR.

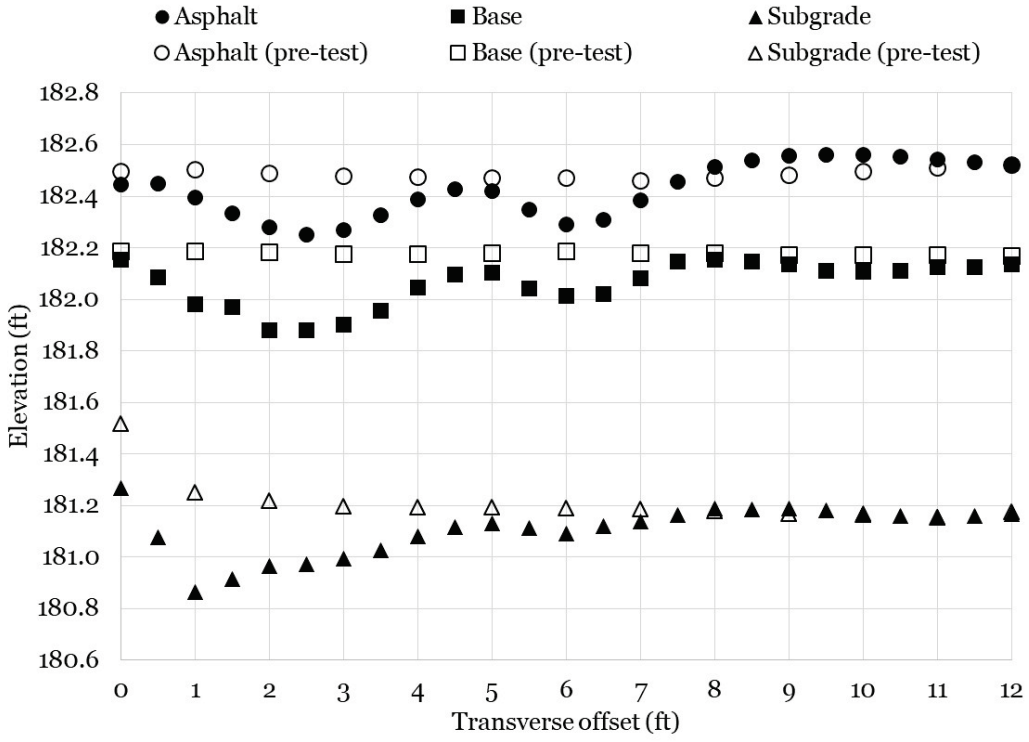

Figure 110. Posttraffic layer deformation for 2 in. HMA, GR, 10 CBR.

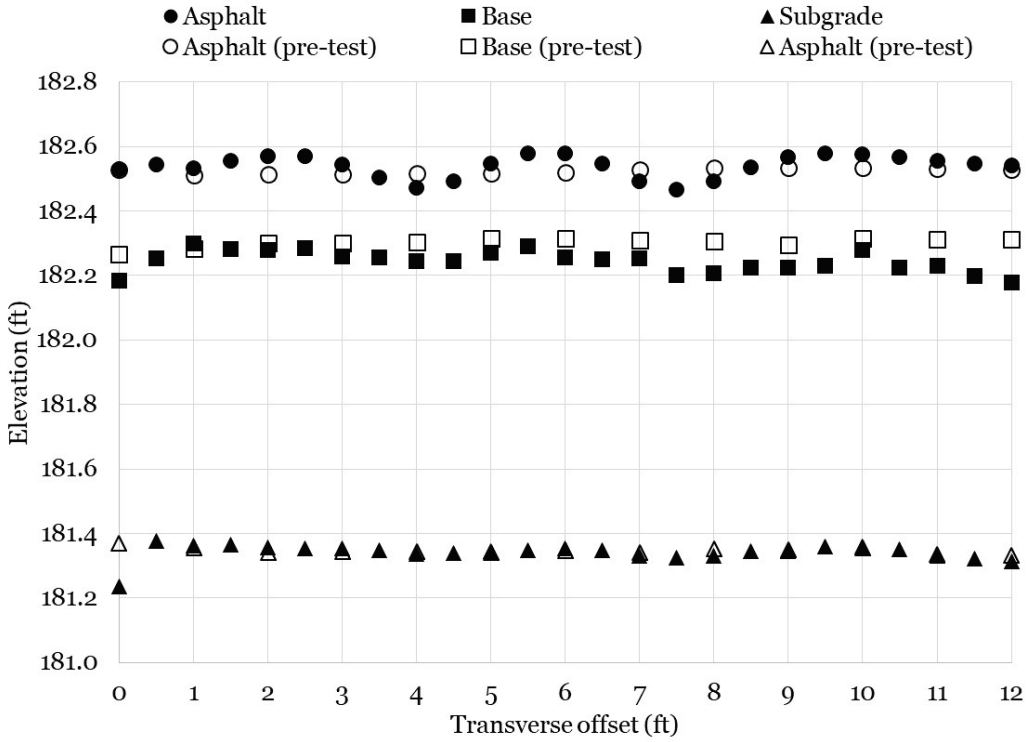

Figure 111. Posttraffic layer deformation for 4 in. HMA, LS, 10 CBR.

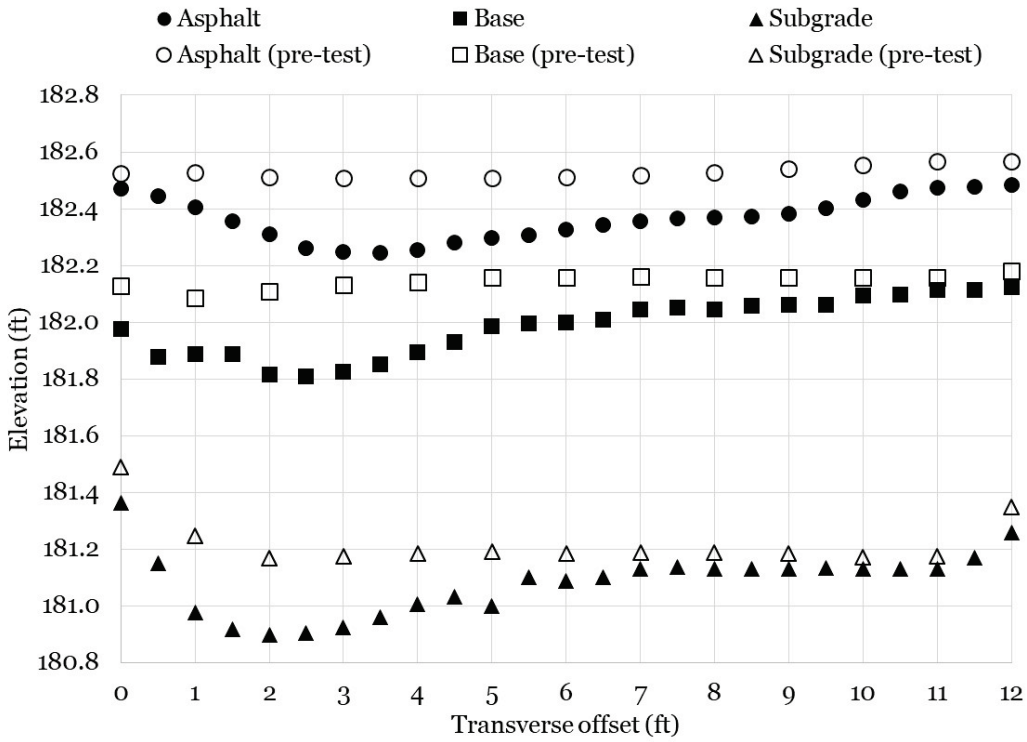

Figure 112. Posttraffic layer deformation for 2 in. HMA, LS, 10 CBR.

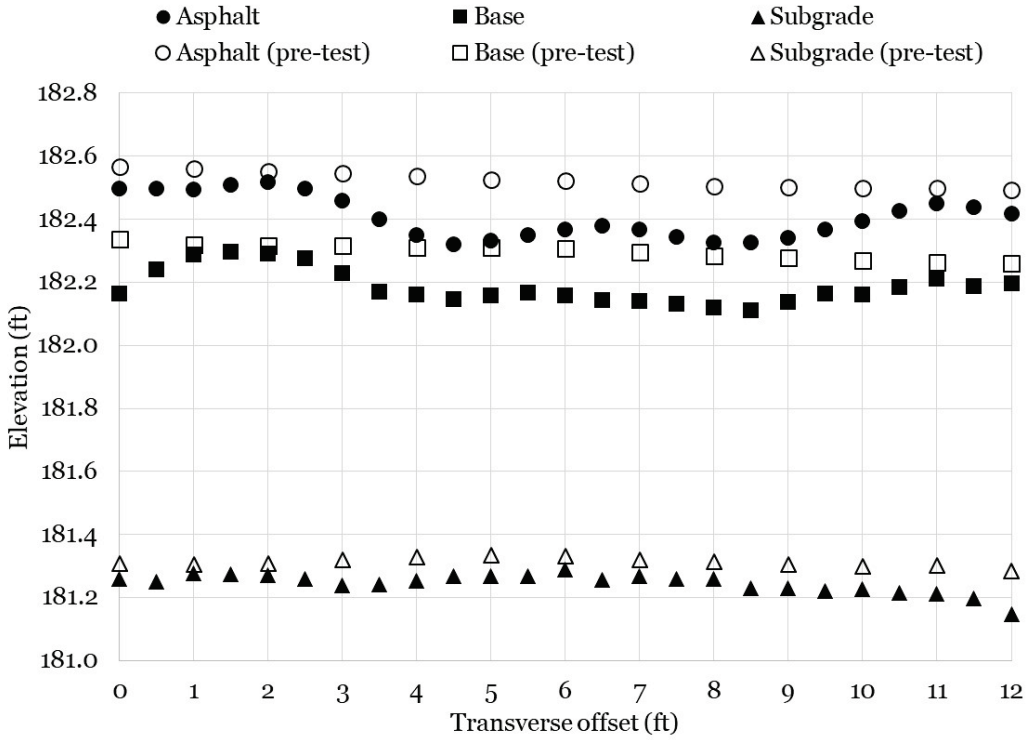

Figure 113. Posttraffic layer deformation for 4 in. HMA, LS, 6 CBR.

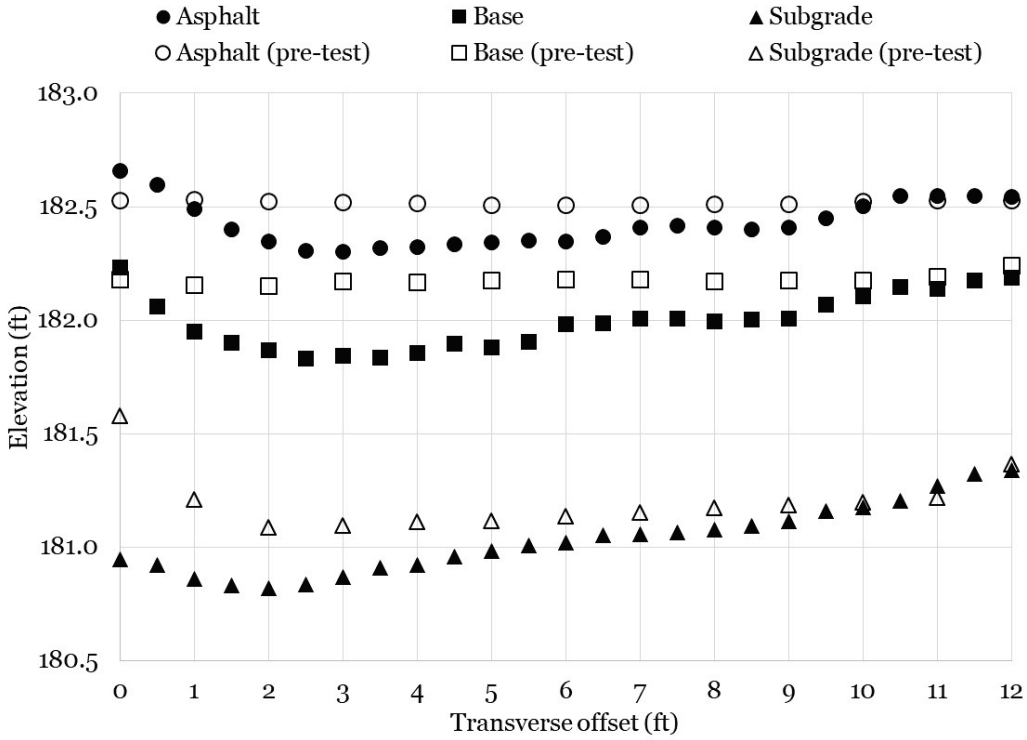

Figure 114. Posttraffic layer deformation for 2HMA, LS, 6 CBR.

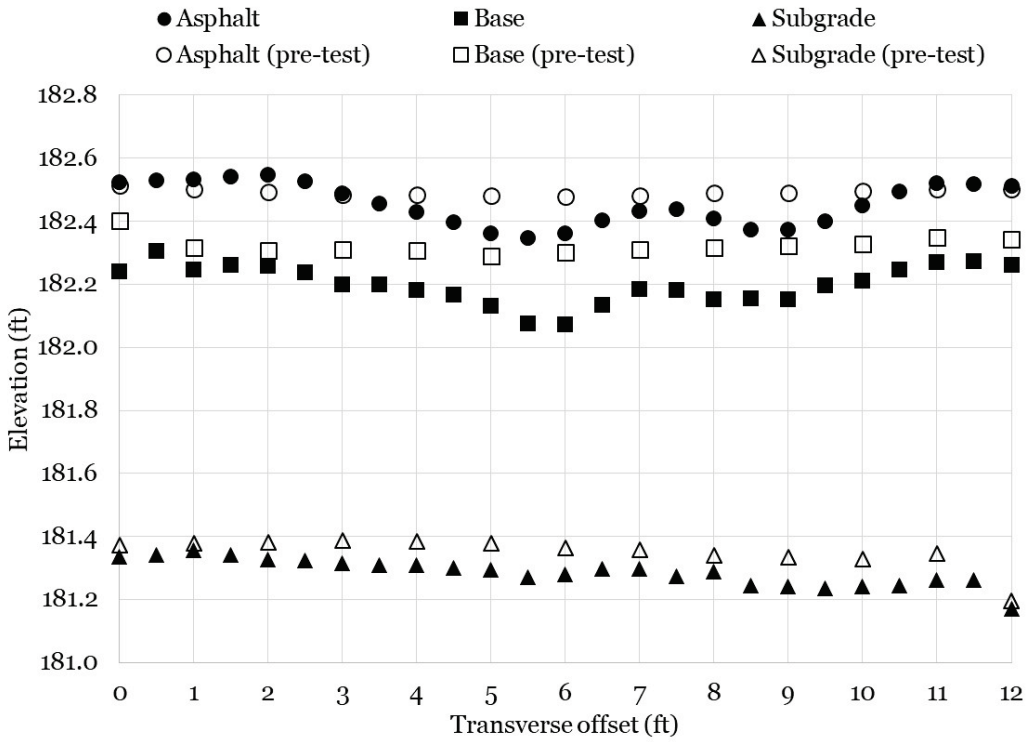

Figure 115. Photographs of excavated cross sections.

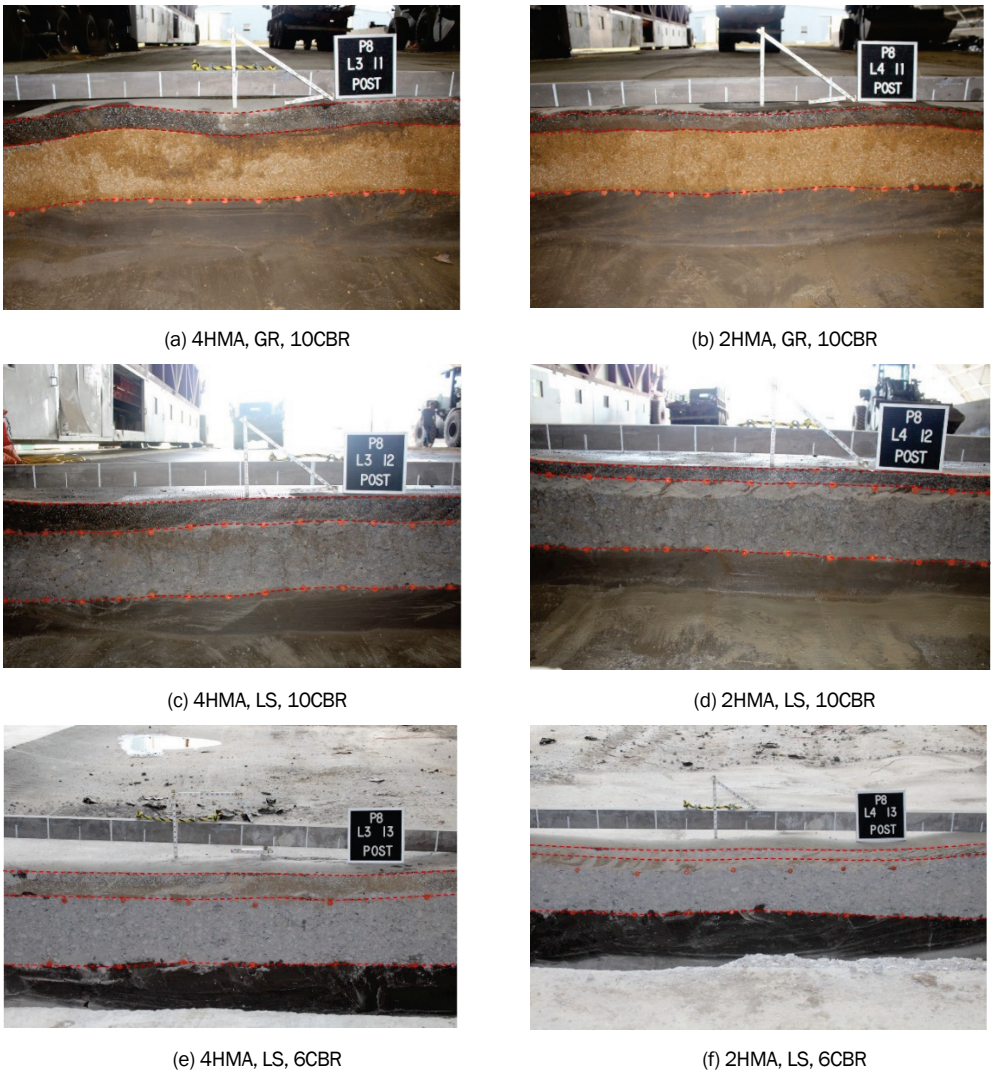

(a) 4HMA, GR, 10CBR

(b) 2HMA, GR, 10CBR

(c) 4HMA, LS, 10CBR

(d) 2HMA, LS, 10CBR

(e) 4HMA, LS, 6CBR

(f) 2HMA, LS, 6CBR

10.2 Posttraffic Material Properties

Measured posttraffic material properties are shown in Table 21. Changes in material properties (posttraffic minus as-built properties are summarized in Table 22. Measured properties represent measurements made in the traffic wheel-path, thus highlight the changes that could be attributed to traffic application.

In the aggregate base layer, an increase in measured compaction was generally observed that could be attributed to aggregate densification under traffic loading and slight reductions in measured moisture content. Increases in CBR in the limestone base layer were measured; however, in the case of the gravel base layer, reductions in CBR were measured. These data tend to

indicate that stress-hardening occurred in the semi-cohesive limestone layer (i.e., measured strength tended to improve with the application of load.) Reductions in CBR in the gravel base layer corroborate forensic elevation measurements in which the greatest deformation was observed in the gravel layer. This suggests that the initially weak gravel layer was a meaningful contributor to pavement failure.

Minor changes were observed in the CH subgrade layer in most cases. Compaction measurements generally indicated a decrease in compaction was observed in some items (4HMA over GR over 10 CBR and 4HMA over LS over 10 CBR), while a slight increase was observed in the other test items. No clear trend could be identified; however, the largest increase was observed in the 2HMA over LS over 6 CBR test item. Similar observations were made regarding measured subgrade CBR. These data suggest that a meaningful amount of densification occurred near the surface of the weaker 6 CBR subgrade layer under P-8 traffic. The instrumentation response data (SDD data in particular) tend to confirm these observations: the 2HMA over LS over 6 CBR test item displayed the highest dynamic and permanent subgrade deflection early in traffic application.

Table 21. Posttraffic material properties.

Property	4 in. HMA, GR, 10 CBR	4 in. HMA, LS, 10 CBR	4 in. HMA, LS, 6 CBR	2 in. HMA, GR, 10 CBR	2 in. HMA, LS, 10 CBR	2 in. HMA, LS, 6 CBR
CH Subgrade (TDD = 92.0 pcf @ TMC = 29.0%, TDD = 88.4 @ TMC = 32%)						
Wet Density (pcf)	117.1	114.2	120.1	117.6	120.1	120.9
Dry Density (pcf)	91.7	89.2	93.8	93.4	93.7	96.0
Nuclear Moisture (%)	27.7	28.1	28.0	25.9	28.2	25.9
Compaction (%)	99.7	96.9	106.1	101.5	101.8	108.5
Oven-Dried Moisture (%)	30.4	30.5	31.7	31.9	30.2	31.5
In-Place CBR (%)	8.1	10.1	8.8	8.8	9.3	9.3
Aggregate Base (MDD = 147.9 pcf @ OMC = 5.2%; 115.1 pcf @ OMC = 8.4)						
Material Type	GR	LS	LS	GR	LS	LS
Wet Density (pcf)	116.6	144.5	150.0	116.4	142.4	146.6
Dry Density (pcf)	113.5	140.3	146.4	113.6	137.6	143.5
Nuclear Moisture (%)	2.8	3.0	2.5	2.4	3.5	2.2
Compaction (%)	98.6	94.9	99.0	98.7	93.0	97.0
Oven-Dried Moisture (%)	2.2	1.9	0.7	2.2	1.8	1.0
In-Place CBR (%)	19*	100+	100+	24*	100+	100+

TDD = target dry density, TMC = target moisture content, MDD = maximum dry density, OMC = optimum moisture content, *Estimated from DCP measurements

Table 22. Change in material properties (posttraffic minus as-built).

Property	4 in. HMA, GR, 10 CBR	4 in. HMA, LS, 10 CBR	4 in. HMA, LS, 6 CBR	2 in. HMA, GR, 10 CBR	2 in. HMA, LS, 10 CBR	2 in. HMA, LS, 6 CBR
CH Subgrade (MDD = 106.1 pcf @ OMC = 17.1%)						
Wet Density (pcf)	-1.1	-2.0	3.5	0.0	0.3	4.4
Dry Density (pcf)	-1.4	-2.8	3.1	1.1	1.5	5.6
Nuclear Moisture (%)	0.9	2.0	-0.1	-2.0	-1.8	-2.6
Compaction (%)	-1.3	-2.6	2.9	1.0	1.4	5.3
Oven-Dried Moisture (%)	1.3	1.4	0.1	2.3	2.5	0.1
In-Place CBR (%)	-1.9	0.1	2.9	-1.0	-1.2	3.4
Aggregate Base (MDD = 147.9 pcf @ OMC = 5.2%; 115.1 pcf @ OMC = 8.4)						
Material Type	GR	LS	LS	GR	LS	LS
Wet Density (pcf)	4.9	-0.2	6.2	0.6	3.6	2.7
Dry Density (pcf)	5.7	1.4	7.6	4.4	4.0	4.2
Nuclear Moisture (%)	-0.9	-0.9	-1.1	-3.2	1.4	-1.2
Compaction (%)	5.0	1.0	5.2	3.8	3.0	2.8
Oven-Dried Moisture (%)		-1.3	-2.1		-0.7	-1.8
In-Place CBR (%)	-11.5*	6.0	0.0	-6.5*	17	29

TDD = target dry density, TMC = target moisture content, MDD = maximum dry density, OMC = optimum moisture content, *Estimated from DCP measurements

11 Implications for Flexible Pavement Design

An analysis was performed to investigate how the results of the flexible pavement traffic tests agreed with existing performance criteria and to develop improved performance predictions. The analyses are described in this chapter.

11.1 Comparison to Existing Design Methodology

Team members compared the passes to failure from the full-scale trafficking tests with performance predictions made using current DoD models and criteria. The recently released Pavement-Transportation Computer Assisted Structural Engineering (PCASE) Version 7.0 was used to determine predicted passes to failure based on as-constructed pavement layer thicknesses and material properties. Specifically, the Airfield Pavement Evaluation (APE) module was used to predict allowable passes to failure. The APE module provides the user with a means to select general layer types, select material types, input material thicknesses, and input layer CBR properties. These capabilities are appropriate for the construction data contained in this report and are appropriate for the types of field data available in an expeditionary environment. The module uses a multi-step process where the passes to failure are computed for each material layer, and the minimum passes to failure represent overall passes to failure for the pavement section. Calculated passes to failure are based on traditional long-term design failure criteria for flexible pavements (1 in. rut depth).

A comparison of actual and predicted passes to failure utilizing the Beta-Alpha hybrid criteria is shown in Table 23. In most cases for 1 in. of rutting, researchers observed that actual passes to failure were greater than predicted passes to failure suggesting there is a level of conservatism in the existing performance criteria. Notably, APE overpredicted passes to failure for the 4 in. HMA over LS over 6 CBR test item.

Similarly, a comparison of actual and predicted passes to failure utilizing the Alpha criteria is shown in Table 24. In both cases we found that the current performance criteria did not provide an adequate prediction of passes to failure for these relatively weak airfield pavement structures. Further, existing performance criteria are generally based on the results of

historical test data where failure was considered 1 in. of rutting; thus, they are not explicitly applicable to contingency operations where an accurate prediction of relatively low passes may be expected, and much greater allowable rut depths on the order of 2 in. are allowed.

Table 23. Comparison of PCASE7 (Beta-Alpha hybrid) predicted passes to failure and actual passes to failure.

	Actual	Actual	Base	Subgrade		Difference	Difference
Item	1 in. rut	2 in. rut	Predicted	Predicted	Minimum	1 in. rut	2 in. rut
4HMA, GR, 10 CBR	8	26	5	129	**5**	3	21
4HMA, LS, 10 CBR	222	608	6,189,838	203	**203**	19	405
4HMA, LS, 6 CBR	99	321	357,070	382	**382**	-283	-61
2HMA, GR, 10 CBR	2	4	1	58	**1**	1	3
2HMA, LS, 10 CBR	260	611	47	51	**47**	213	398
2HMA, LS, 6 CBR	79	230	14	5	**5**	74	156

Table 24. Comparison of PCASE7 (Alpha criteria) predicted passes to failure and actual passes to failure.

	Actual	Actual	Base	Subgrade		Difference	Difference
Item	1 in. rut	2 in. rut	Predicted	Predicted	Minimum	1 in. rut	2 in. rut
4HMA, GR, 10 CBR	8	26	5	492	**5**	3	-466
4HMA, LS, 10 CBR	222	608	6,189,838	696	**696**	-474	-88
4HMA, LS, 6 CBR	99	321	357,070	778	**778**	-679	-457
2HMA, GR, 10 CBR	2	4	1	254	**1**	1	3
2HMA, LS, 10 CBR	260	611	47	229	**47**	213	564
2HMA, LS, 6 CBR	79	230	14	37	**14**	65	216

11.2 Permanent Deformation Modeling for Contingency Criteria

To address the inadequacy of the existing design methodologies, a modeling effort was initiated. In a classical mechanistic-empirical (cME) method, such as that currently used in PCASE, pavement response is calculated using the initial structural condition of the pavement, and an empirical transfer function is used to predict the number of load repetitions to failure. The load repetitions to failure are constrained by data gathered during accelerated pavement testing, which has traditionally been based on approximately 1.0 in. of rutting. Furthermore, this procedure is best suited for the performance of permanent airfields.

However, the nature and urgency of contingency operations allow for less stringent rutting criteria (2.0 in. rutting for the P-8), thus making direct application of the cME method more difficult. Therefore, a new performance prediction method was developed based on the permanent deformation (PD) models used in the AASHTO Mechanistic-Empirical Pavement Design Guide (MEPDG [Witczak and El-Basyouny 2004]).

11.2.1 Fundamental Equations of the Permanent Deformation Model

The PD model is fundamentally a mechanistic-empirical method, as it first computes a mechanistic response at predefined points within a theoretical layered elastic structure due to an aircraft load. It then relates these responses to progressive rutting performance through empirical relationships. The PD model uses layered elastic (LE) theory to compute this mechanistic response. Whereas traditionally the cME method computes the vertical strain (or stress) at the top of the subgrade only to relate to subgrade rutting performance, the PD model accumulates permanent strains from deep within the subgrade up through the structure to the surface. This is accomplished through a sublayering approach, as shown in Figure 116.

Figure 116. Sublayering approach for decomposing the pavement structure with predefined analysis depths.

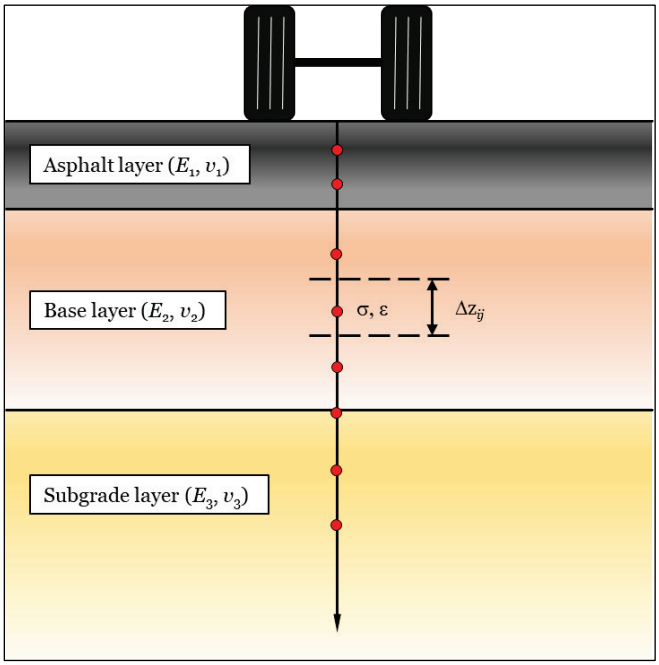

The total accumulated permanent deformation is computed by summing the plastic strains from each sublayer within their respective thicknesses, as shown in Equation 1.

$$\delta_a(N) = \sum_{i=1}^{NL} \sum_{j=1}^{NSL} \varepsilon_{ij}^{p}(N) \Delta z_{ij}, \quad (1)$$

where

δ_a = permanent deformation of pavement (inches),
ε_{ij}^{p} = plastic strain of sublayer *j* in layer *i*,
Δz_{ij} = thickness of sublayer *j* in layer *i*,
N = number of passes of aircraft (or heavy vehicle simulator),
NL = number of pavement layers, and
NSL = number of sublayers in a particular pavement layer.

There are three different material models used to compute the plastic strain used in Equation 1–an HMA material model, an unbound aggregate material model, and a subgrade material model. The HMA material model (Equation 2) is given in terms of HMA temperature, pass level, and resilient vertical strain.

$$\varepsilon_{1j}^{p}(N) = \varepsilon_v\left(\beta_1 a T^{\beta_2 b} N^{\beta_3 c}\right), \quad (2)$$

where

ε_{1j}^{p} = accumulated plastic strain in sublayer *j* of HMA layer after *N* load repetitions,
$\beta_1, \beta_2, \beta_3$ = locally calibrated material constants,
a, b, c = globally calibrated regression constants, and
ε_v = resilient vertical strain computed in sublayer using LE theory.

The unbound aggregate material and subgrade material models are of the same form, Equation 3:

$$\varepsilon_{ij}^{p}(N) = \varepsilon_v \left[\beta_1 \left(\frac{\varepsilon_0}{\varepsilon_r}\right) e^{-\left(\frac{\rho}{N}\right)^{\beta}}\right], \quad (3)$$

where

ε_{ij}^{p} = accumulated plastic strain in sublayer j of layer i after N load repetitions,
β_1 = calibration parameter for unbound and subgrade materials,
$\frac{\varepsilon_0}{\varepsilon_r}, \beta, \rho$ = material properties obtained through transfer functions, and
ε_v = resilient vertical strain computed in sublayer using LE theory.

The parameters $\frac{\varepsilon_0}{\varepsilon_r}, \beta,$ and ρ are determined through empirical transfer functions or constants, based on whether the materials are characterized as an unbound granular material (Equation 4*a* to 4*c*) or a subgrade material (Equation 5*a* to 5*c*).

Unbound Granular

$$\log\left(\frac{\varepsilon_0}{\varepsilon_r}\right) = 0.80978 - 0.06626\omega_c - 0.003077\theta + 0.000003E(t) \quad (4a)$$

$$\log(\beta) = -0.4545 + 0.015525\omega_c + 0.000903\theta - 7.5E - 7E(t) \quad (4b)$$

$$\log(\rho) = -1.78667 + 1.45062\omega_c + 0.0003784\theta^2 - 0.002074{\omega_c}^2\theta - 0.0000105E(t) \quad (4c)$$

Subgrade

$$\log\left(\frac{\varepsilon_0}{\varepsilon_r}\right) = -1.69867 + 0.09121\omega_c - 0.11921\theta + 0.91219E(t) \quad (5a)$$

$$\beta = 0.101094 \quad (5b)$$

$$\log(\rho) = 11.009, \quad (5c)$$

where

ω_c = water content as a function of CBR (%),
θ = bulk stress (psi), and
$E(t)$ = modulus as a function of time (load repetitions).

11.2.2 Aircraft Wander

An important feature of the PD model is its discrete approach to modeling vehicle wander. In addition to the predefined analysis depths using the sublayer approach described in Figure 116, a series of analysis points aligned in the transverse direction extending across the entire width of the test section are used to account for the accumulated permanent deformation due to different lateral offsets of the dual P-8 tires. Stated differently, pavement damage (permanent deformation) is accumulated at each transverse analysis point every single pass of the HVS. The significance of this approach cannot be overstated—rather than computing damage within the footprint of the landing gear, the PD model accumulates damage across the entire width of the test section each HVS pass, regardless of the lateral offset location of the HVS. Damage then is a function of the degree of stress experienced each pass rather than tire location.

Reviewing Figure 117, one can see the dual P-8 gear moving laterally each pass as the HVS shifts position. The permanent deformation due to the moving gear load is computed at each analysis point (red dots) along the entire width of the test section each pass. The fundamental principle of the PD model used in this study is that stress is experienced in some degree at every analysis point each pass regardless of whether the tires from the HVS are directly over those points.

Figure 117. Use of transverse analysis points across width of test section to accumulate permanent deformation during each vehicle pass with wander.

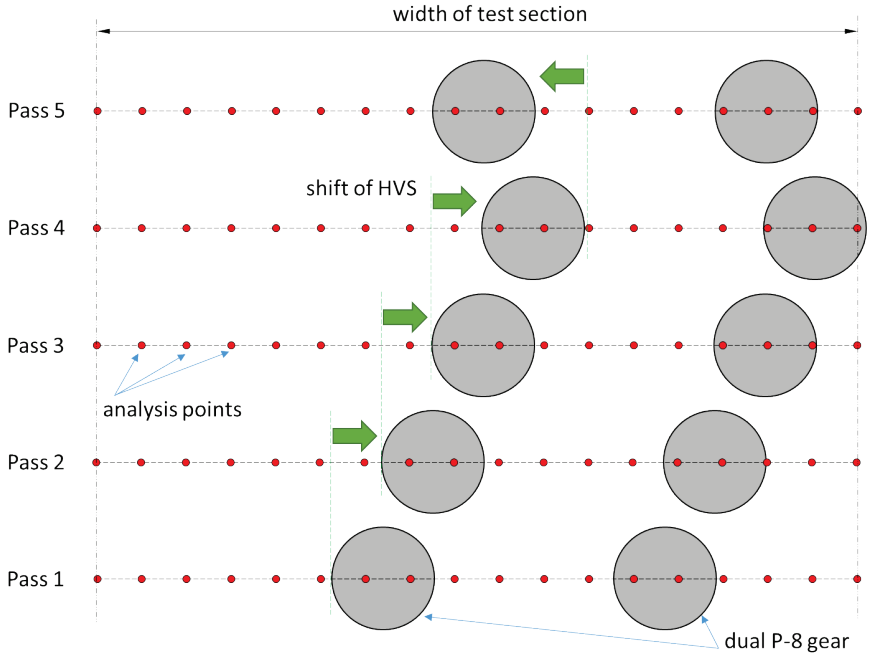

11.2.3 Incremental Damage

One characteristic difference between the cME method and the proposed PD model is that the cME method provides only the projected number of load repetitions to a predefined failure level (e.g., 1.0 in. of rutting), while the PD model provides a history of accumulated permanent deformation for increased levels of load applications based on an incremental damage approach. Not only is damage accumulated across the entire transverse width of the test section each HVS pass, but damage is also accumulated over time. This provides a history of the development of permanent deformation with increasing load applications. For example, while a rut-depth criterion of 2.0 in. was used in this study for the design of contingency flexible pavement structures under a P-8 loading, the proposed PD model easily accommodates the computation of the passes to failure for a particular pavement structure for a modified 2.25 in. rut-depth criteria as shown in Figure 118. In this manner the PD model makes better use of the incremental data collected during full-scale testing and provides a more comprehensive pavement damage approach.

Figure 118. Screenshot of PD model user interface, with plotted rut-depth history and computed pass level for a modified 2.25 in. rut-depth criteria.

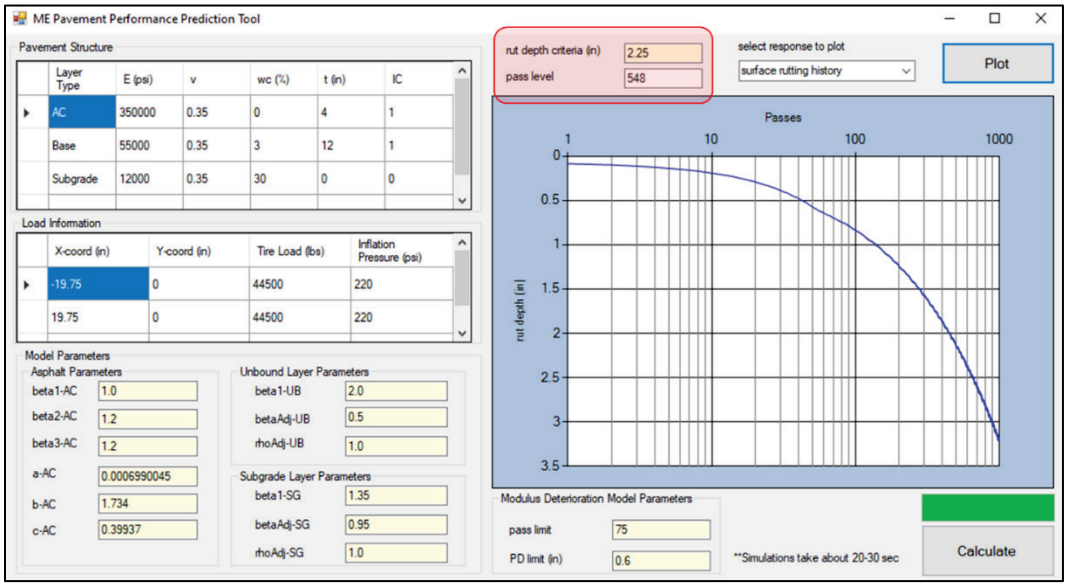

11.2.4 Modulus Deterioration

Another salient feature of the PD model is the methodology to account for modulus deterioration. One can observe in the ISM plots in Figure 59 that there was a noticeable deterioration of each pavement structure's ability to resist deformation under the FWD loading with increased levels of traffic. This is indicative of a change in the pavement structure's stiffness/strength. This could be due to elastic shakedown of the structure under initial loading or possibly due to contributions from plastic deformation. Werkmeister et al. (2001) provide an overview of shakedown theory. This includes an initial elastic response followed by an elastic shakedown phase consisting of elastic settlement of the granular layers, which is proceeded by a plastic shakedown phase where the structure displays a steady-state, purely elastic, resilient response and concludes with an incremental collapse and ratcheting phase where plastic strains accumulate rapidly due to the mobilization of shear planes. Based on the rutting and ISM histories from this study, it seems that there was a rapid transition from the elastic phase to the incremental collapse phase at very low pass levels.

Furthermore, at a certain point in almost all the test items, there seems to be a hardening that occurs where the ISM levels off to a steady state value. While at first glance, it may appear that this could correspond to the plastic shakedown phase described above, it must be distinguished from this due to the high level of accumulated rutting occurring in the structure. To clarify,

"hardening" in this sense is referring to the strain hardening that occurs in the plastic regime during the incremental collapse and ratcheting phase in shakedown theory. Beyond this point, geo-materials reach another kind of steady state condition where there is continuous accumulation of plastic strains with little change in the material modulus (i.e., the ratio of the stress and strain). At this point, the ratcheting behavior from shakedown theory might be described as the "kinematic hardening" of the geo-material under repeated loading. These complex phenomena are typically discarded in conventional pavement performance methodologies. However, it is clear from other data collected (e.g., EPC measurements) that this variation over time must be accounted for in overloaded contingency flexible pavement structures. Consequently, a simple modulus deterioration model (Equation 6) was developed that causes an initial decrease in the upper two layers of the pavement structure followed by a linear hardening of the layer moduli. The current version of this model is a function of the permanent deformation history in the structure where deterioration transitions to hardening upon accumulating a certain level of rutting. This model was calibrated based on the rut-depth history and ISM history plots.

$$E(t) = \begin{cases} E_0[1 - \gamma \log(N)] & when\ \delta_a < \delta_{limit} \\ E_{Steady} & when\ \delta_a \geq \delta_{limit} \end{cases}, \quad (6)$$

where

$E(t)$ = layer modulus as a function of time (N load repetitions) (psi),
E_0 = initial design layer modulus before traffic (psi),
γ = layer modulus decay parameter,
E_{Steady} = steady state layer modulus (psi),
δ_a = current accumulated permanent deformation (in.), and
δ_{limit} = permanent deformation marking transition from deterioration to hardening (in.).

The steady state modulus E_{Steady} is not predefined but is a function of the accumulated permanent deformation δ_{limit} that marks the transition from deterioration to hardening. This transition in permanent deformation must be representative of the behavior observed in the ISM plots and the response measurements in the EPC and rut-depth data. Careful study of all the test item rut-depth histories and ISM plots showed that the limiting permanent deformation for the flexible pavement was approximately 0.6 in. Typically, a sharp bend was observed in both the ISM plots and the

rut-depth histories at this point. The rate of decay characterized by the layer modulus decay parameter γ was calibrated by a sensitivity analysis. Multiple calls were made to the LE response model using a trial section under the FWD load to obtain a feasible relationship between variation of the layer moduli and corresponding ISM.

11.2.5 NonUniform Tire Contact Pressure

Traditional cME methods often assume there is a simplified relationship between the tire load, tire contact pressure, and tire contact area. Of these three tire parameters, the tire load is typically known while the other two require assumptions. First, the contact pressure at the tire-pavement interface is assumed to be equivalent to the inflation pressure inside the tire. Having made this first assumption, a second assumption is then made concerning the estimation of the contact area (namely, that the contact area equals the tire load divided by the inflation pressure). This is a reasonable assumption for conventional pavement design for sustainment and permanent airfields where rutting occurs in the subgrade far from the load. In contingency operations where exceptionally thin pavement structures are encountered, however, there is an increased risk for base failures. Therefore, particular attention must be made to the nonuniform shape of the tire contact pressures. While the inflation pressure is uniform across the entire inside wall of the tire, the contact pressure at the tire-pavement interface is nonuniform in nature. The true shape of the contact pressure distribution is a function of the tire load, inflation pressure, age of the tire, and pavement surface type (among other variables).

A simple method is implemented into the LE response model within the proposed PD model that estimates the P-8 nonuniform contact pressure by assuming the tire interacts with the pavement surface like a rigid circular foundation (Stache and Robinson 2022). This approach assumes that the contact pressure distribution corresponds to high sidewall pressures, characteristic of both aircraft tires and rigid circular foundations (Tielking 1989; Davis and Selvadurai 1996).

While initially this contact pressure distribution is not known, it can be ascertained through inverse analysis such that the contact pressure over the given contact area measured in Figure 24 is statically equivalent to the HVS P-8 tire load (approximately 44,500 lbf). Using this approach, an approximate contact pressure distribution was obtained as shown in Figure 119. It is important to reiterate that the computed contact pressure

distribution shown in Figure 119 is statically equivalent to the load applied to each tire by the HVS. This can be easily confirmed by integrating the contact pressure distribution over the domain of the contact area.

Figure 119. Approximation of nonuniform contact pressure of P-8 tire using the proposed method based on inverse analysis.

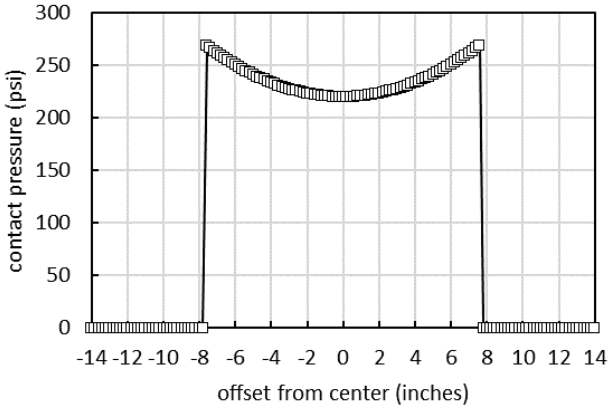

The importance of accurately modeling the contact pressure, particularly for thin flexible pavement structures, is tied to the PD model's mechanistic-empirical process. The formulations described in Equations (1) through (5) above are based on an accurate calculation of the stress state at various points in the pavement structure by the LE response model. Accounting for the nonuniformity of the contact pressure provides more accurate response estimates near surface in the HMA and base layers.

11.2.6 Model Validation Against Measured Test Data

To show the validity of the PD model, comparisons were made between various model outputs and measured field data from the full-scale instrumented tests described in this report. The model was validated against the rut-depth histories of each pavement section, along with the ISM histories and the measured EPC response histories at different depths.

Figure 120 shows comparisons of the rut-depth accumulation with traffic between the proposed PD model predictions and the measurements from the full-scale test sections constructed with the limestone base. Good agreement can be seen throughout with the minor exception of the 2 in. HMA over limestone base with the 10 CBR subgrade. Interestingly, this test item performed nearly the same as the 4 in. HMA over limestone with 10 CBR subgrade. Consequently, this performance was difficult to match closely with the model, because very similar parameters were used

except for the difference in HMA thickness. In general, the PD model performed well in its rut-depth predictive capabilities.

Figure 120. Comparison of rut-depth history between model and full-scale test items.

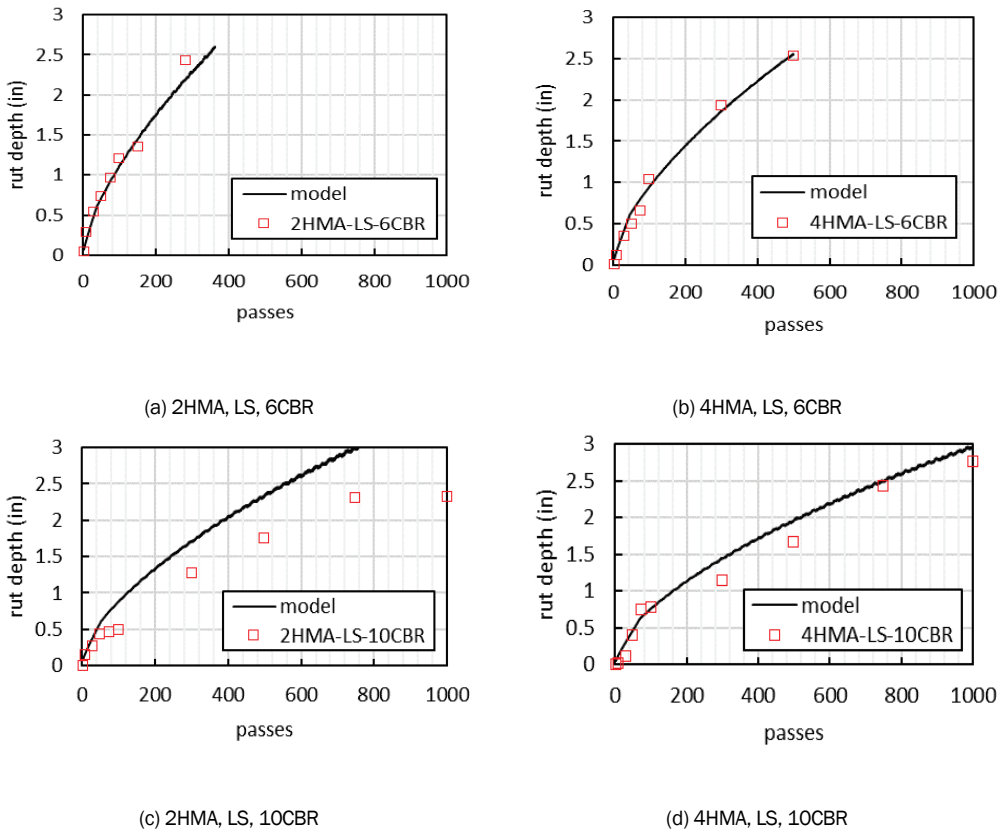

(a) 2HMA, LS, 6CBR

(b) 4HMA, LS, 6CBR

(c) 2HMA, LS, 10CBR

(d) 4HMA, LS, 10CBR

Figure 121 compares model predictions of the vertical stress at the top of the base with those measured by the EPCs in the test sections. Given that the P-8 inflation pressure was 220 psi, the measured vertical stresses 2 in. from the top of the base layer were relatively high. The response model using nonuniform contact pressure approximations coupled with the modulus deterioration model provided reasonable estimates of these measured pressures.

The EPC measurements were reported at each discrete pass level up to 30 passes, and then the maximum EPC measurement was reported over a given interval (e.g., 100 passes, 300 passes, etc.). The first 30 passes show the effects of wander as one of the P-8 tires gets closer to the EPC of interest. Furthermore, beyond 30 passes the effects of modulus deterioration begin to manifest in the form of relatively greater EPC measurements. The PD model seems to account for these two difficult phenomena reasonably well.

Figure 121. Comparison between predicted and measured vertical stress at the top of base.

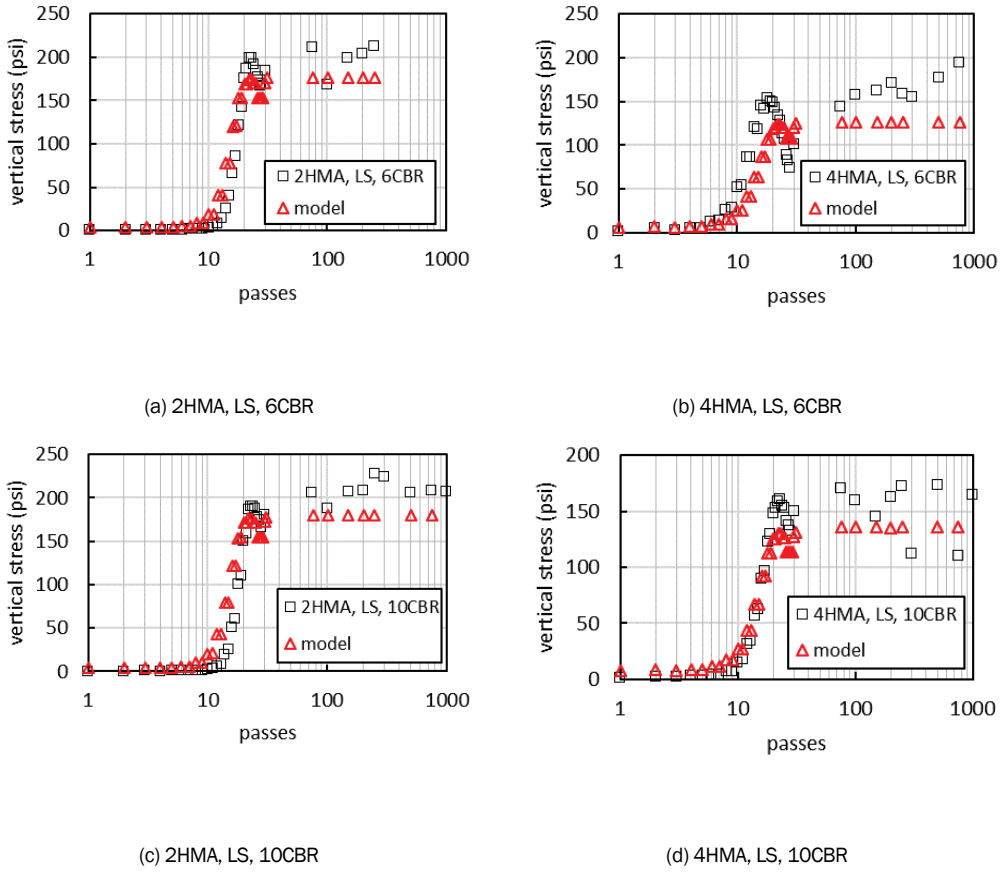

(a) 2HMA, LS, 6CBR

(b) 4HMA, LS, 6CBR

(c) 2HMA, LS, 10CBR

(d) 4HMA, LS, 10CBR

Figure 122 compares model predictions of the vertical stress at middepth of the base with those measured by the EPCs in the test sections. Considering the variability of the material behavior and the complexity of matching stress history with repeated wandering traffic, the PD model does very well at predicting the middepth base EPC measured pressures.

Figure 122. Comparison between predicted and measured vertical stress at middepth of base.

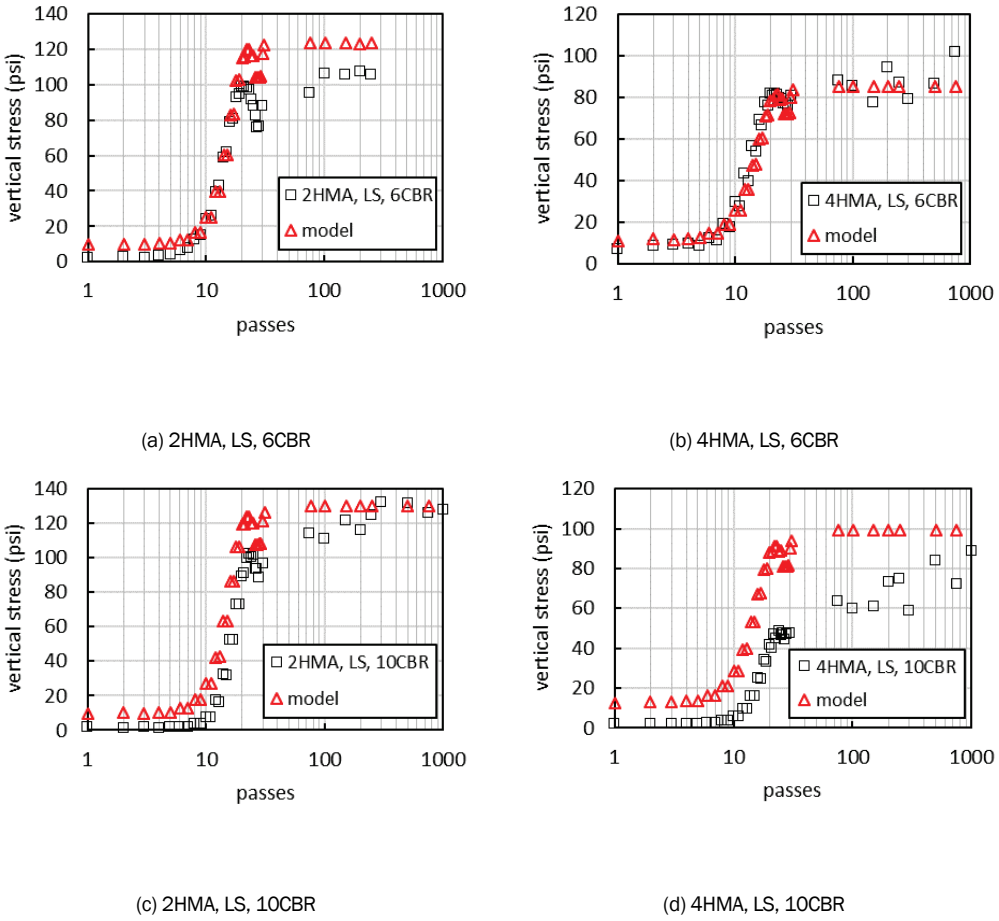

(a) 2HMA, LS, 6CBR

(b) 4HMA, LS, 6CBR

(c) 2HMA, LS, 10CBR

(d) 4HMA, LS, 10CBR

Figure 123 compares model predictions of the vertical stress at the top of the subgrade with those measured by the EPCs in the test sections. It is interesting to note that when originally developing the proposed PD model, estimates of the maximum vertical stress beyond 30 passes were approximately 40 psi using a uniform contact pressure assumption with no inclusion of a modulus deterioration-hardening model. With the inclusion of the modulus deterioration-hardening model and nonuniform contact pressure approximation, the predicted subgrade stresses were significantly closer to those measured in the field. Team members believed that the implementation of these two numerical procedures was instrumental in the overall efficacy of the PD model's predictive capabilities.

Figure 123. Comparison between predicted and measured vertical stress at top of the subgrade.

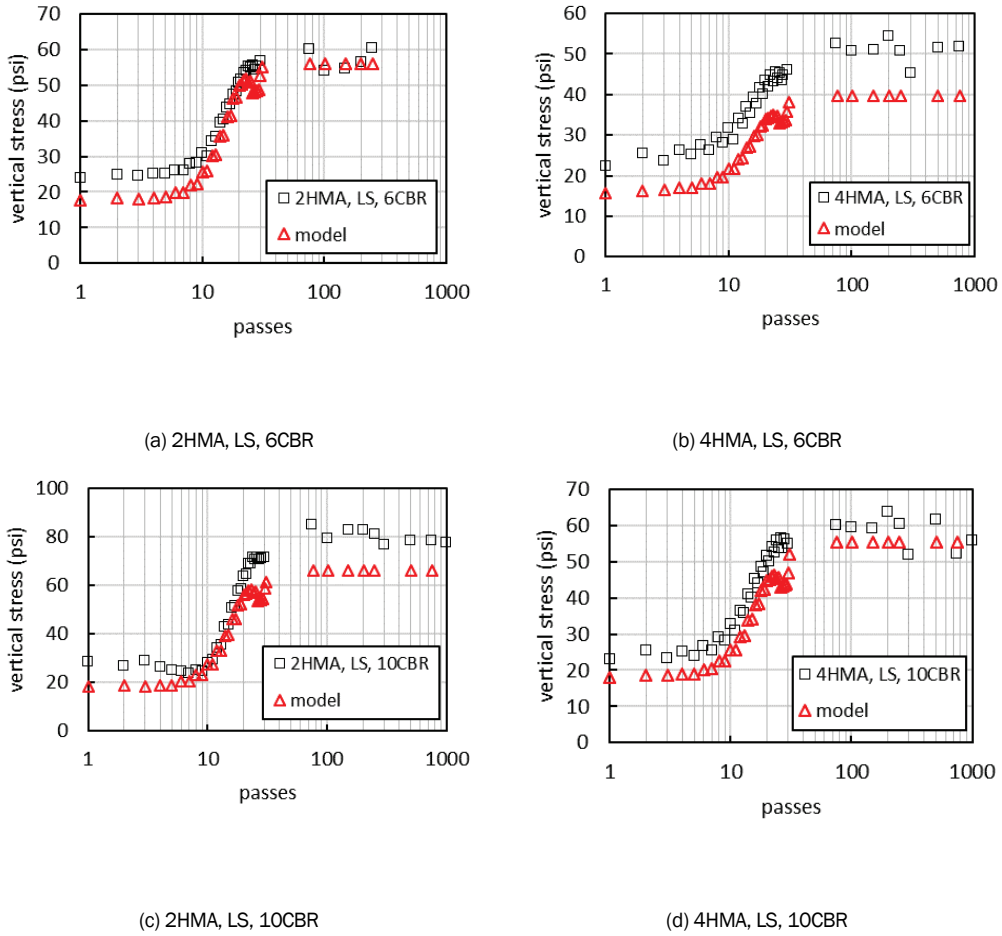

(a) 2HMA, LS, 6CBR

(b) 4HMA, LS, 6CBR

(c) 2HMA, LS, 10CBR

(d) 4HMA, LS, 10CBR

Upon observing the relationship between the rut-depth progression, the EPC measured responses, and the ISM histories, it was apparent that the ability to approximate modulus deterioration and subsequent hardening with repeated load applications was significant. To validate this model, an additional call was made to the LE response model each simulated HVS pass of the P-8 using the FWD load and geometry. During each call to the response model, only the vertical deflection beneath the load was evaluated. This provided an estimate of an ISM using the PD model to compare with the measured ISMs in each test item. Figure 124 shows that the two-part model provides a representative prediction of the true ISM behavior measured in the field tests. More specifically, the bilinear model appears to capture the general trend of modulus deterioration and its corresponding transition to a hardened steady state.

Figure 124. Comparison between model predictions and ISM histories.

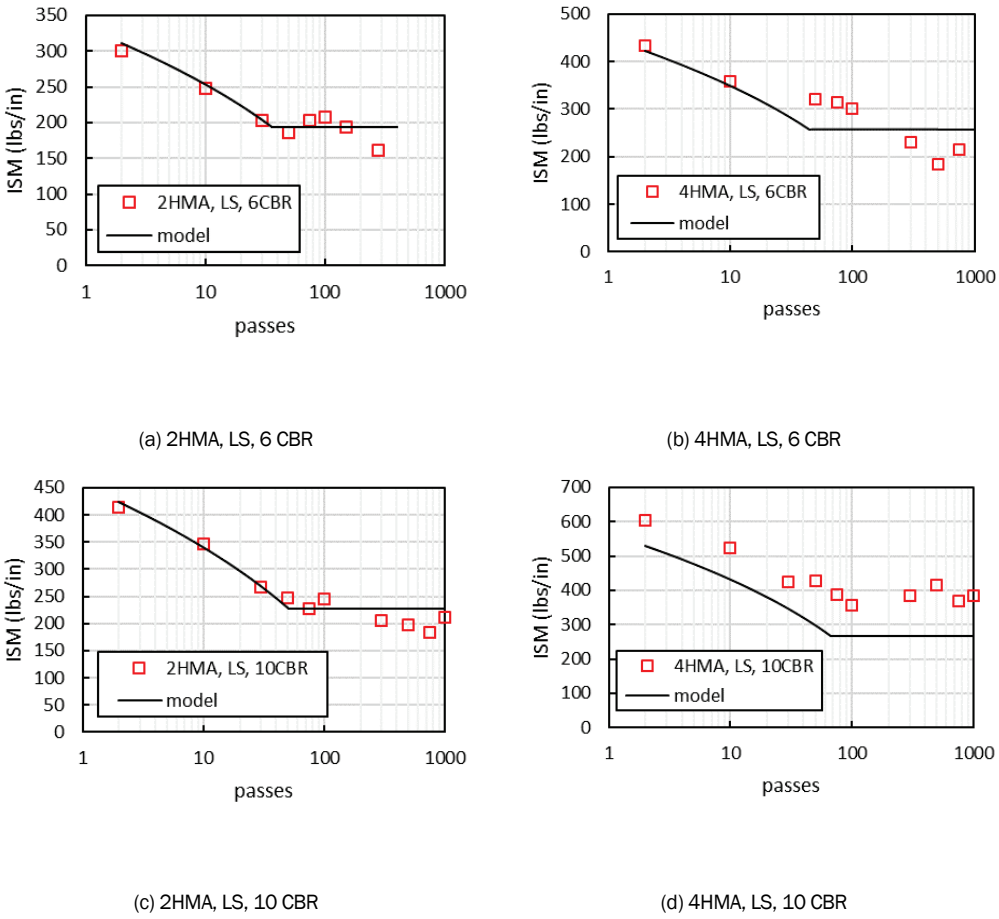

(a) 2HMA, LS, 6 CBR

(b) 4HMA, LS, 6 CBR

(c) 2HMA, LS, 10 CBR

(d) 4HMA, LS, 10 CBR

The parameters in the PD model were required to be calibrated to the local materials used in full-scale testing. The calibration process was conducted against observed material behavior in laboratory and field testing. Once the parameters were calibrated, these parameters remained constant throughout the validation testing against the full-scale instrumented test data. The parameters used for the PD model are provided in Table 25. While it is important to understand that the model still requires exposure to other pavement material types, the parameters used in this study in Table 25 are very close to the global parameters produced by the MEPDG (Witczak and El-Basyouny 2004).

Table 25. Calibrated parameters used in PD model for simulations against full-scale test data.

Parameter	Calibrated Value
Asphalt	
β_1	1.0
β_2	1.2
β_3	1.2
a	0.0006990045
b	1.734
c	0.39937
Unbound	
β_1	2.0
Subgrade	
β_1	1.35

11.2.7 Development of Contingency Flexible Pavement Design Curves

The adequacy of the PD model to predict flexible pavement performance was validated against measured rutting performance and instrumentation response data. Thereafter, the validated PD model was used to predict pavement performance for material properties outside those evaluated in this experiment.

An analysis was conducted to calculate the passes to failure for a variety of material properties including various HMA pavement thicknesses, base course thicknesses, and subgrade CBR values. Separate analyses were conducted for HMA thicknesses of 2 in., 4 in., and 6 in.; these values were representative of HMA thicknesses expected to be realistic for contingency construction efforts. Additionally, a range of subgrade CBR values (4 CBR, 6 CBR, 8 CBR, 10 CBR, and 15 CBR) were analyzed as representative of anticipated subgrade CBR values. Finally, base course thicknesses ranging from a minimum of 4 in. to a maximum of 24 in. were analyzed in 2 in. increments. The calculated passes to failure were used to develop a series of designs curves for each HMA pavement thickness (Figure 125 to Figure 127). **The design curves are based on a minimum 70 CBR base course strength and are valid for expeditionary designs ≤ 1,000 P-8 passes.**

To utilize the design curves, some design parameters should be preselected. First, the HMA thickness should be selected such that the appropriate family of curves is utilized. Additionally, the anticipated or "design" passes to failure should be known. The appropriate design chart is then entered on the *x*-axis (passes to failure) and a vertical line is drawn to intersect the appropriate subgrade CBR value. A horizontal line is then drawn from the intersection of passes-to-failure and subgrade CBR to the *y*-axis (base thickness).

The design charts can be used to determine the impact of changing the HMA thickness on required base course thickness for various subgrade CBR values such that local material availability and cost/construction benefit can be analyzed by the designer.

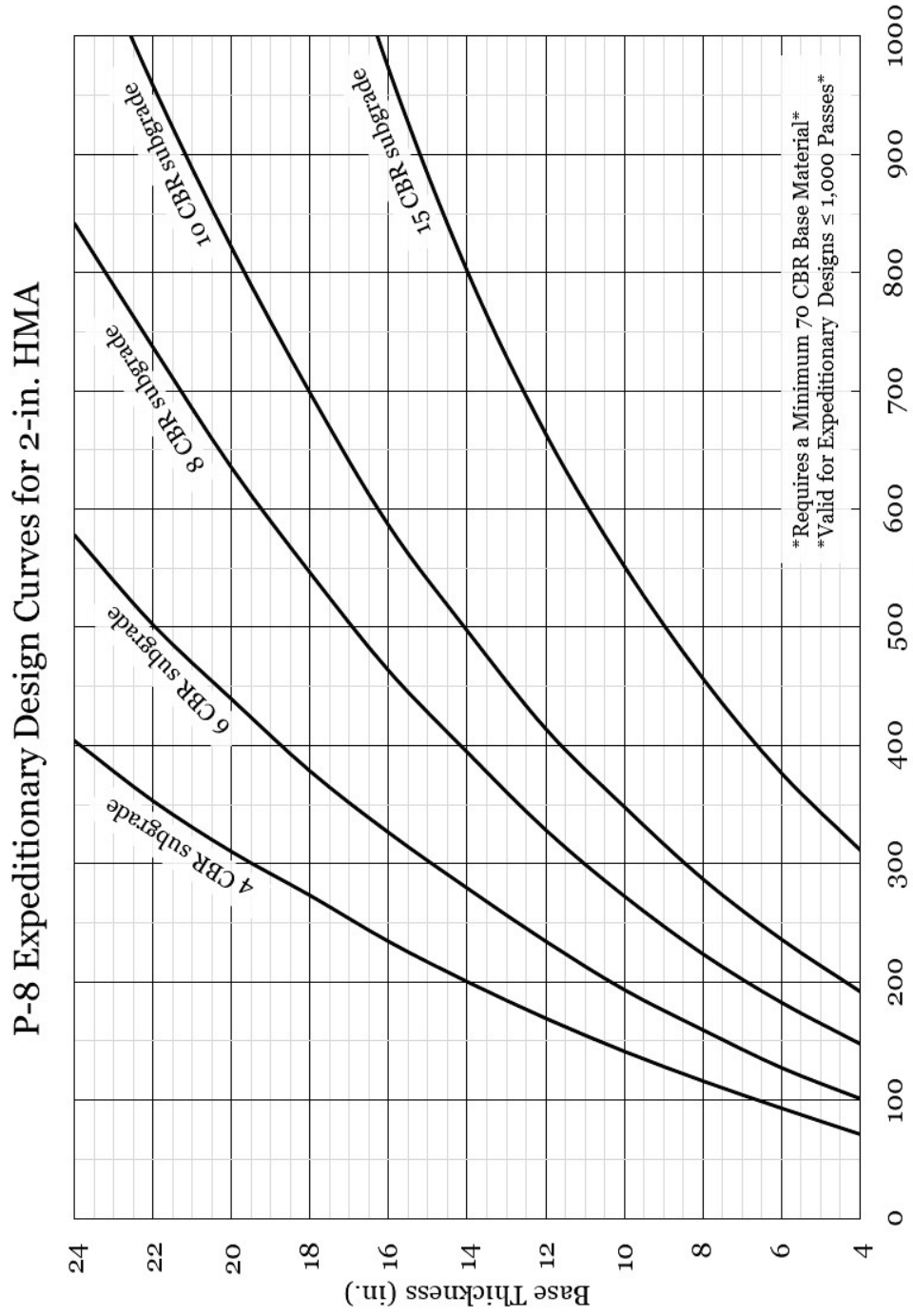

Figure 125. P-8 design curves for 2 in. thick HMA.

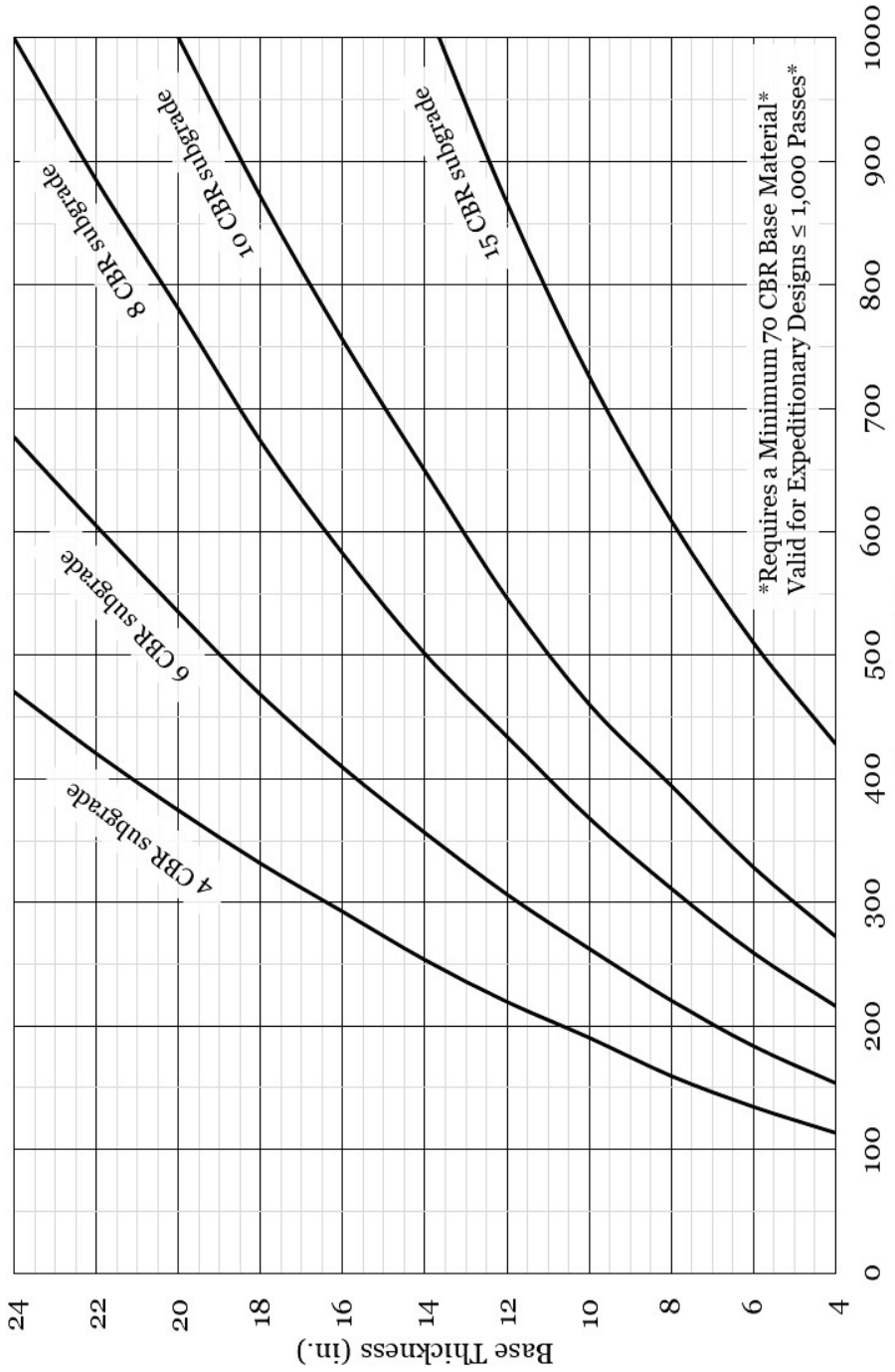

Figure 126. P-8 design curves for 4 in. thick HMA.

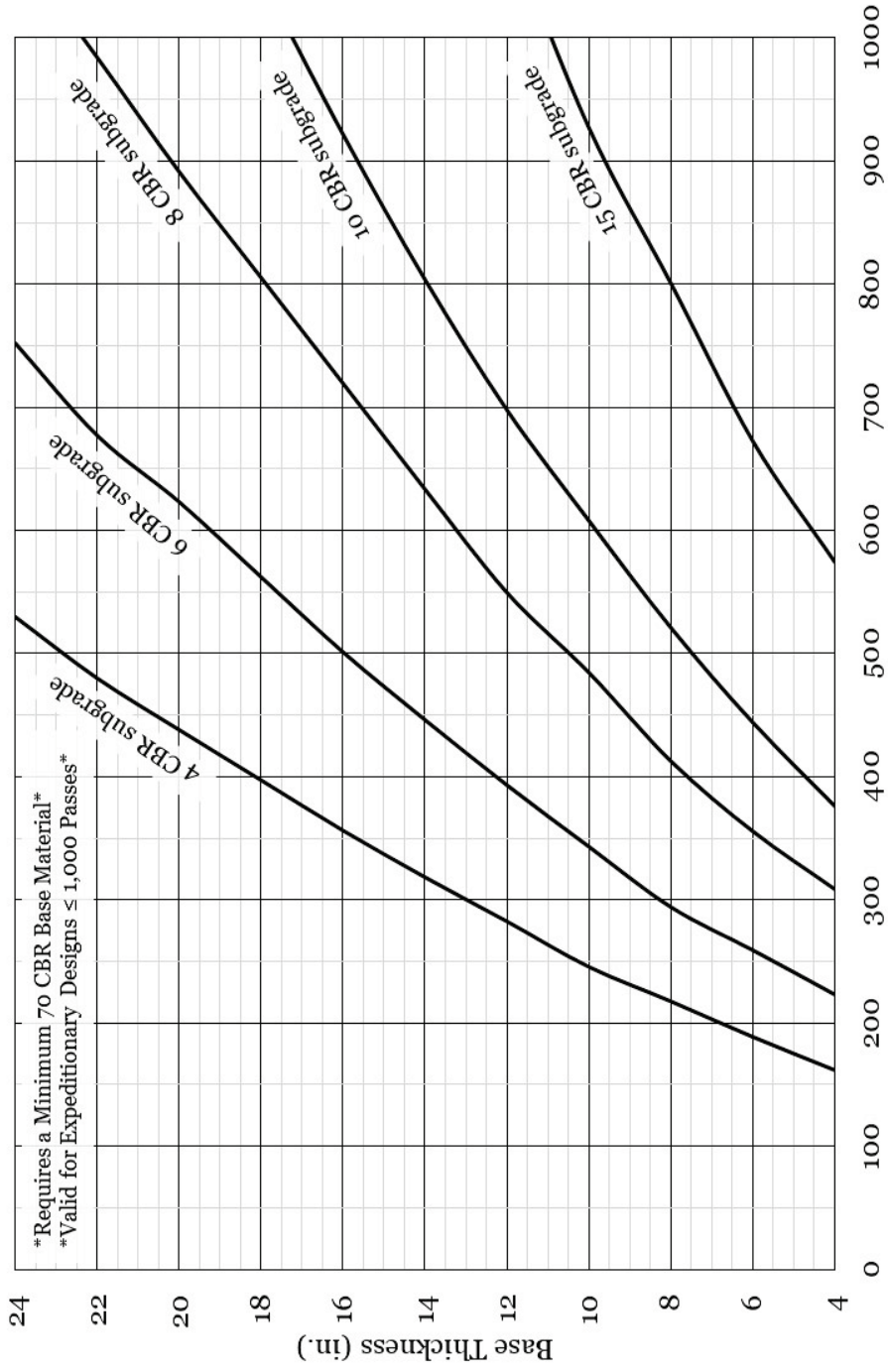

Figure 127. P-8 design curves for 6 in. thick HMA.

The results of the full-traffic test from this experiment were plotted on the design curves and are shown in Figure 128. In general, the data plot to the right of the respective subgrade CBR values. This was expected, because the test items contained a base course CBR exceeding 70 CBR, and more passes to failure would be expected. Further, the data plot near the respective subgrade CBR curves, suggesting that the developed design methodology adequately predicts anticipated performance.

The various design curves can be used to evaluate the impact of changing HMA thickness on the selected base course thickness. Simply, each curve can be entered with the same passes to failure and the same subgrade CBR strength, and a different base course thickness selected. An example is shown in Figure 129. In this case, 500 passes to failure were selected and a subgrade CBR of 9 was selected. For a 2 in. thick HMA layer, a minimum 15 in. thick base course is required. For a 4 in. thick HMA layer, a minimum 12 in. thick base course is required, and for a 6 in. thick HMA layer, a 9 in. thick base course is required. Thus, in the case of the parameters selected for the example, an additional 2 in. of HMA results in an approximate 3 in. reduction in base course thickness.

Figure 128. Results of APT experiment in relation to design curves.

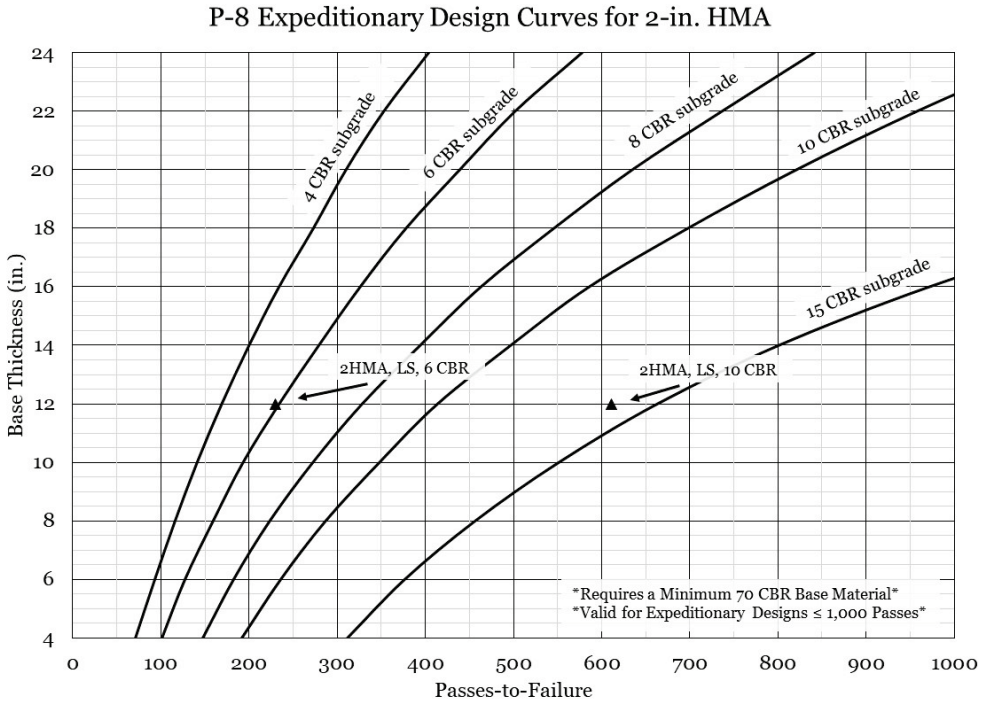

(a) APT results for 2 in. thick HMA

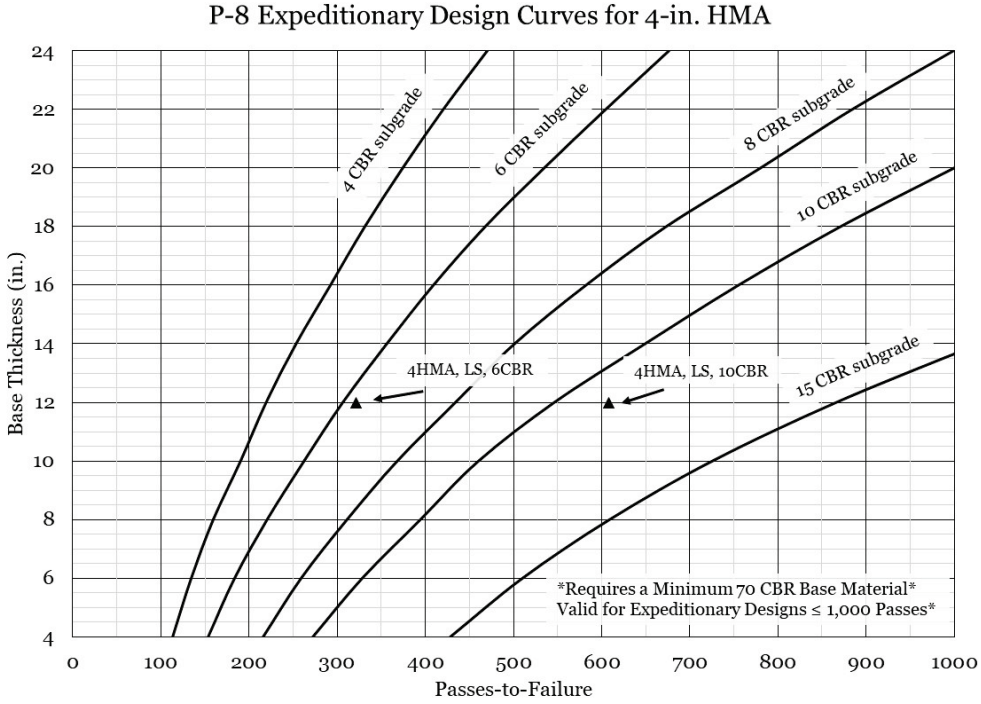

(b) APT results for 4 in. thick HMA

Figure 129. Impact of varying HMA thickness on selected base course thickness.

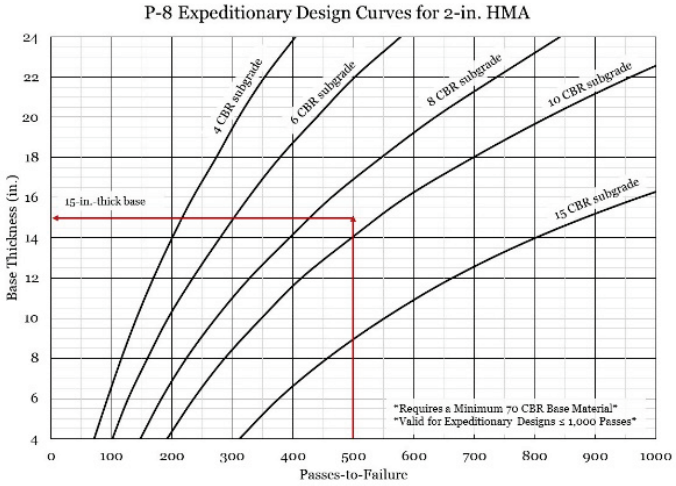

(a) 2 in. HMA base course thickness

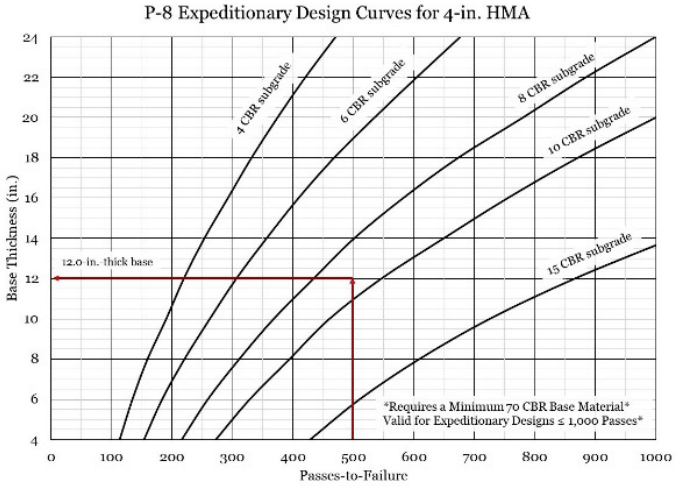

(b) 4 in. HMA base course thickness

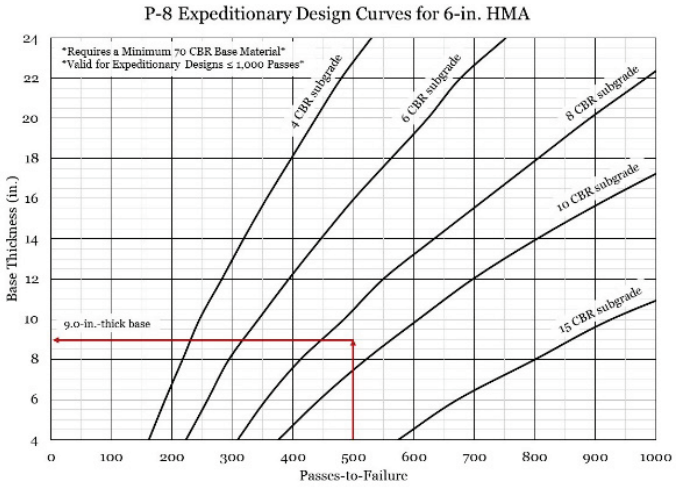

(c) 6 in. HMA base course thickness

12 Summary and Conclusions

A full-scale accelerated pavement test section was constructed with the primary objective of determining minimum thickness requirements for the P-8 Poseidon aircraft for contingency operations (approximately 500 passes). A series of rigid and flexible pavement test items with varying layer thicknesses and material properties were trafficked with ERDC's HVS to provide multiple pass level data points. The results of the experiment yielded the following conclusions:

12.1 Rigid Pavement Test Conclusions

Analysis of the rigid pavement test results yielded the following conclusions for the P-8 aircraft at maximum operational weight:

1. The 8 in. thick PCC sustained 400 passes to the first crack, 2,500 passes to a shattered slab condition, and 7,500 passes to complete failure. The 11 in. thick PCC sustained 50,000 passes with no distress identified. Thus, there was a significant observed performance difference between an 8 in. thick slab thickness and an 11 in. thick slab thickness.
2. Cracking was not observed on the dowelled transverse joint of the 8 in. thick PCC pavement until approximately 7,500 passes compared to 500 passes on the undowelled transverse joint. Thus, rigid pavements with fully dowelled transverse joints would be expected to sustain more passes to failure than rigid pavements with undowelled joints.
3. ISM values in the 8 in. thick PCC tended to decrease with an increase in traffic and observed deterioration (cracking). ISM values in the 11 in. thick PCC remained relatively consistent throughout traffic; this was consistent with the lack of visual deterioration.
4. Subgrade pressure response data trended upward with an increase in traffic in the 8 in. thick PCC, while the subgrade pressure response values in the 11 in. thick PCC were much lower and relatively consistent throughout traffic application. These data suggest that the 11 in. thick PCC was sufficiently thick to limit observed pressure occurring near the top of the subgrade.
5. SSG data tended to show a general increase with increases in traffic; however, limited data were available due to gauge failures early in traffic. Thus, no general trafficking conclusions can be drawn from this data.
6. ESG data in the 8 in. thick PCC trended upward around 300 passes, which was slightly prior to the point at which the first visual crack was

identified. These data suggest that internal deterioration occurred prior to visual confirmation. Increases in ESG response were observed near 1,000 passes in the 11 in. thick PCC; however, a visual inspection did not identify surface cracking at traffic conclusion.

12.2 Minimum Contingency Recommendations for Rigid Pavements

The results of the traffic tests found that existing DoD rigid pavement design criteria is overly conservative—existing criteria overpredicts the required concrete thickness to support P-8 operations. This conservatism becomes more significant for design of rigid pavements for contingency operations. Thus, it is recommended that the minimum contingency rigid pavement cross section meet the requirements shown in Figure 130. The recommended cross section and material properties are based on observations made during the full-scale traffic tests. Further, engineering judgment was used to reduce material strength requirements for contingency requirements below that required in standard airfield pavement design. Thus, materials not meeting the minimum thickness and strength properties recommended herein would be expected to sustain a reduced number of P-8 operations.

Figure 130. Minimum rigid pavement layer thickness for contingency operations.

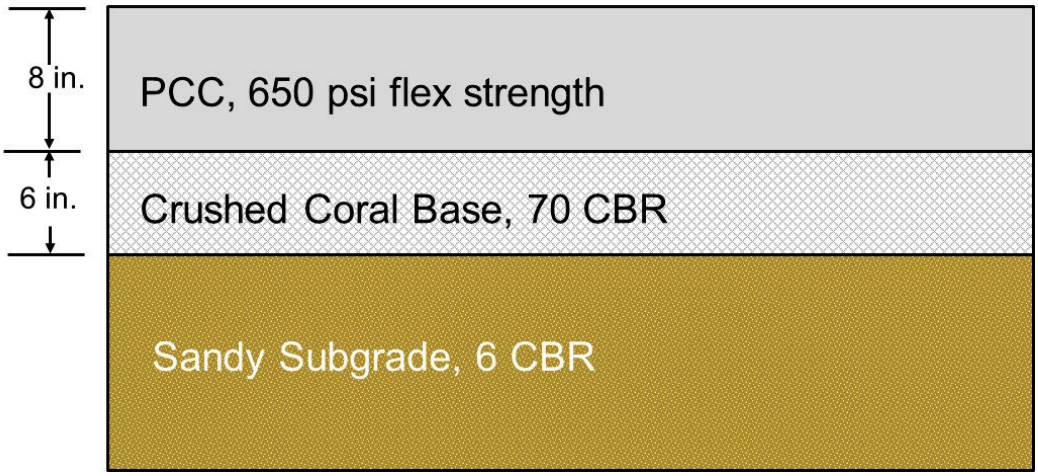

12.3 Flexible Pavement Test Conclusions

Analysis of the flexible pavement test results yielded the following conclusions for the P-8 aircraft at maximum operational weight:

1. Rutting performance data indicated that a competent base layer is required to sustain a reasonable number of P-8 operations. Further,

increased HMA thickness tended to improve rutting performance on a weaker subgrade. On a stiffer subgrade, rutting performance was less sensitive to HMA thickness for the small range of asphalt thickness examined in this study.

2. Initial ISM values were generally capable of identifying differences among the various test items. However, ISM values tended to converge with increased trafficking, except for the 4 in. thick HMA over LS over 10 CBR test item. These data indicated that a minimum 4 in. thick HMA layer over a competent base and a relatively stiff subgrade are required to support a meaningful number of P-8 operations.
3. Subgrade vertical pressure response measurements indicated that an increase in HMA thickness resulted in a reduction in measured vertical pressure. Similarly, inclusion of a competent base layer resulted in reductions in measured subgrade vertical pressure response.
4. The top of base vertical pressure response data indicated that in the 2 in. thick HMA section measured vertical pressure was less in the case of a 10 CBR subgrade. A comparison of the 4 in. thick HMA top of base vertical pressure response data indicated that average measured vertical pressure was statistically equivalent suggesting that subgrade CBR did not have a significant effect on top of base vertical pressure with a thicker HMA layer.
5. Increases in HMA thickness tended to impact middepth measured base vertical pressure response more on the 10 CBR subgrade than the 6 CBR subgrade. An increase in HMA thickness resulted in an average difference of approximately 30 psi on 10 CBR subgrade, compared to an average difference of approximately 6 psi on 6 CBR subgrade.
6. Single-depth deflectometer response data indicated that the largest dynamic and permanent deflections at the subgrade were observed in the gravel base test items, further confirming the importance of a competent aggregate base layer. SDD response data generally followed expected trends; an increase in HMA thickness, increase in base layer strength, or an increase in subgrade CBR resulted in a reduction in both dynamic and permanent subgrade deflection.
7. ASG measurements generally indicated that on a weaker subgrade, an increase in HMA thickness resulted in a decrease in strain values. On a firmer subgrade HMA thickness was not found to have an impact on measured strain values.
8. A forensic investigation of the HMA test items generally confirmed observations made during trafficking. Posttraffic elevation measurements indicated that primary deformation occurred in the

gravel base; however, for the limestone base test items, primary deformation occurred in the subgrade.

12.4 Minimum Contingency Recommendations for Flexible Pavements

The results of the traffic tests found that existing flexible pavement design models were not adequate for contingency pavement performance predictions for the P-8 aircraft. Thus, it is recommended that the minimum contingency flexible pavement cross section meet the requirements shown in Figure 131. These recommendations are based on the results of the full-scale traffic experiments. Further, the traffic results indicated that the performance of a flexible pavement section was highly sensitive to base course strength. Thus, flexible pavements containing base course materials not meeting the minimum strength requirements would be expected to have considerably less passes to failure.

The results of the full-scale flexible pavement experiment were utilized to support an analytical modeling effort to extend flexible pavement thickness recommendations beyond those evaluated. As a result, a series of design curves were developed to allow a designer flexibility in determining pavement thickness recommendations.

Figure 131. Minimum flexible pavement layer thickness for contingency operations.

12.5 ADR Test Conclusions

Analysis of the ADR test results yielded the following conclusions:

1. The ADR repair techniques were found to be generally compatible with a P-8 aircraft except for the FRP surface over a geosynthetic reinforced sand, which sustained only a limited number of aircraft passes.
2. Repairs surfaced with a FRP could sustain a meaningful number of P-8 passes without any observable mat breakage and/or tearing.
3. Cementitious-based repairs could sustain a meaningful number of P-8 passes.
4. The stone and grout surfaced repair exceeded the 500-pass contingency threshold. However, the repair was not capable of sustaining a sustainment level of P-8 passes.

A summary of passes to failure for the ADR repair techniques is shown in Table 26.

Table 26. ADR passes to failure.

Repair Number	Surface	Backfill	Subgrade	Passes to Failure
1	Fiberglass reinforced panels	Geosynthetic reinforced sand	High plasticity clay (10 CBR)	50
2	Fiberglass reinforced panels	Crushed limestone	High plasticity clay (10 CBR)	600
3	Fiberglass reinforced panels	Cement stabilized sand	High plasticity clay (10 CBR)	3,500*
4	Stone and grout	Compacted debris	High plasticity clay (10 CBR)	2,000
5	Calcium-sulfoaluminate concrete	Compacted debris	High plasticity clay (10 CBR)	3,500*
6	Rapid-setting concrete mix	Flowable fill	High plasticity clay (10 CBR)	3,500*

*Repair technique did not achieve failure; traffic halted at 3,500 passes

References

AASHTO (American Association of State and Highway Transportation Officials). 2012. *Standard Specification for Classification of Soils and Soil-Aggregate Mixtures for Highway Construction Purposes*. AASHTO M 145. Washington, DC: Association of American Highway Transportation Officials (AAHTO).

———. 2016. *Standard Method of Test for Bulk Specific Gravity (Gmb) of Compacted Hot Mix Asphalt (HMA) Using Saturated Surface-Dry Specimens*. AASHTO T 166. Washington, DC: Association of American Highway Transportation Officials (AAHTO).

ASTM (American Society for Testing and Materials). 2009a. *Standard Test Method for CBR (California Bearing Ratio) of Soils in Place*. Designation: D 4429-09a. West Conshohocken, PA: ASTM International.

———. 2009b. *Standard Test Method for Air Content of Freshly Mixed Concrete by the Pressure Method*. Designation: C 231-09a. West Conshohocken, PA: ASTM International.

———. 2012. *Standard Test Methods for Laboratory Compaction Characteristics of Soil Using Modified Effort (56,000 ftblf/ft3 [2,700 kN-m/m3])*. Designation: D 1557-12e1. West Conshohocken, PA: ASTM International.

———. 2016. *Standard Test Method for California Bearing Ratio (CBR) of Laboratory-Compacted Soils*. Designation: D 1883-16. West Conshohocken, PA: ASTM International.

———. 2017a. *Standard Practice for Classification of Soils for Engineering Purposes (Unified Soil Classification System)*. Designation: D 2487-17. West Conshohocken, PA: ASTM International.

———. 2017b. *Standard Test Methods for In-Place Density and Water Content of Soil and Soil-Aggregate by Nuclear Methods (Shallow Depth)*. Designation: D 6938-17a. West Conshohocken, PA: ASTM International.

———. 2017c. *Standard Test Methods for Liquid Limit, Plastic Limit, and Plasticity Index of Soils*. Designation: D4318-17c1. West Conshohocken, PA: ASTM International.

———. 2017d. *Standard Test Method for Determination of Water Content of Soil and Rock by Microwave Oven Heating*. Designation: D4643-17. West Conshohocken, PA: ASTM International.

———. 2017e. *Standard Test Method for Temperature of Freshly Mixed Hydraulic-Cement Concrete*. Designation: C 1064/1064M-17. West Conshohocken, PA: ASTM International.

———. 2018. *Standard Test Method for Use of the Dynamic Cone Penetrometer in Shallow Pavement Applications*. Designation: D 6951/6951M-18. West Conshohocken, PA: ASTM International.

———. 2019. *Standard Test Methods for Laboratory Determination of Water (Moisture) Content of Soil and Rock by Mass*. Designation: D 2216-19. West Conshohocken, PA: ASTM International.

———. 2020. *Standard Test Method for Slump of Hydraulic-Cement Concrete*. Designation: C 143/143M-20. West Conshohocken, PA: ASTM International.

———. 2021a. *Standard Test Method for Compressive Strength of Cylindrical Concrete Specimens*. Designation: C 39/39M-21. West Conshohocken, PA: ASTM International.

———. 2021b. *Standard Test Method for Flexural Strength of Concrete (Using Simple Bean with Third-Point Loading)*. Designation: C 78/78M-21. West Conshohocken, PA: ASTM International.

Bell, H. P., B. C. Cox, L. Edwards, L. I. Garcia, N. R. Hoffman, M. Mejias-Santiago, and J. L. Johnson. 2019. *Rapid Airfield Damage Recovery Technology Integration Experiment*. ERDC TR-19-8. Vicksburg, MS; US Army Engineer Research and Development Center.

Carruth, W. D. 2020. *Full-Scale Testing of Commercially Available Cementitious Backfill and Surface Capping Materials for Crater Repairs*. ERDC/GSL TR-20-17. Vicksburg, MS: US Army Engineer Research and Development Center.

Davis, R. O., and A. P. Selvadurai. 1996. *Elasticity and Geomechanics*. Cambridge University Press.

Foster, C. R., and C. D. Burns. 1952. *Development of Tentative CBR Design Curves for Landing Mats*. MP-4-29. Vicksburg, MS: US Army Engineer Waterways Experiment Station.

Hammitt, G. M., and W. Aspinall. 1970. *Thickness Requirements for Unsurfaced Roads and Airfields*. Technical Report S-70-5. Vicksburg, MS: US Army Engineer Waterways Experiment Station.

Robinson, W. J. 2021. Evaluation of the "Effect of Aircraft Tire Inflation Pressure on Thin Asphalt Pavements." *Transportation Research Record: Journal of the Transportation Research Board* 2675(10):986-999.

Rollings, R. S. 1988. *Design of Overlays for Rigid Airport Pavements*. DOT/FAA/PM-87/19. Vicksburg, MS: US Army Engineer Waterways Experiment Station.

Stache, J. M., and W. J. Robinson. 2022. "Effects of Nonuniform Tire Contact Pressures on Near-Surface Pavement Response." *Journal of Transportation Engineering, Part B: Pavements, ASCE* 148(1) 04021077.

Thompson, A. B., and C. D. Burns. 1960. *Criteria for Designing Runways to be Surfaced with Landing Mat and Membrane-Type Materials*. Technical Report 3-539. Vicksburg, MS: US Army Engineer Waterways Experiment Station.

Tielking, J. T. 1989. *Aircraft Tire/Pavement Pressure Distribution*. College Station, TX: Texas Transportation Institute.

USACE (US Army Corps of Engineers). 2001. *Pavement Design for Airfields*. Unified Facilities Criteria 3-260-02. Washington, DC: Department of Defense.

Webster, S. L., R. W. Brown, and J. R. Porter. 1994. *Force Projection Site Evaluation Using the Electrical Cone Penetrometer (ECPO) and the Dynamic Cone Penetrometer (DCP)*. Technical Report GL-94-17. Vicksburg, MS: US Army Engineer Waterways Experiment Station.

Webster, S. L., R. H. Grau, and T. P. Williams. 1992. *Description and Application of Dual-Mass Dynamic Cone Penetrometer*. Instruction Report GL 92-3. Vicksburg, MS: US Army Engineer Waterways Experiment Station.

Werkmeister, S., A. R. Dawson, and F. Wellner. 2001. "Permanent Deformation Behavior of Granular Materials and the Shakedown Concept." *Transportation Research Record: Journal of the Transportation Research Board* 1757(1):75–81.

Witczak, M. W., and M. M. El-Basyouny. 2004. Mechanistic-Empirical Pavement Design Guide. *Appendix GG-1: Calibration of Permanent Deformation Models for Flexible Pavements. Guide for Mechanistic–Empirical Design of New and Rehabilitated Pavement Structures*. Washington, DC: AASHTO.

Appendix A: 8 in. Thick PCC Data

Table A-1. Pretest HWD data.

Location		Load (lbf)	Deflection (mils)							ISM (kips/in.)
X (ft.)	Y (ft.)		D1	D2	D3	D4	D5	D6	D7	
1.5	18.5	38,998	38.32	32.19	26.59	21.95	18.10	14.32	11.5	1018
10.0	18.5	40,060	18.54	16.76	14.41	12.40	11.63	9.00	7.63	2161
19.3	18.5	40,071	22.58	21.74	17.65	14.41	11.76	9.35	7.59	1775
20.8	18.5	40,071	23.65	20.35	16.66	13.72	11.88	8.99	7.44	1694
30.0	18.5	40,214	18.80	17.02	14.47	12.24	11.02	8.75	7.52	2139
39.3	18.5	38,932	33.52	20.22	15.54	11.91	10.19	7.06	5.50	1161
40.8	18.5	39,293	33.57	26.48	20.55	15.96	12.55	9.64	7.63	1170
50.0	18.5	40,279	18.89	16.72	13.99	11.88	11.08	8.50	7.14	2132
59.3	18.5	39,885	27.28	27.10	20.67	16.06	12.88	9.71	7.66	1462
1.5	11.5	39,381	34.02	27.83	21.96	17.06	13.70	10.28	8.26	1158
10.0	11.5	39,951	19.84	17.63	14.63	11.84	9.72	7.74	6.51	2014
19.3	11.5	38,779	21.59	20.44	16.11	12.58	10.14	7.68	6.46	1796
20.8	11.5	40,082	22.40	19.56	15.69	12.32	9.69	7.64	6.59	1789
30.0	11.5	40,301	20.50	18.28	15.05	12.02	9.66	7.41	6.35	1966
39.3	11.5	19,389	16.51	14.44	6.82	5.21	4.07	3.16	2.64	1174
40.8	11.5	19,061	18.77	13.65	9.70	6.81	5.50	3.75	3.03	1016
50.0	11.5	40,006	21.30	18.69	14.98	11.78	9.43	7.48	6.15	1878
59.3	11.5	40,038	22.78	22.44	17.07	12.82	9.88	7.89	6.50	1758
1.5	4.0	38,001	41.75	34.41	27.38	21.44	16.78	12.65	9.99	910
10.0	4.0	39,293	21.04	19.33	16.53	13.77	11.72	9.31	7.72	1868
19.3	4.0	40,060	22.56	20.85	17.52	14.33	11.83	9.27	7.72	1776
20.8	4.0	40,115	22.94	20.95	17.68	14.36	11.98	9.31	7.86	1749
30.0	4.0	39,819	24.33	22.05	18.55	15.31	12.81	9.84	7.93	1637
39.3	4.0	38,658	37.10	31.71	23.00	17.31	13.19	9.96	8.00	1042
40.8	4.0	38,570	36.25	28.87	22.07	16.63	13.03	9.77	7.93	1064
50.0	4.0	39,984	22.74	20.61	17.37	14.31	11.81	9.28	7.65	1758
59.3	4.0	39,480	29.46	29.84	22.56	17.28	13.5	10.37	8.35	1340

Table A-2. Posttest HWD data.

Location		Load (lbf)	Deflection (mils)							ISM (kips/in.)
X (ft.)	Y (ft.)		D1	D2	D3	D4	D5	D6	D7	
1.5	18.5	46,173	51.10	42.42	34.36	27.57	22.47	17.29	13.84	1018
10.0	18.5	48,298	27.05	24.92	21.51	18.18	15.72	12.24	10.11	2161
19.3	18.5	46,699	41.98	38.81	28.22	20.36	15.78	10.56	7.83	1775
20.8	18.5	46,436	38.66	30.43	23.00	17.28	13.32	9.38	7.28	1694
30.0	18.5	47,652	28.15	29.01	26.61	20.25	14.94	10.88	8.48	2139
39.3	18.5	46,907	41.56	38.04	29.46	21.01	14.85	9.91	7.06	1161
40.8	18.5	46,491	54.25	41.66	30.26	21.08	15.32	9.59	6.65	1170
50.0	18.5	48,429	26.40	23.21	18.97	15.15	12.53	9.42	7.94	2132
59.3	18.5	45,735	47.63	53.53	40.82	30.01	22.61	15.74	10.95	1462
1.5	11.5	45,614	54.10	42.53	32.39	24.42	18.83	14.00	11.02	1158
10.0	11.5	48,254	24.91	23.39	19.07	15.53	13.07	9.95	8.02	2014
19.3	11.5	46,326	43.01	43.46	33.03	22.62	15.56	10.45	8.40	1796
20.8	11.5	46,370	54.25	43.04	30.28	19.94	13.21	9.81	8.52	1789
30.0	11.5	45,647	53.70	45.89	34.09	23.88	16.05	11.20	9.12	1966
39.3	11.5	45,472	54.79	53.16	33.93	19.98	13.51	10.07	8.21	1174
40.8	11.5	45,264	52.31	42.89	30.50	20.32	13.78	9.78	8.12	1016
50.0	11.5	45,965	47.71	36.24	25.18	16.75	12.90	10.07	8.49	1878
59.3	11.5	47,060	34.41	32.81	23.88	17.35	13.18	10.05	8.18	1758
1.5	4.0	45,625	57.82	47.29	37.67	29.37	23.50	17.51	13.96	910
10.0	4.0	47,455	27.21	25.05	21.84	18.42	15.52	12.07	9.94	1868
19.3	4.0	46,994	40.98	55.25	30.82	23.23	17.90	13.15	10.71	1776
20.8	4.0	46,994	38.63	32.54	26.00	20.12	16.22	11.70	9.41	1749
30.0	4.0	46,337	49.70	53.04	36.39	28.03	21.65	15.22	10.73	1637
39.3	4.0	45,154	60.03	46.47	31.22	21.69	16.81	12.33	9.67	1042
40.8	4.0	46,512	44.92	37.73	28.39	20.62	15.17	10.77	9.09	1064
50.0	4.0	46,983	39.98	32.79	25.08	18.93	15.07	10.81	8.48	1758
59.3	4.0	38,417	33.63	33.03	24.74	18.57	14.40	10.79	8.52	1340

Table A-3. Total crack length with passes.

Cumulative Passes	Crack Length (ft)
500	13.2
546	24.6
650	26.7
750	42.3
1000	43.8
2000	62.5
3000	107.1
5000	133.9
7500	193.5
10000	301.2
3000	107.1

Table A-4. FWD data at pass 0.

Pass	Sta.	Condition	Load	D0	D1	D2	D3	D4	D5	D6	ISM
0	20.1	X-Joint	23,140	13.16	12.09	9.57	7.51	6.11	4.62	3.94	1758
0	20.2	Joint	23,097	13.58	11.35	9.19	7.31	6.00	4.63	3.38	1701
0	30.1	Mid	23,086	12.17	10.66	8.86	7.15	6.04	4.52	2.63	1897
0	30.2	Mid	23,064	12.29	10.72	8.88	7.06	5.99	4.44	3.12	1877
0	30.3	Mid	23,042	12.13	10.79	8.82	7.01	5.86	4.45	3.51	1900
0	40.1	X-Joint	22,539	21.09	12.15	9.02	6.68	5.30	3.91	3.73	1069
0	40.2	Joint	22,736	21.22	15.66	11.33	8.20	6.37	4.61	3.31	1071
0	45	Quarter	22,998	12.34	10.74	8.67	6.93	5.67	4.31	3.50	1864

Note: Sta. = station, Load = lbf, D*n* = mils, ISM = impulse stiffness modulus (kips/in.)

Table A-5. FWD data at pass 1.

Pass	Sta.	Condition	Load	D0	D1	D2	D3	D4	D5	D6	ISM
1	20.1	X-Joint	22,911	13.74	12.46	9.84	7.68	6.25	4.72	4.00	1667
1	20.2	Joint	22,878	13.47	11.74	9.41	7.42	6.11	4.67	3.78	1698
1	30.1	Mid	22,867	12.09	10.77	8.96	7.22	6.04	4.59	3.56	1891
1	30.2	Mid	22,867	12.07	10.73	8.96	7.19	5.95	4.57	3.82	1895
1	30.3	Mid	22,889	12.27	10.81	8.90	7.13	5.94	4.56	3.53	1865
1	40.1	X-Joint	22,342	23.40	11.89	8.73	6.50	5.31	3.96	3.72	955
1	40.2	Joint	22,462	19.93	15.06	10.99	8.06	6.34	4.61	3.69	1127
1	45	Quarter	22,790	12.54	10.84	8.83	7.02	5.77	4.41	3.15	1817

Note: Sta. = station, Load = lbf, D*n* = mils, ISM = impulse stiffness modulus (kips/in.)

Table A-6. FWD data at pass 10.

Pass	Sta.	Condition	Load	D0	D1	D2	D3	D4	D5	D6	ISM
10	20.1	X-Joint	23,031	14.04	12.48	9.84	7.67	6.26	4.68	3.66	1640
10	20.2	Joint	23,107	13.50	11.64	9.51	7.41	6.13	4.70	3.21	1712
10	30.1	Mid	23,129	12.18	10.80	9.02	7.29	6.14	4.56	2.72	1899
10	30.2	Mid	23,195	12.26	10.96	9.08	7.24	6.02	4.39	3.43	1892
10	30.3	Mid	23,009	12.21	10.94	8.94	7.10	5.79	4.45	4.31	1884
10	40.1	X-Joint	22,692	25.56	12.03	8.89	6.56	5.19	3.89	3.51	888
10	40.2	Joint	22,659	22.61	16.84	12.18	8.68	6.73	4.93	2.34	1002
10	45	Quarter	22,943	12.97	10.94	8.89	6.99	5.81	4.36	2.96	1769

Note: Sta. = station, Load = lbf, D*n* = mils, ISM = impulse stiffness modulus (kips/in.)

Table A-7. FWD data at pass 30.

Pass	Sta.	Condition	Load	D0	D1	D2	D3	D4	D5	D6	ISM
30	20.1	X-Joint	22,911	15.17	13.24	10.30	7.89	6.39	4.77	3.91	1510
30	20.2	Joint	22,998	14.44	12.21	9.79	7.64	6.27	4.75	3.44	1593
30	30.1	Mid	22,987	12.37	11.04	9.16	7.41	6.20	4.58	3.61	1858
30	30.2	Mid	22,922	12.56	11.08	9.16	7.35	6.01	4.46	3.82	1825
30	30.3	Mid	22,922	12.44	11.11	9.15	7.28	5.94	4.52	3.98	1843
30	40.1	X-Joint	22,615	24.43	10.72	8.06	6.11	4.84	3.74	3.04	926
30	40.2	Joint	22,451	25.55	18.71	13.28	9.42	7.19	5.15	2.80	879
30	45	Quarter	22,812	12.83	11.17	9.04	7.13	5.89	4.48	3.47	1778

Note: Sta. = station, Load = lbf, D*n* = mils, ISM = impulse stiffness modulus (kips/in.)

Table A-8. FWD data at pass 50.

Pass	Sta.	Condition	Load	D0	D1	D2	D3	D4	D5	D6	ISM
50	20.1	X-Joint	22,812	15.00	13.43	10.43	8.02	6.46	4.83	4.16	1521
50	20.2	Joint	22,801	14.45	12.31	9.85	7.72	6.30	4.83	3.44	1578
50	30.1	Mid	22,823	12.65	11.07	9.20	7.50	6.24	4.70	3.95	1804
50	30.2	Mid	22,801	12.42	11.15	9.26	7.40	6.14	4.56	3.67	1836
50	30.3	Mid	22,856	12.48	11.34	9.22	7.36	6.02	4.54	4.13	1831
50	40.1	X-Joint	22,517	26.92	10.20	7.52	5.74	4.79	3.67	2.92	836
50	40.2	Joint	22,397	24.85	18.65	13.31	9.44	7.29	5.18	2.59	901
50	45	Quarter	22,747	12.99	11.31	9.10	7.20	5.93	4.52	3.57	1751

Note: Sta. = station, Load = lbf, D*n* = mils, ISM = impulse stiffness modulus (kips/in.)

Table A-9. FWD data at pass 75.

Pass	Sta.	Condition	Load	D0	D1	D2	D3	D4	D5	D6	ISM
75	20.1	X-Joint	22,779	14.20	13.24	10.34	7.97	6.44	4.79	3.93	1604
75	20.2	Joint	22,758	14.80	12.46	9.87	7.69	6.28	4.79	3.59	1538
75	30.1	Mid	22,725	12.93	11.01	9.13	7.37	6.13	4.63	3.80	1758
75	30.2	Mid	22,801	12.40	11.07	9.16	7.31	6.09	4.59	3.78	1839
75	30.3	Mid	22,801	12.42	11.07	9.14	7.28	6.02	4.61	3.91	1836
75	40.1	X-Joint	22,440	23.77	10.54	7.94	6.00	4.87	3.78	3.13	944
75	40.2	Joint	22,309	23.98	18.07	12.89	9.20	7.10	5.07	2.82	930
75	45	Quarter	22,670	12.86	11.23	9.00	7.12	5.89	4.47	3.65	1763

Note: Sta. = station, Load = lbf, D*n* = mils, ISM = impulse stiffness modulus (kips/in.)

Table A-10. FWD data at pass 100.

Pass	Sta.	Condition	Load	D0	D1	D2	D3	D4	D5	D6	ISM
100	20.1	X-Joint	22,615	15.60	13.71	10.54	8.02	6.47	4.84	3.90	1450
100	20.2	Joint	22,604	15.96	12.61	9.96	7.74	6.31	4.77	3.83	1416
100	30.1	Mid	22,725	12.46	11.10	9.23	7.48	6.25	4.66	3.76	1824
100	30.2	Mid	22,736	12.59	11.13	9.25	7.43	6.15	4.60	3.73	1806
100	30.3	Mid	22,714	12.43	11.13	9.19	7.30	6.00	4.63	4.04	1827
100	40.1	X-Joint	22,298	27.37	10.29	7.68	5.82	4.78	3.74	3.21	815
100	40.2	Joint	22,233	24.78	18.44	13.26	9.35	7.17	5.17	2.68	897
100	45	Quarter	22,637	12.96	11.33	9.10	7.20	5.96	4.52	3.72	1747

Note: Sta. = station, Load = lbf, D*n* = mils, ISM = impulse stiffness modulus (kips/in.)

Table A-11. FWD data at pass 300.

Pass	Sta.	Condition	Load	D0	D1	D2	D3	D4	D5	D6	ISM
300	20.1	X-Joint	22,670	15.70	14.13	10.86	8.32	6.65	4.94	3.86	1444
300	20.2	Joint	22,572	15.35	12.82	10.08	7.87	6.39	4.83	4.00	1470
300	30.1	Mid	22,626	12.86	11.28	9.35	7.55	6.30	4.78	3.90	1759
300	30.2	Mid	22,703	12.71	11.32	9.40	7.59	6.26	4.79	3.76	1786
300	30.3	Mid	22,681	13.79	11.37	9.37	7.48	6.14	4.71	4.06	1645
300	40.1	X-Joint	22,178	26.68	15.28	11.07	8.01	6.21	4.49	3.76	831
300	40.2	Joint	22,167	27.06	19.96	14.17	10.07	7.74	5.59	3.48	819
300	45	Quarter	22,550	13.56	11.52	9.26	7.32	6.04	4.58	3.48	1663

Note: Sta. = station, Load = lbf, D*n* = mils, ISM = impulse stiffness modulus (kips/in.)

Table A-12. FWD data at pass 500.

Pass	Sta.	Condition	Load	D0	D1	D2	D3	D4	D5	D6	ISM
500	20.1	X-Joint	23,064	14.97	13.65	10.59	8.09	6.50	4.84	3.98	1541
500	20.2	Joint	23,009	15.94	12.62	9.97	7.74	6.31	4.77	3.68	1443
500	30.1	Mid	23,042	13.21	11.18	9.23	7.44	6.19	4.76	4.09	1744
500	30.2	Mid	23,009	12.61	11.17	9.22	7.42	6.17	4.76	4.30	1825
500	30.3	Mid	22,987	12.57	11.17	9.26	7.46	6.16	4.90	3.73	1829
500	40.1	X-Joint	22,648	25.20	21.30	15.06	10.50	7.84	5.22	4.04	899
500	40.2	Joint	22,451	33.93	24.09	16.69	11.56	8.71	6.13	3.90	662
500	45	Quarter	22,878	13.37	11.33	9.13	7.20	5.95	4.53	3.45	1711

Note: Sta. = station, Load = lbf, D*n* = mils, ISM = impulse stiffness modulus (kips/in.)

Table A-13. FWD data at pass 750.

Pass	Sta.	Condition	Load	D0	D1	D2	D3	D4	D5	D6	ISM
750	20.1	X-Joint	22,790	17.06	14.64	11.14	8.45	6.72	5.05	4.37	1336
750	20.2	Joint	22,834	16.15	13.47	10.50	8.09	6.58	4.96	3.84	1414
750	30.1	Mid	22,911	13.34	11.56	9.51	7.68	6.50	5.12	4.01	1717
750	30.2	Mid	22,900	13.09	11.54	9.55	7.75	6.57	5.11	3.98	1749
750	30.3	Mid	22,856	13.09	11.69	9.72	7.97	6.65	5.05	3.97	1746
750	40.1	X-Joint	22,397	29.61	19.37	11.93	6.65	5.44	4.36	3.76	756
750	40.2	Joint	22,331	28.63	18.92	11.16	8.35	6.78	5.21	2.74	780
750	45	Quarter	22,725	13.54	11.69	9.43	7.46	6.18	4.80	3.61	1678

Note: Sta. = station, Load = lbf, D*n* = mils, ISM = impulse stiffness modulus (kips/in.)

Table A-14. FWD data at pass 1,000.

Pass	Sta.	Condition	Load	D0	D1	D2	D3	D4	D5	D6	ISM
1000	20.1	X-Joint	22,725	16.13	14.48	11.13	8.50	6.76	5.01	3.97	1409
1000	20.2	Joint	22,758	15.54	13.13	10.32	7.98	6.51	4.95	3.90	1464
1000	30.1	Mid	22,758	15.16	11.59	9.60	7.72	6.46	5.20	3.75	1501
1000	30.2	Mid	22,812	13.39	11.55	9.59	7.80	6.61	5.09	4.20	1704
1000	30.3	Mid	22,790	13.19	11.79	9.78	8.04	6.75	5.07	4.20	1728
1000	40.1	X-Joint	22,364	27.26	20.86	12.89	6.77	5.29	4.30	3.54	820
1000	40.2	Joint	22,353	29.41	19.55	11.56	8.60	6.84	5.11	2.81	760
1000	45	Quarter	22,648	13.53	11.86	9.52	7.52	6.22	4.75	3.71	1674

Note: Sta. = station, Load = lbf, D*n* = mils, ISM = impulse stiffness modulus (kips/in.)

Table A-15. FWD data at 3,000 passes.

Pass	Sta.	Condition	Load	D0	D1	D2	D3	D4	D5	D6	ISM
3000	20.1	X-Joint	22,736	18.04	15.84	12.00	8.98	7.09	5.32	4.14	1260
3000	20.2	Joint	22,768	18.19	14.84	11.37	8.69	6.93	5.16	3.71	1252
3000	30.1	Mid	22,812	14.79	13.50	12.12	9.24	7.14	5.14	3.53	1542
3000	30.2	Mid	22,779	15.82	15.88	12.28	8.75	6.63	4.91	4.03	1440
3000	30.3	Mid	22,681	18.72	16.39	11.61	7.97	6.09	4.87	3.96	1212
3000	40.1	X-Joint	22,528	26.96	25.59	15.43	7.89	5.97	4.67	3.57	836
3000	40.2	Joint	22,419	26.78	20.07	13.82	9.55	7.09	4.93	2.65	837
3000	45	Quarter	22,615	19.15	14.85	11.03	8.27	6.70	5.11	3.86	1181

Note: Sta. = station, Load = lbf, D*n* = mils, ISM = impulse stiffness modulus (kips/in.)

Table A-16. FWD data at 5,000 passes.

Pass	Sta.	Condition	Load	D0	D1	D2	D3	D4	D5	D6	ISM
5000	20.1	X-Joint	22,747	19.26	17.07	12.27	8.43	6.80	5.04	4.10	1181
5000	20.2	Joint	22,714	18.71	15.19	11.41	8.60	6.87	5.11	3.81	1214
5000	30.1	Mid	22,670	18.07	14.59	11.35	8.62	6.86	5.19	4.35	1255
5000	30.2	Mid	22,758	16.88	15.98	12.33	8.75	6.65	4.88	3.97	1348
5000	30.3	Mid	22,670	18.77	16.91	11.88	8.16	6.07	4.78	4.03	1208
5000	40.1	X-Joint	22,495	27.03	25.19	15.24	7.84	6.07	4.57	3.55	832
5000	40.2	Joint	22,451	25.15	20.17	14.62	9.91	7.01	4.66	3.61	893
5000	45	Quarter	22,473	22.54	16.39	11.46	8.05	6.35	4.91	3.90	997

Note: Sta. = station, Load = lbf, D*n* = mils, ISM = impulse stiffness modulus (kips/in.)

Table A-17. FWD data at pass 7,500.

Pass	Sta.	Condition	Load	D0	D1	D2	D3	D4	D5	D6	ISM
7500	20.1	X-Joint	22,867	22.25	19.96	13.51	8.20	6.67	4.99	3.99	1028
7500	20.2	Joint	22,834	21.09	16.87	12.10	8.99	7.10	5.17	3.89	1083
7500	30.1	Mid	22,768	21.03	16.53	12.45	9.15	7.13	5.23	3.96	1083
7500	30.2	Mid	22,878	18.37	17.52	13.35	9.28	6.95	5.07	3.99	1245
7500	30.3	Mid	22,801	21.31	18.13	12.64	8.46	6.39	4.79	3.48	1070
7500	40.1	X-Joint	22,648	27.50	26.64	16.22	8.49	6.34	4.73	3.74	824
7500	40.2	Joint	22,594	27.50	21.06	14.92	10.20	7.30	4.85	2.86	822
7500	45	Quarter	22,637	24.30	17.95	12.33	8.20	6.25	4.93	3.30	932

Note: Sta. = station, Load = lbf, D*n* = mils, ISM = impulse stiffness modulus (kips/in.)

Table A-18. FWD data at pass 10,000.

Pass	Sta.	Condition	Load	D0	D1	D2	D3	D4	D5	D6	ISM
10000	20.1	X-Joint	22,648	25.50	22.83	15.20	8.93	6.97	4.88	3.98	888
10000	20.2	Joint	22,550	25.38	19.55	13.81	9.66	7.14	5.04	3.34	888
10000	30.1	Mid	22,517	22.64	17.73	13.57	9.80	7.22	5.29	4.29	995
10000	30.2	Mid	22,637	20.59	19.13	14.22	9.52	7.39	5.42	4.03	1099
10000	30.3	Mid	22,495	23.07	19.33	13.59	9.37	7.12	5.24	4.09	975
10000	40.1	X-Joint	22,473	29.60	26.98	16.65	8.71	6.82	4.92	3.79	759
10000	40.2	Joint	22,386	28.97	21.92	15.26	10.25	7.54	5.15	2.22	773
10000	45	Quarter	22,429	25.83	18.63	12.73	8.35	6.23	4.78	3.18	868

Note: Sta. = station, Load = lbf, D*n* = mils, ISM = impulse stiffness modulus (kips/in.)

Table A-19. FWD data at pass 15,000.

Pass	Sta.	Condition	Load	D0	D1	D2	D3	D4	D5	D6	ISM
15000	20.1	X-Joint	22,495	25.99	25.50	18.03	12.04	8.05	5.33	4.32	866
15000	20.2	Joint	22,408	29.27	23.37	16.32	10.93	7.67	5.17	3.85	766
15000	30.1	Mid	22,309	28.87	24.20	18.19	12.62	9.23	6.42	3.73	773
15000	30.2	Mid	22,375	28.90	24.53	17.83	12.17	9.30	6.34	4.98	774
15000	30.3	Mid	22,331	27.95	23.65	17.27	12.55	9.22	6.42	5.00	799
15000	40.1	X-Joint	22,244	31.68	28.41	18.17	10.48	7.88	5.47	4.28	702
15000	40.2	Joint	22,233	29.07	22.86	16.56	11.20	8.35	5.63	3.55	765
15000	45	Quarter	22,364	24.78	19.13	13.41	8.92	6.74	5.06	4.04	903

Note: Sta. = station, Load = lbf, D*n* = mils, ISM = impulse stiffness modulus (kips/in.)

Table A-20. Earth pressure cell response data.

Pass	Quarter Slab (EP1) (psi)	Midslab (EP2) (psi)
1	7.7	8.2
10	8.4	8.4
30	8.4	8.4
50	8.6	8.5
300	9.2	9.6
500	9.6	9.9
750	10.1	9.9
1000	10.4	10.1
3000	17.1	12.2
5000	18.3	12.6
7500	20.9	14.2
10000	22.9	17.9
15000	23.5	19.4

Table A-21. SSG response data.

Loc.	ND	ND	ND	ND	MS	MS	MS	MS	D	D	D	D
Desig.	SL1	ST1	SL2	ST2	SL3	ST3	SL4	ST4	SL5	ST5	SL6	ST6
Pass	Strain (micro)											
1	105.1	84.4	91.9	59.0	161.9	54.1	162.6	50.6	141.1	61.9	142.7	50.7
10	108.8	109.7	115.4	82.4	181.4	65.0	174.4	68.3	150.7	93.8	143.8	63.1
30	197.1	257.7	123.1	169.2	235.1	124.1	193.2	106.8	161.5	191.0	160.8	109.4
50	111.8	176.6	126.8	121.1	196.1	96.0	182.2	89.8	161.9	121.8	148.8	103.6
300	NDat	506.3	NDat	NDat	NDat	NDat	NDat	NDat	177.3	273.7	187.8	197.4
500	NDat	NDat	NDat	NDat	NDat	NDat	NDat	NDat	192.0	309.3	197.0	239.1
750	NDat	NDat	NDat	NDat	NDat	NDat	NDat	NDat	243.7	312.8	200.3	237.9
1000	NDat	NDat	NDat	NDat	NDat	NDat	NDat	NDat	247.3	NDat	207.1	266.1
3000	NDat	NDat	NDat	NDat	NDat	NDat	NDat	NDat	NDat	NDat	462.4	NDat
5000	NDat	NDat	NDat	NDat	NDat	NDat	NDat	NDat	NDat	NDat	NDat	NDat
7500	NDat	NDat	NDat	NDat	NDat	NDat	NDat	NDat	NDat	NDat	NDat	NDat
10000	NDat	NDat	NDat	NDat	NDat	NDat	NDat	NDat	NDat	NDat	NDat	NDat
15000	NDat	NDat	NDat	NDat	NDat	NDat	NDat	NDat	NDat	NDat	NDat	NDat

Note: ND = nondowelled, MS = midslab, D = dowelled, SL = surface longitudinal, ST = surface transverse, NDat = no data available

Table A-22. ESG response data.

Loc.	ND	ND	ND	ND	MS	MS	MS	MS	D	D	D	D
Desig.	EL1	ET1	EL2	ET2	EL3	ET3	EL4	ET4	EL5	ET5	EL6	ET6
Pass	Strain (micro)											
1	36.3	27.8	37.2	17.0	60.5	15.4	57.2	14.3	56.3	43.2	57.4	17.5
10	37.0	46.5	50.1	24.4	69.2	17.4	61.5	16.7	65.7	60.5	58.6	20.5
30	43.2	156.3	46.3	61.4	76.4	38.9	70.6	39.9	66.2	83.4	61.7	44.9
50	39.0	112.1	42.0	51.4	73.4	29.1	67.2	24.7	53.5	68.5	53.5	35.3
300	43.8	285.7	87.1	415.4	127.6	105.9	101.1	42.9	90.5	218.6	68.1	163.6
500	52.4	266.7	95.3	383.5	154.2	138.8	108.9	49.1	132.2	317.9	71.0	240.7
750	41.9	130.4	129.0	428.1	108.8	166.1	62.8	69.3	108.0	423.9	60.7	235.4
1000	40.8	131.9	168.1	459.2	64.7	144.6	64.2	72.5	83.1	305.2	60.0	233.0
3000	36.4	149.8	190.7	438.5	783.3	245.8	1206.7	220.4	425.0	2318.0	168.9	268.9
5000	40.1	121.9	188.7	402.4	341.2	272.6	667.1	219.6	373.8	1393.7	NDat	258.3
7500	38.3	160.5	182.3	488.8	279.0	342.0	549.0	209.9	368.1	1468.0	NDat	283.6
10000	38.2	NDat	193.4	548.2	177.8	500.5	474.1	331.9	540.5	1879.4	NDat	395.0
15000	38.1	NDat	165.9	321.4	212.6	216.6	379.3	149.8	941.0	739.9	NDat	468.9

Note: ND = nondowelled, MS = midslab, D = dowelled, EL = embedded longitudinal, ET = embedded transverse, NDat = no data available

Appendix B: 11 in. Thick PCC Data

Table B-1. HWD pretest data.

Location		Load (lbf)	Deflection (mils)							ISM (kips/in.)
X (ft.)	Y (ft.)		D1	D2	D3	D4	D5	D6	D7	
59.5	18.5	47413	38.61	32.52	27.11	22.50	19.02	15.13	12.43	1228
50	18.5	49518	16.2	15.12	13.75	12.39	11.4	9.78	8.59	3057
40.75	18.5	48901	25.86	26.5	22.26	18.63	16.15	12.42	9.99	1891
39.25	18.5	48473	25.51	22.19	18.92	15.9	13.81	10.86	8.97	1900
30	18.5	49262	18.5	17.43	15.84	14.19	13.09	11.22	9.87	2663
20.75	18.5	48484	32.41	27.94	23.42	19.46	17.14	12.84	10.33	1496
19.25	18.5	47980	30.65	26.42	22.28	18.59	16.23	12.46	10.2	1565
10	18.5	49120	19.63	18.38	16.47	14.55	13.66	10.99	9.48	2502
1.5	18.5	48451	26.92	28.69	23.44	19.37	17	12.75	10.32	1800
59.5	11.5	48046	31.45	25.78	21.03	16.98	14.67	11.15	9.11	1528
50	11.5	49667	14.96	13.74	12.2	10.6	9.39	7.57	6.24	3320
40.75	11.5	48681	19.83	19.31	15.55	12.48	10.31	8.05	6.5	2455
39.25	11.5	48911	17.23	14.79	12.46	10.4	8.81	7.06	5.74	2839
30	11.5	49678	13.85	12.69	11.37	9.91	8.79	7.26	6.12	3587
20.75	11.5	48911	20.19	21.99	15.14	12.22	10.28	7.85	6.47	2423
19.25	11.5	48528	20.76	17.13	13.95	11.29	9.57	7.39	6.05	2338
10	11.5	49667	14.91	13.58	11.99	10.33	9.06	7.39	6.17	3331
1.5	11.5	49240	17.95	18.05	14.9	12.26	10.39	8.04	6.54	2743
59.5	4	46918	39.86	32.84	27.08	22.18	18.54	14.52	11.85	1177
50	4	49251	17.81	16.62	15.03	13.22	11.83	9.76	8.23	2765
40.75	4	48824	20.96	22.27	19.24	15.55	12.8	9.98	8.09	2329
39.25	4	48966	22.61	18.96	15.74	12.82	10.93	8.51	7.02	2166
30	4	49525	14.94	13.82	12.45	10.95	9.79	8.14	6.95	3315
20.75	4	47958	21.77	23.48	18.95	15.19	12.72	9.52	7.76	2203
19.25	4	48627	21.91	18.44	15.31	12.55	10.65	8.39	6.97	2219
10	4	49393	16.26	15.07	13.46	11.77	10.19	8.46	6.98	3038
1.5	4	49218	20.17	20.97	17.49	14.53	12.13	9.58	7.7	2440

Table B-2. HWD pretest data.

Location		Load (lbf)	Deflection (mils)							ISM (kips/in.)
X (ft.)	Y (ft.)		D1	D2	D3	D4	D5	D6	D7	
59.5	18.5	47619	42.69	35.29	28.66	23.17	18.74	14.51	11.44	1115
50	18.5	49886	16.20	14.99	13.43	11.74	10.46	9.03	8.48	3079
40.75	18.5	47268	52.29	33.56	27.23	21.63	16.93	12.47	9.16	904
39.25	18.5	47969	53.50	43.53	34.98	27.37	21.30	16.17	12.30	897
30	18.5	49678	19.50	18.46	16.93	15.25	13.68	11.96	10.39	2548
20.75	18.5	47115	42.76	39.29	32.21	25.71	20.25	15.23	11.45	1102
19.25	18.5	47696	41.87	35.36	28.94	23.13	18.99	13.98	10.74	1139
10	18.5	49613	19.59	18.41	16.70	15.02	14.18	11.95	10.48	2533
1.5	18.5	46228	49.70	15.35	13.30	11.35	9.29	7.54	5.98	930
59.5	11.5	47871	37.13	30.21	24.15	19.26	15.38	11.91	9.29	1289
50	11.5	49886	14.42	13.29	11.78	10.20	8.82	7.31	6.00	3460
40.75	11.5	47038	46.96	7.40	6.80	5.65	5.44	4.57	3.86	1002
39.25	11.5	47969	38.20	30.63	24.31	19.07	14.39	11.60	8.97	1256
30	11.5	49930	14.87	13.91	12.69	11.04	9.48	7.74	6.36	3358
20.75	11.5	48868	29.39	25.19	20.07	15.63	12.31	8.94	6.93	1663
19.25	11.5	49021	29.21	23.38	18.30	14.11	10.94	8.21	6.44	1678
10	11.5	50215	14.18	12.98	11.40	9.82	8.48	7.07	5.93	3541
1.5	11.5	48353	28.27	11.56	9.90	8.64	7.46	6.06	4.93	1710
59.5	4	47652	38.53	31.73	25.84	20.80	16.24	13.01	10.47	1237
50	4	49656	16.96	15.71	13.86	11.80	9.72	7.83	6.65	2928
40.75	4	47794	39.76	12.25	9.85	8.18	6.76	5.74	4.78	1202
39.25	4	47937	41.43	33.33	26.59	20.90	16.22	12.52	9.71	1157
30	4	49536	15.37	14.43	13.10	11.48	9.91	8.31	6.85	3223
20.75	4	48101	33.90	30.81	24.59	19.43	14.06	11.20	8.55	1419
19.25	4	47969	32.29	26.21	20.96	16.23	12.47	9.58	7.50	1486
10	4	49733	16.47	15.31	13.72	11.94	10.07	8.57	6.96	3020
1.5	4	48353	28.06	31.87	15.88	13.11	11.02	8.47	6.80	1723

Table B-3. FWD data at pass 0.

Pass	Sta.	Condition	Load	D0	D1	D2	D3	D4	D5	D6	ISM
0	40.2	X-Joint	23064	10.33	9.91	8.02	6.41	5.39	4.09	2.7	2233
0	40.1	Joint	22965	10.33	8.41	6.94	5.67	4.81	3.72	2.63	2223
0	35	Quarter	23064	6.9	6.2	5.56	4.87	4.32	3.53	2.93	3343
0	30	Mid	23042	6.99	6.31	5.6	4.85	4.34	3.57	2.83	3296
0	20.2	X-Joint	22834	11.53	9.1	7.39	5.96	5	3.83	2.88	1980
0	20.1	Joint	22779	12.07	9.58	7.71	6.16	5.15	3.94	2.53	1887
0	10	Mid	22943	9.66	6.6	5.85	5.08	4.48	3.63	2.98	2375

Note: Sta. = station, Load = lbf, D*n* = mils, ISM = impulse stiffness modulus (kips/in.)

Table B-4. FWD data at pass 10.

Pass	Sta.	Condition	Load	D0	D1	D2	D3	D4	D5	D6	ISM
10	40.2	X-Joint	22900	11.4	10.11	8.15	6.5	5.46	4.15	2.65	2009
10	40.1	Joint	22856	10.61	8.53	7.06	5.76	4.86	3.77	2.82	2154
10	35	Quarter	22889	7.15	6.42	5.66	4.93	4.41	3.62	2.94	3201
10	30	Mid	22889	6.73	6.31	5.66	4.98	4.42	3.6	3.08	3401
10	20.2	X-Joint	22681	12.72	8.61	7.05	5.74	4.84	3.78	3.01	1783
10	20.1	Joint	22626	12.81	10.37	8.32	6.55	5.48	4.18	2.75	1766
10	10	Mid	22856	7.71	6.7	5.95	5.16	4.56	3.7	2.85	2964

Note: Sta. = station, Load = lbf, D*n* = mils, ISM = impulse stiffness modulus (kips/in.)

Table B-5. FWD data at pass 50.

Pass	Sta.	Condition	Load	D0	D1	D2	D3	D4	D5	D6	ISM
50	40.2	X-Joint	23184	11.47	9.96	8.03	6.46	5.37	4.11	3.21	2021
50	40.1	Joint	23118	10.57	8.75	7.22	5.88	4.98	3.92	2.55	2187
50	35	Quarter	23173	7.07	6.49	5.73	5	4.46	3.69	3.2	3278
50	30	Mid	23107	6.97	6.3	5.65	4.97	4.44	3.65	3.02	3315
50	20.2	X-Joint	22911	12.8	8.58	7.03	5.73	4.87	3.76	2.94	1790
50	20.1	Joint	22856	13.44	10.62	8.47	6.67	5.6	4.19	2.78	1701
50	10	Mid	23031	7.12	6.69	5.95	5.13	4.57	3.68	2.95	3235

Note: Sta. = station, Load = lbf, D*n* = mils, ISM = impulse stiffness modulus (kips/in.)

Table B-6. FWD data at pass 100.

Pass	Sta.	Condition	Load	D0	D1	D2	D3	D4	D5	D6	ISM
100	40.2	X-Joint	22801	12.81	10.22	8.17	6.55	5.43	4.11	3.18	1780
100	40.1	Joint	22812	10.96	9.21	7.48	6.04	5.08	3.9	2.93	2081
100	35	Quarter	22867	7.61	6.46	5.71	4.98	4.43	3.68	3.17	3005
100	30	Mid	22922	6.87	6.33	5.69	5	4.44	3.66	3.04	3337
100	20.2	X-Joint	22670	12.36	8.59	7.06	5.76	4.86	3.8	2.93	1834
100	20.1	Joint	22594	16	11.26	8.9	7	5.78	4.35	2.95	1412
100	10	Mid	22867	7.59	6.73	5.95	5.18	4.56	3.7	3.13	3013

Note: Sta. = station, Load = lbf, D*n* = mils, ISM = impulse stiffness modulus (kips/in.)

Table B-7. FWD data at pass 300.

Pass	Sta.	Condition	Load	D0	D1	D2	D3	D4	D5	D6	ISM
300	40.2	X-Joint	23272	13.32	9.15	7.4	5.98	5.02	3.84	2.85	1747
300	40.1	Joint	23239	11.5	9.43	7.79	6.23	5.28	4.08	2.37	2021
300	35	Quarter	23282	7.39	6.6	5.82	5.04	4.48	3.7	3.15	3150
300	30	Mid	23326	7.22	6.32	5.67	4.98	4.44	3.65	2.93	3231
300	20.2	X-Joint	23097	12.87	8.81	7.19	5.85	4.91	3.78	3.09	1795
300	20.1	Joint	22943	15.03	11.55	9.07	7.11	5.8	4.41	3.3	1526
300	10	Mid	23151	8.77	6.69	5.91	5.14	4.54	3.69	2.89	2640

Note: Sta. = station, Load = lbf, D*n* = mils, ISM = impulse stiffness modulus (kips/in.)

Table B-8. FWD data at pass 500.

Pass	Sta.	Condition	Load	D0	D1	D2	D3	D4	D5	D6	ISM
500	40.2	X-Joint	23107	15.72	7.86	6.43	5.26	4.43	3.48	2.89	1470
500	40.1	Joint	23086	13.59	11.04	8.9	7.08	5.95	4.53	2.69	1699
500	35	Quarter	23217	7.76	6.81	5.98	5.19	4.59	3.78	3.25	2992
500	30	Mid	23173	6.97	6.39	5.75	5.07	4.52	3.74	3.09	3325
500	20.2	X-Joint	22911	14.25	9.23	7.52	6.06	5.07	3.92	2.98	1608
500	20.1	Joint	22878	14.51	11.94	9.38	7.36	6.03	4.54	3.2	1577
500	10	Mid	22998	7.37	6.78	6	5.19	4.58	3.71	3.04	3120

Note: Sta. = station, Load = lbf, D*n* = mils, ISM = impulse stiffness modulus (kips/in.)

Table B-9. FWD data at pass 1,000.

Pass	Sta.	Condition	Load	D0	D1	D2	D3	D4	D5	D6	ISM
1000	40.2	X-Joint	22714	14.94	7.51	6.12	5.03	4.29	3.36	2.75	1520
1000	40.1	Joint	22725	12.66	10.31	8.35	6.7	5.58	4.35	3.06	1795
1000	35	Quarter	22889	7.43	6.68	5.88	5.11	4.56	3.74	3.08	3081
1000	30	Mid	22900	6.88	6.43	5.8	5.11	4.55	3.74	3.39	3328
1000	20.2	X-Joint	22626	13.21	8.6	7.04	5.73	4.83	3.75	3.05	1713
1000	20.1	Joint	22670	16.16	12.43	9.72	7.58	6.19	4.64	3.22	1403
1000	10	Mid	22954	7.42	6.83	6.04	5.24	4.63	3.76	3.11	3094

Note: Sta. = station, Load = lbf, D*n* = mils, ISM = impulse stiffness modulus (kips/in.)

Table B-10. FWD data at pass 1,500.

Pass	Sta.	Condition	Load	D0	D1	D2	D3	D4	D5	D6	ISM
1500	40.2	X-Joint	23020	15.5	8.53	6.88	5.56	4.68	3.61	2.9	1485
1500	40.1	Joint	23097	13.59	10.91	8.73	6.91	5.78	4.34	2.65	1700
1500	35	Quarter	23206	7.39	6.67	5.86	5.07	4.52	3.72	3.14	3140
1500	30	Mid	23217	7.04	6.37	5.7	5	4.48	3.68	3.03	3298
1500	20.2	X-Joint	22922	14.02	8.75	7.15	5.8	4.86	3.76	2.86	1635
1500	20.1	Joint	23173	14.23	11.37	9.01	7.13	5.84	4.44	3.28	1628
1500	10	Mid	23097	7.88	6.74	5.96	5.17	4.54	3.68	3.05	2931

Note: Sta. = station, Load = lbf, D*n* = mils, ISM = impulse stiffness modulus (kips/in.)

Table B-11. FWD data at pass 3,000.

Pass	Sta.	Condition	Load	D0	D1	D2	D3	D4	D5	D6	ISM
3000	40.2	X-Joint	23184	14.5	9.36	7.63	6.15	5.17	3.98	2.43	1599
3000	40.1	Joint	22976	12.33	10.06	8.17	6.57	5.58	4.26	3.14	1863
3000	35	Quarter	23129	7.72	6.77	5.99	5.2	4.62	3.84	3.35	2996
3000	30	Mid	22998	7.17	6.53	5.89	5.19	4.65	3.83	3.14	3208
3000	20.2	X-Joint	22758	13.13	8.8	7.24	5.88	4.96	3.88	2.9	1733
3000	20.1	Joint	22736	14.98	11.5	9.15	7.26	6	4.55	3.15	1518
3000	10	Mid	22922	7.31	6.94	6.14	5.33	4.72	3.83	3.08	3136

Note: Sta. = station, Load = lbf, D*n* = mils, ISM = impulse stiffness modulus (kips/in.)

Table B-12. FWD data at pass 5,000.

Pass	Sta.	Condition	Load	D0	D1	D2	D3	D4	D5	D6	ISM
5000	40.2	X-Joint	23009	19.13	6.33	5.28	4.39	3.82	3.09	2.31	1203
5000	40.1	Joint	22911	14.56	11.67	9.37	7.42	6.13	4.68	3.14	1574
5000	35	Quarter	23206	7.73	6.89	6.07	5.24	4.63	3.84	3.14	3002
5000	30	Mid	23118	6.89	6.42	5.78	5.09	4.56	3.74	3.04	3355
5000	20.2	X-Joint	22834	14.17	9.33	7.51	6.04	5.03	3.87	3.16	1611
5000	20.1	Joint	22878	14.85	11.8	9.3	7.28	5.98	4.55	3.05	1541
5000	10	Mid	23064	7.69	6.74	6	5.23	4.57	3.73	3.07	2999

Note: Sta. = station, Load = lbf, D*n* = mils, ISM = impulse stiffness modulus (kips/in.)

Table B-13. FWD data at pass 7,500.

Pass	Sta.	Condition	Load	D0	D1	D2	D3	D4	D5	D6	ISM
7500	40.2	X-Joint	22943	19.7	5.48	4.6	3.94	3.51	2.88	2.45	1165
7500	40.1	Joint	22943	14.89	11.74	9.39	7.45	6.16	4.66	3.06	1541
7500	35	Quarter	23097	8.29	6.94	6.08	5.26	4.67	3.85	3.17	2786
7500	30	Mid	23097	7.05	6.45	5.83	5.15	4.6	3.81	3.17	3276
7500	20.2	X-Joint	22856	13.45	9.46	7.7	6.16	5.15	3.96	3.18	1699
7500	20.1	Joint	22768	16.02	12.3	9.59	7.5	6.14	4.6	3.53	1421
7500	10	Mid	22976	7.39	6.8	6.02	5.24	4.62	3.79	3.09	3109

Note: Sta. = station, Load = lbf, D*n* = mils, ISM = impulse stiffness modulus (kips/in.)

Table B-14. FWD data at pass 10,000.

Pass	Sta.	Condition	Load	D0	D1	D2	D3	D4	D5	D6	ISM
10000	40.2	X-Joint	22911	19.33	5.19	4.54	3.89	3.53	2.86	2.24	1185
10000	40.1	Joint	22998	13.79	11.14	8.97	7.17	5.98	4.53	3.29	1668
10000	35	Quarter	23097	7.61	6.9	6.04	5.26	4.67	3.85	3.27	3035
10000	30	Mid	23162	6.9	6.5	5.84	5.14	4.58	3.78	3.16	3357
10000	20.2	X-Joint	22889	13.19	9.74	7.89	6.35	5.3	4.07	3.3	1735
10000	20.1	Joint	22867	14.06	11.3	8.96	7.11	5.86	4.46	3.31	1626
10000	10	Mid	22998	7.52	6.79	6.02	5.24	4.62	3.78	3.07	3058

Note: Sta. = station, Load = lbf, D*n* = mils, ISM = impulse stiffness modulus (kips/in.)

Table B-15. FWD data at pass 15,000.

Pass	Sta.	Condition	Load	D0	D1	D2	D3	D4	D5	D6	ISM
15000	40.2	X-Joint	22714	16.17	7.77	6.39	5.2	4.44	3.47	2.5	1405
15000	40.1	Joint	22725	12.23	9.98	8.04	6.41	5.35	4.08	2.91	1858
15000	35	Quarter	22878	7.03	6.52	5.72	4.97	4.43	3.66	3.05	3254
15000	30	Mid	22845	6.85	6.32	5.69	5	4.44	3.6	3.06	3335
15000	20.2	X-Joint	22659	11.93	9	7.28	5.87	4.93	3.81	2.97	1899
15000	20.1	Joint	22594	13.45	10.6	8.43	6.68	5.54	4.21	3.12	1680
15000	10	Mid	22790	6.97	6.66	5.89	5.1	4.49	3.63	3.11	3270

Note: Sta. = station, Load = lbf, D*n* = mils, ISM = impulse stiffness modulus (kips/in.)

Table B-16. FWD data at pass 20,000.

Pass	Sta.	Condition	Load	D0	D1	D2	D3	D4	D5	D6	ISM
20000	40.2	X-Joint	22779	15.75	7.6	6.24	5.1	4.35	3.44	2.68	1446
20000	40.1	Joint	22714	11.38	9.49	7.79	6.36	5.34	4.13	3.23	1996
20000	35	Quarter	22954	7.33	6.74	6	5.23	4.7	3.91	3.2	3132
20000	30	Mid	22987	7.63	6.93	6.37	5.7	5.07	4.16	3.58	3013
20000	20.2	X-Joint	22725	10.19	9.69	7.92	6.41	5.42	4.19	3.29	2230
20000	20.1	Joint	22626	15.35	12.15	9.64	7.6	6.3	4.76	3.37	1474
20000	10	Mid	22943	7.99	6.93	6.16	5.34	4.72	3.84	3.24	2871

Note: Sta. = station, Load = lbf, D*n* = mils, ISM = impulse stiffness modulus (kips/in.)

Table B-17. FWD data at pass 30,000.

Pass	Sta.	Condition	Load	D0	D1	D2	D3	D4	D5	D6	ISM
30000	40.2	X-Joint	22583	23.53	5.4	4.77	4.17	3.72	3.06	2.51	960
30000	40.1	Joint	22845	14.3	11.72	9.44	7.57	6.3	4.75	3.56	1598
30000	35	Quarter	22922	8.38	7.48	6.56	5.67	5.03	4.12	3.44	2735
30000	30	Mid	23020	7.93	7.27	6.66	5.87	5.15	4.17	3.41	2903
30000	20.2	X-Joint	22736	13.36	10.58	8.53	6.82	5.67	4.33	3.32	1702
30000	20.1	Joint	22604	15.67	12.44	9.73	7.67	6.31	4.73	3.55	1443
30000	10	Mid	22911	7.75	6.89	6.02	5.26	4.65	3.76	3.02	2956

Note: Sta. = station, Load = lbf, D*n* = mils, ISM = impulse stiffness modulus (kips/in.)

Table B-18. FWD data at pass 40,000.

Pass	Sta.	Condition	Load	D0	D1	D2	D3	D4	D5	D6	ISM
40000	40.2	X-Joint	22779	25.77	5.7	5	4.3	3.78	3.09	2.42	884
40000	40.1	Joint	22845	17.11	13.35	10.5	8.19	6.66	4.85	3.35	1335
40000	35	Quarter	23140	8.37	7.36	6.38	5.46	4.81	3.93	3.24	2765
40000	30	Mid	23097	7.56	6.89	6.22	5.4	4.75	3.85	3.07	3055
40000	20.2	X-Joint	22878	13.67	11.38	9.09	7.15	5.83	4.34	3.33	1674
40000	20.1	Joint	22692	17.35	13.54	10.35	7.91	6.39	4.67	3.33	1308
40000	10	Mid	23009	8.59	6.63	5.86	5.08	4.47	3.68	2.91	2679

Note: Sta. = station, Load = lbf, D*n* = mils, ISM = impulse stiffness modulus (kips/in.)

Table B-19. FWD data at pass 50,000.

Pass	Sta.	Condition	Load	D0	D1	D2	D3	D4	D5	D6	ISM
50000	40.2	X-Joint	22725	20.6	7.11	6.01	5.08	4.4	3.5	2.85	1103
50000	40.1	Joint	22889	14.39	11.44	9.15	7.24	5.94	4.43	3.28	1591
50000	35	Quarter	22976	8.09	7.36	6.49	5.57	4.88	3.97	3.26	2840
50000	30	Mid	23118	7.5	7	6.35	5.6	4.92	3.96	3.2	3082
50000	20.2	X-Joint	22889	12.56	10.59	8.52	6.75	5.57	4.2	3.23	1822
50000	20.1	Joint	22779	13.09	10.6	8.43	6.71	5.54	4.18	3.2	1740
50000	10	Mid	22911	8.04	6.69	5.84	5.09	4.46	3.62	3.28	2850

Note: Sta. = station, Load = lbf, D*n* = mils, ISM = impulse stiffness modulus (kips/in.)

Table B-20. Earth pressure cell response data.

Pass	Midslab (EP1) (psi)	Joint (EP2) (psi)
1	2.1	3.4
10	2.3	4.5
30	2.1	4.2
50	2.2	4.9
300	2.3	5.6
500	2.3	4.9
750	2.3	5.3
1000	2.1	5.9
3000	2.1	6.1
5000	2.1	6.4
7500	2.2	6.3
10000	2.1	6.4
15000	2.1	6.8
20000	2.1	6.9
30000	2.5	6.7
40000	2.8	6.4
50000	3.0	6.9

Appendix C: Flexible Pavement Data

Table C-1. Rut-depth data.

Pass	4HMA, GR, 10 CBR	2HMA, GR, 10 CBR	4HMA, LS, 6 CBR	2HMA, LS, 6 CBR	4HMA, LS, 10 CBR	2HMA, LS, 10 CBR
0	0.00	0.00	0.00	0.00	0.00	0.00
1	ND	0.63	ND	ND	ND	ND
2	0.19	0.97	0.00	0.05	0.00	0.00
3	ND	1.60	ND	ND	ND	ND
4	0.50	2.22	ND	ND	ND	ND
5	ND	2.31	ND	ND	ND	ND
6	0.75	NT	ND	ND	ND	ND
8	0.97	NT	ND	ND	ND	ND
10	ND	NT	0.13	0.29	0.02	0.15
12	1.34	NT	ND	ND	ND	ND
16	1.69	NT	ND	ND	ND	ND
20	2.00	NT	ND	ND	ND	ND
28	2.72	NT	ND	ND	ND	ND
30	NT	NT	0.35	0.54	0.10	0.27
50	NT	NT	0.49	0.73	0.40	0.44
75	NT	NT	0.66	0.96	0.75	0.47
100	NT	NT	1.03	1.21	0.77	0.50
150	NT	NT	ND	1.35	ND	ND
283	NT	NT	ND	2.44	ND	ND
300	NT	NT	1.94	NT	1.15	1.28
500	NT	NT	2.53	NT	1.67	1.75
750	NT	NT	3.19	NT	2.44	2.31
1000	NT	NT	NT	NT	2.77	2.33

ND = no data collected; NT = no test traffic applied

Table C-2. ISM data.

Pass	4HMA, GR, 10 CBR	2HMA, GR, 10 CBR	4HMA, LS, 6 CBR	2HMA, LS, 6 CBR	4HMA, LS, 10 CBR	2HMA, LS, 10 CBR
0	298	208	491	375	585	458
1	ND	145	ND	ND	ND	ND
2	217	ND	434	300	603	415
3	ND	153	ND	ND	ND	ND
4	205	ND	ND	ND	ND	ND
6	205	NT	ND	ND	ND	ND
8	201	NT	ND	ND	ND	ND
10	185	NT	359	248	525	346
12	183	NT	ND	ND	ND	ND
20	172	NT	ND	ND	ND	ND
28	183	NT	ND	ND	ND	ND
30	NT	NT	ND	203	425	267
50	NT	NT	320	186	427	247
75	NT	NT	314	203	387	228
100	NT	NT	300	207	357	245
150	NT	NT	ND	194	ND	ND
283	NT	NT	ND	161	ND	ND
300	NT	NT	230	NT	383	206
500	NT	NT	185	NT	414	197
750	NT	NT	214	NT	368	184
1000	NT	NT	NT	NT	384	211

ND = no data collected; NT = no test traffic applied

Table C-3. Subgrade pressure cell response data.

Pass	4HMA, GR, 10 CBR	2HMA, GR, 10 CBR	4HMA, LS, 6 CBR	2HMA, LS, 6 CBR	4HMA, LS, 10 CBR	2HMA, LS, 10 CBR
1	32.1	16.6	22.4	23.8	23.0	28.4
2	32.6	20.9	25.4	25.0	25.6	26.7
3	33.5	27.0	23.7	24.6	23.2	28.8
4	35.2	36.9	26.2	25.3	25.3	26.4
5	34.8	51.1	25.1	25.2	24.0	25.3
6	38.9	NT	27.5	26.0	26.7	24.6
7	38.5	NT	26.2	26.1	25.5	23.8
8	44.1	NT	29.3	27.9	29.2	25.0
9	43.7	NT	28.0	28.2	28.3	24.8
10	51.3	NT	31.7	30.9	32.7	28.1
11	50.7	NT	29.0	30.0	30.8	29.5
12	59.3	NT	34.0	34.4	36.5	34.2
13	57.2	NT	32.7	35.6	35.7	35.6
14	66.7	NT	36.9	39.4	41.1	43.1
15	67.8	NT	35.3	40.3	40.0	43.9
16	74.8	NT	39.4	43.7	45.1	50.8
17	71.2	NT	37.7	44.6	43.9	51.6
18	78.3	NT	41.7	47.5	48.6	57.8
19	76.3	NT	40.0	48.4	47.2	58.6
20	79.9	NT	43.6	50.7	51.7	63.8
21	74.1	NT	41.9	51.7	50.1	64.5
22	73.0	NT	44.9	53.4	54.2	69.1
23	78.6	NT	43.2	54.0	52.4	69.1
24	71.3	NT	45.5	55.3	55.9	71.4
25	74.7	NT	43.9	55.0	53.8	70.9
26	66.8	NT	45.3	55.6	56.4	71.6
27	71.6	NT	43.6	54.3	53.8	70.7
28	67.6	NT	44.9	55.3	56.2	71.0
30	NT	NT	46.1	56.8	55.0	71.4
75	NT	NT	52.6	60.1	60.1	84.9
100	NT	NT	50.9	54.2	59.5	79.5
150	NT	NT	51.0	54.6	59.1	82.7
200	NT	NT	54.4	56.5	63.9	82.8
250	NT	NT	50.8	60.4	60.5	81.3

Table C-3. Subgrade pressure cell response data.

Pass	4HMA, GR, 10 CBR	2HMA, GR, 10 CBR	4HMA, LS, 6 CBR	2HMA, LS, 6 CBR	4HMA, LS, 10 CBR	2HMA, LS, 10 CBR
300	NT	NT	45.4	NT	51.8	76.6
500	NT	NT	51.6	NT	61.6	78.4
750	NT	NT	51.7	NT	52.2	78.5
1000	NT	NT	NT	NT	56.0	77.8

ND = no data collected; NT = no test traffic applied

Table C-4. Top of base pressure cell response data.

Pass	4HMA, GR, 10 CBR	2HMA, GR, 10 CBR	4HMA, LS, 6 CBR	2HMA, LS, 6 CBR	4HMA, LS, 10 CBR	2HMA, LS, 10 CBR
1	11.6	3.4	2.0	0.9	1.2	0.4
2	7.9	0.9	5.4	1.0	2.8	0.4
3	6.6	0.5	3.0	1.4	2.0	0.7
4	7.8	22.2	6.0	1.2	3.5	0.4
5	9.1	41.7	6.1	1.3	2.9	0.6
6	10.6	NT	12.4	1.4	4.7	0.5
7	17.5	NT	14.4	1.6	4.0	0.5
8	20.1	NT	27.0	1.6	7.6	0.7
9	31.9	NT	29.5	2.1	7.6	0.9
10	36.2	NT	52.4	3.0	14.6	2.0
11	52.4	NT	54.2	5.8	18.3	3.0
12	62.7	NT	86.9	8.4	31.8	6.1
13	85.6	NT	86.7	14.7	34.8	8.6
14	104.6	NT	121.2	26.0	56.7	19.3
15	123.0	NT	118.5	40.5	62.3	25.0
16	148.3	NT	145.2	66.1	89.9	51.0
17	162.0	NT	142.1	85.5	96.5	60.4
18	175.0	NT	153.9	121.0	123.2	100.2
19	181.9	NT	149.7	142.1	129.5	110.2
20	180.8	NT	148.5	175.8	148.1	150.0
21	171.4	NT	143.2	186.5	152.8	158.5
22	164.4	NT	134.3	199.5	158.4	187.1
23	164.1	NT	127.8	199.0	160.4	189.8
24	159.8	NT	113.8	191.6	155.0	189.8
25	161.5	NT	106.8	184.8	153.2	188.3
26	151.7	NT	89.0	176.8	141.8	177.6
27	158.1	NT	82.3	166.8	137.1	174.7
28	169.1	NT	74.2	169.1	132.2	166.2
30	NT	NT	100.7	183.8	150.4	179.9
75	NT	NT	144.6	211.1	170.9	205.6
100	NT	NT	158.1	168.4	160.1	187.8
150	NT	NT	163.0	198.8	145.6	207.5
200	NT	NT	171.0	204.6	162.9	208.9
250	NT	NT	159.0	212.6	172.0	227.5

Table C-4. Top of base pressure cell response data.

Pass	4HMA, GR, 10 CBR	2HMA, GR, 10 CBR	4HMA, LS, 6 CBR	2HMA, LS, 6 CBR	4HMA, LS, 10 CBR	2HMA, LS, 10 CBR
300	NT	NT	155.0	NT	112.0	224.4
500	NT	NT	177.6	NT	173.0	205.6
750	NT	NT	193.8	NT	110.7	208.2
1000	NT	NT	NT	NT	164.4	206.6

ND = no data collected; NT = no test traffic applied

Table C-5. Middepth of base pressure cell response data.

Pass	4HMA, GR, 10 CBR	2HMA, GR, 10 CBR	4HMA, LS, 6 CBR	2HMA, LS, 6 CBR	4HMA, LS, 10 CBR	2HMA, LS, 10 CBR
1	18.6	15.5	7.1	2.2	1.9	1.9
2	15.5	20.7	8.6	2.9	2.0	1.3
3	19.4	19.9	9.1	2.5	2.1	1.9
4	17.4	38.6	9.4	3.5	2.2	1.4
5	21.7	54.5	8.5	4.1	1.9	1.5
6	20.8	NT	11.9	6.6	2.6	1.9
7	28.3	NT	10.9	7.9	2.4	2.1
8	30.5	NT	18.9	12.7	3.7	3.6
9	39.9	NT	17.2	15.1	3.5	3.6
10	46.6	NT	29.7	24.2	5.6	7.6
11	55.8	NT	27.7	25.9	5.6	7.7
12	67.7	NT	43.2	39.4	9.7	17.3
13	75.6	NT	39.7	43.2	9.8	16.4
14	89.1	NT	56.7	58.9	16.0	32.4
15	101.4	NT	53.6	61.9	16.0	31.9
16	109.7	NT	69.2	78.7	25.0	52.6
17	113.4	NT	66.5	80.6	24.4	52.2
18	119.2	NT	77.7	93.1	34.1	72.7
19	124.1	NT	75.9	94.5	33.1	73.2
20	124.9	NT	81.8	99.2	41.9	89.2
21	120.0	NT	80.9	99.3	40.3	91.3
22	120.0	NT	82.0	98.3	47.1	99.8
23	122.1	NT	81.1	96.9	45.1	102.3
24	123.7	NT	79.8	91.7	48.8	100.5
25	121.2	NT	79.4	87.8	46.3	101.6
26	117.4	NT	76.9	82.3	47.5	93.5
27	115.5	NT	76.9	76.0	44.2	93.6
28	129.7	NT	76.1	76.6	46.8	88.5
30	NT	NT	80.5	88.3	47.7	96.9
75	NT	NT	88.3	95.3	63.5	114.1
100	NT	NT	85.4	106.3	59.9	110.9
150	NT	NT	77.6	105.7	60.7	121.8
200	NT	NT	94.6	107.3	73.5	115.8
250	NT	NT	86.9	105.7	74.9	124.5

Table C-5. Middepth of base pressure cell response data.

Pass	4HMA, GR, 10 CBR	2HMA, GR, 10 CBR	4HMA, LS, 6 CBR	2HMA, LS, 6 CBR	4HMA, LS, 10 CBR	2HMA, LS, 10 CBR
300	NT	NT	79.4	NT	58.6	132.0
500	NT	NT	86.6	NT	84.0	131.7
750	NT	NT	101.7	NT	72.2	126.3
1000	NT	NT	NT	NT	89.0	128.1

ND = no data collected; NT = no test traffic applied

Table C-6. Dynamic single-depth deflectometer response data.

Pass	4HMA, GR, 10 CBR	2HMA, GR, 10 CBR	4HMA, LS, 6 CBR	2HMA, LS, 6 CBR	4HMA, LS, 10 CBR	2HMA, LS, 10 CBR
1	0.1548	0.1068	0.1195	0.1363	0.0684	0.0702
2	0.1504	0.1045	0.1450	0.1483	0.0763	0.0721
3	0.1651	0.0211	0.1303	0.1518	0.0733	0.0753
4	0.1662	0.1151	0.1527	0.1617	0.0802	0.0755
5	0.1786	0.1323	0.1481	0.1694	0.0804	0.0786
6	0.1851	NT	0.1615	0.1736	0.0848	0.0774
7	0.1968	NT	0.1560	0.1806	0.0840	0.0796
8	0.2082	NT	0.1704	0.1878	0.0901	0.0797
9	0.2120	NT	0.1645	0.1935	0.0896	0.0819
10	0.2331	NT	0.1798	0.2036	0.0964	0.0840
11	0.2447	NT	0.1583	0.1820	0.0882	0.0823
12	0.2696	NT	0.1861	0.2079	0.1026	0.0894
13	0.2613	NT	0.1800	0.2157	0.1018	0.0946
14	0.2931	NT	0.1979	0.2287	0.1112	0.1003
15	0.3226	NT	0.1906	0.2372	0.1101	0.1064
16	0.3396	NT	0.2083	0.2541	0.1196	0.1132
17	0.3537	NT	0.2006	0.2588	0.1176	0.1202
18	0.3704	NT	0.2182	0.2766	0.1276	0.1270
19	0.3829	NT	0.2099	0.2793	0.1257	0.1343
20	0.3715	NT	0.2267	0.2980	0.1257	0.1404
21	0.3462	NT	0.2184	0.2986	0.1352	0.1477
22	0.3462	NT	0.2339	0.3175	0.1327	0.1544
23	0.3262	NT	0.2249	0.3136	0.1384	0.1608
24	0.2809	NT	0.2389	0.3272	0.1463	0.1634
25	0.2446	NT	0.2294	0.3191	0.1424	0.1685
26	0.2105	NT	0.2413	0.3253	0.1488	0.1670
27	0.1857	NT	0.2309	0.3126	0.1445	0.1706
28	0.1635	NT	0.2427	0.3231	0.1445	0.1675
30	NT	NT	0.2522	0.3325	0.1511	0.1737
75	NT	NT	0.2617	0.2877	0.1689	0.2358
100	NT	NT	0.2349	0.2397	0.1591	0.2257
150	NT	NT	0.3093	0.2111	0.1795	0.2710
200	NT	NT	0.2475	0.2056	0.2075	0.2805
250	NT	NT	0.2175	0.2888	0.1970	0.3030

Table C-6. Dynamic single-depth deflectometer response data.

Pass	4HMA, GR, 10 CBR	2HMA, GR, 10 CBR	4HMA, LS, 6 CBR	2HMA, LS, 6 CBR	4HMA, LS, 10 CBR	2HMA, LS, 10 CBR
300	NT	NT	0.2291	NT	0.2052	0.2821
500	NT	NT	0.1932	NT	0.2166	0.2927
750	NT	NT	0.1591	NT	0.2152	ND
1000	NT	NT	NT	NT	0.2172	ND

ND = no data collected; NT = no test traffic applied

Table C-7. Permanent single-depth deflectometer response data.

Pass	4HMA, GR, 10 CBR	2HMA, GR, 10 CBR	4HMA, LS, 6 CBR	2HMA, LS, 6 CBR	4HMA, LS, 10 CBR	2HMA, LS, 10 CBR
1	0.0237	0.0154	0.0164	0.0088	0.0025	0.0003
2	0.0320	0.0266	0.0278	0.0121	0.0042	0.0000
3	0.0512	0.0217	0.0383	0.0190	0.0063	0.0017
4	0.0602	0.0334	0.0473	0.0220	0.0075	0.0021
5	0.0787	-0.0024	0.0556	0.0261	0.0095	0.0028
6	0.0920	NT	0.0619	0.0281	0.0104	0.0030
7	0.1127	NT	0.0692	0.0320	0.0125	0.0034
8	0.1300	NT	0.0750	0.0345	0.0135	0.0040
9	0.1530	NT	0.0823	0.0392	0.0158	0.0041
10	0.1780	NT	0.0879	0.0427	0.0169	0.0054
11	0.2095	NT	0.0943	0.0503	0.0195	0.0037
12	0.2449	NT	0.1039	0.0568	0.0225	0.0058
13	0.2773	NT	0.1136	0.0699	0.0263	0.0061
14	0.3201	NT	0.1229	0.0764	0.0299	0.0084
15	0.3735	NT	0.1330	0.0899	0.0343	0.0093
16	0.4200	NT	0.1435	0.1016	0.0384	0.0126
17	0.4717	NT	0.1543	0.1186	0.0430	0.0150
18	0.5254	NT	0.1657	0.1338	0.0472	0.0194
19	0.5852	NT	0.1776	0.1529	0.0530	0.0232
20	0.6279	NT	0.1898	0.1693	0.0581	0.0291
21	0.6615	NT	0.2024	0.1905	0.0645	0.0343
22	0.7161	NT	0.2144	0.2084	0.0701	0.0414
23	0.7720	NT	0.2275	0.2306	0.0765	0.0481
24	0.8173	NT	0.2392	0.2494	0.0816	0.0547
25	0.8530	NT	0.2525	0.2691	0.0874	0.0613
26	0.8822	NT	0.2637	0.2867	0.0912	0.0667
27	0.9077	NT	0.2765	0.3010	0.0975	0.0724
28	0.9283	NT	0.2864	0.3170	0.1004	0.0764
30	NT	NT	0.3062	0.3451	0.1004	0.0838
75	NT	NT	0.4437	0.5403	0.1595	0.1835
100	NT	NT	0.4622	0.5832	0.1690	0.2213
150	NT	NT	0.5465	0.6021	0.2087	0.2603
200	NT	NT	0.7415	0.6095	0.3075	0.3495
250	NT	NT	0.7840	0.6073	0.3277	0.4032

Table C-7. Permanent single-depth deflectometer response data.

Pass	4HMA, GR, 10 CBR	2HMA, GR, 10 CBR	4HMA, LS, 6 CBR	2HMA, LS, 6 CBR	4HMA, LS, 10 CBR	2HMA, LS, 10 CBR
300	NT	NT	0.8049	NT	0.3359	0.4255
500	NT	NT	0.9432	NT	0.4858	0.4599
750	NT	NT	0.9662	NT	0.5750	ND
1000	NT	NT	NT	NT	0.6806	ND

ND = no data collected; NT = no test traffic applied

Table C-8. Longitudinal ASG response data.

Pass	4HMA, GR, 10 CBR	2HMA, GR, 10 CBR	4HMA, LS, 6 CBR	2HMA, LS, 6 CBR	4HMA, LS, 10 CBR	2HMA, LS, 10 CBR
1	533	628	ND	243	91	91
2	499	734	ND	297	107	125
3	590	769	ND	372	94	115
4	510	1053	ND	329	121	144
5	522	1670	ND	241	115	147
6	518	NT	ND	331	147	145
7	522	NT	ND	214	134	160
8	581	NT	ND	322	168	137
9	527	NT	ND	218	155	178
10	630	NT	ND	317	192	125
11	608	NT	ND	301	173	174
12	719	NT	ND	177	209	89
13	739	NT	ND	171	211	201
14	876	NT	ND	81	246	95
15	1017	NT	ND	122	271	208
16	1195	NT	ND	257	292	126
17	1290	NT	ND	229	342	193
18	1473	NT	ND	448	335	360
19	1641	NT	ND	409	395	287
20	1716	NT	ND	471	365	434
21	1770	NT	ND	420	420	438
22	1683	NT	ND	418	385	132
23	1983	NT	ND	403	428	260
24	1758	NT	ND	421	391	139
25	1933	NT	ND	421	425	254
26	1670	NT	ND	433	376	207
27	1764	NT	ND	463	408	259
28	1820	NT	ND	473	371	283
30	NT	NT	ND	483	441	169
75	NT	NT	ND	925	577	479
100	NT	NT	ND	991	592	587
150	NT	NT	ND	1133	590	617
200	NT	NT	ND	1610	581	724
250	NT	NT	ND	1709	768	714

Table C-8. Longitudinal ASG response data.

Pass	4HMA, GR, 10 CBR	2HMA, GR, 10 CBR	4HMA, LS, 6 CBR	2HMA, LS, 6 CBR	4HMA, LS, 10 CBR	2HMA, LS, 10 CBR
300	NT	NT	ND	NT	652	1178
500	NT	NT	ND	NT	826	1194
750	NT	NT	ND	NT	676	ND
1000	NT	NT	ND	NT	710	ND

ND = no data collected; NT = no test traffic applied

Table C-9. Transverse ASG response data.

Pass	4HMA, GR, 10 CBR	2HMA, GR, 10 CBR	4HMA, LS, 6 CBR	2HMA, LS, 6 CBR	4HMA, LS, 10 CBR	2HMA, LS, 10 CBR
1	716	900	249	159	71	64
2	452	1076	255	244	89	39
3	635	ND	296	281	77	70
4	400	1499	272	291	95	51
5	569	1275	231	258	72	79
6	379	NT	256	314	80	55
7	529	NT	221	302	83	81
8	350	NT	240	337	78	66
9	470	NT	210	320	94	77
10	285	NT	205	340	80	88
11	332	NT	301	451	172	107
12	119	NT	177	299	105	116
13	241	NT	171	307	144	66
14	922	NT	81	222	143	140
15	1352	NT	122	214	152	81
16	1680	NT	257	160	171	115
17	1684	NT	229	279	141	150
18	1350	NT	448	636	212	355
19	1202	NT	409	689	219	340
20	954	NT	471	645	278	303
21	1519	NT	420	465	286	184
22	1302	NT	418	387	280	248
23	1001	NT	403	400	285	223
24	863	NT	421	412	288	268
25	691	NT	421	350	292	180
26	ND	NT	433	405	356	246
27	ND	NT	463	548	336	173
28	ND	NT	473	675	417	276
30	NT	NT	483	416	308	239
75	NT	NT	490	1219	564	630
100	NT	NT	425	1471	456	453
150	NT	NT	537	1884	451	670
200	NT	NT	775	2091	593	786
250	NT	NT	703	2319	491	994

Table C-9. Transverse ASG response data.

Pass	4HMA, GR, 10 CBR	2HMA, GR, 10 CBR	4HMA, LS, 6 CBR	2HMA, LS, 6 CBR	4HMA, LS, 10 CBR	2HMA, LS, 10 CBR
300	NT	NT	923	NT	405	ND
500	NT	NT	ND	NT	579	ND
750	NT	NT	ND	NT	430	ND
1000	NT	NT	ND	NT	495	ND

ND = no data collected; NT = no test traffic applied

Abbreviations

Term	Definition
AASHTO	American Association of State and Highway Transportation Officials
ADR	Airfield damage repair
APE	Airfield Pavement Evaluation
ASG	Asphalt strain gauges
ASTM	American Society for Testing and Materials
CBR	California bearing ratio
C_c	Coefficient of Curvature
CH	High-plasticity clay
cME	Classical Mechanistic-Emperical
C_u	Coefficient of uniformity
CS	Compressive strength
CSA	Calcium-sulfoaluminate
CTL	Compact track loader
DCP	Dynamic cone penetrometer
DoD	Department of Defense
EPC	Earth pressure cell
ERDC	Engineer Research and Development Center
ESG	Embedded strain gauge
FOD	Foreign object debris
FWD	Falling-weight deflectometer
FRP	Fiberglass-reinforced panel
GR	Crushed gravel
HMA	Hot-mix asphalt
HWD	Heavy-weight deflectometer
HVS	Heavy Vehicle Simulator
ISM	Impulse stiffness modulus
JE	Joint efficiency
LE	Layered elastic
LL	Liquid limit
LS	Crushed limestone
LOE	Line of equality
LVDT	Linear variable displacement transducer
MDD	Maximum dry density
MEPDG	Mechanistic-Empirical Pavement Design Guide
NAVFAC EXWC	Naval Facilities Engineering and Expeditionary Warfare Center
NM	Not measured
NMAS	Nominal maximum aggregate size
OD	Oven dry
OMC	Optimum moisture content
PCASE	Pavement-Transportation Computer Assisted Structural Engineering
PCC	Portland cement concrete

PD	Permanent deformation
PI	Plasticity index
PL	Plastic limit
PP	Pore pressure
RAP	Recycled asphalt pavement
RCA	Recycled concrete aggregate
RS	Rapid setting
SDD	Single-depth deflectometer
SSG	Surface strain gauge
SW	Well-graded sand
TDD	Target dry density
TMC	Target moisture content
TS	Tensile strength
USACE	United States Army Corps of Engineers
USCS	United Soil Classification System

REPORT DOCUMENTATION PAGE

Form Approved
OMB No. 0704-0188

1. REPORT DATE *(DD-MM-YYYY)*	2. REPORT TYPE	3. DATES COVERED *(From - To)*
March 2023	Final	

4. TITLE AND SUBTITLE

Naval Expeditionary Runway Construction Criteria:

P-8 Poseidon Pavement Requirements

5a. CONTRACT NUMBER

5b. GRANT NUMBER

5c. PROGRAM ELEMENT NUMBER

6. AUTHOR(S)

W. Jeremy Robinson, Jeremiah M. Stache, Jeb. S. Tingle, Carlos R. Gonzalez, Anastasios M. Ioannides, and James T. Rushing

5d. PROJECT NUMBER
488187

5e. TASK NUMBER

5f. WORK UNIT NUMBER

7. PERFORMING ORGANIZATION NAME(S) AND ADDRESS(ES)

Geotechnical and Structures Laboratory
US Army Engineer Research and Development Center
3909 Halls Ferry Road
Vicksburg, MS 39180-6199

8. PERFORMING ORGANIZATION REPORT NUMBER

ERDC/GSL TR-23-4

9. SPONSORING / MONITORING AGENCY NAME(S) AND ADDRESS(ES)

Naval Facilities Engineering and Expeditionary Warfare Center (NAVFAC EXWC)
1100 23rd Ave.
Port Hueneme, CA 93043

10. SPONSOR/MONITOR'S ACRONYM(S)

11. SPONSOR/MONITOR'S REPORT NUMBER(S)

12. DISTRIBUTION / AVAILABILITY STATEMENT

DISTRIBUTION STATEMENT A. Approved for public release; distribution is unlimited.

13. SUPPLEMENTARY NOTES

Funding Account Code B36399

14. ABSTRACT

A full-scale airfield pavement test section was constructed and trafficked by the US Army Engineer Research and Development Center to determine minimum rigid and flexible pavement thickness requirements to support contingency operations of the P-8 Poseidon aircraft. Additionally, airfield damage repair solutions were tested to evaluate the compatibility of those solutions with the P-8 Poseidon. The test items consisted of various material thickness and strengths to yield a range of operations to failure allowing development of performance predictions at a relatively lower number of design operations than are considered in traditional sustainment pavement design scenarios. Test items were trafficked with a dual-wheel P-8 test gear on a heavy-vehicle simulator. Flexible pavement rutting, rigid pavement cracking and spalling, instrumentation response, and falling-weight deflectometer data were monitored at select traffic intervals. The results of the trafficking tests indicated that existing design predictions were generally overconservative. Thus, minimum pavement layer thickness recommendations were made to support a minimum level of contingency operations. The results of full-scale flexible pavement experiment were utilized to support an analytical modeling effort to extend flexible pavement thickness recommendations beyond those evaluated.

15. SUBJECT TERMS

Expeditionary pavement
Accelerated pavement testing
Minimum thickness design
Airfield damage repair
P-8A Poseidon
Military bases
Runways (Aeronautics)–Evaluation
Pavements–Materials–Testing
Pavements–Materials–Evaluation

16. SECURITY CLASSIFICATION OF:			17. LIMITATION OF ABSTRACT	18. NUMBER OF PAGES	19a. NAME OF RESPONSIBLE PERSON
a. REPORT	b. ABSTRACT	c. THIS PAGE			19b. TELEPHONE NUMBER *(include area code)*
Unclassified	Unclassified	Unclassified	SAR	206	